Investigations of the early stages of recrystallization in interstitial-free and low-carbon steel sheets

Traka, K.

DOI
10.4233/uuid:962f6655-a1b8-4c38-8467-0b2b651ab629

Publication date
2022

Document Version
Final published version

Citation (APA)
Traka, K. (2022). *Investigations of the early stages of recrystallization in interstitial-free and low-carbon steel sheets*. [Dissertation (TU Delft), Delft University of Technology]. https://doi.org/10.4233/uuid:962f6655-a1b8-4c38-8467-0b2b651ab629

INVESTIGATIONS OF THE EARLY STAGES OF RECRYSTALLIZATION IN INTERSTITIAL-FREE AND LOW-CARBON STEEL SHEETS

INVESTIGATIONS OF THE EARLY STAGES OF RECRYSTALLIZATION IN INTERSTITIAL-FREE AND LOW-CARBON STEEL SHEETS

Dissertation

For the purpose of obtaining the degree of Doctor
at Delft University of Technology
by the authority of the Rector Magnificus, Prof. dr. ir. T.H.J.J. van der Hagen,
chair of the Board of Doctorates,
to be defended publicly on Wednesday 29 June 2022 at 12:30 o'clock

by

Konstantina TRAKA

Master of Science in Naval Architecture and Marine Engineering,
National Technical University of Athens, Athens, Greece,

born in Los Angeles, USA.

This dissertation has been approved by the promotors:

promotor: prof. dr. ir. J. Sietsma
promotor: prof. dr. -ing. Habil. D. Raabe
copromotor: dr. ir. C. Bos

Composition of the doctoral committee:

Rector Magnificus,	chairperson
Prof. dr. ir. J. Sietsma,	Delft University of Technology, promotor
Prof. dr. -ing. Habil. D. Raabe,	Max-Planck-Institut für Eisenforschung GmbH, promotor
Dr. ir. C. Bos	Delft University of Technology, copromotor

Independent Members:

Prof. dr. ir. L.A.I. Kestens,	Delft University of Technology
Prof. dr. I. Steinbach,	Ruhr-Universität Bochum
Prof. dr. B. Hutchinson,	Swerim AB
Prof. dr. S.H. Choi	Sunchon National University

Reserved Member::

Prof. dr. M.J. Santofimia Navarro
Delft University of Technology

Keywords: Recrystallization nucleation; Selective subgrain growth; Orientation selection; Full-field modelling; Cellular-automata
Printed by: Proefschrijftmaken

ISBN XXX-XX-XXXX-XXX-X

An electronic version of this dissertation is available at
http://repository.tudelft.nl/.

CONTENTS

List of Figures

List of Tables

List of abbreviations

Abbreviation	Meaning
BSE	Backscatter electron.
CA	Cellular-automaton.
CASIPT	Cellular-automata sharp-interface model for phase transformations (simulation package).
CP	Crystal plasticity.
DAMASK	Düsseldorf Advanced Material Simulation Kit (simulation package).
FFT	Fast Fourier transform.
GND	Geometrically necessary dislocations.
HAGB	High-angle grain boundary.
ICP	Inductively coupled plasma.
IF steel	Interstitial-free steel.
IPF	Inverse pole figure.
LAGB	Low-angle grain boundary.
EBSD	Electron backscatter diffraction.
EDX	Energy-dispersive X-ray spectroscopy.
GOS	Grain orientation spread.
LC steel	Low-carbon steel.
KAM	Kernel average misorientation.
MC-Potts	Monte-Carlo Potts.
MPF	Multi phase-field.
ND	Normal direction of the sheet.
ODF	Orientation distribution function.
OES	Optical emission spectroscopy.
PDE	Partial differential equation.
RD	Rolling direction of the sheet.
RVE	Representative volume element: used to indicate a simulation's input.
SE	Secondary electron.
SEM	Scanning electron microscope.
SSD	Statistically stored dislocations.
TD	Transverse direction of the sheet.
TEM	Transmission electron microscopy.
TF	Taylor factor.
α-fiber	Crystal orientations with $\langle 1\,1\,0\rangle \parallel$RD.
γ-fiber	Crystal orientations with $\langle 1\,1\,1\rangle \parallel$ND
ζ-fiber	Crystal orientations with $\langle 1\,1\,0\rangle \parallel$ND.
ϑ- fiber orientation	Crystal orientations with $\langle 1\,0\,0\rangle \parallel$ND
ϕ_1, Φ, ϕ_2	The three Euler angles based on the ZXZ convention, i. e. on a reference system xyz the crystal orientation is defined by successive rotations: ϕ_1 around z, then Φ around x, and then ϕ_2 again (around the new) z.
$\{h\,k\,l\}\langle u\,v\,w\rangle$	Notation indicating that the crystal orientation has $\langle h\,k\,l\rangle \parallel$ND and $\langle u\,v\,w\rangle \parallel$RD.

SUMMARY

The present thesis investigates recrystallization and related phenomena in interstitial free (IF) and low carbon (LC) microstructures. Emphasis is given mostly on the early stages of recrystallization, i. e. nucleation stage. The investigations are performed with experimental measurements and computer simulations. In all studies, recrystallization is observed with close coupling to the deformation substructure. Crystallographic texture analysis is used as a means to: (a) confirm trends between the simulated and experimental microstructure and (b) interpret the evolution of recrystallization in terms of selective subgrain growth. The goal of this thesis is to obtain insight into recrystallization initiation and evolution in low alloyed cold rolled steel sheets.

The first study (Chapter 2) incorporates a site-specific experimental investigation with the use of 2D electron backscatter diffraction (EBSD) to assess primary recrystallization in low carbon (LC) steel cold-rolled up to 65% thickness reduction. Various samples of the sheet are subjected to isothermal annealing at 600 °C. The heating is interrupted in specific time intervals to characterize the microstructure in marked areas. At each sample, the partially recrystallized microstructure is observed in correspondence to the prior deformed state. It is shown that grains characterized by high intergranular orientation gradients in the as-deformed state recrystallize fast, whereas grains with low interior misorientations resist. The spatial heterogeneity of recrystallization is also confirmed from the large variability of the recrystallization kinetics when quantified in different regions of the sheet, especially during the early stages of annealing. Despite the variability in the kinetics, rapid recrystallization is confirmed to take place in the first 20 s of heating, during which 40-60% of the material recrystallizes. Thenceforth, the recrystallization kinetics decrease insofar as even after additional 340 s of heating there is still some deformed material. The latter is attributed to the low stored energy in some regions, to the concurrence of recovery and to the particle pinning (Zener force) at grain boundaries. As for the crystallographic texture, the recrystallized volume is characterized by mostly γ-fiber ($\langle 1\,1\,1\rangle \parallel$ normal direction, ND), α-fiber ($\langle 1\,1\,0\rangle \parallel$ rolling direction, RD) and ζ-fiber ($\langle 1\,1\,0\rangle \parallel$ ND) texture. Given that γ- and α-fiber texture components comprised the material already at the as-deformed state, it is clear that the ζ-fiber orientations are particularly favored during the recrystallization of the present material. This is attributed to the fact that such components are located in fragmented regions within deformed grains and therefore have sufficient driving force to recrystallize while also preserving high misorientation from their surroundings (i. e. they are mobile).

Although the above study shows the onset and evolution of recrystallization in close coupling to the deformation substructure, nucleation cannot be traced for two reasons: (a) a one-to-one comparison of the state at each material element through the microstructure evolution is not feasible and (b) distinguishing strain-free volumes from the deformed matrix requires the recrystallized volume to have already expanded at least for a few micrometers.

For this reason, the next studies involve the use of computer simulations where the nucleation stage is also modelled. In particular, a cellular-automaton (CA) model for grain and subgrain growth simulations is developed, in a way that it allows its application to deformation substructures of highly strained materials described at the mesoscopic scale, i. e. where the state variables (crystal orientation) exhibit high spatial variations insofar as many elementary volumes (cells) are dissimilar from their surroundings. The present approach has two main advantages when used for recrystallization simulations: (a) nucleation is not imposed but it occurs naturally out of the evolving substructure and (b) all stages included in recrystallization annealing (primary & secondary recrystallization, grain growth) are described in the same physics based framework[1]. This enables recrystallization and related phenomena to be simultaneously simulated, which is crucial, especially since different regions in the material can undergo for example recovery or grain growth at the same time another region recrystallizes. Hence, any attempt to model recrystallization nucleation can only be done by applying a subgrain/grain coarsening algorithm without differentiating the kinematic and transformation rules between primary recrystallization (nucleation and growth), secondary recrystallization, and grain growth.

Such full-field simulations of recrystallization, i. e. by using a model that operates with kinematic and transformation rules likewise for grain coarsening phenomena, were introduced by works, e. g. by Humphreys [3] and Holm *et al.* [4], who used a network and the probabilistic CA method based on the multistate Monte-Carlo (MC) Potts kinetics, respectively, in artificially generated grain/subgrain structures and varied the mobility and size of particular boundaries and subgrains. Such works served as the basis for the full-field modeling of recrystallization in terms of selective grain/subgrain growth that followed. In particular, using input from crystal plasticity (CP) full-field simulations and electron backscatter diffraction (EBSD), Han *et al.* [5] and Bate [6], and Suwa *et al.* [7], respectively, used deterministic grain coarsening techniques such as the multi phase-field (MPF) method [8–12], the deterministic curvature-driven CA method [13] and the network model described in [3].

Such works are very important and pertinent to our current understanding of recrystallization, because the stage of nucleation is unresolved in terms of the physical mechanisms leading to such pronounced selective subgrain growth and orientation selection. Therefore, the approach taken in this thesis is similar to the aforementioned works, yet based on a different assumption regarding the substructure. In particular, in [6], [5] and [7] the authors had to assume and generate an artificial substructure based on the mesoscopic quantification of the stored deformation energy. This means that the substructure is assumed to be uniform and equiaxed at the level of grains, [5] or generated as (often as equiaxed) with a qualitative conversion of stored energy-related indicators such as the image quality (IQ) [7] or the von Mises stress [6].

However, in highly plastically strained steels, the substructure also comprises rectangular and elongated subgrains, while especially in regions of interest (i. e. deformation heterogeneities) the substructure is not uniform. On the other hand, generating the subgrains based on the gradients of the IQ or the stress, means that (a) heterogeneous subgrain formation is assumed to take place prior to the simulation and (b) a part of the competitive subgrain growth at the early stages of recrystallization has already taken place prior to the

[1] This framework was explained by Humphreys *et al.* [1], Humphreys [2] and it was implemented in the present thesis in a full-field description.

simulation. Despite the physical basis of all these techniques, here we want to investigate the growth competition of material elements by using the input deformed state as it is measured/modelled (i. e. unmodified) such that nucleation occurs naturally only due to discontinuous subgrain growth and high-angle boundaries' bulging. In other words, the aim here is to follow a different path: instead of assuming the substructure and generating it artificially, to operate based on a different assumption, i. e. that the input deformed state shows the actual substructure. Therefore, the modeling approach requires the use of a grain/subgrain coarsening algorithm that can operate even in highly deformed regions where the mesh size is close or even equal to the actual subgrain size. As this is not feasible with the present deterministic full-field methods, a deterministic CA method is developed, which in terms of driving force, is very similar to the well-known probabilistic CA based on MC-Potts kinetics algorithm.

The developed CA model is described in (Chapter 3) where it is also extensively tested for its applicability in different grids, with the use of representative volume elements (RVEs) of simple grain coarsening examples (Chapter 3). A bicrystal, a tricrystal and a polycrystal (characterized by random crystallographic texture) RVE are used for this purpose. Thenceforth, the model is applied to deformed starting microstructures.

The recrystallization simulations concern a cold-deformed IF steel sheet, of 75% thickness reduction. The temperature-time profile applied is in accord with the experimental measurement that is used for validation purposes. For the first investigation (Chapter 4), a 2D EBSD scan which consists of only a few deformed grains is used as starting microstructure. Deformation features (e. g. shear and deformation bands, grain boundaries) are distinguished and with a one-to-one comparison to the subsequent recrystallization several insights are obtained. The subgrains that successfully recrystallize are mostly located at intergranular boundaries. Deformation bands exhibit high relevance to recrystallization and the following mechanism is established: subgrains invade in bands that consist of smaller subgrains. After surpassing the first band, the recrystallized volume in most cases stops expanding as it meets similar crystal orientations. If, however, the recrystallization front meets high orientation gradients the recrystallized volume may continue to grow. A particularly favorable configuration for nucleation concerns regions where intersecting deformation bands are present. It is shown that such deformation features facilitate the onset of recrystallization. As for grain boundaries, these also act as nucleation sites, but are less active compared to intergranular recrystallization. This is attributed to the fact that the recrystallized volume produced by the motion of grain boundaries typically meets a rather coarse substructure which cannot provide sufficiently high driving forces. The microtexture evolution during the simulation is such that the deformation texture of combined γ- and α-fiber changes into a mostly γ-fiber texture. This trend is confirmed by the experimental measurement of the annealed state, that was performed in the investigated IF steel after following the associated heat treatment.

In the next study (Chapter 5), additional simulations are performed using more inputs, i. e. 2D orientation maps obtained from EBSD. The aim of this study is to obtain insight into the extent of recovery (discontinuous subgrain growth) and its relationship with the γ-fiber texture formation. Again, a one-to-one comparison is used to trace the state variables of each CA cell upon the analysis. In order to arrive in reliable quantifications, the effect of the resolution is also studied and discussed at each stage of the investigation. This is because the grid spacing of the EBSD may be larger than the subgrain size (especially in regions

of high stored energy) and thus any quantification is required to be done in simulations of different resolutions. Having established which quantifications depend on the resolution used, the different nucleation mechanisms that naturally occur through the simulation are investigated regarding their extent and relationship with crystallographic texture formation. It is shown that recovery, in terms of discontinuous subgrain growth, indeed occurs, but it neither dominates as a nucleation mechanism, nor is it responsible for forming the γ-fiber texture. Rather, recrystallization initiates directly at high-angle grain boundaries (HAGBs). Considering the previous investigation regarding the substructure topology, these HAGBs are mostly intergranular. As for the transition of the deformation to the recrystallization texture, this is shown to be a gradual phenomenon that happens during the expansion of the recrystallized volume. In particular, it is not the subgrains that initiate growing through HAGBs that are characterized by the recrystallization texture of the material, but only the ones that continue being competitive.

The last study (Chapter 6) incorporates a 3D coupled computation framework, where the input for simulating recrystallization is obtained from a crystal plasticity dislocation-density based simulation, performed based on advanced remeshing techniques introduced by Sedighiani *et al.* [14], Sedighiani [15]. The latter allows us to perform a simulation for high-level of deformation while preserving a sufficiently high resolution insofar as we can assume that the material elements are close to the actual subgrain size. Hence, in line with the objective of the present thesis[2], we apply the CA model - likewise in the previous chapters - and observe the selective subgrain growth in 3D. The coupled computation is applied to a simple bicrystal under isothermal annealing conditions at 800 °C. Despite its limited statistics, the deformed bicrystal incorporates in-grain orientation gradients and hence selective subgrain growth occurs during the recrystallization simulation. Additionally, the simulated microtexture evolution shows relevant trends with the material's recrystallization texture, which highlights the importance of the in-grain description and high resolution when modeling deformation and recrystallization. The evolution of recrystallization is discussed in different principal cross-sections and in the three-dimensional volume. The latter shows that the highest recrystallization rate is found in the range of $10-15$ s instead of the first seconds of heating. Thenceforth, the applicability of the coupled approach and its potential to address numerous scientific matters in the field of recrystallization are discussed.

The thesis ends (Chapter 7) with summarizing the performed studies, methods and findings. Aspects for which the present thesis forms a basis for future applications in line with contemporary research directions and availabilities in the field of recrystallization are also discussed.

[2]Normally, coupled deformation and recrystallization approaches are performed such that the dislocation content within material elements can be exploited. However, the main idea of the present thesis is to treat the material elements as subgrains or parts of them, in order to simulate nucleation.

REFERENCES

[1] F. J. Humphreys, G. S. Rohrer, and A. D. Rollett, *Recrystallization and related annealing phenomena*, third edition ed. (Elsevier, Amsterdam Oxford Cambridge, MA, 2017).

[2] F. J. Humphreys, *A unified theory of recovery, recrystallization and grain growth, based on the stability and growth of cellular microstructures—I. The basic model,* Acta Materialia **45**, 4231 (1997).

[3] J. F. Humphreys, *A Microstructural Model of Recrystallization,* Materials Science Forum **113-115**, 329 (1993).

[4] E. Holm, M. Miodownik, and A. Rollett, *On abnormal subgrain growth and the origin of recrystallization nuclei,* Acta Materialia **51**, 2701 (2003).

[5] F. Han, B. Tang, H. Kou, J. Li, and Y. Feng, *Effects of subgrain size and static recrystallization on the mechanical performance of polycrystalline material: A microstructure-based crystal plasticity finite element analysis,* Progress in Natural Science: Materials International **25**, 58 (2015).

[6] P. Bate, *Modelling deformation microstructure with the crystal plasticity finite–element method,* Philosophical Transactions of the Royal Society of London. Series A: Mathematical, Physical and Engineering Sciences **357**, 1589 (1999).

[7] Y. Suwa, M. Tomita, Y. Tanaka, and K. Ushioda, *Phase-field Simulation of Recrystallization in Cold Rolling and Subsequent Annealing of Pure Iron Exploiting EBSD Data of Cold-rolled Sheet,* ISIJ International **61**, 350 (2021).

[8] J. W. Cahn and S. M. Allen, *A MICROSCOPIC THEORY FOR DOMAIN WALL MOTION AND ITS EXPERIMENTAL VERIFICATION IN Fe-Al ALLOY DOMAIN GROWTH KINETICS,* Le Journal de Physique Colloques **38**, C7 (1977).

[9] I. Steinbach, F. Pezzolla, B. Nestler, M. Seeßelberg, R. Prieler, G. Schmitz, and J. Rezende, *A phase field concept for multiphase systems,* Physica D: Nonlinear Phenomena **94**, 135 (1996).

[10] J. Eiken, B. Böttger, and I. Steinbach, *Multiphase-field approach for multicomponent alloys with extrapolation scheme for numerical application,* Physical Review E **73**, 066122 (2006).

[11] E. Miyoshi and T. Takaki, *Extended higher-order multi-phase-field model for three-dimensional anisotropic-grain-growth simulations,* Computational Materials Science **120**, 77 (2016).

[12] E. Miyoshi and T. Takaki, *Validation of a novel higher-order multi-phase-field model for grain-growth simulations using anisotropic grain-boundary properties,* Computational Materials Science **112**, 44 (2016).

[13] K. Kremeyer, *Cellular Automata Investigations of Binary Solidification,* Journal of Computational Physics **142**, 243 (1998).

[14] K. Sedighiani, V. Shah, K. Traka, M. Diehl, F. Roters, J. Sietsma, and D. Raabe, *Large-deformation crystal plasticity simulation of microstructure and microtexture evolution through adaptive remeshing,* International Journal of Plasticity **146**, 103078 (2021).

[15] K. Sedighiani, *Crystal Plasticity Simulation of Microstructure and Microtexture Evolution during Large Plastic Deformation*, Ph.D. thesis, Delft University of Technology, Netherlands (2022).

1

INTRODUCTION

1.1. RECRYSTALLIZATION ANNEALING

Recrystallization and related phenomena (recovery, grain growth) are thermally activated processes involved in the heat treatment known as recrystallization annealing. This heat treatment is applied subsequent to deformation to restore the ductility of the metal, which is significantly reduced after cold working. However, this occurs at the expense of strength and hardness, which decrease during recrystallization annealing. Generally, recrystallization annealing alters several microstructural aspects that determine important metallic properties including magnetic, mechanical, electrical. For this reason, tailoring the material properties upon metal manufacturing requires the understanding and controlling of the microstructure evolution during recrystallization.

In the case of cold-rolled low alloyed steels, such as interstitial-free (IF) and low-carbon (LC) steel sheets, the microstructure control associated with recrystallization annealing is focused on attaining optimum values of strength and formability. While the former depends on the annealed microstructure's grain size the latter is also majorly affected by the crystallographic texture [1]. More specifically, the strength is associated with the dislocations mean free path and hence it is readily determined from the recrystallized sheet's average grain size (known as Hall-Petch strengthening). As for the formability of the sheet, this relates to both the grain size and the crystallographic texture of the annealed sheet. The grain size affects the hardening of the metal and hence it is also considered upon controlling the microstructure with regard to metal forming. The crystallographic texture of the material affects its formability because the strain distribution and plastic flow depend on the crystal orientation. To achieve good drawability, the annealed sheet should be characterized by high normal anisotropy and small planar anisotropy - known as Lankford values r and Δr [1]. This is typically accomplished when the recrystallized material is characterized by high fractions of orientation components with $\langle 1\,1\,1 \rangle \parallel$ normal direction (ND). Some texture components amount to very different normal and planar anisotropy values (e. g. see values for some texture components in [2]) insofar as small changes in the recrystallized sheet's

texture can majorly change its formability. Hence, understanding the onset and evolution of recrystallization and related phenomena in IF and LC steel sheets has been of high interest for many decades.

1.2. RECRYSTALLIZATION IN STEEL SHEETS - THEORETICAL BACKGROUND

During deformation the free energy of the material becomes high, primarily due to the increase in the dislocation density [3]. For example in cold-rolled low-alloyed steels, a thickness reduction above 50% typically changes the dislocation density from approximately $10^{11}/\mathrm{m}^2$ to $10^{14}-10^{16}/\mathrm{m}^2$. Driven by the reduction of this excess in free energy, recrystallization occurs: defined as the growth of strain-free volumes via the migration of high-angle grain boundaries (HAGBs). During this process, the prior elongated grains characterized by interior orientation gradients and high dislocation density are gradually replaced by equiaxed strain-free grains.

The origin of these strain-free grains is often related to the deformed material. In particular, when the deformation structure arranges in dislocation cells and subgrains [4] the formation of strain-free volumes is attained by the growth of particular subgrains, i. e. the so called nuclei. The subgrain formation and growth mechanism was developed around 70 years ago by works such as [4–11] to explain the process of nucleation in recrystallization and has been used as fundamental knowledge ever since.

Although the process of nucleation is indeed well-explained by the subgrain formation and growth mechanism, there are still many complications. Most are related to the fact that there are numerous dislocation cells and subgrains comprising the deformation substructure, while only few nucleate. Even if we consider that a HAGB is required for a subgrain to recrystallize, still there are numerous subgrains that abut or form HAGBs. Therefore the term nucleation does not correspond to a particular mechanism but rather to the fact that some subgrains grow faster than their surroundings insofar as their expanded volume becomes distinguishable at the mesoscopic scale. Considering that the boundary migration rate - in the case of recrystallization and grain growth - can be decomposed in the product of a kinetic factor (mobility) and driving force [5, 12], a subgrain will grow faster than others if it has (and preserves) high mobility and larger size compared to its changing neighbourhood. These prerequisites are known as kinetic and energy[1] advantage. And there are numerous mechanisms that relate to either of the two, and that are able to explain particular phenomena, for example regarding the evolution of specific texture components. Here it should be mentioned that crystallographic texture formation, besides its high industrial relevance in terms of microstructure control, has majorly contributed to the field of recrystallization by serving as a statistical tool for providing, questioning, and validating scientific insights.

Table 1.1 summarizes the nucleation mechanisms relevant to IF and LC steel sheets[2]. As is shown, many mechanisms are responsible for providing either a kinetic or an energy

[1] The energy advantage is also known as size advantage. However, to be more precise the term energy advantage will be used since the energy stored at subgrain boundaries is also related to their misorientation.

[2] For detailed explanations and findings regarding the nucleation of recrystallization the reader is prompted to books and reviews such as [2, 13–21].

advantage to particular subgrains. And while Table 1.1 includes the mechanisms that are already established, there are still more reasons that are able to explain the selective growth of subgrains, such as the effect of the dislocation character in the mobility of HAGBs [22] or variations in the small-angle boundaries mobility [23]. Eventually, the problem of recrystallization nucleation in terms of selective subgrain growth is still unresolved [24].

Table 1.1: Nucleation mechanisms participating.

Mechanism	**Contribution**	**Relevant studies**
Static subgrain formation	Subgrain formation continues upon heating and happens heterogeneously resulting in only some subgrains being larger (i. e. energy advantage) and more misoriented (i. e. kinetic advantage) than the rest.	[25, 26]
Discontinuous subgrain growth	Subgrains growing in regions with high orientation gradients form HAGBs and become kinetically unstable (i. e. kinetic advantage).	[6, 7, 9, 27–29]
HAGB bulging	Subgrains in contact with HAGBs can have or obtain larger size if the abutting substructure (on the other side of the HAGB) has much smaller subgrains (i. e. energy advantage).	[10, 11, 28–33]
Subgrain coalescence	Pairs of subgrains rotate into the same crystal orientation, thus forming a larger subgrain (i. e. energy advantage) of higher misorientation (i. e. kinetic advantage) from its surroundings.	[19, 34, 35]
Inhomogeneous particle pinning/solute drag	Boundaries with orientation relationships close to the ideal coincidence site lattice (CSL) relationship are less attractive to particles/solutes and hence are exempted from the Zener force (i. e. energy advantage) or from the solute drag (i. e. kinetic advantage).	[36–38]

1.3. OUTLINE OF THE THESIS

The structure of the present thesis incorporates six chapters where:

- Chapter 2 presents an experimental investigation of recrystallization annealing applied to a 65% thickness reduction LC steel sheet. The study is conducted in quasi in situ conditions: samples of the steel sheet are isothermally heated at 600°C and repeatedly interrupted for microstructure characterization in marked regions. The latter is accomplished with the use of electron backscatter diffraction (EBSD). The studies are focused on relating the deformation structure with the subsequent recrystallization. In particular, the inhomogeneity of recrystallization is discussed and it is related to the spatial distribution of misorientations at the prior deformed state. Relevant phenomena such as particle pinning at grain boundaries and texture formation are also observed and discussed.

- Chapter 3 presents a boundary energy-driven algorithm for grain and subgrain growth

simulations based on the deterministic cellular automaton (CA) method. The algorithm differs from the existing deterministic models as it does not calculate the boundary curvature but the energy change resulting from a cell's re-orientation. The reasons for taking this approach are explained in detail in Chapter 3 and Chapter 4. In this chapter, the algorithm is described, extensively tested in simple grain structures (bicrystal, tricrystal, polycrystal), and discussed regarding its applicability in different CA grids. The aim of this chapter is to present the model that is used in the subsequent chapters for recrystallization simulations and to establish the appropriate grids and input settings.

- Chapter 4 investigates recrystallization using the method described in Chapter 3 applied to a deformed IF steel sheet of 75% thickness reduction. The latter is obtained through 2D high resolution EBSD. The goal of this study is to investigate the onset and evolution of recrystallization by using (a) a method that does not impose nucleation but allows it to naturally occur through the simulation and (b) a one-to-one comparison between the temporal evolution of recrystallization and the prior deformation structure. The aim is to discuss the effect of the deformation topology in the subsequent recrystallization. More specifically, deformation features such as shear bands, deformation bands and grain boundaries are distinguished and investigated regarding their role in facilitating recrystallization.

- Chapter 5 studies the extent of recovery (discontinuous subgrain growth) and its effect on the γ-fiber texture formation that accommodates recrystallization in the IF steel sheet. For this purpose, 2D EBSD orientation maps are used as starting microstructures. Each input corresponds to a different grid spacing such that the effect of the resolution can be separated when conducting the necessary quantifications.

- Chapter 6 presents a 3D coupled deformation-recrystallization computation framework. In particular, a crystal plasticity dislocation-density based model is used to provide the starting microstructure for the recrystallization simulation. A simulation is presented and discussed in a deformed bicrystal. The goal of this study is to investigate the applicability of a very promising approach - namely the combination of the particular physics-based models. More specifically, the simulated deformed bicrystal incorporates deformation features (e. g. shear bands) and heterogeneously distributed in-grain misorientations which result in a realistic recrystallization simulation where nucleation occurs naturally. The temporal evolution of the microstructure, the microtexture and the kinetics and presented in this chapter and eventually the approach is discussed regarding its applicability and importance for future investigations.

- Chapter 7 summarizes the studies performed in the present thesis and highlights the main findings. The research work is evaluated for its advantages/disadvantages and discussed regarding its potential to address current issues related to recrystallization. Additionally, various future advances are described based on the approach followed in this thesis.

REFERENCES

[1] Lankford, Snyder, and Bausher, *New criteria for predicting the press performance of deep drawing sheets,* Transactions of the American Society for Metals **42**, 1197 (1950).

[2] F. J. Humphreys, G. S. Rohrer, and A. D. Rollett, *Recrystallization and related annealing phenomena*, third edition ed. (Elsevier, Amsterdam Oxford Cambridge, MA, 2017).

[3] Taylor, G. I., *The mechanism of plastic deformation of crystals. Part I.—Theoretical,* Proceedings of the Royal Society of London. Series A, Containing Papers of a Mathematical and Physical Character **145**, 362 (1934).

[4] R. Cahn, *Recrystallization of single crystals after plastic bending,* Journal of the Institute of Metals **76**, 121 (1949).

[5] J. Burke and D. Turnbull, *Recrystallization and grain growth,* Progress in Metal Physics **3**, 220 (1952).

[6] P. A. Beck, *The Formation of Recrystallization Nuclei,* Journal of Applied Physics **20**, 633 (1949).

[7] R. W. Cahn, *A New Theory of Recrystallization Nuclei,* Proceedings of the Physical Society. Section A **63**, 323 (1950).

[8] R. Cahn, *Internal strains and recrystallization,* Progress in Metal Physics **2**, 151 (1950).

[9] A. Cottrell, *Theory of dislocations,* Progress in Metal Physics **4**, 205 (1953).

[10] P. A. Beck, P. R. Sperry, and H. Hu, *The Orientation Dependence of the Rate of Grain Boundary Migration,* Journal of Applied Physics **21**, 420 (1950).

[11] C. H. Li, E. Edwards, J. Washburn, and E. Parker, *Stress-induced movement of crystal boundaries,* Acta Metallurgica **1**, 223 (1953).

[12] D. Turnbull, *Theory of Grain Boundary Migration Rates,* JOM **3**, 661 (1951).

[13] K. Lücke and M. Hölscher, *Rolling and Recrystallization Textures of BCC Steels,* Textures and Microstructures **14**, 585 (1991).

[14] L. A. I. Kestens and H. Pirgazi, *Texture formation in metal alloys with cubic crystal structures,* Materials Science and Technology **32**, 1303 (2016).

[15] P. R. Rios, F. Siciliano Jr, H. R. Z. Sandim, R. L. Plaut, and A. F. Padilha, *Nucleation and growth during recrystallization,* Materials Research **8**, 225 (2005).

[16] R. D. Doherty, *Recrystallization and texture,* Progress in Materials Science **42**, 39 (1997).

[17] D. Raabe and K. Lücke, *Rolling and Annealing Textures of BCC Metals,* Materials Science Forum **157-162**, 597 (1994).

[18] G. Gottstein and L. S. Shvindlerman, *Grain boundary migration in metals: thermodynamics, kinetics, applications*, 2nd ed., CRC series in materials science and technology (Taylor & Francis, Boca Raton, 2010) oCLC: ocn166358378.

[19] W. B. Hutchinson, *Development and control of annealing textures in low-carbon steels,* International Metals Reviews **29**, 25 (1984).

[20] B. Hutchinson, *Deformation microstructures and textures in steels,* Philosophical Transactions of the Royal Society of London. Series A: Mathematical, Physical and Engineering Sciences **357**, 1471 (1999).

[21] D. Raabe, *Recovery and Recrystallization: Phenomena, Physics, Models, Simulation,* in *Physical Metallurgy* (Elsevier, 2014) pp. 2291–2397.

[22] M. Winning, G. Gottstein, and L. Shvindlerman, *On the mechanisms of grain boundary migration,* Acta Materialia **50**, 353 (2002).

[23] M. Winning, A. Rollett, G. Gottstein, D. Srolovitz, A. Lim, and L. Shvindlerman, *Mobility of low-angle grain boundaries in pure metals,* Philosophical Magazine **90**, 3107 (2010).

[24] K. Ushioda, *Advances in research on deformation and recrystallization for the development of high-functional steels,* Science and Technology of Advanced Materials **21**, 29 (2020).

[25] R. L. Every and M. Hatherly, *Oriented Nucleation in Low-Carbon Steels,* Texture **1**, 183 (1974).

[26] M. R. Barnett and L. Kestens, *Formation of {111} and {111} Textures in Cold Rolled and Annealed IF Sheet Steel.* ISIJ International **39**, 923 (1999).

[27] J. Walter and E. Koch, *Substructures and recrystallization of deformed (100)[001]-oriented crystals of high-purity silicon-iron,* Acta Metallurgica **11**, 923 (1963).

[28] E. Holm, M. Miodownik, and A. Rollett, *On abnormal subgrain growth and the origin of recrystallization nuclei,* Acta Materialia **51**, 2701 (2003).

[29] F. Han, B. Tang, H. Kou, J. Li, and Y. Feng, *Cellular automata modeling of static recrystallization based on the curvature driven subgrain growth mechanism,* Journal of Materials Science **48**, 7142 (2013).

[30] J. Bailey and P. Hirsch, *The recrystallization process in some polycrystalline metals,* Proceedings of the Royal Society of London. Series A. Mathematical and Physical Sciences **267**, 11 (1962).

[31] I. L. Dillamore, C. J. E. Smith, and T. W. Watson, *Oriented Nucleation in the Formation of Annealing Textures in Iron,* Metal Science Journal **1**, 49 (1967).

[32] Y. Suwa, M. Tomita, Y. Tanaka, and K. Ushioda, *Phase-field Simulation of Recrystallization in Cold Rolling and Subsequent Annealing of Pure Iron Exploiting EBSD Data of Cold-rolled Sheet,* ISIJ International **61**, 350 (2021).

[33] B. Hutchinson, *Nucleation of recrystallisation,* Scripta Metallurgica et Materialia **27**, 1471 (1992).

[34] Y. Inokuti and R. Doherty, *Transmission kossel study of the structure of compressed iron and its recrystallization behaviour,* Acta Metallurgica **26**, 61 (1978).

[35] Y. Inokuti and R. D. Doherty, *Transmission Kossel Study of the Structure of Cold-Rolled Iron and its Nucleation Behaviour,* Texture of Crystalline Solids **2**, 143 (1977).

[36] G. Ibe and K. Lücke, *Über die spontane Keimbildung bei der Herstellung von Einkristallen durch Rekristallisation,* Kristall und Technik **2**, 177 (1967).

[37] K. Verbeken, L. Kestens, and M. Nave, *Re-evaluation of the Ibe–Lücke growth selection experiment in a Fe–Si single crystal,* Acta Materialia **53**, 2675 (2005).

[38] Zener, C., *Private communication to C.S. Smith. Cited in Trans. Am. Inst. Min. Engrs 175 15.* (1948).

2

SITE-SPECIFIC QUASI IN SITU INVESTIGATION OF PRIMARY STATIC RECRYSTALLIZATION IN A LOW CARBON STEEL

In the present work, the recrystallization behavior of a low carbon steel cold-rolled up to 65 % thickness reduction is studied. A quasi in situ setup that enables site-specific characterization is employed to gain a local picture of the nucleation and recrystallization process. Investigations in the microstructure evolution of individual samples confirm a relationship between the kernel average misorientation (KAM) values of the deformation structure and the subsequent onset and evolution of recrystallization. This, in combination with the orientation-dependent deformation inhomogeneity, results in the deformed grains with orientations within the γ-fiber (<1 1 1> // normal direction, ND) being the first to recrystallize, while the α-fiber (<1 1 0> // rolling direction, RD) grains exhibit high resistance on recrystallizing. The recrystallized grains are characterized mostly by γ- and α-fiber orientations and then by ζ-fiber (<1 1 0> // ND) orientation components. As only the latter are essentially absent from the prior deformation texture, their presence in the recrystallized material indicates that such orientation components are favoured during selective subgrain growth (nucleation) in the present material.

Parts of this chapter have been published in [1] by M. Diehl, L. Kertsch, K. Traka, D. Helm, and D. Raabe, Site-specific quasi in situ investigation of primary static recrystallization in a low carbon steel, Materials Science and Engineering: A 755, 295 (2019).

2.1. INTRODUCTION

As a topic of high industrial relevance, the evolution of microstructure and crystallographic texture resulting from primary static recrystallization [2] during the annealing step has been extensively studied, e.g. by Hölscher *et al.* [3], Raabe and Lücke [4, 5], Inagaki [6], Hutchinson [7], Samajdar *et al.* [8, 9], and Barnett [10], Barnett and Kestens [11]. From these previous studies[1] it is known that a comprehensive understanding of recrystallization requires to consider the full thermo–chemo–mechanical history of the material, starting at least with its state after hot rolling.

Some features already present in the hot rolled state remain mostly unchanged during cold rolling and can, therefore, influence the recrystallization behavior. These features include chemical inhomogeneity and—with the exception of changes due to internal fracture—precipitate size and distribution. Moreover, despite the severe texture formation during cold rolling, even certain recovery texture components from the hot rolling texture can be passed down to the deformation texture [4, 15, 16].

During cold rolling the grains accumulate high defect densities, i.e. mainly dislocations, and form crystallographic textures which are characteristic of the imposed near-plane strain deformation. In most low carbon steels the cold rolling texture is characterized by the gradual build up of a pronounced α-fiber ($\langle 1\,1\,0\rangle \parallel$ rolling direction, RD) and γ-fiber ($\langle 1\,1\,1\rangle \parallel$ normal direction, ND) texture [17]. Typically, the α-fiber texture accumulates lower dislocation densities and weaker local orientation gradients compared to most texture components on the γ-fiber[2].

Primary static recrystallization during annealing subsequent to the cold rolling process alters mainly two aspects of the material state: It firstly replaces the elongated and heavily deformed grains of the cold-rolled microstructure by small, globular grains with low dislocation density and secondly, it changes the crystallographic texture insofar as it often diminishes the prevalent α- and strengthens the γ-fiber texture components [8, 9]. The recrystallization tendency correlates strongly with the crystallographic orientation as the latter determines the degree of plastic deformation and, hence, the stored energy. Recovery in regions with low recrystallization tendency can further amplify the differences in stored energy, even to such an extent that only partial recrystallization occurs. Other factors retarding or hampering recrystallization include grain boundary pinning due to second phase particles [18, 19], impurity drag due to solute decoration of the grain boundaries and the limited mobility of grain boundary junctions [20].

For beneficial mechanical properties, i.e. good formability, a fully recrystallized microstructure that consists of small globular grains and a pronounced γ-fiber is desirable [21]. Such a microstructure can only be obtained when sufficient preceding deformation provides a high enough driving force for recrystallization, the heating rate is fast enough to suppress extensive recovery, and the annealing lasts for a sufficient amount of time to allow for newly formed crystals to sweep the adjacent deformation microstructure. For low carbon steels, a thickness reduction by at least 60 % during cold rolling, heating rates higher than several

[1] See also the older overview articles by Hutchinson [12] and Ray *et al.* [13] and the concise, recent one by Kestens and Pirgazi [14].

[2] Note that an orientation component can belong at the same time to more than one fibers - e. g. in the case of α- and γ-fiber $\{1\,1\,1\}\langle 1\,1\,0\rangle$ belongs to both.

$K\,s^{-1}$, and a annealing time of 1 min or longer at temperatures above 600 °C should result in a fully recrystallized microstructure [22].

In the present work, the recrystallization behavior of a commercial low carbon steel (DC04 grade) is studied. A quasi *in situ* setup [10, 23–26] that enables site-specific characterization is employed to gain a local picture of the nucleation and recrystallization process. This approach, which is based on scanning electron microscopy/electron backscatter diffraction imaging (SEM/EBSD) allows to link nucleation and growth directly to microstructural features such as grain shape, crystallographic orientation, and deformation level. For an investigation on the effects of second phase particles, the material is characterized additionally by secondary electron (SE) imaging. More specifically, the influence of Fe_3C carbides at the grain boundaries and dispersed manganese sulphide (MnS) precipitates is investigated. Finally, the combination of multiple measurement series allows to complement the observed behavior at the microstructure scale with global texture evolution data.

The study is structured as follows: First, in Section 2.2, the material is specified and the two employed experimental setups are presented. The results are presented in Section 2.3 which forms the basis for the following discussion (Section 2.4).

2.2. EXPERIMENTAL INVESTIGATION

2.2.1. MATERIAL

The material used in this study is a DC04 mild steel. Its chemical composition, measured with infrared absorption after combustion (content of C and S) and inductively coupled plasma and optical emission spectrometry (ICP-OES, remaining elements), is given in Table 2.1.

Table 2.1: Chemical composition of the investigated material in wt%. Balance is Fe.

C	Mn	Cr	Cu	Mo	N	Ni	P	S	Si	Al	Ti
0.044	0.185	0.0186	0.0225	0.0017	0.0052	0.0105	0.0066	0.0121	0.0060	0.0426	0.0013

The material was industrially cold rolled to approximately 65 % thickness reduction. Fig. 2.1 shows optical micrographs of the hot rolled and subsequently cold rolled material. The hot-rolled microstructure (Fig. 2.1a) consists of globular grains and two different kinds of precipitates: small globular MnS precipitates are randomly distributed within the grains and larger carbides are located along the grain boundaries. As a consequence of cold rolling, the initially globular grains became elongated and some of the carbides broke up into smaller pieces (Fig. 2.1b).

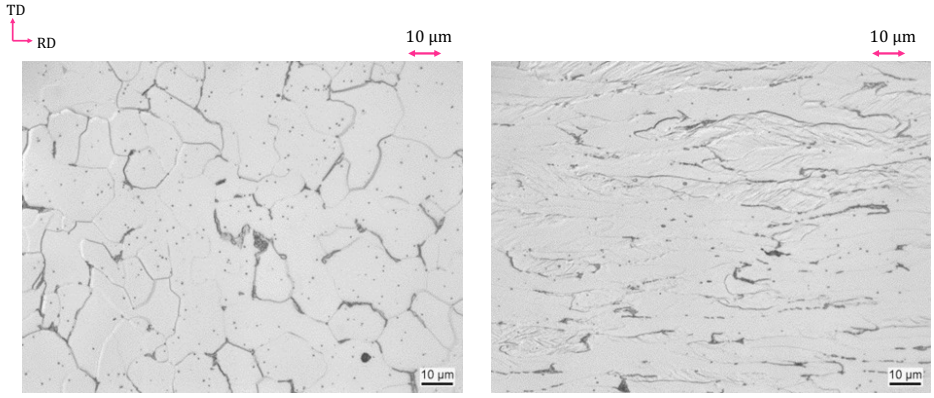

(a) After hot rolling (b) After cold rolling

Figure 2.1: Light microscopy images of the DC04 microstructure; (a) is the hot-rolled material and (b) the cold-rolled material.

2.2.2. QUASI *in situ* RECRYSTALLIZATION OBSERVATION APPROACH

The employed quasi *in situ* characterization approach, presented in similar form e.g. by Zhang *et al.* [25] and Zeng *et al.* [26], is based on interrupted annealing heat treatments. Interrupting the heat treatment is necessary to perform site-specific EBSD imaging which has an acquisition time much longer than the time required for full recrystallization in the investigated material in cold rolled state. Two challenges are associated with this approach: Firstly, a high quality of the sample surface for the EBSD measurements needs to be preserved, i.e. deterioration due to oxidation needs to be avoided. Secondly, recovery processes during heating up and cooling down for the measurements should be minimized. It should be noted that, while several studies reveal that the free surface only has a minor influence on the recrystallization behavior [27–29], nucleation events in the subsurface material cannot be tracked with this approach.

In the following, the two setups used in this study to perform the measurements are presented. In both setups, a polished sample (surface perpendicular to the normal direction, i. e. ND) was first characterized by means of EBSD and SE and then heat-treated and characterized with EBSD several times.

SETUP A - LONG HEATING RANGE

The first setup consists of a Gleeble 3150 integrated digital closed loop control thermal and mechanical testing system and a Zeiss SUPRA 40VP scanning electron microscope with TSL Orientation Imaging Microscopy for EBSD.

In order to minimize oxidation, the evacuated test chamber was twice flushed with argon before the experiment. Then, the heat treatment was performed in a low-pressure argon atmosphere. At the beginning of each cycle, the sample was heated up by resistance heating to 600 °C within 5 s using a two step procedure in order to prevent an overshoot of the temperature. To rapidly cool down the sample for the EBSD characterization, the heat dis-

charge of the cooled jaws was enhanced by exposing the sample to an argon stream. By this, a cooling rate of $-40\,\mathrm{K\,s^{-1}}$ until 300 °C was reached. The measured time–temperature diagram of one experiment is shown in Fig. 2.2a. Since after several heat treatment cycles the quality of the polished surface was not sufficient for EBSD characterization anymore, for total annealing times longer than 20 s the sample was slightly re-polished after the heat treatment steps. Scans were taken with a step width of 0.5 µm. After the last heat treatment step, the specimen was etched with 3 % nitric acid in ethanol and investigated by SE and energy-dispersive X-ray spectroscopy (EDX).

SETUP B - SHORT HEATING RANGE

For the heat treatment in this setup, a Bähr DIL 805A/D dilatometer was employed. To prevent corrosion, the chamber of the dilatometer was evacuated and flushed with argon three times before each heating cycle. The experiment itself was conducted in a low-pressure argon atmosphere. Via inductive heating the sample was heated up from room temperature to 600 °C in 4 s (average heating rate of $145\,\mathrm{K\,s^{-1}}$). Flushing with Nitrogen enabled cooling rates of approx. $-150\,\mathrm{K\,s^{-1}}$ until 100 °C was reached, see Fig. 2.2b). As in setup A, the overshooting of the temperature owing to the limited response time of the control system at high heating rates was minimized by decreasing the heating rate before approaching the target temperature. However, despite decreasing the heating rate at 530 °C, overshooting could not be completely prevented (see red curves in Fig. 2.3a). A JEOL JSM 6500F FEG-SEM microscope with an EDAX/TSL was used for EBSD and SE characterization. EBSD measurements have been performed at a step width of 0.25 µm, a small safety margin ensured that an overlapping area for each sample was achieved.

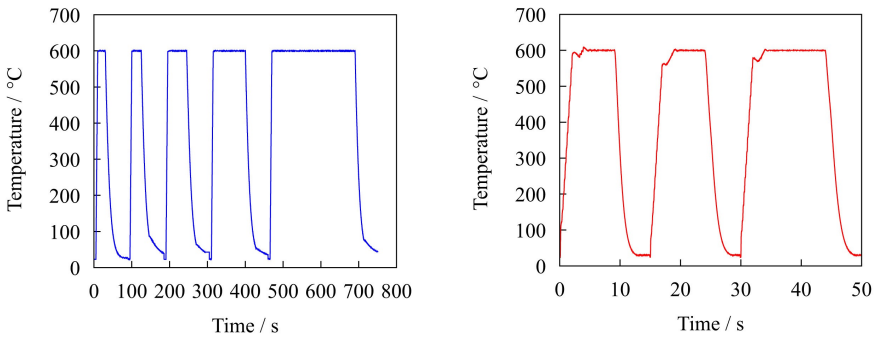

(a) Setup A – sample 1

(b) Setup B – sample 5

Figure 2.2: Temperature-time profile where (a) represents setup A, as measured for sample 1 (b) represents setup B, as measured for sample 5.

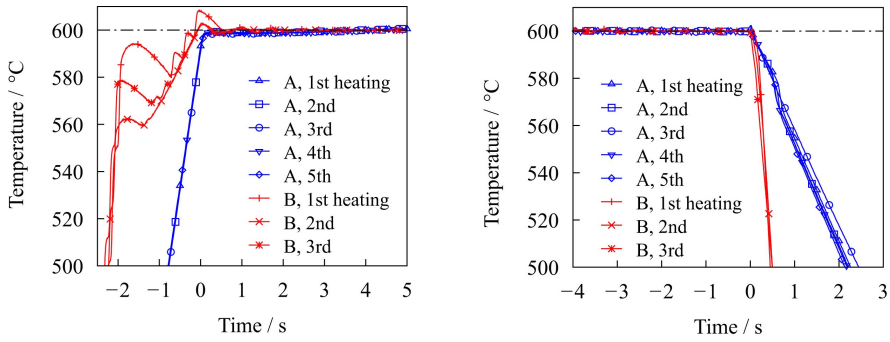

Figure 2.3: Measured temperature-time profile where (a) represents the heating cycles with time 0 s corresponding to the nominal beginning of annealing and (b) represents the cooling cycles with time 0 s corresponding to the nominal end of annealing.

2.2.3. POST PROCESSING

The orientation data has been processed and analyzed with the TSL OIM software in versions 5.3 and 7.3, respectively. Filtering operations include Neighbor Orientation Correlation, Neighbor CI (Confidence Index) Correlation, Grain CI Standardization, and Dilation. Additional analysis, such as calculating the orientation distribution functions (ODF) to plot the intensity of orientation components with $\phi_2 = 45°$, has been performed with the MTEX toolbox for MATLAB [30].

2.3. RESULTS

Altogether, the results of six specimens are presented. Two specimens have been heat-treated using setup A for a total nominal time of 400 s (sample 1, five steps) and 360 s (sample 2, six steps), respectively. After cropping all scans to the same area, they have a size of 146 µm × 170 µm (sample 1) and 142 µm × 161 µm (sample 2). Setup B has been used to subject three samples (sample 3, sample 4, and sample 5) to a three-step heat treatment with a nominal time of 5 s + 5 s + 10 s = 20 s and one (sample 6) to a single step one (i.e. 5 s). Sample 4, sample 5, and sample 6 encompass an area of approx. 100 µm × 300 µm while sample 3 has a size of approx. 600 µm × 600 µm. The measured area of all samples includes the sheet's RD and the transverse direction (TD), while sample 3 was additionally characterized in a longitudinal section (i. e. RD-ND) after the final heating step.

2.3.1. TIME–TEMPERATURE PROFILE

The measured temperature evolution over time is shown in Fig. 2.2 and selected details (end of heating/start of cooling) are given in Fig. 2.3. Here and in the following figures, blue lines belong to setup A and red lines to setup B. Fig. 2.3a shows that setup A allows heating from

560 °C to 600 °C within only 0.5 s compared to 2 s in the case of setup B where a slower heating rate is employed in an attempt to minimize overshooting. On the other hand, cooling from 600 °C to 560 °C takes almost 1 s with setup A compared to less than 0.3 s in setup B (Fig. 2.3b). In summary, the samples heat-treated with setup B are approximately 2 s longer in the critical temperature region 560 °C to 600 °C than prescribed while for the ones treated with setup A the actual heating duration is only 1 s longer than the nominal one.

2.3.2. RECRYSTALLIZED VOLUME FRACTION

By selecting measurement points belonging to regions with low Grain Orientation Spread (GOS), recrystallized grains are identified and the recrystallized volume fraction v is determined. The resulting evolution of v over the nominal heat treatment duration is shown in Fig. 2.4. The error bars added in the graph incorporate the uncertainty upon estimating the recrystallized fraction based on the orientation gradients. In particular, a 3% error is assumed to account for possible misidentifications of recrystallized/deformed regions - e. g. due to misorientation artifacts induced by surface polishing. A consistent trend among the different setups and samples is seen in this figure. However, some unsystematic variations between the five samples can be observed:

- after 5 s, between 4 vol.% (sample 3) and 36 vol.% (sample 6) recrystallized volume fraction is observed.
- sample 1 has 14 vol.% of remaining non-recrystallized grains after 400 s while sample 2 is essentially fully recrystallized after 360 s (3 vol.% are not recrystallized).

These variations exceed the uncertainty of 3% incorporated in the identification of the recrystallized volume and hence cannot be attributed to a systematic experimental error. The differences in the recrystallized fraction between the samples can be explained by considering the statistical sample size of each scan. More specifically, besides sample 3, all scanned areas comprise less than 200 µm at each dimension. As will be discussed later in Section 2.3.6 - see Fig. 2.14 - already along the RD the recrystallized fraction varies majorly.

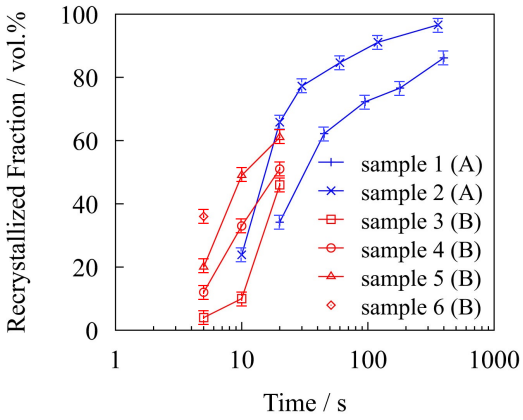

Figure 2.4: Comparison of the evolution of the recrystallized volume fraction of all samples presented in this study.

2.3.3. MACRO-TEXTURE

To investigate the evolution of the overall crystallographic texture in the early stage of recrystallization (up to 20 s), the ODF is calculated for the combined data of samples 3 to 5 and plotted in section $\phi_2 = 45°$. The initial texture is given in Fig. 2.5a and the texture after annealing for 20 s at 600 °C in Fig. 2.5b.

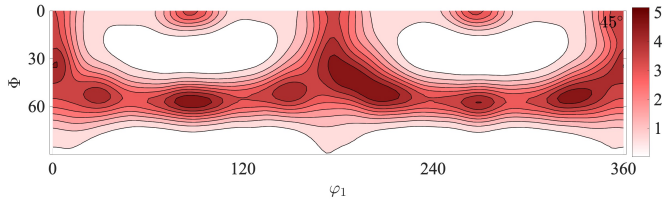

(a) 0 s: initial state (cold-rolled)

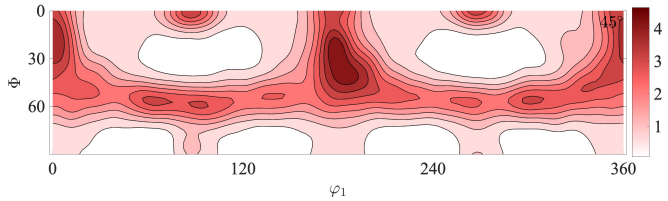

(b) After 20 s at 600 °C

Figure 2.5: Samples 3 to 5: ODF quantified and plotted in section $\phi_2 = 45°$ for (a) the initial condition after cold rolling and (b) after 20 s of annealing at 600 °C.

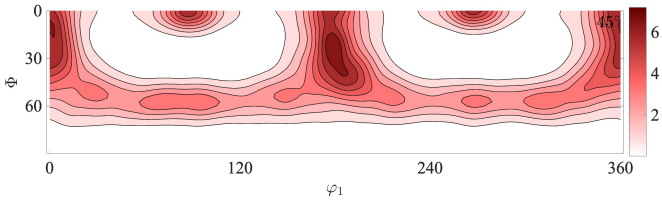

(a) 20 s: Non-recrystallized volume

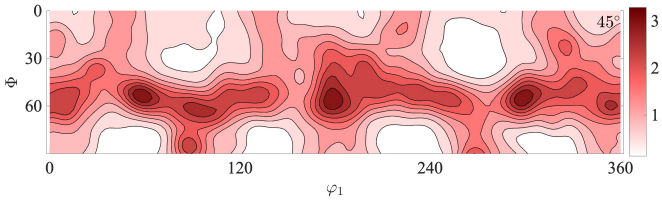

(b) 20 s: Recrystallized volume

Figure 2.6: Samples 3 to 5: ODF quantified and plotted in section $\phi_2 = 45°$ for the material after 20 s annealing of at 600 °C where (a) corresponds to the (still) deformed material and (b) to the recrystallized areas.

In the as-received condition, the typical plane strain compression texture of a material with bcc crystal structure is visible, i.e. the pronounced α- and γ-fibers are present. After the final heat treatment, Fig. 2.5b, the texture is weaker but qualitatively similar. To further investigate the orientation-dependency in recrystallization, the combined data of samples 3 to 5 are shown for non-recrystallized and recrystallized regions after 20 s in Fig. 2.6. It becomes obvious that the recrystallization texture differs from the deformation texture. More precisely, the intensity of $\langle 1\,1\,0\rangle \| \mathrm{RD}$ and $\langle 1\,1\,1\rangle \| \mathrm{ND}$ fibers decreases, although the latter still constitutes a large portion of the recrystallized volume. On the other hand, orientations with $\langle 1\,1\,0\rangle \| \mathrm{ND}$, and particularly the Goss (i. e. $\{1\,1\,0\}\langle 1\,0\,0\rangle$) and rotated Goss (i. e. $\{1\,1\,0\}\langle 1\,1\,0\rangle$) components dominate the texture evolution, especially since their respective intensities at the prior deformed state were insignificant.

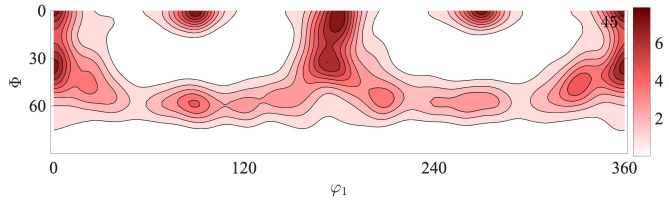

(a) 0 s: initial state (cold-rolled)

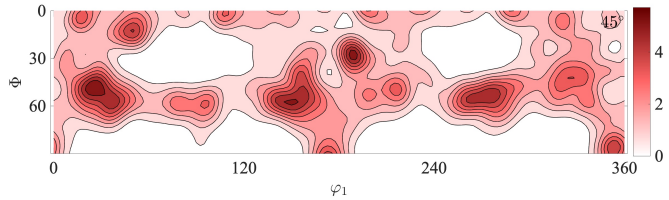

(b) After 400 s (sample 1) and 360 s (sample 2) at 600 °C: only recrystallized volume

Figure 2.7: Samples 1 and 2: ODF quantified and plotted in section $\phi_2 = 45°$ for (a) the initial condition after cold rolling and (b) the recrystallized volume after the heat treatment with setup A. The orientations of the recrystallized grains from sample 1 after 400 s and from sample 2 after 360 s are combined.

The findings from setup B, focusing on the initial stage of recrystallization, are complemented by results from setup A which give the texture evolution until almost full recrystallization. The ODFs of the combined data from samples 1 and 2 in cold rolled condition and after the heat treatment are given in Fig. 2.7, as plotted in section $\phi_2 = 45°$. Fig. 2.7a shows the initial condition. Fig. 2.7b shows the texture of the recrystallized grains after the last heat treatment step. Despite the significant difference in statistics between the two setups ($47,682\ \mu m^2$ is the total scanned area in setup A and $390,000\ \mu m^2$ in setup B), the results from setup A are in a certain compliance with the observations of setup B. Of course, the limited statistics of setup B cannot compare with the results derived from the data in setup A. However, the observed trends in terms of texture evolution between the two setups are not in disagreement, thus revealing no substantial trend reversal during the later stage of recrystallization.

2.3.4. TEXTURE COMPONENTS AND INDIVIDUAL ORIENTATIONS

For a more detailed analysis of the texture evolution, characteristic fiber components and individual orientations have been independently studied. All measured points that deviate by up to 10° from the nominal fiber direction or orientation, respectively, have been considered for the following analysis.

Fig. 2.8 shows the evolution of α-, γ-, and ζ-fiber components in sample 3 to 5 for all points (Fig. 2.8a) and separately for the non-recrystallized (Fig. 2.8b) and recrystallized (Fig. 2.8c) volume.

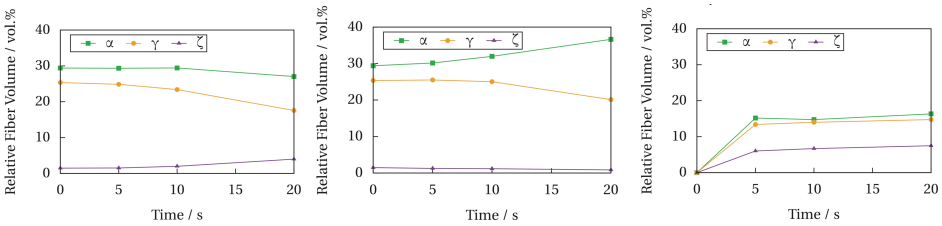

(a) Whole volume (b) Non-recrystallized volume (c) Recrystallized volume

Figure 2.8: Evolution of the texture fibers of samples 3 to 5. The misorientation range is 10°. The volume corresponds to (a) the whole material (b) the non-recrystallized material and (c) the recrystallized material.

As expected from the intensities of Goss and rotated Goss components shown in Fig. 2.5a, Fig. 2.6b and Fig. 2.7, the ζ-fiber is totally absent in the deformation texture and appears only during recrystallization. The initially slightly weaker γ-fiber decreases also slightly faster than the α-fiber (Fig. 2.8a). The separate consideration of the non-recrystallized (Fig. 2.8b) and the recrystallized (Fig. 2.8c) volume allows to investigate the reasons for this observation: while the growth-rates are similar, see Fig. 2.8c, recrystallized grains preferentially consume orientations belonging to the γ-fiber (Fig. 2.8b).

As for the individual orientations, quantifying their respective volume fractions[3] reveals that neither the "rotated cube" orientation, $\{0\,0\,1\}\langle 1\,1\,0\rangle$, (maximum of 5 % volume fraction in the deformed state) nor the Goss orientation (maximum of 1 % after recrystallization) exist with a significant volume fraction in any sample at any state.

2.3.5. DISLOCATION DENSITY

To determine the stored energy, the density of geometrically necessary dislocations (GNDs) can be estimated with an approach described in Field *et al.* [31]. It should be noted that 1) the technique gives only a lower bound, and 2) statistically stored dislocations (SSDs) might also contribute significantly to the total dislocation density, i.e. the stored energy. Therefore, interpretation is limited to a relative comparison. Fig. 2.9 shows the GND evolution in the deformation and recrystallized microstructure of sample 3-5. As expected, the GND density is much lower in the recrystallized microstructure. Moreover, it can be seen that during annealing the GND density in the deformation microstructure and in the recrystallized microstructure decreases significantly.

[3] The volume fractions are calculated based on the misorientation from the ideal component, using a threshold of 10°.

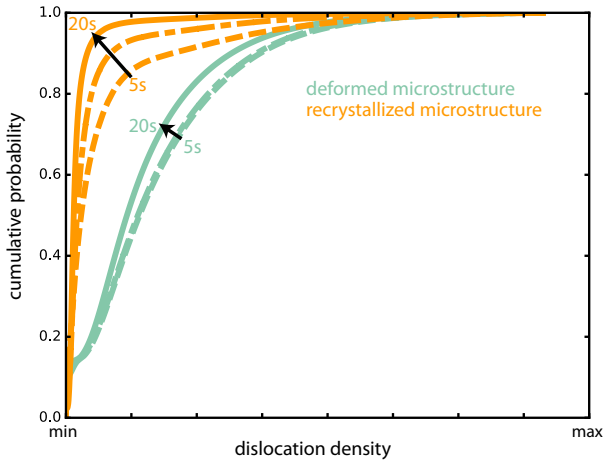

Figure 2.9: Sample 3 to 5: Evolution of GND density during the annealing in the recrystallized and deformed microstructure.

2.3.6. MICROSTRUCTURE

The microstructure of sample 1, colored according to the inverse pole figure (IPF) maps parallel to ND, is shown in Fig. 2.10 in the initial condition and after the first (20 s), second (45 s), and fifth (400 s) annealing step. The alignment of the grains stretched during cold rolling with RD (horizontal) is clearly visible in the initial condition (Fig. 2.10a). The initial microstructure consists mainly of regions with the ⟨1 0 0⟩ and the ⟨1 1 1⟩ parallel to ND, colored in red and blue, respectively. The inhomogeneous deformation in the grains can be seen from the color gradients, their varying wavelengths reveal that some grains are continuously bent while others have an alternating in-grain orientation spread. Within the first 20 s of annealing, approximately 100 new grains (recognizable by the absence of in-grain orientation scatter) appeared at the surface. These new grains either nucleated at the surface or nucleated in the subsurface microstructure and grew to the surface. As seen from Fig. 2.10b, the grain size of these new grains varies significantly. Moreover, many of the grains have orientations that are only seen as small fragments in the highly deformed regions at the initial microstructure, e.g. an alignment of the ⟨1 1 0⟩ direction with ND (green). After another heating range of 25 s, Fig. 2.10c, more grains nucleated and the previously recrystallized grains grew further. Finally, Fig. 2.10d shows the microstructure after 400 s, i.e. after five annealing steps. Most of the microstructure is replaced with newly formed grains with an average diameter (assuming equivalent circular grain areas) below 50 µm. The randomization of the texture observed in the section $\phi_2 = 45°$ of the ODF (Section 2.3.3) manifests itself in a very colorful IPF map. Still, 14 % of the scanned volume is not recrystallized after this time. This fraction forms few relatively large areas, from which the former grain shapes are still visible to some extent. As the remaining deformation microstructure has reddish colors, their ⟨1 0 0⟩ direction is aligned with ND.

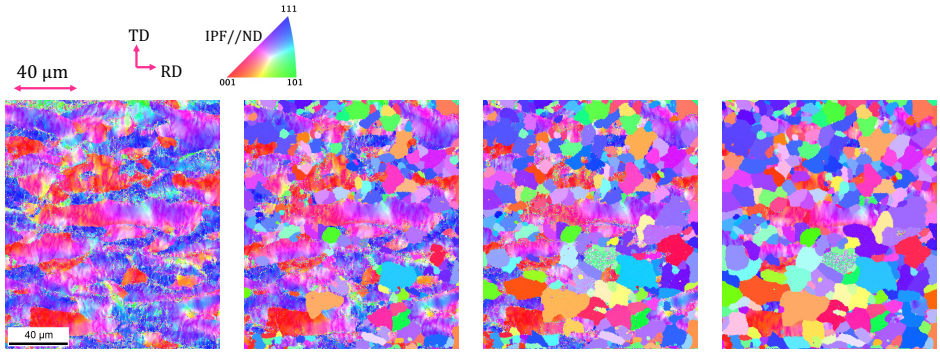

(a) 0 s (b) 20 s: $v = 34\%$ (c) 20 s + 25 s: $v = 62\%$ (d) 20 s + 25 s + 50 s + + 85 s + 220 s: $v = 86\%$

Figure 2.10: Sample 1: Microstructure shown at different annealing states. The recrystallized fraction is denoted by v.

After the heat treatment, sample 1 and sample 3 were etched and investigated by SEM in order to study the influence of local microstructural features on the recrystallization behavior. Two types of second phase particles were detected by SEM and EDX, manganese sulphides (MnS) and cementite (Fe_3C). While the first are randomly dispersed globular particles with diameters between 0.1 µm and 0.5 µm, the latter are larger elongated precipitates that are preferably located along the prior grain boundaries. Complementary investigations of hot rolled DC04 sheet showed that Fe_3C is formed during hot processing at the boundaries of the globular grains, cf. Fig. 2.1a.

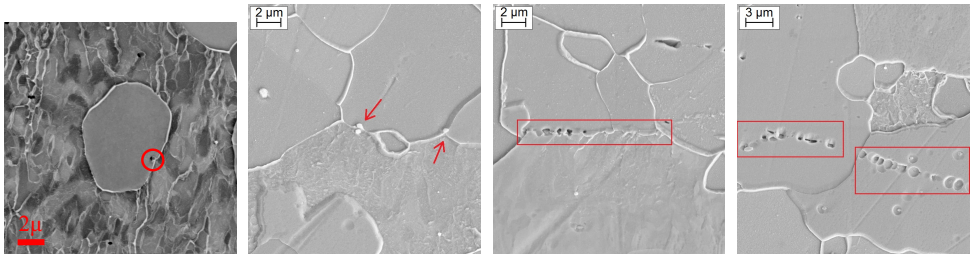

(a) BSE image, sample 3 after 30 s annealing. A MnS precipitate at the boundary between a recrystallized grain (center) and the deformed surrounding.

(b) SE image, sample 1 after 400 s annealing. MnS precipitates at the boundary between a recrystallized and a deformed grain (center) and at a triple point (right).

(c) SE image, sample 1 after 400 s annealing. Pits formed by cementite precipitates at the boundary between a recrystallized and a deformed grain.

(d) SE image, sample 1 after 400 s annealing. Pits formed by cementite precipitates, probably located at a prior grain boundary, now inside recrystallized grains.

Figure 2.11: High magnification Secondary Electron (SE) and Backscatter Electron (BSE) images of particle–recrystallization interaction events.

During cold rolling, the grains are strongly elongated, such that the cementite breaks into smaller pieces and gets detached. As Fig. 2.11a and Fig. 2.11b show, MnS precipitates

are often observed at boundaries/triple points. This is observed at boundaries between two recrystallized grains as well as between a recrystallized and a deformed grain. Occasionally, MnS particles are observed at triple points of the two-dimensional section, see Fig. 2.11b. On the contrary, Fe_3C is rarely directly observed after the heat treatment. This, however, might be an artifact of the experimental investigations as the repeated heating, cooling, and polishing, might have removed some of the incoherent precipitates leaving only small pits in the matrix. After annealing, some of the grain boundaries occupied with cementite are still present as can be seen in Fig. 2.11c but such prior boundaries are also found inside recrystallized grains, see Fig. 2.11d.

Similar as for sample 1 in Fig. 2.10, the IPF maps of sample 5 are shown in Fig. 2.12. Despite minimal cleaning efforts using the TSL OIM software, less non-indexed points are observed in Fig. 2.12b in comparison to Fig. 2.10a. Grains belonging to the α-fiber appear in green color in Fig. 2.12a and the ones belonging to the γ-fiber appear in blue color in Fig. 2.12b-Fig. 2.12e. Since only some grains in the deformed microstructure appear as green color in Fig. 2.12a and at the same time in red color in Fig. 2.12b, the observation of a low fraction of rotated cube grains is confirmed ($v = 0.5\,\%$ in this sample).

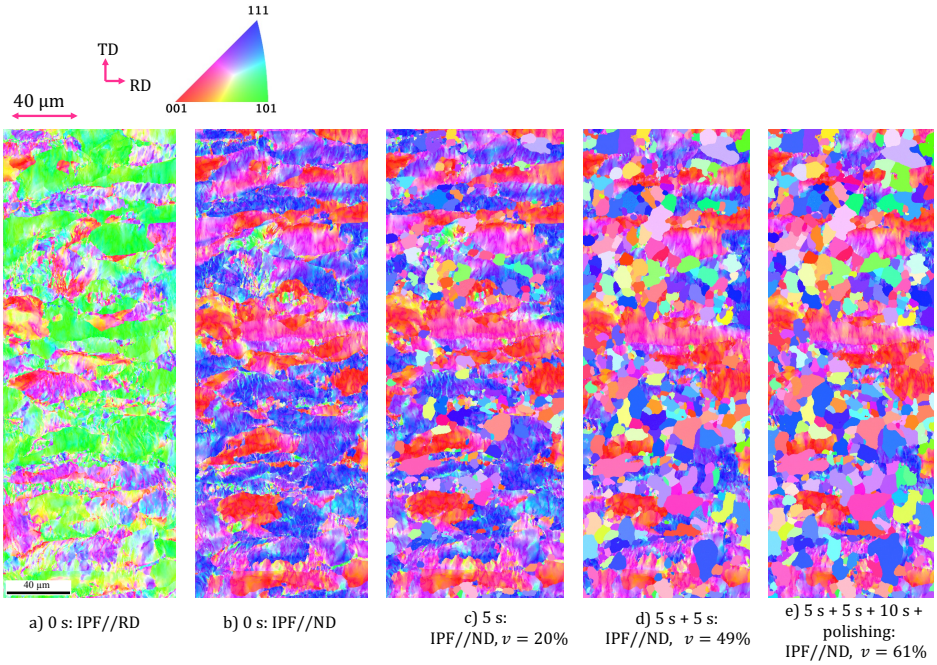

Figure 2.12: Sample 5: Microstructure shown at different annealing states. The recrystallized fraction is denoted by v.

As already apparent from Fig. 2.4, recrystallization happens comparably fast in this sample, i.e. after 10 s the recrystallized volume fraction is already at 49 % in sample 5 while after 20 s only a value of 34 % is reported from sample 1. Still, qualitatively the same observations can be made: Regions with the $\langle 1\,0\,0 \rangle$ orientation parallel to ND show the lowest recrystal-

lization tendency and grains with γ-fiber texture are preferentially consumed. This means that new grains appear in regions where the highest deformation has been accumulated: A comparison between the initial microstructure (Fig. 2.12b) and the microstructure after the first heat treatment with duration of nominally 5 s (Fig. 2.12c) shows that a significant portion of the recrystallization microstructure is located in regions in which the orientation is fluctuating at a high frequency in the deformed state.

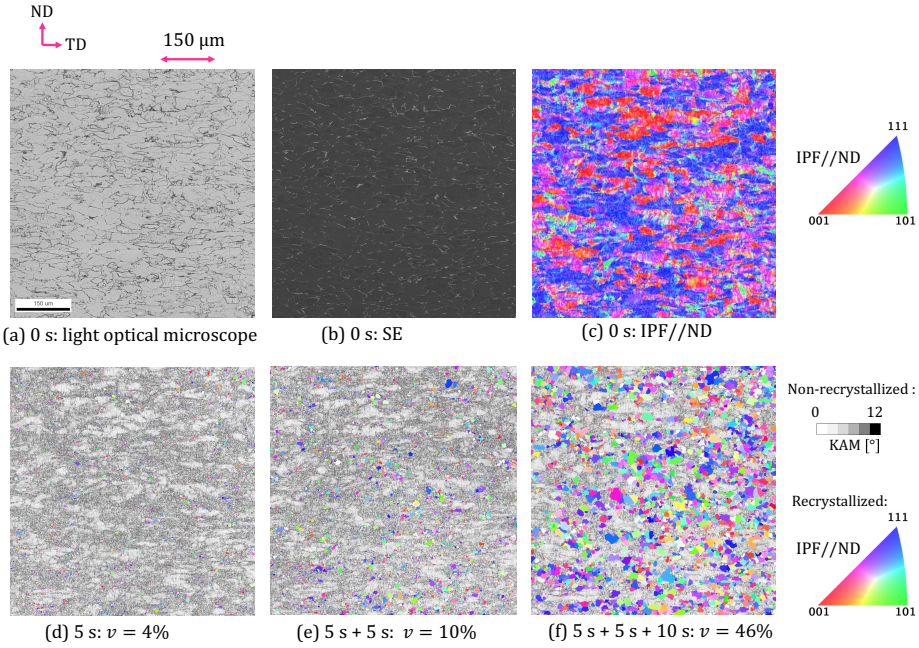

(a) 0 s: light optical microscope (b) 0 s: SE (c) 0 s: IPF//ND

(d) 5 s: $v = 4\%$ (e) 5 s + 5 s: $v = 10\%$ (f) 5 s + 5 s + 10 s: $v = 46\%$

Figure 2.13: Sample 3: Initial microstructure and partially recrystallized states plotted with combined IPF and KAM maps. The scanned area is equal to 600 µm × 600 µm and the recrystallized fraction is denoted by v.

Fig. 2.13 shows the initial microstructure of the larger sample 3 from SE imaging, light optical microscopy imaging, and EBSD together with EBSD maps of the recrystallization process. The grain boundaries are clearly visible from the light optical microscopy image (Fig. 2.13a); the SE image (Fig. 2.13b) reveals that most of them are decorated with cementite. Besides the prevalent ⟨1 0 0⟩ ∥ ND and ⟨1 1 1⟩ ∥ ND regions already seen in the IPF maps of sample 1 and sample 5, regions having ⟨1 1 0⟩ are also occasionally observed in Fig. 2.13c. The EBSD maps showing the recrystallization process (Fig. 2.13d-Fig. 2.13f) are composed from the Kernel Average Misorientation[4] in the deformed microstructure and the IPF ∥ ND in the recrystallization microstructure. From these images, it can be seen that sample 3 shows a comparably slow recrystallization rate and only after 10 s the recrystallization microstructure is obvious. As an addition to the finding from Section 2.3.4 that

[4]The Kernel Average Misorientation (KAM) is evaluated for each pixel up for its neighborhood until (and up to) the distance of the 3rd nearest neighbors with a cutoff of 12°.

a significant portion of the recrystallization texture belongs to the ζ-fiber, the microstructure maps reveal that these new grains are preferentially located in highly deformed regions. Considering the fact that these orientations are found in such fragmented regions, their preferential growth can be explained by the fact that they are more likely to preserve their high misorientation (i. e. kinetic instability) when consuming the adjacent deformed matrix.

Sample 3 was cut along the TD after the third heating cycle, i.e. nominally 20 s at 600 °C and characterized with a coarse resolution to measure an area of approximately 200 µm × 800 µm. Fig. 2.14 reveals two important aspects: First, the grain shape of the deformed grains can be described as "wavy", indicating that the grains size calculations from ND sections give too small values. Second, the variability in the recrystallized volume fraction is relatively high, i.e. there are regions of 200 µm × 200 µm (approximately 1/5 of the whole area) with less than 20 % recrystallized volume fraction and regions of the same size with more than 60 %. This observation explains the variations in the recrystallization evolution between the samples shown earlier, i. e. Fig. 2.4.

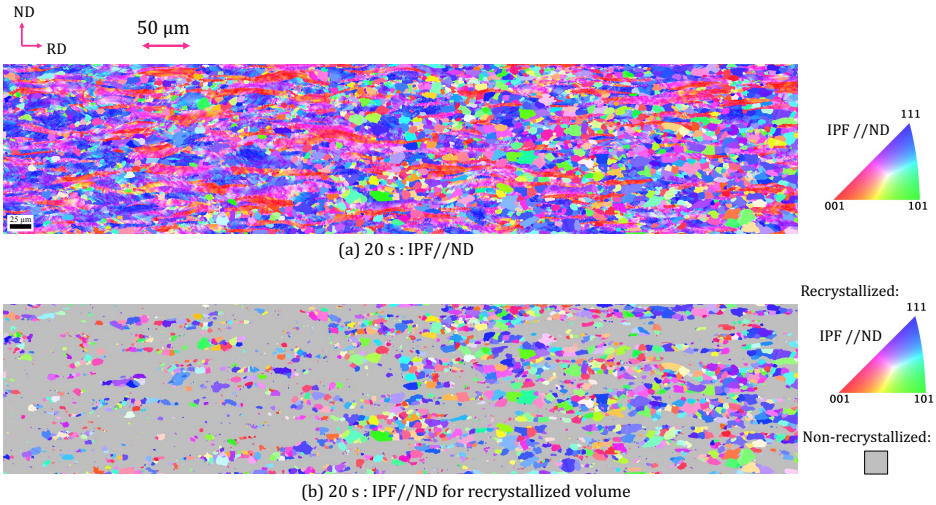

Figure 2.14: Sample 3 at 20 s where a) shows the microstructure and b) the recrystallized volumes only.

2.4. DISCUSSION

In the following, the employed approach is critically discussed and the findings with respect to the physics of nucleation and recrystallization are discussed.

2.4.1. SPATIAL CORRELATION

The presented EBSD images show that the employed approach enables the site-specific tracking of the microstructure evolution in highly deformed materials with high spatial resolution. By comparing the non-recrystallized regions before and after the polishing, it can

be seen that no significant error is introduced due to the slight polishing that is required in between some heating cycles.

However, it was not possible to overlay the measurement points from subsequent measurement steps in a one-to-one fashion. This is due to two inaccuracies: First, the manual mounting in the EBSD system always results in a slight misalignment. This misalignment can be corrected by linear deformation-like operation, which, however, will not make it possible to track individual pixels. Second, the slight temperature fluctuations in the electron microscope during one measurement cycle introduce nonlinear distortions. These distortions would require elaborated post-processing. While similar approaches exist for general image processing, the routines used to align slices in 3D EBSD [32, 33] seem to be a promising approach. However, it is not clear how they could cope with the abrupt changes in microstructure caused by the formation of new grains.

Another limitation of surface measurements is the missing in-depth information. This especially means that the nucleation environment cannot be investigated as any grain appearing at the surface might have been nucleated below.

2.4.2. ANNEALING CONDITIONS

The interrupted annealing aims at simulating continuous annealing at 600 °C. The heating and cooling required for the SEM measurements, therefore, disturb the desired heat treatment and might cause recovery and, hence, either retard recrystallization by reducing the stored energy or lead to the formation of nuclei via subgrain formation. As site-specific recovery dislocation density estimates are influenced by polishing, only the global quantities presented in Section 2.3.5 are discussed here. The results clearly show that on average also the non-recrystallized areas show a noticeable deformation energy reduction, which can be explained in various ways:

1. The regions that are preferentially consumed are the ones with higher dislocation density, and therefore the overall GND density is decreased.

2. The regions that are not consumed by a new grain have a decreased GND density due to recovery in terms of subgrain coarsening and dislocation annihilation.

Since higher dislocation density promotes recovery and recrystallization, subtle differences in deformation microstructure and heating conditions determine where recovery takes place [34]. It is obvious from the spatially resolved analysis (Section 2.3.6) that grains with higher dislocation density are consumed first, hence it can be assumed that the first effect dominates under the heating conditions investigated here. Moreover, the different time intervals used between setup A and setup B do not lead to a significantly different recrystallization behavior as would be the case if recovery between the nominal annealing cycles played an important role.

An additional source of inaccuracy is the overshooting of the temperature during heating which is especially pronounced in setup B. Retrospectively, it would have been better to reduce the initial heating rate to decrease the kink angle when reducing the heat rate before reaching the nominal temperature. Still, the consistency of the results obtained from both setups shows that their temperature control is sufficiently precise.

2.4.3. STATISTICAL RELEVANCE

The recrystallization rates of the different samples are in good agreement if one takes into account the highly non-linear kinetics of recrystallization. The observed scatter seems to be caused by the limited size of the individual specimens which is individually not fully representative for the material. This reasoning is also supported by the partially recrystallized state shown in Fig. 2.14, which shows that even within the same longitudinal area there is high variability in the recrystallization kinetics. In contrast, the texture evolution is consistent among the samples and can be predicted with good reliability even from the individual samples. This observation is affirmed by the fact that the observed texture evolution is not in contradiction with known results from similar materials [35, 36].

2.4.4. NUCLEATION SITES AND ORIENTATION

The results show that the local tendency of the deformed microstructure to be consumed by new grains can be approximately predicted from the deformation state in cold rolled condition. More precisely, the KAM or GND values in the deformation microstructure allow us to envision which regions are consumed first. This directly relates to crystallographic orientation, i.e. grains with a higher TAYLOR factor (typically γ-fiber) are among the ones that are consumed first. This finding is in agreement with previous studies [35]. Moreover, the regions of high grain fragmentation are the ones where new grains nucleate first. While in silicon steels typically Goss-oriented grains nucleate in the highly fragmented shear band regions [37], in interstitial free (IF) steels they are the nucleation sites for γ-fiber grains [10]. In this study, it is also found that only a few Goss grains nucleate but a substantial fraction of the ζ-fiber—which contains the Goss orientation—is found. Despite the appearance of "new" orientations, the spatial maps (Figs. 2.10 and 2.13) show—in agreement with texture plots (Figs. 2.6 and 2.7)—that the orientation of many recrystallized grains can be related to the orientations found in the vicinity of their appearance. However, a direct one-to-one observation of this behavior is difficult to obtain as nucleation also occurs in sub-surface regions which are not accessible to the employed surface characterization approach. In addition, a further increased spatial resolution would be required to resolve all sub-grain structures found in the heavily deformed grains with γ orientation to characterize all crystallographic orientation present at the surface in the vicinity of a nucleation event.

2.4.5. INFLUENCE OF PRECIPITATES

Precipitates can pin moving grain boundaries, e.g. by Zener pinning [2]. While at some places the motion of the recrystallization front is retarded due to the presence of cementite and MnS precipitates, cf. Fig. 2.11, precipitates are also found in the interior of newly formed grains. According to the Zener equation [38], the pinning force of such particles is proportional to the particle volume fraction and inversely proportional to the mean particle size. As seen in Fig. 2.1a, the MnS precipitates are randomly distributed in the microstructure and the individual precipitates are small (diameters below 0.5 µm) and of globular shape. Hence, Zener pinning can explain the jagged shape of the grain boundaries.

The cementite precipitates are larger, of elongated shape, and are very heterogeneously

distributed, predominantly along prior grain boundaries of the hot-rolled microstructure. In the cold-rolled microstructure, the broken precipitates are still limited only to the grain boundaries. Therefore, they can only effectively pin new grain boundaries when they cross the grain boundaries of the cold-rolled microstructure. Although cementite precipitates can locally delay recrystallization, cf. Fig. 2.11c, it can be assumed that the inhomogeneous distribution and large particle size prevents effective grain boundary pinning.

2.5. CONCLUSIONS

2.5.1. SUMMARY OF DISCUSSED ITEMS

Quasi *in situ* experiments have been performed using two different setups which allow to track microstructure evolution with high resolution in time and space. Consistent results among various samples have been collected which grounds the present study on a statistically relevant basis.

The influence of crystallographic orientation on the recrystallization behavior from previous mean-field investigations is confirmed [35, 36]: from the kernel average misorientation (KAM) values of the deformation structure, the consumption tendency can be predicted. Crystallographic analysis shows that the most deformed regions have either a γ-fiber orientation or belong to heavily fragmented shear band regions. New grains nucleate especially in such highly deformed regions and inherit often the orientation from the deformation microstructure [10]. This leads to an increase of the ζ-fiber via nucleation from the highly deformed region and an initial decrease of the γ-fiber which is preferentially consumed due to its high stored energy. As α-fiber and γ-fiber are present with the same volume fraction in recrystallized grains, the fully recrystallized microstructure has roughly the same volume fraction of both components. While from an industrial perspective a higher volume fraction of γ-fiber would be beneficial, for the strain level of $\varepsilon = 65\,\%$, such behavior is not surprising [35]. The overall weakening of the texture can be explained by the preferred nucleation in regions with very high grain fragmentation. The large differences in the stored energy due to dislocations are decisive for the tendency to recrystallize and dominate over the effects of precipitates.

2.5.2. GENERAL DISCUSSION AND OUTLOOK

The design, experiments and analyses conducted to address the evolution of recrystallization were performed by a very systematic and straightforward approach. Hence, although the insight obtained from the performed analyses is rather limited to confirming aspects within our current understanding of recrystallization in LC steel, the investigation itself is meaningful and such confirmations are still important given the advances and contemporary availabilities of experimental equipment. As for the inability to extract further information for the nucleation stage from the datasets analyzed here, this is related to the fact that: (a) a one-to-one comparison of the state at each material site is not feasible, and such an attempt could even lead to unreliable conclusions (for example due to small deviations in the spatial coordinates of individual material elements the energy advantage of subgrains could be in fact reversed) and (b) because the recrystallized volumes through the microstructure evo-

lution can only be differentiated from the still deformed material after having expanded at least a few micrometers. This means that the very early stages of the substructure evolution cannot be observed. For these reasons, all the next chapters use computer simulations as a means to investigate recrystallization, with a method developed and tailored to address the nucleation stage.

REFERENCES

[1] M. Diehl, L. Kertsch, K. Traka, D. Helm, and D. Raabe, *Site-specific quasi in situ investigation of primary static recrystallization in a low carbon steel,* Materials Science and Engineering: A **755**, 295 (2019).

[2] R. Doherty, D. Hughes, F. Humphreys, J. Jonas, D. Jensen, M. Kassner, W. King, T. McNelley, H. McQueen, and A. Rollett, *Current issues in recrystallization: a review,* Materials Science and Engineering: A **238**, 219 (1997).

[3] M. Hölscher, D. Raabe, and K. Lücke, *Rolling and recrystallization textures of bcc steels,* Steel Research International **62**, 567 (1991).

[4] D. Raabe and K. Lücke, *Annealing textures of BCC metals,* Scripta Metallurgica et Materialia **27**, 1533 (1992).

[5] D. Raabe and K. Lücke, *Rolling and Annealing Textures of BCC Metals,* Materials Science Forum **157-162**, 597 (1994).

[6] H. Inagaki, *Fundamental Aspect of Texture Formation in Low Carbon Steel.* ISIJ International **34**, 313 (1994).

[7] W. B. Hutchinson, *Practical Aspects of Texture Control in Low Carbon Steels,* Materials Science Forum **157-162**, 1917 (1994).

[8] I. Samajdar, B. Verlinden, P. Van Houtte, and D. Vanderschueren, *γ-Fibre recrystallization texture in IF-steel: an investigation on the recrystallization mechanisms,* Materials Science and Engineering: A **238**, 343 (1997).

[9] I. Samajdar, B. Verlinden, and P. Van Houtte, *Development of recrystallization texture in IF-steel: an effort to explain developments in global texture from microtextural studies,* Acta Materialia **46**, 2751 (1998).

[10] M. R. Barnett, *Role of In-grain Shear Bands in the Nucleation of //ND Recrystallization Textures in Warm Rolled Steel.* ISIJ International **38**, 78 (1998).

[11] M. R. Barnett and L. Kestens, *Formation of {111} and {111} Textures in Cold Rolled and Annealed IF Sheet Steel.* ISIJ International **39**, 923 (1999).

[12] W. B. Hutchinson, *Development and control of annealing textures in low-carbon steels,* International Metals Reviews **29**, 25 (1984).

[13] R. K. Ray, J. J. Jonas, and R. E. Hook, *Cold rolling and annealing textures in low carbon and extra low carbon steels,* International Materials Reviews **39**, 129 (1994).

[14] L. A. I. Kestens and H. Pirgazi, *Texture formation in metal alloys with cubic crystal structures,* Materials Science and Technology **32**, 1303 (2016).

[15] D. Raabe, *On the influence of the chromium content on the evolution of rolling textures in ferritic stainless steels,* Journal of Materials Science **31**, 3839 (1996).

[16] K. Banerjee, *Evaluation of Annealing Texture in IF and EDD Steel Sheets,* Materials and Manufacturing Processes **22**, 462 (2007).

[17] B. Hutchinson, *Deformation microstructures and textures in steels,* Philosophical Transactions of the Royal Society of London. Series A: Mathematical, Physical and Engineering Sciences **357**, 1471 (1999).

[18] M. Gómez, A. Quispe, and S. F. Medina, *Influence of the Microalloying Elements on the Temporary Inhibition of Static Recrystallization by Strain-Induced Precipitates,* steel research international **85**, 1440 (2014).

[19] T. Kozmel and S. Tin, *Effects of Carbides on the Microstructural Evolution in Submicron Grain 9310 Steel During Isothermal Heat Treatment,* Metallurgical and Materials Transactions A **46**, 3208 (2015).

[20] G. Gottstein and L. Shvindlerman, *Grain boundary junction engineering,* Scripta Materialia **54**, 1065 (2006).

[21] D. B. Lewis and F. B. Pickering, *Development of recrystallization textures in ferritic stainless steels and their relationship to formability,* Metals Technology **10**, 264 (1983).

[22] M. R. Barnett and J. J. Jonas, *Influence of Ferrite Rolling Temperature on Grain Size and Texture in Annealed Low C and IF Steels.* ISIJ International **37**, 706 (1997).

[23] M. Kiaei, R. Chiron, and B. Bacroix, *Investigation of recrystallization mechanisms in steels during in situ annealing in a SEM,* Scripta Materialia **36**, 659 (1997).

[24] A. Lens, C. Maurice, and J. H. Driver, *Grain boundary mobilities during recrystallization of Al–Mn alloys as measured by in situ annealing experiments,* Materials Science and Engineering: A **403**, 144 (2005).

[25] J. Zhang, L. Morsdorf, and C. C. Tasan, *Multi-probe microstructure tracking during heat treatment without an in-situ setup: Case studies on martensitic steel, dual phase steel and β-Ti alloy,* Materials Characterization **111**, 137 (2016).

[26] Z. R. Zeng, Y. M. Zhu, S. W. Xu, M. Z. Bian, C. H. J. Davies, N. Birbilis, and J. F. Nie, *Texture evolution during static recrystallization of cold-rolled magnesium alloys,* Acta Materialia **105**, 479 (2016).

[27] F. J. Humphreys and M. Ferry, *Combined In-Situ Annealing and EBSD of Deformed Aluminium Alloys,* Materials Science Forum **217-222**, 529 (1996).

[28] Y. Huang and F. J. Humphreys, *Measurements of grain boundary mobility during recrystallization of a single-phase aluminium alloy,* Acta Materialia **47**, 2259 (1999).

[29] P. J. Hurley and F. J. Humphreys, *A study of recrystallization in single-phase aluminium using in-situ annealing in the scanning electron microscope,* Journal of Microscopy **213**, 225 (2004).

[30] F. Bachmann, R. Hielscher, and H. Schaeben, *Texture Analysis with MTEX – Free and Open Source Software Toolbox,* Solid State Phenomena **160**, 63 (2010).

[31] D. P. Field, P. B. Trivedi, S. I. Wright, and M. Kumar, *Analysis of local orientation gradients in deformed single crystals,* Ultramicroscopy **103**, 33 (2005).

[32] S. Zaefferer, S. I. Wright, and D. Raabe, *Three-Dimensional Orientation Microscopy in a Focused Ion Beam–Scanning Electron Microscope: A New Dimension of Microstructure Characterization,* Metallurgical and Materials Transactions A **39**, 374 (2008).

[33] P. J. Konijnenberg, S. Zaefferer, S. B. Lee, A. D. Rollett, G. S. Rohrer, and D. Raabe, *Advanced Methods and Tools for Reconstruction and Analysis of Grain Boundaries from 3D-EBSD Data Sets,* Materials Science Forum **702-703**, 475 (2011).

[34] I. Kapoor, Y. Lan, A. Rijkenberg, Z. Li, and V. Janik, *Quasi in-situ analysis of geometrically necessary dislocation density in α-fibre and γ-fibre during static recrystallization in cold-rolled low-carbon Ti-V bearing microalloyed steel,* Materials Characterization **145**, 686 (2018).

[35] A. Miroux, H. Réglé, and B. Bacroix, *Effect of Cold Rolling Level on Recrystallization Textures in Low Carbon Steel Sheets - Modelling,* Materials Science Forum **273-275**, 433 (1998).

[36] C. Herrera, N. Lima, A. F. Filho, R. Plaut, and A. Padilha, *Texture and mechanical properties evolution of a deep drawing medium carbon steel during cold rolling and subsequent recrystallization,* Journal of Materials Processing Technology **209**, 3518 (2009).

[37] D. Dorner, S. Zaefferer, and D. Raabe, *Retention of the Goss orientation between microbands during cold rolling of an Fe3%Si single crystal,* Acta Materialia **55**, 2519 (2007).

[38] P. A. Manohar, M. Ferry, and T. Chandra, *Five Decades of the Zener Equation,* ISIJ International **38**, 913 (1998).

3

CELLULAR-AUTOMATON MODEL FOR BOUNDARY ENERGY-DRIVEN GRAIN/SUBGRAIN GROWTH

In order to overcome challenges when modelling recrystallization based on switching rules identical to grain/subgrain coarsening, particularly for highly deformed materials described in the mesoscopic view where the grid spacing is close to - or even equal to/larger than - the actual subgrain size, a cellular-automaton (CA) is developed. The model operates based on deterministic transformation rules: a cell re-orients to an adjacent dissimilar crystal orientation with a rate that relates to the migrating boundaries' mobility and the energy change associated with its surrounding boundaries. The algorithm is implemented in 2D square and hexagonal grids and in a 3D cubic grid. Investigations in these grids by varying the number of neighbours per cell and the grid-related input settings are presented in simple bicrystal, tricrystal, and polycrystal grain structures. The analysis reveals which grids are appropriate to simulate grain coarsening phenomena in terms of decreasing the artifacts associated with the boundary energy anisotropy. The kinetics upon simulating simple curvature-driven grain coarsening are also discussed and analyzed for their sensitivity in the grid-related settings. Discussions and comparisons to existing CA full-field approaches of the boundary motion associated with grain/subgrain coarsening are also presented.

Parts of this chapter have been published in [1] by K. Traka, K. Sedighiani, C. Bos, J. Galan Lopez, K. Angenendt, D. Raabe, and J. Sietsma, Topological aspects responsible for recrystallization evolution in an IF-steel sheet – Investigation with cellular-automaton simulations, Computational Materials Science 198, 110643 (2021).

3.1. INTRODUCTION

3.1.1. CELLULAR-AUTOMATA MODELS FOR GRAIN COARSENING - BACKGROUND

The CA method incorporates an algorithm that describes the discrete spatial and temporal evolution of physical processes by applying kinematic and transformation rules that change the state variables of elementary volumes (cells). The kinematics and transformation rules are defined according to the observation or underlying mechanism of the phenomenon that is simulated. The concept of the CA algorithm was first introduced by Von Neumann *et al.* [2]. Detailed description and relevant terminology of the CA method particularly in the field of metallurgy can be found in [3, 4]. Processes such as grain growth, which are driven by incremental changes of the energy state of boundaries are suitable to be described by cellular-automaton models. This is because the CA method enables the definition of dissimilar sites (i. e. cells with neighbours in different grains) which gives information on the interfacial size and shape in terms of boundary segments/areas between cells. With the use of appropriate constitutive state variables and kinematic rules, these local changes result in the transformation of cells imitating grain coarsening phenomena.

More specifically, the capillary-driven motion of grains is usually modelled by the consideration of the boundary energy change resulting from a cell's re-orientation, i. e. when a cell is fully consumed by an adjacent neighbour cell and inherits its crystal orientation. Thenceforth, the decision rule for whether a cell will re-orient is found by a prescribed probability (to each CA cell) that relates to the aforementioned energy change. This method was introduced by Anderson *et al.* [5, 6] as an extension of the Ising model [7] and it is known as Monte-Carlo (MC) Potts kinetics model. MC-Potts grain growth simulations have been investigated and used numerous times - e. g. in [8–17].

On the other hand, in deterministic CA simulations, the current state's boundary curvature is approximated. The latter is done by comparing the number of elementary volumes constituting the grains/subgrains abutting to the boundary. The boundaries' velocity can then be found from the driving force which is proportional to their curvature. Thenceforth, the decision for whether a cell re-orients is made based on its area/volume that has been surpassed by the boundary. This method was first introduced to simulate the solidification process [18] and was later adopted for simulating grain growth-related phenomena [19–24].

3.1.2. PRESENT METHOD AND PURPOSE

The approach that is presented here operates based on the deterministic CA method (see [4] for details), yet it is also similar to the aforementioned MC algorithm. This is because it approximates the incremental change of the energy state upon a cell switch. The underlying physical mechanisms and technical assumptions that are made to derive the kinematic and transformation rules in the CA algorithm are explained in detail in Section 3.2. The algorithm is implemented in the simulation package CASIPT [25, 26] (Cellular Automata Sharp Interface Phase Transformations).

The reason for developing a deterministic CA method for grain/subgrain coarsening instead of using the existing one developed by Kremeyer [18], is not related to advancing our

current understanding of normal grain coarsening phenomena. Rather, it has to do with developing a method that is applicable to simulating the associated boundary motion on prior deformed structures (i. e. recrystallization) described at the mesoscopic scale, e. g. by electron backscatter diffraction (EBSD) measurements. More specifically, as explained in Section 3.1.1, the existing curvature-driven grain coarsening CA algorithm approximates the driving force for boundary motion based on the difference in the number of CA cells constituting the surrounding subgrains. This means that: (a) subgrains of the same size, but of different misorientation on their surrounding boundaries (i. e. different values kernel average misorientation, KAM) cannot compete, which is not ideal if we want to consider the energy advantage at the mesoscopic scale, (b) a subgrain/grain grows into adjacent subgrains/grains only when it contains at least half the number of cells of a predefined neighborhood (typically 5x5 cells), and hence a subgrain grows when it is described from at least 15 cells, which is not typical when dealing with grid spacings close to the actual subgrain size and (c) it is not yet clear how curvature-driven algorithms operate when dealing with rather different shapes, such as rectangular and/or elongated subgrains, which are expected to be found for example in banded deformation features.

These indicate that using the existing CA method for subgrain coarsening, or other curvature-based methods, in a highly plastically strained material requires the simulation to be done in at least an order of magnitude finer mesh size in comparison to the actual subgrain size, and more specifically on what is considered to be a subgrain for the computational grid. Hence, EBSD data or deformation simulations can still serve as inputs, but only if the substructure is then artificially generated either by following grain mean-field attributes (e. g. as was done by Han *et al.* [27]) or by assuming some pixels to be a part of a subgrain after the very early stages of recovery, as was done by Suwa *et al.* [28].

One way to avoid the artificial generation of the substructure, and simply operate the subgrain/grain coarsening algorithm in the mesocopic scale (e. g. as measured by EBSD) is to approximate the actual energy release and therefore driving force for a cell switch. In other words, the driving force for a cell to re-orient comes from the energy change considering all the boundaries that surround the elementary volume prior to and after its re-orientation. Hence, we neither need to define grains/subgrains nor require multiple cells to constitute a subgrain/grain for it to grow. Instead, each CA cell describes a crystal orientation, and whether or not this is part of a subgrain/grain or it itself describes the actual subgrain does not matter. When in adjacent CA cells one is surrounded by boundaries amounting to larger energy in comparison to the other, there is a positive driving force to re-orient it. And this can be due to the curvature of the boundary separating them (e. g. grain growth) or due to the presence of a substructure and hence dislocations stored at the boundaries surrounding this cell (e. g. primary recrystallization). Hence, all the recrystallization-related phenomena are modelled under the same transformation rule.

Altogether, the developed CA method, although deterministic, shares the same basis with the probabilistic CA method based on MC-Potts kinetics for grain coarsening explained earlier in Section 3.1.1. Despite some expected differences - inherent to their respective fundamentals - when comparing a probabilistic Potts kinetics and a deterministic computer method, the approach taken here can be understood as a deterministic alternative to the MC-Potts CA method, at least when it comes to normal grain coarsening phenomena. The differences between the latter and the present CA method are discussed later, in Section 3.7.

3.2. MODEL DESCRIPTION

The CA algorithm can operate in different grids, namely in square, cubic, and hexagonal (regular hexagons) grid, and can consider boundaries within the 1st Von Neumann or the Moore neighbourhood (see [3, 4]).

In the following sections, the model is described with expressions regardless of the grid settings used. Illustrations regarding its implementation in the different grid settings will be shown wherever relevant. The following terms will be used when referring to specific grid settings:

- Sq(1,1): A 2D square grid that considers the 1st Von Neumann (i. e. nearest) neighbours for each cell - i. e. all square cells that share a side (distance is equal to the square's side).
- Sq(1,2): A 2D square grid that considers the Moore neighbourhood for each cell - i. e. all square cells that share either a side or a vertex (distance is equal to the square's side or diagonal).
- Hex(1,1): A 2D hexagonal grid (regular hexagons) that considers the 1st Von Neumann (i. e. nearest) neighbours for each cell i. e. all hexagonal cells that share a side (distance is equal to twice the hexagon's height).
- Cub(2,2): A 3D cubic grid that considers the Moore neighbourhood for each cell i. e. all cubic cells that share either a face, an edge, or a vertex (distance is equal to the face's side, face's diagonal, or main diagonal).

3.2.1. CONSTITUTIVE STATE VARIABLES USED IN THE AUTOMATON GRID

In the automaton grid every cell i is assigned a crystal orientation g_i. Each boundary area between material volumes i and j carries an interfacial energy value equal to:

$$E_{ij}[\mathrm{J}] = \gamma(g_i, g_j) \cdot A_{ij} \quad \forall ij : \delta_{ij} = 0 \tag{3.1}$$

where in Eq. (3.1):

- $A_{ij}[\mathrm{m}^2]$ is the area of the ij boundary plane.
- $\gamma(g_i, g_j)[\mathrm{J/m}^2]$ is the interface energy density between two unlike adjacent orientations g_i,g_j.
- δ_{ij} is a Kronecker-like operator defined as:

$$\delta_{ij} = \begin{cases} 1 \text{ if } \theta_{ij} < \theta_{min} \\ 0 \text{ if } \theta_{ij} >= \theta_{min} \end{cases} \tag{3.2}$$

where in Eq. (3.2):

- $\theta_{ij}[^\circ]$ is the misorientation between orientations g_i and g_j.

- $\theta_{min}[^\circ]$ is the lower cut-off misorientation to consider the existence of a boundary between i and j.

For low angle grain boundaries (LAGBs) the energy density decreases with the dislocation content and hence misorientation angle in accord with the Read-Shockley equation which reads [29]:

$$\gamma(g_i, g_j) = \begin{cases} \gamma_{HAGB} & \text{if } \theta_{ij} \geq \theta_{HAGB} \\ \gamma_{HAGB} \cdot \dfrac{\theta_{ij}}{\theta_{HAGB}} \cdot \left(1 - \ln\left(\dfrac{\theta_{ij}}{\theta_{HAGB}}\right)\right) & \text{if } \theta_{ij} < \theta_{HAGB} \end{cases} \tag{3.3}$$

where in Eq. (3.3):

- $\theta_{HAGB}[^\circ]$ is the lower threshold misorientation to consider a HAGB.

3.2.2. INCREMENTAL ENERGY RELEASE DURING KINETIC EVOLUTION OF THE CA

EXPRESSION

If the automaton cell i with orientation g_i, is swept by the boundary with its neighbour cell j, it assumes the new orientation g_j. The energy release on cell's i neighbourhood is calculated as:

$$\Delta E_{g_i \to g_j}[\mathrm{J}] = \sum_k A_{ik} \cdot (1 - \delta_{ik}) \cdot \gamma(g_i, g_k) - \sum_k (1 - c \cdot \delta_{lkij}) \cdot A_{ik} \cdot (1 - \delta_{jk}) \cdot \gamma(g_j, g_k) \text{ for } c \in (0, 1] \tag{3.4}$$

where in Eq. (3.4):

- k is an index referring to cells with $A_{ik} \neq 0$, i. e. k is neighbour of cell i.
- $c \in (0, 1]$ is constant that is related to the configuration of the grid.

The four indices' Kronecker-like operator δ_{lkij} and the constant c used in Eq. (3.4) are here introduced to account for the cases that two adjacent similarly oriented cells j and k may grow together. This assumption is made because long before cell j consumes cell i, a neighbour cell of the same orientation can have also started to grow toward its own closest neighbours. This is due to the high local curvature that would otherwise be created and "drag" the similarly oriented regions. When $\delta_{lkij} = 1$ a neighbour cell l, which is oriented as j, can grow together with j cell to transform cell k. Cell k is another neighbour of cell i, thus the next state's energy reduces by $c \cdot \gamma(g_j, g_k) \cdot A_{ik}$, since a fraction of cell's k volume (defined as c) will have the same orientation as i, which is g_j. The four indices' Kronecker-like operator used in Eq. (3.4) is then defined as:

$$\delta_{lkij} = \begin{cases} 1 \text{ if } \exists\, l : \vec{ji} = \vec{lk} \wedge \delta_{jl} = 1 \wedge \delta_{lk} = 0 \\ 0 \text{ if not} \end{cases} \tag{3.5}$$

where in Eq. (3.5):

- $\vec{ji}$ is the position vector of cell's i center with respect to the center of cell j.

Figs. 3.1 and 3.2 illustrate the assumption that is made upon calculating the energy state after a cell's re-orientation, using the grid Hex(1,1) and Sq(1,1), respectively. In both examples, cell 27 grows into cell 21. If we assume the energy state after cell 21 re-orients into g_{27} without considering that also other cells will get partially consumed (i. e. if $c = 0$), then the energy change is equal to 0. More specifically, in Fig. 3.1a cell 21 is surrounded by 2 boundaries. If we do not consider that cell 28 grows into cell 22 the same direction as cell 27 grows into cell 21 we arrive in the dashed boundaries 21, 22 and 28, 22 and therefore cell 21 is surrounded by 2 boundaries after its re-orientation and we have zero energy change. The same happens in the hexagonal grid. If cells 15 and 22 are not considered when we examine the energy change for cell's 21 re-orientation, then cell 21 has 3 boundaries (dashed lines in Fig. 3.2b) after cell 27 grows into it. But cell 21 was surrounded by 3 boundaries also before its re-orientation Fig. 3.2a so again the energy change is equal to 0.

These implications occur because the CA algorithm operates under the sharp-interface condition [4] and hence does not consider that long before cell 21 re-orients completely, adjacent cells would have also re-oriented at least a part of cells that are neighbours to cell 21. This would happen because otherwise high local curvature is created between the growing cell and its neighbours (e. g. between cell 21 and 22 in Fig. 3.2b). So in reality, the boundaries after the re-orientation of cell 21 would not be like the dashed lines shown in Fig. 3.1b and Fig. 3.2b, but rather like the boundaries indicated inside cell 22 in Fig. 3.1b and inside cells 22 and 15 in Fig. 3.2b. Therefore, when we examine the growth of a cell into another - here 27 into 21, it is reasonable to assume less energy for the next state depending on the growing cell's neighbourhood. The exact formulation is for the examples presented is described in Fig. 3.1c and Fig. 3.2c. For the other two grids - namely Sq(1,2) and Cub(2,2) the effect of c and δ_{lkij} is similar to the one shown in Fig. 3.1 for Sq(1,1).

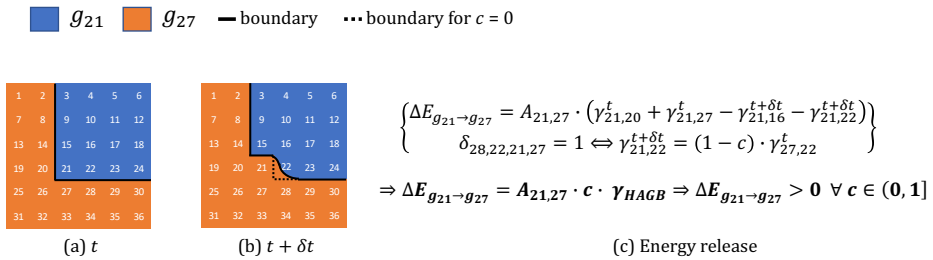

(a) t (b) $t+\delta t$ (c) Energy release

Figure 3.1: The role of c - illustration in Sq(1,1) grid; (a) two grains at the current state - time t (b) the configuraion that is assumed for calculating the energy state at time $t+\delta t$ (c) calculation of energy release.

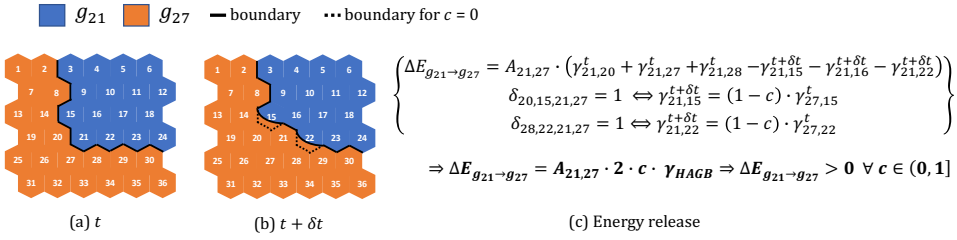

Figure 3.2: The role of c - illustration in Hex(1,1) grid; (a) two grains at the current state - time t (b) the configuraion that is assumed for calculating the energy state at time $t + \delta t$ (c) calculation of energy release.

It should be made clear that the correction introduced here (i. e. δ_{lkij} and c) regarding the next state's energy is an approximation. It does not mean that adjacent cells (e. g. cell 28 in Figs. 3.1 and 3.2) are indeed imposed an additional growth rate to other cells (e. g. into cell 22 in Figs. 3.1 and 3.2). These will be examined for the growth into their dissimilar neighbourhood independently of whether cell 27 grows into cell 21. The intention of the suggested correction is simply to calibrate and assign a driving force for the growth of cells that would otherwise not grow, although there is clearly curvature at the boundary near cell 21. For example, in the MC method, this calibration is done by assuming that if the boundary size/energy change is 0 the cell still can transform. So here we use c as a means to calibrate the energy calculations in a reasonable way, i. e. by assuming that the CA grid overestimates the next state's energy due to the sharp-interface condition.

3.2.3. KINEMATIC RULE

If the energy release in Eq. (3.4) is found positive the boundary segment ij exerts a driving force to re-orient the adjacent cell's i volume V_i, which is equal to:

$$\Delta G_{g_i \to g_j}[\mathrm{J/m^3}] = \frac{\Delta E_{g_i \to g_j}[\mathrm{J}]}{V_i[\mathrm{m^3}]} \tag{3.6}$$

This driving force displaces the boundary ij with velocity:

$$\begin{aligned} \vec{v}_{g_i \to g_j}[\mathrm{m/s}] &= M(g_i, g_j)[\mathrm{m^4/Js}] \cdot \Delta G_{g_i \to g_j}[\mathrm{J/m^3}] \cdot \vec{u}_{ji} \xRightarrow{(3.4),(3.6)} \\ \vec{v}_{g_i \to g_j}[\mathrm{m/s}] &= M(g_i, g_j) \cdot \Bigg(\sum_k A_{ik} \cdot (1 - \delta_{ik}) \cdot \gamma(g_i, g_k) - \\ &\sum_k (1 - c \cdot \delta_{lkij}) \cdot A_{ik} \cdot (1 - \delta_{jk}) \cdot \gamma(g_j, g_k) \Bigg) \cdot \vec{u}_{ji} / V_i \end{aligned} \tag{3.7}$$

where in Eq. (3.7):

- $\vec{u}_{ji}$ is the unit vector normal to the plane ij.

In Eq. (3.7) $M(g_i, g_j)$ is the boundary mobility [30, 31], which depends on the boundary's misorientation as follows [32]:

$$M(g_i,g_j) = \begin{cases} M_{HAGB} & \text{if } \theta_{ij} \geq \theta_{HAGB} \\ M_{HAGB} \cdot \left(1 - \exp\left(-5 \cdot \left(\frac{\theta_{ij}}{\theta_{HAGB}}\right)^4\right)\right) & \text{if } \theta_{ij} < \theta_{HAGB} \end{cases} \tag{3.8}$$

where in Eq. (3.8) M_{HAGB} is defined as [30]:

$$M_{HAGB}[\mathrm{m}^4/\mathrm{Js}] = M_0 \cdot \exp\left(\frac{-Q_g}{R \cdot T}\right) \tag{3.9}$$

In Eq. (3.9):

- Q_g[J/mol] is the activation energy for boundary migration.
- $R = 8.314$ J/mol · K is the universal gas constant.
- T[K] is the applied temperature.
- M_0[m^4/Js] is the pre-exponential factor.

The pressure on the boundary ij imposes a force equal to:

$$\vec{F}_{ij,g_i \to g_j}[\mathrm{N}] = \Delta G_{g_i \to g_j} \cdot A_{ij} \cdot \vec{u}_{ji} \tag{3.10}$$

Every cell k which is neighbour to cell i and is misoriented less than θ_{min} from the growing orientation g_j (i. e. $\delta_{kj} = 1$) will grow toward cell i perpendicularly to the boundary's ik plane, with velocity given from Eq. (3.7) - i. e. the same as boundary's ij. Hence, the total force for re-orientation of a cell i results from all migrating boundaries and their relative direction, such that:

$$\vec{F}_{g_i \to g_j}[\mathrm{N}] = \sum_k \delta_{kj} \cdot \vec{F}_{ik,g_i \to g_j} \Rightarrow \left\| \vec{F}_{g_i \to g_j}[\mathrm{N}] \right\| = \sqrt{\sum_{u_r = x,y,z} \left(\sum_k \delta_{kj} \cdot \left| \vec{F}_{ik,g_i \to g_j} \cdot \vec{u}_r \right| \right)^2} \tag{3.11}$$

where in Eq. (3.11):

- $\vec{u}_r$ is the unit vector for the r axis of the reference system - here $r = \{x, y, z\}$.

After some time δt the boundary will have traveled an average distance equal to $\left\| \vec{v}_{g_i \to g_j} \right\| \cdot \delta t$ and the force will have performed a work equal to the energy difference:

$$\left\| \vec{F}_{g_i \to g_j} \right\| \cdot \left\| \vec{v}_{g_i \to g_j} \right\| \cdot \delta t = \Delta E_{g_i \to g_j} \tag{3.12}$$

Defining $\dot{f}_{g_i \to g_j}$ as the growth rate of g_j in cell i, we have:

$$\dot{f}_{g_i \to g_j} = 1/\delta t \xrightarrow{(3.4),(3.6),(3.7),(3.11),(3.12)}$$
$$\dot{f}_{g_i \to g_j} = M_{g_i \to g_j} \cdot \sqrt{\sum_{u_r = x,y,z} \left(\sum_k \delta_{kj} \cdot \left| \vec{F}_{ik, g_i \to g_j} \cdot \vec{u}_r \right| \right)^2} / V_i \tag{3.13}$$

3.2.4. TRANSFORMATION RULE

A cell i re-orients to g_j with rate $\dot{f}^t_{g_i \to g_j}$ from Eq. (3.13) calculated at time t. The simulation's time step δt_{CA} at time t is found by the maximum growth rate among all growing orientations such as:

$$\delta t_{CA} = 1/max\{\dot{f}^t_{g_i \to g_j}\} \tag{3.14}$$

And the re-orientated fraction of each cell i is:

$$f^{t+\delta t_{CA}}_{g_i \to g_j} = \dot{f}^t_{g_i \to g_j} \cdot \delta t_{CA} + f^t_{g_i \to g_j} \tag{3.15}$$

Cell i re-orients completely into g_j when $f^t_{g_i \to g_j}$ becomes equal to (or exceeds) the value of 1. Until then, besides the re-orientation fraction that is stored at every simulation step, cell i is considered to be oriented as g_i - i. e. the algorithm operates under the sharp-interface condition. The description of the algorithm's steps can be found in Section 3.3.

3.2.5. GRID-RELATED SETTINGS

In this section, the implementation of the methodology described in the grids investigated is presented.

SQUARE GRID WITH NEAREST NEIGHBOURS

Fig. 3.3 shows the boundaries and forces considered in Sq(1,1). The parameter α refers to the side of the grid's elementary unit. Implementing the algorithm in grid Sq(1,1) requires the following (see Fig. 3.3):

- the volume of a cell i is $V_i = \left(\delta x_{CA}\right)^2 \cdot \left|\vec{z}_{CA}\right| \ \forall\, i$.
- $\alpha = \delta x_{CA}$.
- the area of a boundary ij is $A_{ij} = \delta x_{CA} \cdot \left|\vec{z}_{CA}\right| \ \forall\, A_{ij} \neq 0$.
- the direction of the force a boundary ij exerts is $\vec{u}_{ji} \in \{\vec{u}_x, -\vec{u}_x, \vec{u}_y, -\vec{u}_y\}$.

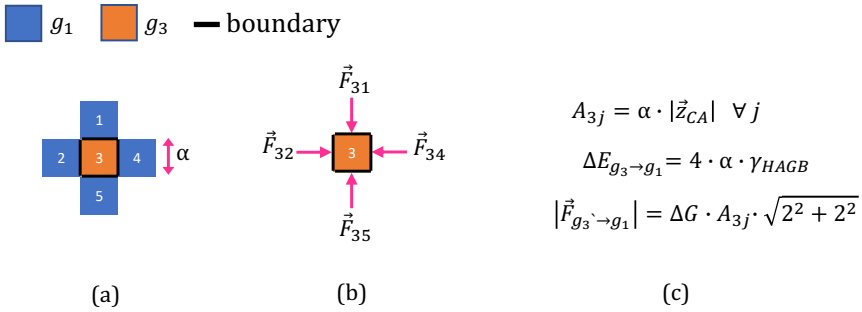

Figure 3.3: Energy change and re-orientation force in Sq(1,1); The images show (a) the boundaries considered for cell 3 (b) the direction of the force that each boundary exerts (c) the calculated expressions for the energy and re-orientation force.

HEXAGONAL GRID WITH NEAREST NEIGHBOURS

Fig. 3.4 shows the boundaries and forces considered in Hex(1,1). The settings that are required for simulations in Hex(1,1) read (see Fig. 3.4):

- the volume of a cell $V_i = \left(3 \cdot \sqrt{3}/2\right) \left(\delta x_{CA} / \left(\sqrt{3}/2 \cdot 2\right)\right)^2 \cdot |\vec{z}_{CA}| \ \forall\, i.$
- $\alpha = \delta x_{CA} \cdot \left(2 \cdot \sqrt{3}/2\right).$
- the area of a boundary ij is $A_{ij} = \delta x_{CA} \cdot |\vec{z}_{CA}| \,/\, \left(2 \cdot \sqrt{3}/2\right) \ \forall\, A_{ij} \neq 0.$
- the direction of the force a boundary ij exerts is $\vec{u}_{ji} \in \{\vec{u}_x\,,\ -\vec{u}_x\,,\ \cos(60°) \cdot \vec{u}_x + \sin(60°) \cdot \vec{u}_y\,,\ -\cos(60°) \cdot \vec{u}_x + \sin(60°) \cdot \vec{u}_y\,,\ -\cos(60°) \cdot \vec{u}_x - \sin(60°) \cdot \vec{u}_y\,,\ \cos(60°) \cdot \vec{u}_x - \sin(60°) \cdot \vec{u}_y\}.$

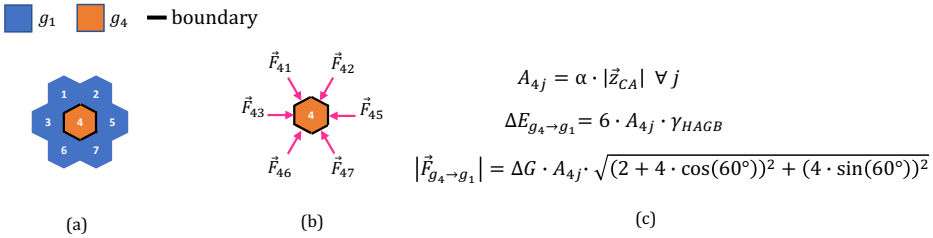

Figure 3.4: Energy change and re-orientation force in Hex(1,1); The images show (a) the boundaries considered for cell 4 (b) the direction of the force that each boundary exerts (c) the calculated expressions for the energy and re-orientation force.

SQUARE GRID WITH NEAREST AND DIAGONAL NEIGHBOURS

For Sq(1,2), as shown in Fig. 3.5, the area of a 1^{st} Von Neumann boundary is half the α. This is because here also the diagonal neighbours are considered and therefore both the boundary energy surrounding a cell and the number of boundaries migrating have increased compared to the Sq(1,1) grid. In Sq(1,2) the algorithm is implemented with the following settings (see Fig. 3.5):

- the volume of a cell i is $V_i = \left(\delta x_{CA}\right)^2 \cdot \left|\vec{z}_{CA}\right| \ \forall\, i$.
- $\alpha = \delta x_{CA}$.
- 4 boundaries ij have area $A_{ij} = 0.5 \cdot \delta x_{CA} \cdot \left|\vec{z}_{CA}\right|$ and 4 boundaries have area $A_{ij} = 0.5 \cdot \cos(45°) \cdot \delta x_{CA} \cdot \left|\vec{z}_{CA}\right|$.
- the direction of the force a boundary ij exerts is $\vec{u}_{ji} \in \{\vec{u}_x\ ,\ -\vec{u}_x, \vec{u}_y\ ,\ -\vec{u}_y\ ,\ \cos(45°)\cdot\vec{u}_x + \cos(45°)\cdot\vec{u}_y\ ,\ \cos(45°)\cdot\vec{u}_x - \cos(45°)\cdot\vec{u}_y\ ,\ -\cos(45°)\cdot\vec{u}_x + \cos(45°)\cdot\vec{u}_y\ ,\ -\cos(45°)\cdot\vec{u}_x - \cos(45°)\cdot\vec{u}_y\}$.

In the above settings, $\vec{u}_x$ and $\vec{u}_y$ are the unit vectors of the (Cartesian) reference system. As for $\vec{z}_{CA}$, it has direction perpendicular to the 2D grid and it is of arbitrary magnitude - it cancels out with $\vec{z}_{CA}$ from V_i in Eq. (3.6). Hence, $\vec{z}_{CA}$ does not affect 2D simulations, and it is only included in the above settings to be consistent with the equations expressed in the methodology (which apply to both 2D and 3D grids).

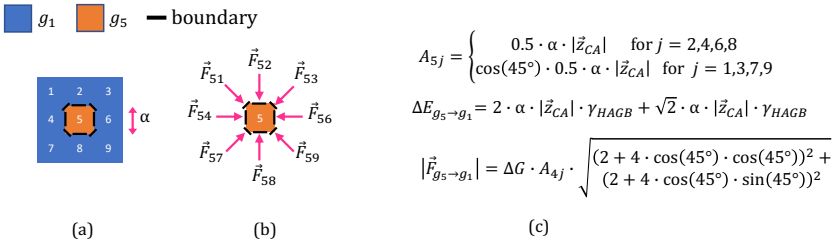

Figure 3.5: Energy release and re-orientation force in Sq(1,2); The images show (a) the boundaries considered for cell 5 (b) the direction of the force that each boundary exerts (c) the calculated expressions for the energy and re-orientation force.

3.3. ALGORITHM'S STEPS

At the initial state, the automaton identifies the orientation of every cell as a unique property. Every interfacial cell i (cell of at least one neighbour differently oriented, i. e. $\exists j : A_{ij} \neq 0 \wedge \delta_{ij} = 0$ where δ_{ij} is defined in Eq. (3.2)) is stored at every time step. In a certain time step the algorithm performs the following:

- Step 1: A loop initiates for all the cells which are defined as interfacial cells.

- Step 2: For the interfacial cell i a loop initiates on its neighbours. The misorientation is calculated and stored for every pair of cells i and j. By using then Eq. (3.3) the value of $\gamma(g_i, g_j)$ is found and $\gamma(g_i, g_j) \cdot A_{ik}$ is added to the current state's energy (of cell i). A second loop initiates for each neighbour $k \neq j$ of cell i. This is to calculate the misorientation between j and the other k cells which are neighbours of i, and it will be used later. At the end of the double loop, i cell's energy (second term in Eq. (3.4)) and the misorientation with all neighbours of i have been calculated.

- Step 3: For the same interfacial cell i the neighbours of the cell are looped again - now as candidates to re-orient i. The direction of boundary migration, i. e. $\vec{u}_{ji}$ for every j cell is stored for the possible re-orientation of i into g_j. Inside this loop, the neighbours of i are looped once more to calculate the next state's energy for every candidate re-orientation (with the use of the calculated misorientations from step 2, and Eq. (3.3)) by assuming the next state's boundaries, i. e. between i and k where i is supposed to be orientated as j. If cell k is similarly oriented as j (i. e. $\delta_{jk} = 1$ in Eq. (3.2)), the direction of growth $\vec{u_{ki}}$ for the cell k is stored since k will grow together with cell j. Then the loop continues since a boundary between i and k will not exist if i re-orients as g_j. If not, then first the cell l is considered, which is found from equating the position vectors $\vec{ji} = \vec{lk}$. Eq. (3.5) is then applied for the combination of cells i, j, k, l - i. e. if cell l is similarly oriented as j (which is growing into i) and can grow into cell k in the same direction as j will grow into i. If this cell l is found eligible to grow into k (i. e. $\delta_{lkij} = 1$ in Eq. (3.5)) the boundary energy between k and i, after the latter re-orients into g_j is added in the next state's energy as $(1-c) \cdot \gamma(g_j, g_k) \cdot A_{ik}$. If l is not eligible, then the boundary energy is added as $\gamma(g_j, g_k) \cdot A_{ik}$. This loop continues in the same way for all cells k. At the end of this loop, the next state's energy for cell j growing into i is calculated and substituted in Eq. (3.4) together with the current state's energy for cell i which was calculated in step 2. If the energy release is positive then the re-orientation rate is found (see Eq. (3.13)) for cell i re-orienting as j, by using Eq. (3.9), Eq. (3.8), Eq. (3.4), and $\vec{u}_r, \vec{u}_{ki} \forall k : \delta_{jk} = 1$ including $k = j$ (as mentioned the position vectors $\vec{u}_{ki}$ were stored). If the re-orientation rate of i into g_j is positive and larger than any other re-orientation rate for cell i then the re-orientation rate is stored together with the orientation g_j for the cell i.

- Step 4: Step 3 is done for all cells j that are candidates to re-orient cell i and at the end one (the faster) re-orientation rate $\dot{f}_{g_i \to g_j}$ for cell i (if any) is kept along with g_j.

- Step 5: Steps 2-4 are performed for every interfacial cell i. After all interfacial cells i are looped and their re-orientation rate is defined the maximum re-orientation rate $\dot{f}_{max}$ at the current time step is found. The time step's (i. e. incremental simulation time) value is found as $\delta t = 1/\dot{f}_{max}$, for the particular time of the simulation.

- Step 6: The time step δt is added to the simulation's time and then every cell i is looped to apply the new re-orientation fraction given in Eq. (3.15). If a cell i has a re-orientation fraction larger or equal to 1 it transforms (i. e. re-orients) to the favorable orientation and the re-orientation fraction is set back to zero. The cell i - now oriented as g_j - is then stored in order to recalculate the relevant interfacial cells.

- Step 7: The neighbours of every i cell that re-oriented at the current time step are found and added to the structure of interfacial cells. The procedure from step 1 starts again.

3.4. TEST SIMULATIONS - GRID EFFECTS

3.4.1. PURPOSE AND INPUT

CA algorithms for grain growth simulations contain grid effects due to the boundary energy being dependent on the angle between the grain boundary and the reference system - likewise, the surface energy depends on the crystallographic plane [33, 34]. Detailed analyses on the extent of this effect when different grid settings are used to apply the MC method have been performed by Anderson *et al.* [5], Holm and Battaile [14], Holm E. [35] - see also the reviews by Rollett and Manohar [36] and Rollett [37]. Although the present algorithm is in practice very similar to the MC method, it is necessary to investigate the different grid settings for two reasons:

- Although certain grid types have been established as acceptable when used within the MC method [35–37], the boundary energy is still dependent on the boundary orientation (with respect to the horizontal axis). Hence, a simulation may still incorporate grid artifacts even when acceptable grid settings are used.

- In the present method, the assumption explained in Eq. (3.5) and illustrated in Figs. 3.1 and 3.2 is also sensitive to the boundary orientation. Therefore an investigation for how the value of c affects the boundary energy anisotropy is necessary.

This section reviews the evolution of grain growth simulations for different grids and settings in simple cases, i. e. bicrystal RVEs and triple junctions as well in a polycrystal RVE. The thermodynamic and kinetic parameters are shown in Table 3.1, although it should be clarified that as the present simulations are meant to investigate the extent of modeling artifacts and the kinetic outcome, accurate values are not necessary to obtain meaningful results. The same applies to the crystal structure, i. e. in this chapter it does not matter whether grain growth takes place in austenite or ferrite, which is why, besides the polycrystal RVE (which is actually a strain-free ferritic microstructure measured by EBSD) all other tests are done by simulations at 1000 °C. It should also be clarified, that in accord with the deterministic CA transformation rules, the temperature only affects the connection between real time and simulation time steps. In other words, the tests presented here are not sensitive to the temperature with regard to the purpose for which they were performed.

Table 3.1: Input parameters used in test simulations.

Quantity	Value	Description
Q_g	140 kJ/mol	activation energy for boundary migration
M_0	$2.84 \cdot 10^{-6}$ m^4/Js	pre-exponential factor of HAGBs mobility
γ_{HAGB}	0.5 J/m^2	the energy per unit area of a HAGB

3.4.2. SIMULATIONS WITH PERIODIC BOUNDARY CONDITIONS: BICRYSTAL AND TRICRYSTAL

In this section the algorithm is applied to a bicrystal and a triple junction. In all simulations within this section, periodic boundary conditions are considered. In other words, a cell contacting the RVE's edge can migrate toward any of its neighbours, including the boundary cells located at the opposite edge, i. e. cells located symmetrically (at principal axes x,y,z) with respect to the RVE's center.

BICRYSTAL

As shown in Figs. 3.6 to 3.8 grain 1 grows towards the center of curvature indicated by the boundary. The parameter c affects the kinetics such that a higher value for c makes the grain growth faster. As a consequence, for the same number of simulation steps, less time has passed. This is because the driving force is ascending with c.

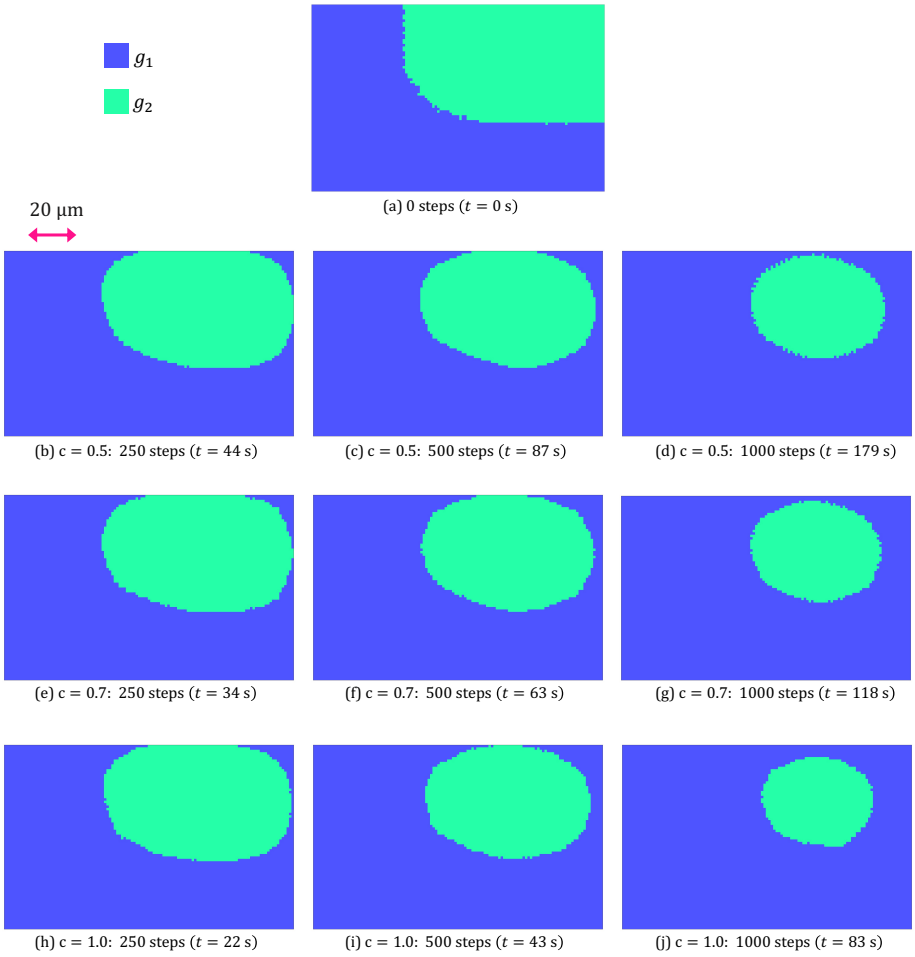

Figure 3.6: Bicrystal RVE at 1000 °C simulated in Sq(1,1): The maps show the evolution at (a) 0 time steps - 0 s (b) 250 time steps for $c = 0.5$ (c) 500 time steps for $c = 0.5$ (d) 1000 time steps for $c = 0.5$ (e) 250 time steps for $c = 0.7$ (f) 500 time steps for $c = 0.7$ (g) 1000 time steps for $c = 0.7$ (h) 250 time steps for $c = 1.0$ (i) 500 time steps for $c = 1.0$ and (j) 1000 time steps for $c = 1.0$.

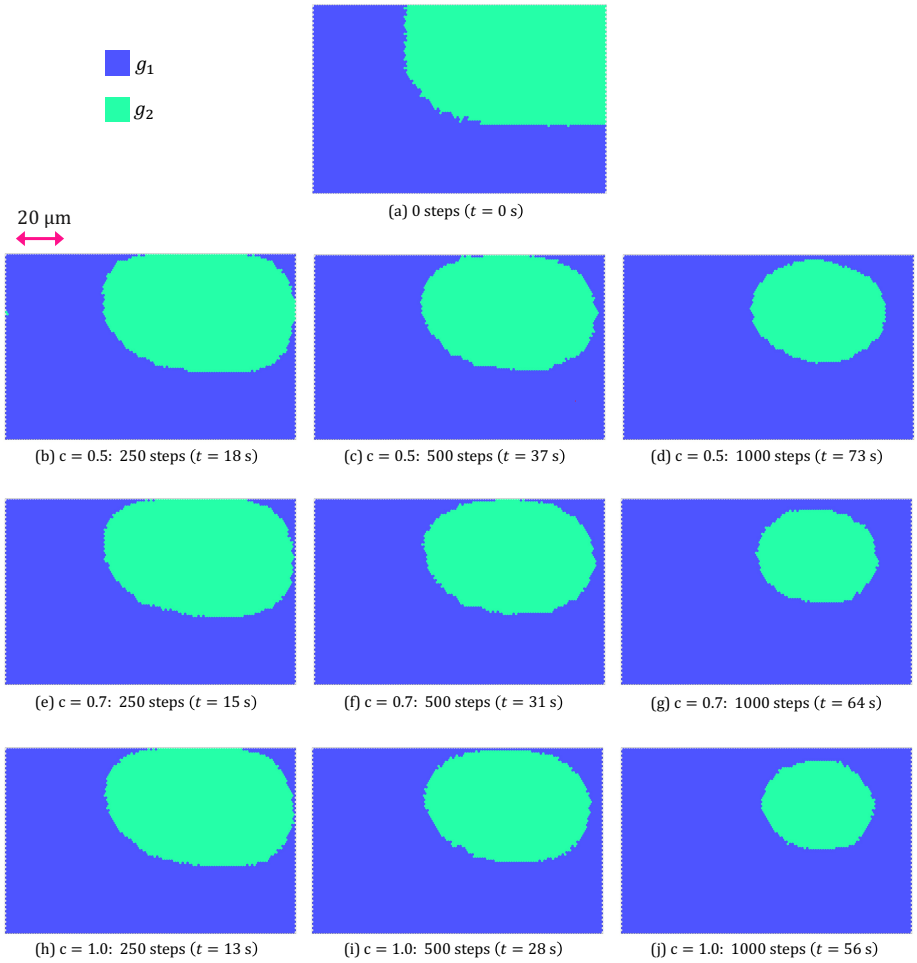

Figure 3.7: Bicrystal RVE at 1000 °C simulated in Hex(1,1): The maps show the evolution at (a) 0 time steps - 0 s (b) 250 time steps for $c = 0.5$ (c) 500 time steps for $c = 0.5$ (d) 1000 time steps for $c = 0.5$ (e) 250 time steps for $c = 0.7$ (f) 500 time steps for $c = 0.7$ (g) 1000 time steps for $c = 0.7$ (h) 250 time steps for $c = 1.0$ (i) 500 time steps for $c = 1.0$ and (j) 1000 time steps for $c = 1.0$.

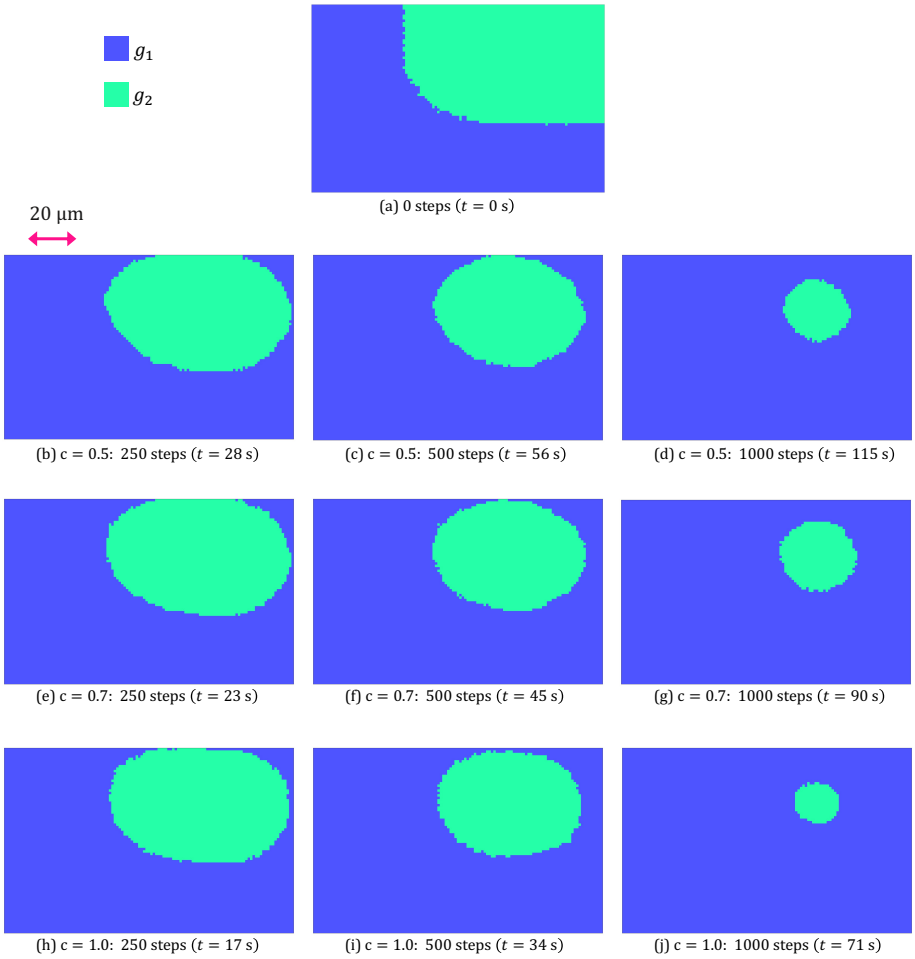

Figure 3.8: Bicrystal RVE at 1000 °C simulated in Sq(1,2): The maps show the evolution at (a) 0 time steps - 0 s (b) 250 time steps for $c = 0.5$ (c) 500 time steps for $c = 0.5$ (d) 1000 time steps for $c = 0.5$ (e) 250 time steps for $c = 0.7$ (f) 500 time steps for $c = 0.7$ (g) 1000 time steps for $c = 0.7$ (h) 250 time steps for $c = 1.0$ (i) 500 time steps for $c = 1.0$ and (j) 1000 time steps for $c = 1.0$.

TRIPLE JUNCTION

Fig. 3.9, Fig. 3.10, and Fig. 3.11 show the grain growth evolution in Sq(1,1), Hex(1,1), and Sq(1,2) respectively, when the RVE includes a triple junction.

Figure 3.9: Tricrystal RVE at 1000 °C simulated in Sq(1,1): The maps show the evolution at (a) 0 time steps - 0 s (b) 50 time steps for $c = 0.5$ (c) 250 time steps for $c = 0.5$ (d) 500 time steps for $c = 0.5$ (e) 50 time steps for $c = 0.7$ (f) 250 time steps for $c = 0.7$ (g) 500 time steps for $c = 0.7$ (h) 50 time steps for $c = 1.0$ (i) 250 time steps for $c = 1.0$ and (j) 500 time steps for $c = 1.0$.

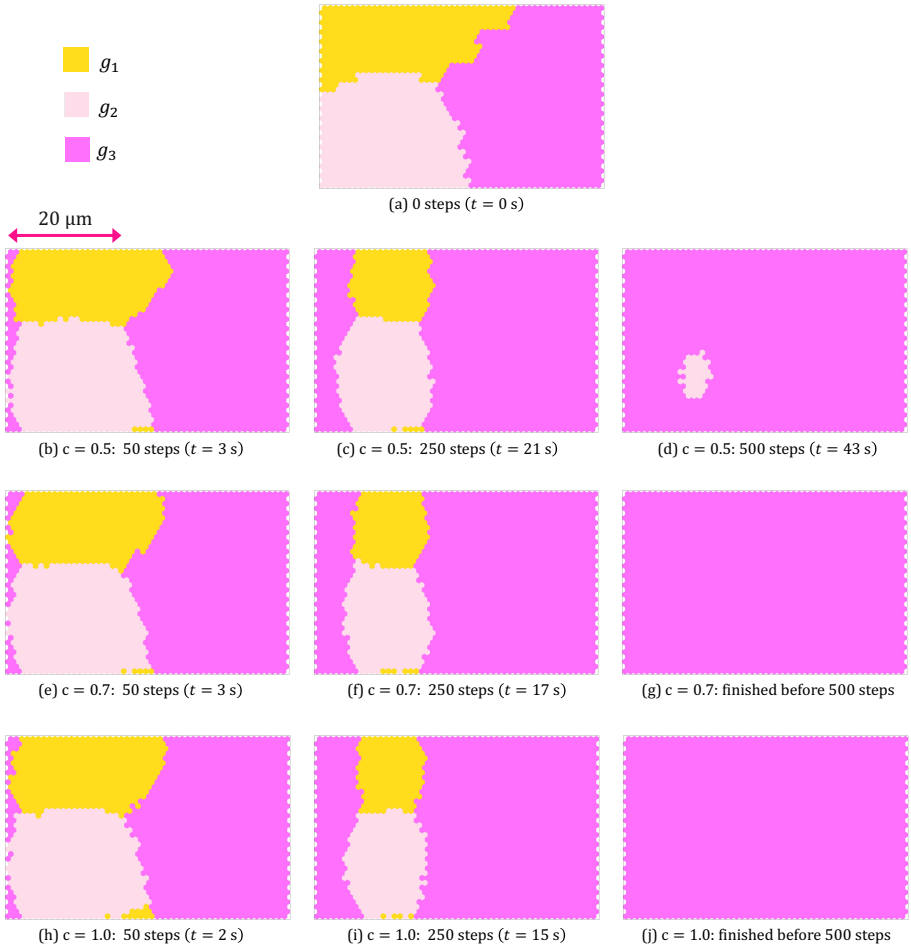

Figure 3.10: Tricrystal RVE at 1000 °C simulated in Hex(1,1): The maps show the evolution at (a) 0 time steps - 0 s (b) 50 time steps for $c = 0.5$ (c) 250 time steps for $c = 0.5$ (d) 500 time steps for $c = 0.5$ (e) 50 time steps for $c = 0.7$ (f) 250 time steps for $c = 0.7$ (g) 500 time steps for $c = 0.7$ (h) 50 time steps for $c = 1.0$ (i) 250 time steps for $c = 1.0$ and (j) 500 time steps for $c = 1.0$.

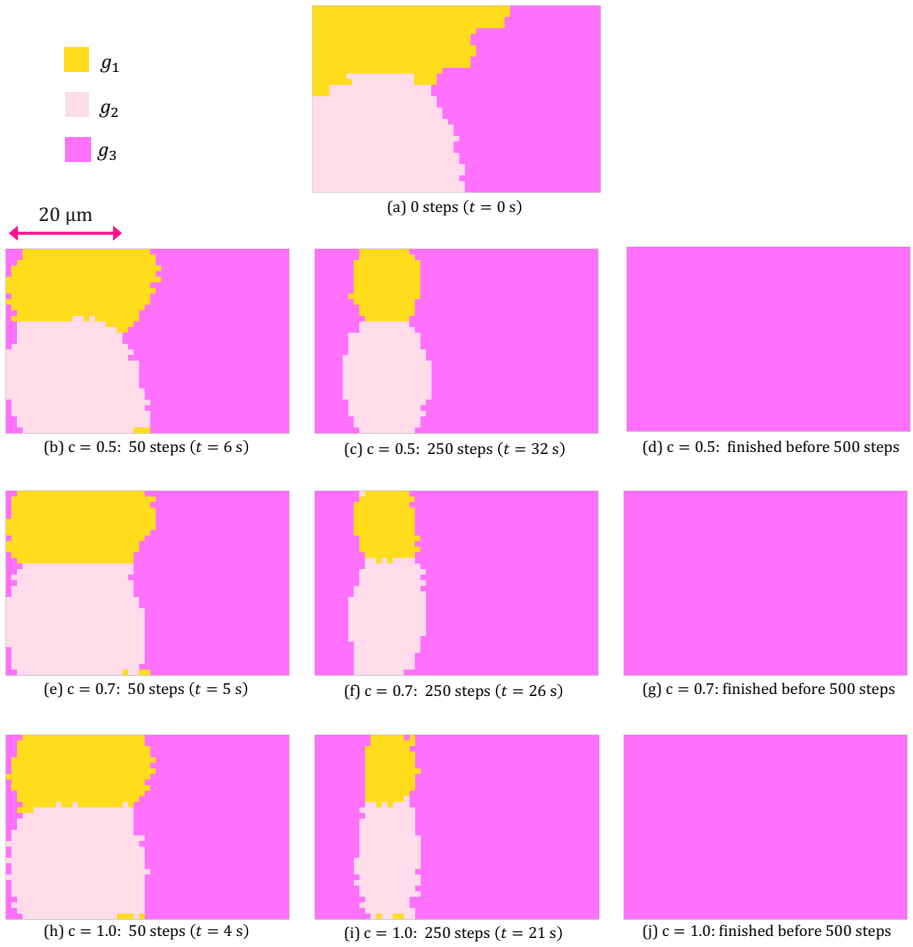

Figure 3.11: Tricrystal RVE at 1000 °C simulated in Sq(1,2): The maps show the evolution at (a) 0 time steps - 0 s (b) 50 time steps for $c = 0.5$ (c) 250 time steps for $c = 0.5$ (d) 500 time steps for $c = 0.5$ (e) 50 time steps for $c = 0.7$ (f) 250 time steps for $c = 0.7$ (g) 500 time steps for $c = 0.7$ (h) 50 time steps for $c = 1.0$ (i) 250 time steps for $c = 1.0$ and (j) 500 time steps for $c = 1.0$.

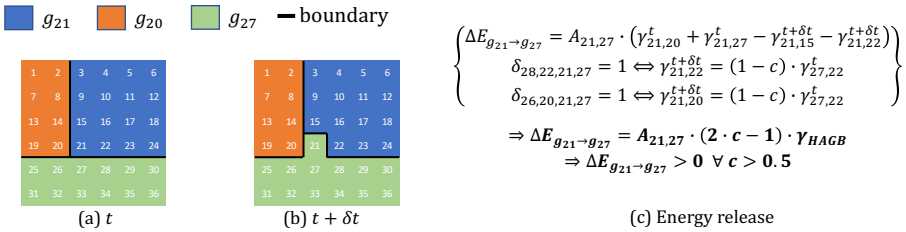

Figure 3.12: Example of energy states calculation in grid Sq(1,1) for $c = 0.5$. The maps show the evolution at (a) the current state (b) the next state (c) the energy release.

As shown in Figs. 3.9 to 3.11, in the presence of a triple junction, the grain that dominates is indicated also by the angle at the triple junction. In this case, the pink grain comprises the largest angle and hence grows at the expense of the other two. However, Fig. 3.9d shows that in the case Sq(1,1), when $c = 0.5$ this does not happen. Rather, the boundaries attain stability when they become straight and further grain growth is inhibited. This is because in such a grid (i. e. Fig. 3.9), for $c = 0.5$, the two pink cells in the triple junction cannot grow into the two adjacent dissimilar cells, since the driving force there will be equal to 0. For larger values of c, there is a driving force for the boundaries comprising the triple junction. This is explained in Fig. 3.12, where a triple junction is studied locally. It would be expected that the grain that comprises the larger angle, namely g_{27}, would grow. However, as shown in Fig. 3.12c, the value of c needs to be larger than 0.5 to yield a positive driving force.

3.4.3. BICRYSTAL WITH RESTRICTED BOUNDARIES

This section reviews the grain growth simulations when periodic boundary conditions are disabled. Hence, the equilibrium configuration of the grain boundary is predefined by the pinned regions that lie in the RVE's edges.

Fig. 3.13, Fig. 3.14, and Fig. 3.15 show the grain growth evolution for different grid-related settings, in a bicrystal RVE where the boundary is expected to stabilize at around $-30°$ to the horizontal axis. As shown in Figs. 3.14 and 3.15, when the boundary is confined by two stable configurations, its curvature will gradually decrease, until a straight boundary is reached. In Hex(1,1) and Sq(1,2), the boundary becomes straight, regardless of the chosen value of c. However, this is not the case for Fig. 3.13 where it is clear that the grid affects the simulations insofar as the grain boundary stabilizes without being truly straight. Moreover, there is no value for c that enables the simulation in Sq(1,1) to indeed result in a straight boundary.

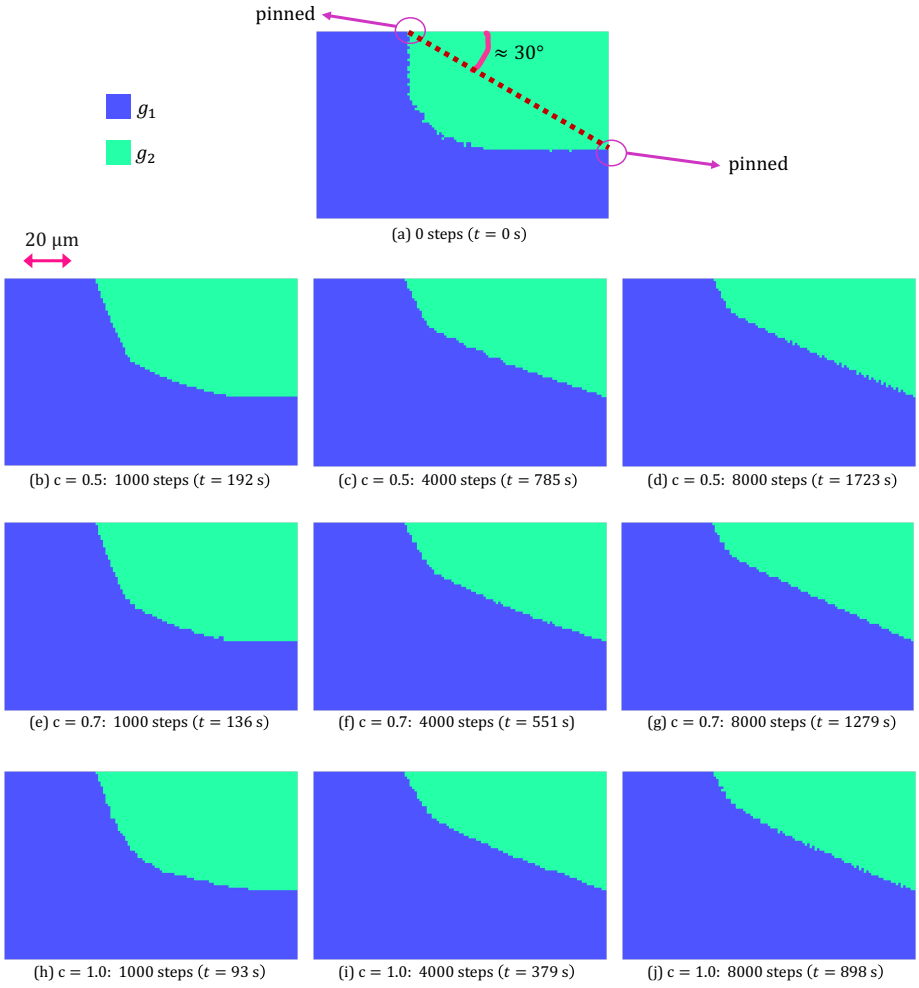

Figure 3.13: Bicrystal RVE at 1000 °C simulated in Sq(1,1) with confined boundary. The maps show the evolution at (a) 0 time steps - 0 s (b) 1000 time steps for $c = 0.5$ (c) 4000 time steps for $c = 0.5$ (d) 8000 time steps for $c = 0.5$ (e) 1000 time steps for $c = 0.7$ (f) 4000 time steps for $c = 0.7$ (g) 8000 time steps for $c = 0.7$ (h) 1000 time steps for $c = 1.0$ (i) 4000 time steps for $c = 1.0$ and (j) 8000 time steps for $c = 1.0$.

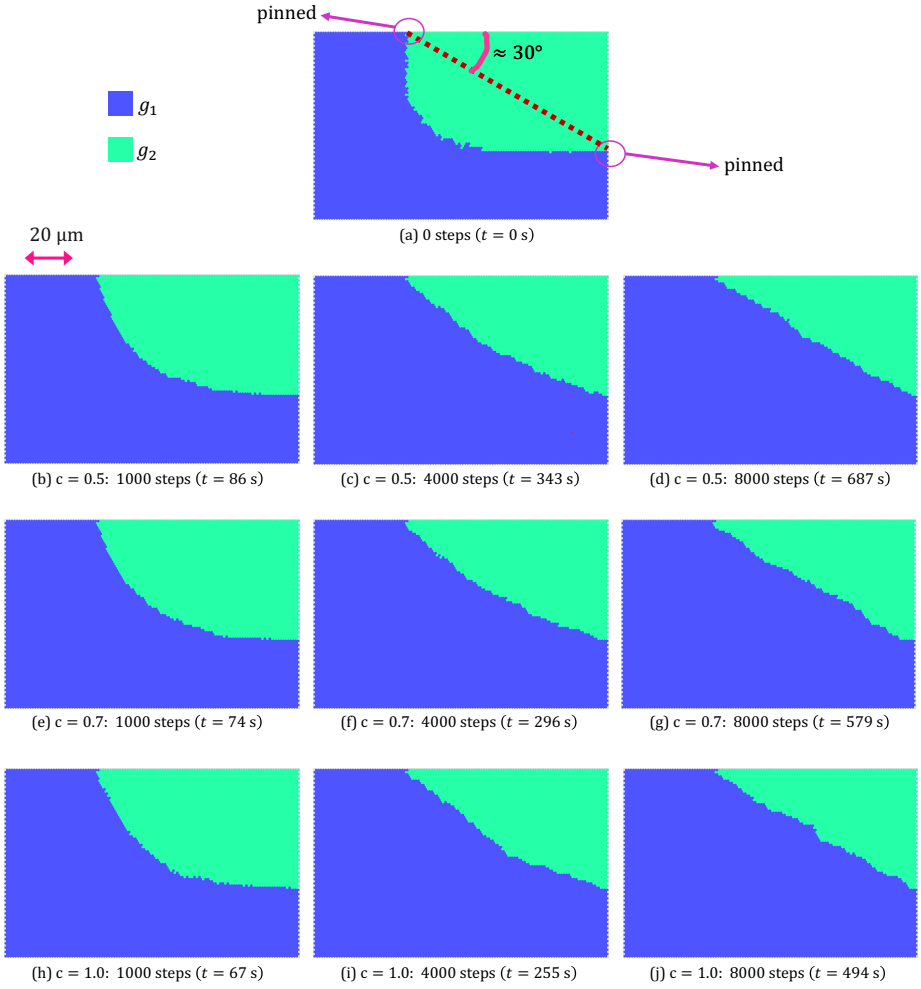

Figure 3.14: Bicrystal RVE at 1000 °C simulated in Hex(1,1) with confined boundary. The maps show the evolution at (a) 0 time steps - 0 s (b) 1000 time steps for $c = 0.5$ (c) 4000 time steps for $c = 0.5$ (d) 8000 time steps for $c = 0.5$ (e) 1000 time steps for $c = 0.7$ (f) 4000 time steps for $c = 0.7$ (g) 8000 time steps for $c = 0.7$ (h) 1000 time steps for $c = 1.0$ (i) 4000 time steps for $c = 1.0$ and (j) 8000 time steps for $c = 1.0$.

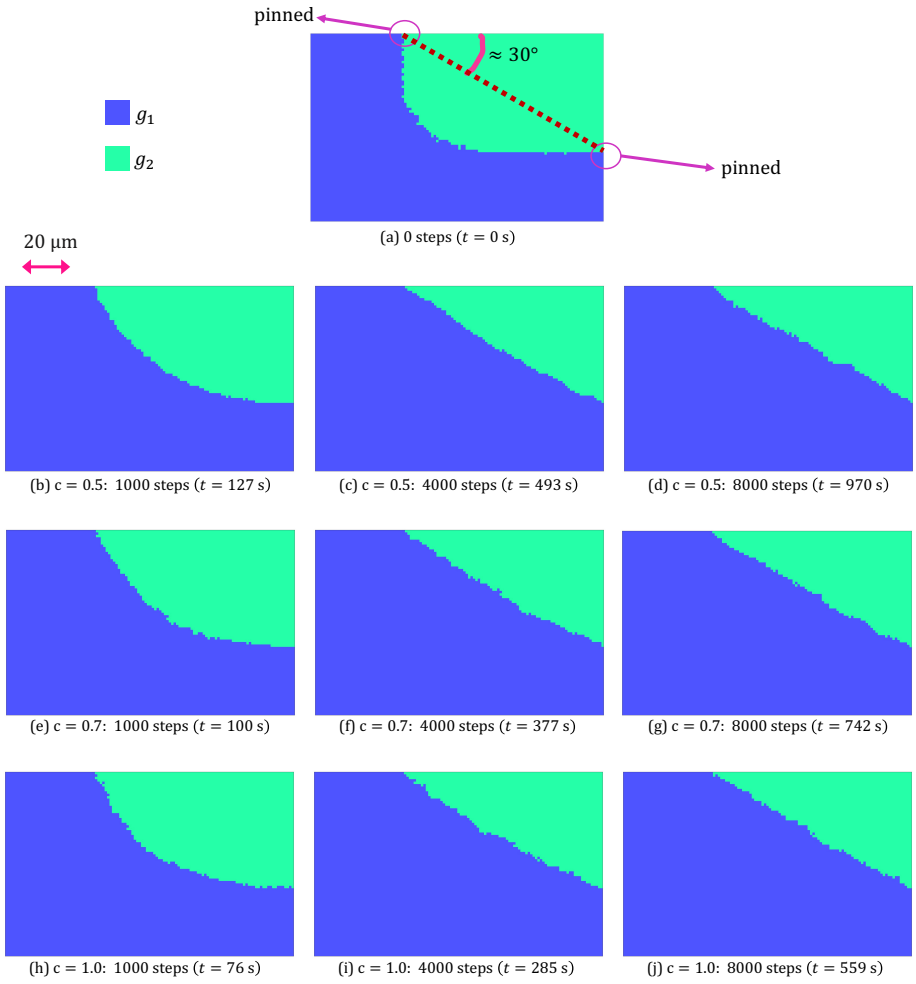

Figure 3.15: Bicrystal RVE at 1000 °C simulated in Sq(1,2) with confined boundary. The maps show the evolution at (a) 0 time steps - 0 s (b) 1000 time steps for $c = 0.5$ (c) 4000 time steps for $c = 0.5$ (d) 8000 time steps for $c = 0.5$ (e) 1000 time steps for $c = 0.7$ (f) 4000 time steps for $c = 0.7$ (g) 8000 time steps for $c = 0.7$ (h) 1000 time steps for $c = 1.0$ (i) 4000 time steps for $c = 1.0$ and (j) 8000 time steps for $c = 1.0$.

3.4.4. POLYCRYSTAL

To examine the grain growth evolution in this approach, the algorithm was applied to a 2D microstructure, which consists of randomly oriented and almost equiaxed grains. The microstructure was obtained by performing EBSD analysis on the hot-rolled state of an IF-steel, where the grains are strain-free due to the preceded austenite-to-ferrite transformation

[1].

The input RVE was then created, by preserving the grains' morphology from the real microstructure, yet the crystallographic orientations were re-assigned to each grain such that the microstructure is characterized by random crystallographic texture.

Fig. 3.16 shows the microstructure simulated at 1000 time steps, using Sq(1,1), for $c = \{0.5, 0.7, 1\}$. As is shown, these simulations exhibit a distinct sensitivity of the microstructural morphology with respect to the value of c. A high density of boundaries with angles (to the horizontal axis) around 0° and 90° is observed when $c = 0.5$. This happens here due to the stability of triple junctions, which was explained in Section 3.4.2. However, by increasing the value of c and particularly when $c = 1$ the prevalent boundaries seem to be oriented 45° to the horizontal axis. Similar grid effects - i. e. either a high frequency of 0° and 90° boundaries or a predominance of 45° boundaries - have been observed when the Sq(1,1) grid is used for the MC algorithm [5, 14, 35, 38].

Less pronounced grid effects in Sq(1,1) seem to correspond to $c = 0.7$ where apparently the distribution of boundary orientations is more uniform. However, as shown earlier in Section 3.4.3, the limited options of boundary orientations in Sq(1,1) that allow a straight boundary to be reached already contain major grid artifacts. Hence, the apparently reasonable grain growth simulation seen for $c = 0.7$ is attributed to an apparent balance between decreasing the energy at triple junctions and grain boundaries. Fig. 3.17 shows the microstructure simulated at 1000 time steps, using Hex(1,1), for $c = \{0.5, 0.7, 1\}$. As shown here, neither high density in specific boundary orientations nor a high sensitivity of the latter to the value of c is observed. The same concerns Sq(1,2) that is presented in Fig. 3.18.

Altogether, the analysis regarding grid artifacts reveals that Hex(1,1) and Sq(1,2) are appropriate grids for grain growth simulations in 2D. On the other hand, Sq(1,1) has already shown various drawbacks upon incorporating the analytical expressions due to the anisotropy of the boundary energy at different boundary angles to the horizontal axis. Although the algorithm contains some features which differ from the MC method for grain growth simulations, the above conclusions are in compliance with the ones reported in [35–37].

[1] Further details on the heat treatment, composition, etc. are not discussed here because they are not necessary to obtain meaningful results. The EBSD analysis on this material was only performed to obtain a microstructure where the grains are strain-free and hence only grain growth occurs. As explained later, each grain's crystallographic orientation was re-assigned such that the RVE would be characterized by random texture.

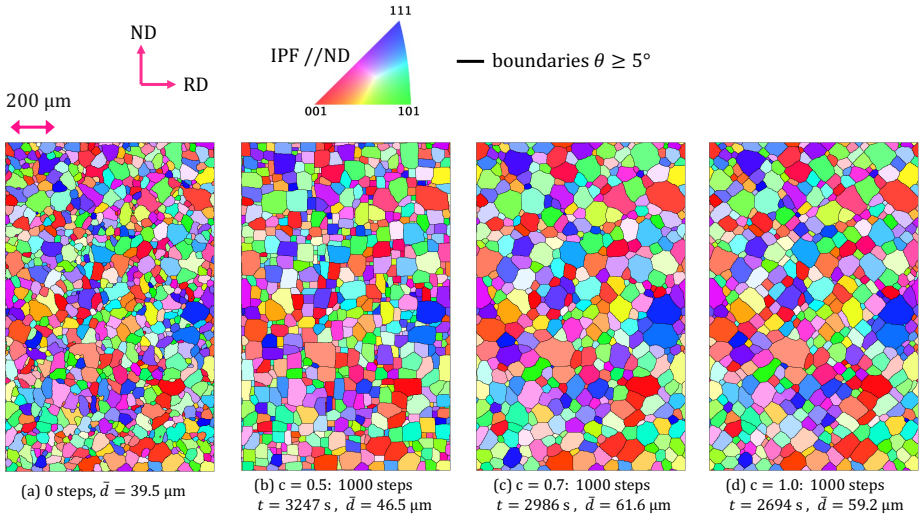

Figure 3.16: Polycrystal RVE at 800 °C simulated in Sq(1,1) shown at (a) 0 time steps (b) 1000 time steps - for $c = 0.5$ (c) 1000 time steps for $c = 0.7$ (d) 1000 time steps for $c = 1.0$.

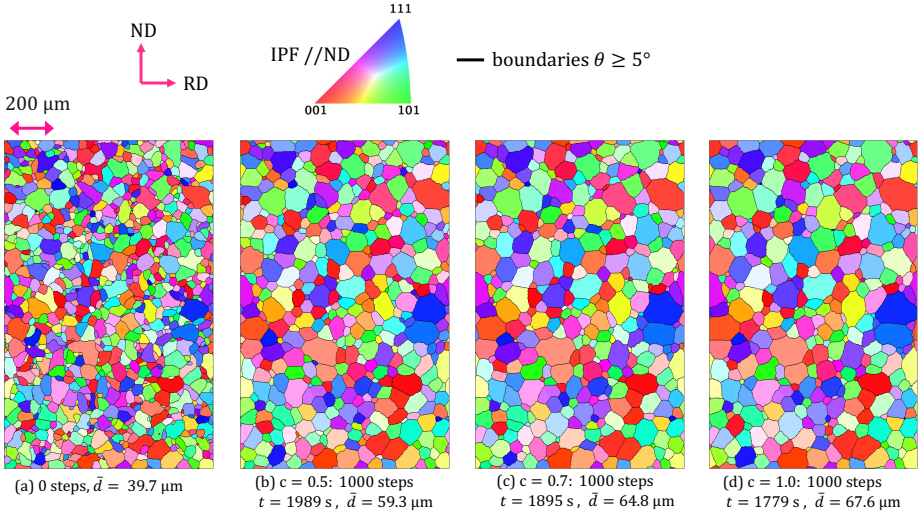

Figure 3.17: Polycrystal RVE at 800 °C simulated in grid Hex(1,1) shown at (a) 0 time steps (b) 1000 time steps - for $c = 0.5$ (c) 1000 time steps for $c = 0.7$ (d) 1000 time steps for $c = 1.0$.

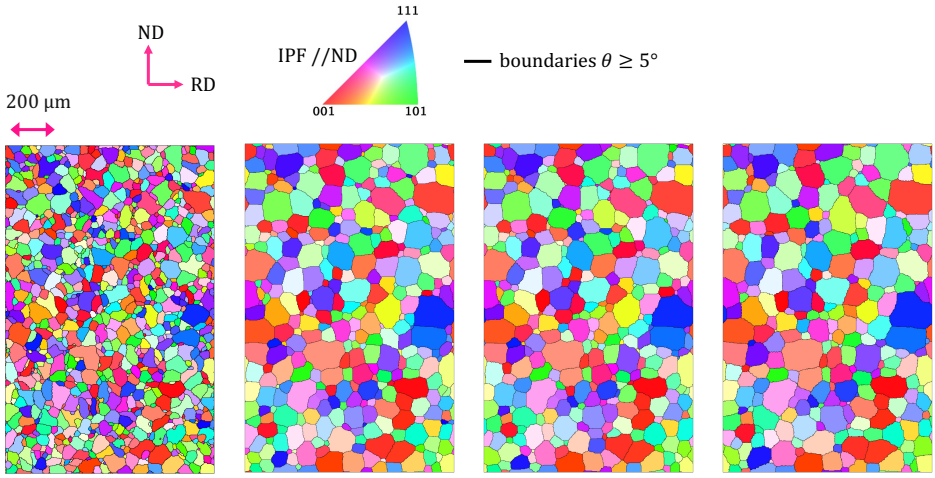

(a) 0 steps, $\bar{d} = 39.5$ µm

(b) c = 0.5: 1000 steps
$t = 3283$ s, $\bar{d} = 68.8$ µm

(c) c = 0.7: 1000 steps
$t = 2489$ s, $\bar{d} = 70.2$ µm

(d) c = 1.0: 1000 steps
$t = 2352$ s, $\bar{d} = 76.7$ µm

Figure 3.18: Polycrystal RVE at 800 °C simulated in grid Sq(1,2) shown at (a) 0 time steps (b) 1000 time steps - for $c = 0.5$ (c) 1000 time steps for $c = 0.7$ (d) 1000 time steps for $c = 1.0$.

3.5. 3D SIMULATIONS

3.5.1. DESCRIPTION

The extension of the model in 3D is done by including the perpendicular direction in the Sq(1,2) grid, which as shown in the previous sections and in [35–37] is appropriate for grain growth simulations. Therefore a cell i has 26 j neighbours, such that:

- 6 boundaries are of area $A_{ij} = 0.5^2 \cdot \delta x_{CA} \cdot \delta x_{CA}$ and the force at each boundary is directed as $\vec{u}_{ji} = \{\vec{u}_x, -\vec{u}_x, \vec{u}_y, -\vec{u}_y, \vec{u}_z, -\vec{u}_z\}$.
- 12 boundaries are of area $A_{ij} = 0.5^2 \cdot \frac{1}{\sqrt{2}} \cdot \delta x_{CA} \cdot \delta x_{CA}$ and the force at each boundary is directed as:
$\vec{u}_{ji} = \{\cos(45°) \cdot \vec{u}_x + \sin(45°) \cdot \vec{u}_y$,
$\cos(45°) \cdot \vec{u}_x - \sin(45°) \cdot \vec{u}_y$,
$-\cos(45°) \cdot \vec{u}_x + \sin(45°) \cdot \vec{u}_y$,
$-\cos(45°) \cdot \vec{u}_x - \sin(45°) \cdot \vec{u}_y$,
$\cos(45°) \cdot \vec{u}_x + \sin(45°) \cdot \vec{u}_z$,
$\cos(45°) \cdot \vec{u}_x - \sin(45°) \cdot \vec{u}_z$,
$-\cos(45°) \cdot \vec{u}_x + \sin(45°) \cdot \vec{u}_z$,
$-\cos(45°) \cdot \vec{u}_x - \sin(45°) \cdot \vec{u}_z$,
$\cos(45°) \cdot \vec{u}_y + \sin(45°) \cdot \vec{u}_z$,
$\cos(45°) \cdot \vec{u}_y - \sin(45°) \cdot \vec{u}_z$,
$-\cos(45°) \cdot \vec{u}_y + \sin(45°) \cdot \vec{u}_z$,
$-\cos(45°) \cdot \vec{u}_y - \sin(45°) \cdot \vec{u}_z\}$.

- 8 boundaries are of area $A_{ij} = 0.5^2 \cdot \frac{1}{\sqrt{3}} \cdot \delta x_{CA} \cdot \delta x_{CA}$ and the force at each boundary is directed as:
$\vec{u}_{ji} = \{\cos(\arctan(\sqrt{2})) \cdot \vec{u}_x + \cos(\arctan(\sqrt{2})) \cdot \vec{u}_y + \cos(\arctan(\sqrt{2})) \cdot \vec{u}_z$,
$\cos(\arctan(\sqrt{2})) \cdot \vec{u}_x + \cos(\arctan(\sqrt{2})) \cdot \vec{u}_y - \cos(\arctan(\sqrt{2})) \cdot \vec{u}_z$,
$\cos(\arctan(\sqrt{2})) \cdot \vec{u}_x - \cos(\arctan(\sqrt{2})) \cdot \vec{u}_y - \cos(\arctan(\sqrt{2})) \cdot \vec{u}_z$,
$\cos(\arctan(\sqrt{2})) \cdot \vec{u}_x - \cos(\arctan(\sqrt{2})) \cdot \vec{u}_y + \cos(\arctan(\sqrt{2})) \cdot \vec{u}_z$,
$-\cos(\arctan(\sqrt{2})) \cdot \vec{u}_x + \cos(\arctan(\sqrt{2})) \cdot \vec{u}_y + \cos(\arctan(\sqrt{2})) \cdot \vec{u}_z$,
$-\cos(\arctan(\sqrt{2})) \cdot \vec{u}_x - \cos(\arctan(\sqrt{2})) \cdot \vec{u}_y + \cos(\arctan(\sqrt{2})) \cdot \vec{u}_z$,
$-\cos(\arctan(\sqrt{2})) \cdot \vec{u}_x + \cos(\arctan(\sqrt{2})) \cdot \vec{u}_y - \cos(\arctan(\sqrt{2})) \cdot \vec{u}_z$,
$\cos(\arctan(\sqrt{2})) \cdot \vec{u}_x - \cos(\arctan(\sqrt{2})) \cdot \vec{u}_y - \cos(\arctan(\sqrt{2})) \cdot \vec{u}_z \cos(\arctan(\sqrt{2}))\}$.

3.5.2. TEST SIMULATION IN 3D

The applicability of the Cub(2,2) grid is examined here using a bicrystal RVE where the embedded grain is a sphere. Fig. 3.19 shows the simulated grains at 1000 simulation steps, using the Cub(2,2) grid, for the values of $c = 0.5$, $c = 0.7$, and $c = 1$. The grain in the center is a sphere and it is plotted in the three (Cartesian) cross-sections that include its center. As expected, at a certain time step, differences between the cross-sections xy, xz and yz are not significant.

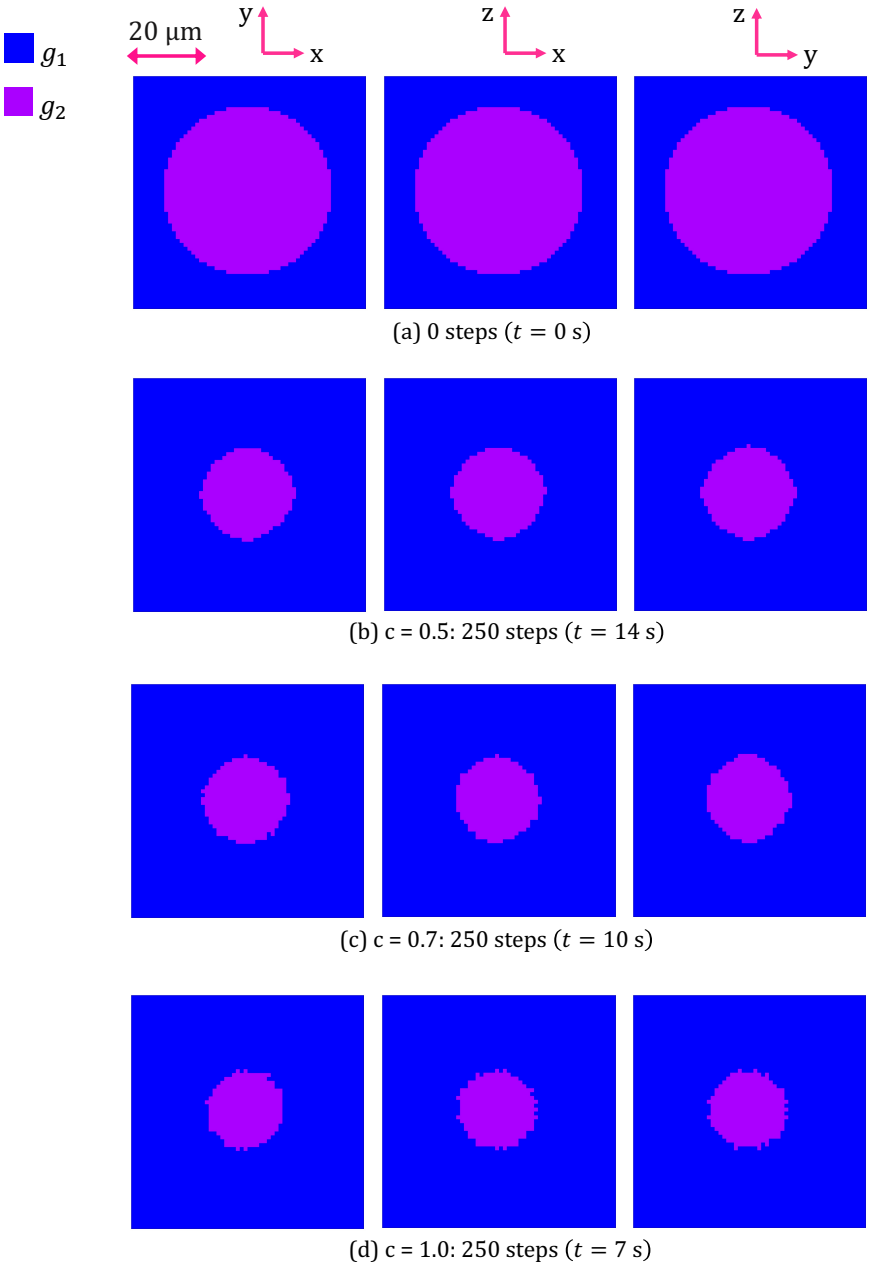

(a) 0 steps ($t = 0$ s)

(b) c = 0.5: 250 steps ($t = 14$ s)

(c) c = 0.7: 250 steps ($t = 10$ s)

(d) c = 1.0: 250 steps ($t = 7$ s)

Figure 3.19: Bicrystal RVE at 1000 °C in Cub(2,2): The maps show the xy, xz and yz (middle) cross sections at (a) 0 time steps - 0 s (b) 250 time steps for $c = 0.5$ (c) 250 time steps for $c = 0.7$ (d) 250 time steps for $c = 1.0$.

3.6. TEST SIMULATIONS - KINETICS

In this section, the grain growth evolution is presented and discussed regarding the kinetics. Only the grids that are not significantly affected by grid artifacts are used here - namely Hex(1,1) and Sq(1,2) in 2D and Cub(2,2) in 3D. More specifically, we investigate the shrinkage evolution of a spherical/circular grain embedded in another grain, i. e. for Cub(2,2) the RVE is shown in Fig. 3.19. The RVEs used in Hex(1,1), Sq(1,2) correspond to the middle cross-section (e. g. xy) of the 3D RVE shown in Fig. 3.19.

3.6.1. EFFECTS OF GRID-SPACING - RESOLUTION

Here we study the dependence of the CA's kinetic evolution on the grid-spacing/resolution that is used. For each grid, the RVE was remeshed in various values of δx_{CA}, ranging from $0.5\ \mu m - 2\ \mu m$, while preserving the physical size of the grains, i. e. the number of cells describing the RVE changes accordingly such that the length scale does not change.

Figs. 3.20 to 3.22 show the diameter of the embedded circular/spherical grain, simulated at different RVEs for Hex(1,1), Sq(1,2) and Cub(2,2), respectively. The figures correspond to $c = 0.7$ - because the insights obtained for $c = 0.5$, $c = 1.0$ are similar. As is shown, there are no significant differences upon changing the grid spacing/resolution that is used.

From the model description, it is clear that the kinetic outcome is not dependent on the grid-spacing. This is because the rate at which a cell reorients (Eq. (3.13)) is proportional to the square of the migrating boundaries' area per volume. Hence, the re-orientation rate is always inversely proportional to the power of the grid spacing - for both 2D and 3D grids. This is important because it complies with the constant area reduction rate incorporated in the theory of curvature-driven grain coarsening explained by Mullins [39], Von Neumann, J. [40], and substantiated in both 2D and 3D grain growth descriptions - e. g. by Anderson *et al.* [5], Shvindlerman *et al.* [41], Hillert [42], Palmer *et al.* [43], Hilgenfeldt *et al.* [44].

As for the effects of the RVE's resolution (i. e. number of cells) on the kinetics, this cannot be assessed from the model description. Changing the number of cells describing an RVE can lead to either an overestimation or to an underestimation of the kinetics. Hence, Figs. 3.20 to 3.22 are particularly insightful in this view. It is shown that the most pronounced variations on the simulated grain diameter characterize the range of coarser resolutions. Oppositely, for finer RVEs, an incremental change in the resolution yields smaller differences in the predicted grain diameter, in comparison to that of coarser RVEs, i. e. the predicted values converge. Altogether, it is concluded that the grid-spacing/resolution dependency is minor.

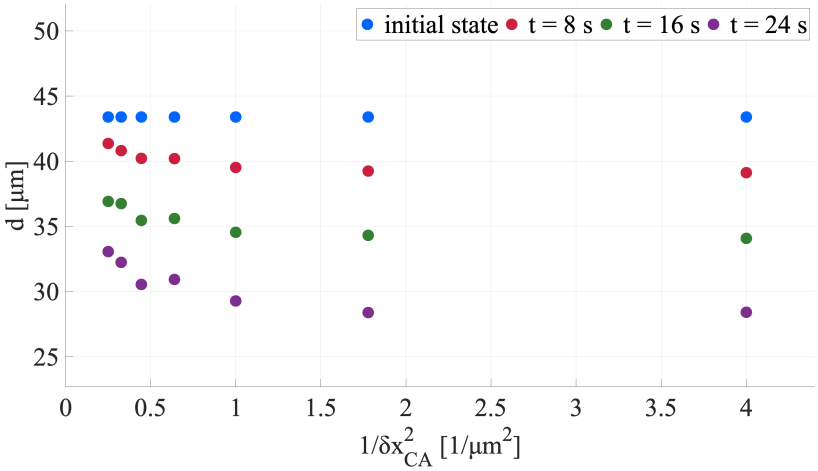

Figure 3.20: Dependency of grain growth kinetics on resolution and grid-spacing in Hex(1,1) the simulations are done using $c = 0.7$ at 1000 °C. The grain diameter is shown for the embedded circular grain at different times as a function of the resolution/grid-spacing.

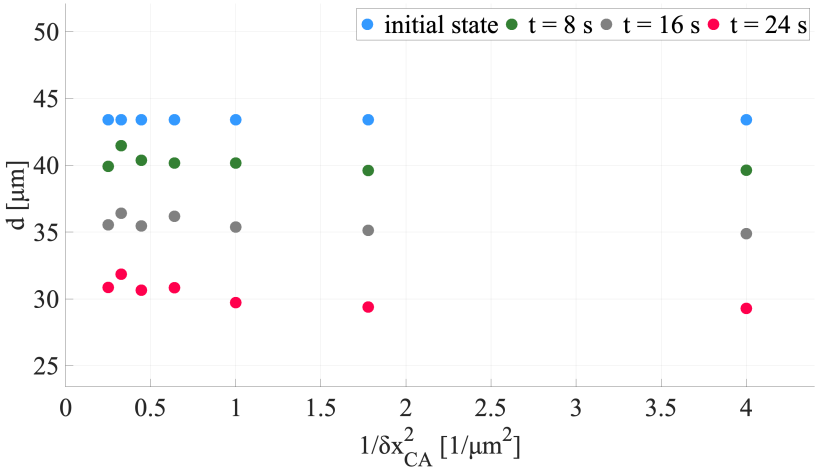

Figure 3.21: Dependency of grain growth kinetics on resolution and grid-spacing in Sq(1,2): the simulations are done using $c = 0.7$ at 1000 °C. The grain diameter is shown for the embedded circular grain at different times as a function of the resolution/grid-spacing.

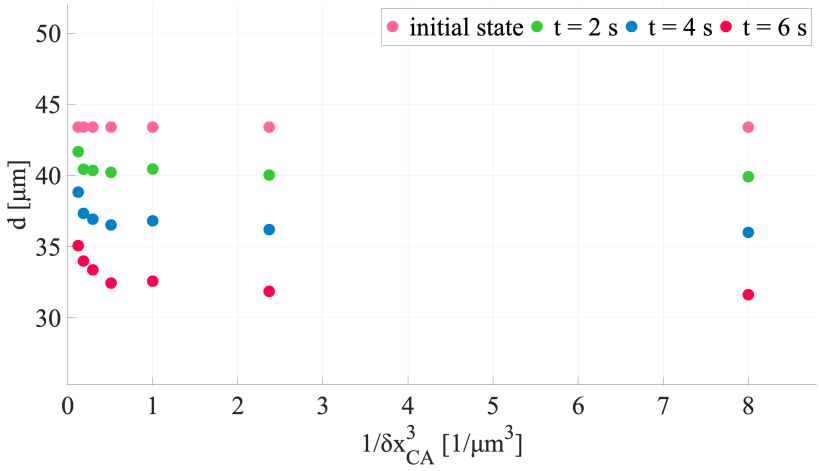

Figure 3.22: Dependency of grain growth kinetics on resolution and grid-spacing in Cub(2,2): the simulations are done using $c = 0.7$ at 1000 °C. The grain diameter is shown for the embedded spherical grain at different times as a function of the resolution/grid-spacing.

3.6.2. SHRINKAGE RATE - SPHERE AND CIRCLE

The shrinkage evolution of the spherical grain is shown in Fig. 3.25 for Cub(2,2), and of the circular grain in Fig. 3.24 and Fig. 3.23 for Sq(1,2) and Hex(1,1), respectively. The simulated values are fitted with the theoretical expression of ideal grain growth developed by Smith [45, 46] and Burke and Turnbull [31] where the time evolution of the diameter of a grain enclosed by a boundary with constant curvature is equal to:

$$d^2 = d_0^2 + k \cdot t \tag{3.16}$$

where d_0^2 is the grain diameter at the initial state, i. e. $t = 0$ s.

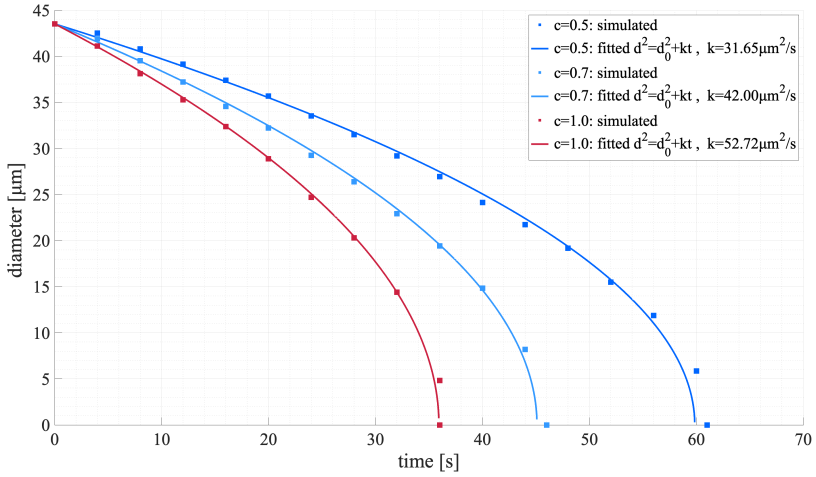

Figure 3.23: Shrinkage evolution at 1000 °C for the circular grain in Hex(1,1): The kinetics are evaluated for $c = 0.5$, $c = 0.7$ and $c = 1.0$. The simulated data are fitted with the theoretical analytical expression for ideal grain growth.

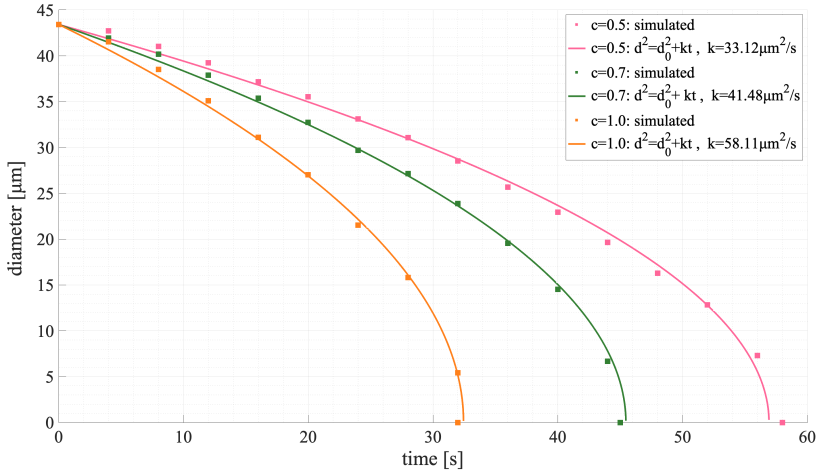

Figure 3.24: Shrinkage evolution at 1000 °C for the circular grain in Sq(1,2): The kinetics are evaluated for $c = 0.5$, $c = 0.7$ and $c = 1.0$. The simulated data are fitted with the theoretical analytical expression for ideal grain growth.

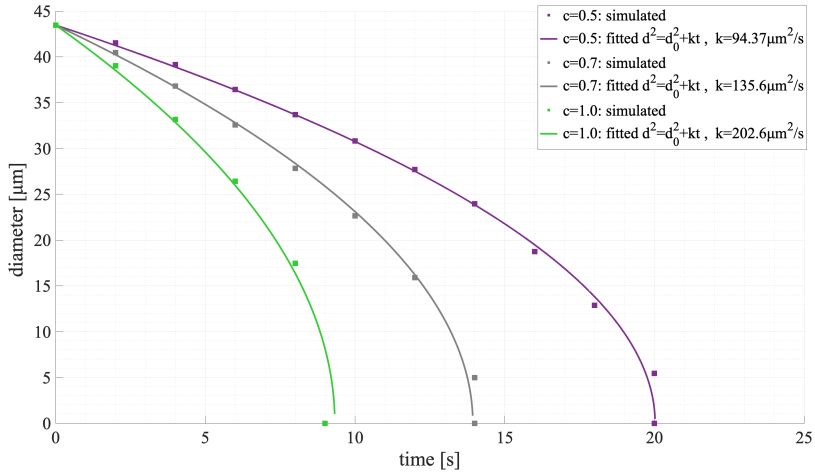

Figure 3.25: Shrinkage evolution at 1000 °C for the spherical grain in Cub(2,2): The kinetics are evaluated for $c = 0.5$, $c = 0.7$ and $c = 1.0$. The simulated data are fitted with the theoretical analytical expression for ideal grain growth.

As is shown in Fig. 3.25, Fig. 3.24 and Fig. 3.23 the parabolic relationship between time and grain diameter is confirmed for all simulations. The value of c, as expected, affects the kinetics by increasing the value of k, thus indicating faster shrinkage. The simulated data fit well the theoretical expression of grain growth which confirms that indeed the grain's area reduces with constant rate in both 2D and 3D descriptions [5, 31, 36, 39–42, 45–47].

3.6.3. SCALING GRID-RELATED KINETICS

Table 3.2 summarizes the kinetics for ideal grain growth in the investigated grids from the analysis performed in Section 3.6.2.

Table 3.2: Kinetics in 2D (circle) and 3D (sphere) simulation of grain shrinkage at 1000 °C.

	Time steps required	Physical time required [s]	k_{grid} [$\mu m^2/s$]
Hex(1,1) and $c = 0.5$	740	61.2	31.7
Sq(1,2) and $c = 0.5$	453	58.5	33.1
Cub(2,2) and $c = 0.5$	339	20.5	94.4
Hex(1,1) and $c = 0.7$	665	46.3	42
Sq(1,2) and $c = 0.7$	459	45.4	41.5
Cub(2,2) and $c = 0.7$	330	14.3	135.6
Hex(1,1) and $c = 1.0$	600	36.1	52.7
Sq(1,2) and $c = 1.0$	423	32.7	58.1
Cub(2,2) and $c = 1.0$	317	9.95	202.6

Regarding the value of k_{grid} between different grid settings, it is clear that Hex(1,1) and Sq(1,2) give close results (for the same value of c), whereas a 3D curvature-driven simulation amounts to faster shrinking compared to 2D simulations. There are two main reasons for this:

- Unless a grain boundary in 3D would have curvature in only two dimensions (e. g. cylinder) the energy release and hence driving force in the CA is underestimated in a 2D grid.
- The number of cells growing into the adjacent dissimilar cells is higher in the Cub(2,2) than in the Sq(1,2) grid. Hence the re-orientation rate for a cell is higher in the 3D.

While the first explanation is expected from analytical theory, i. e. the driving force is larger in a spherical grain compared to a cylindrical, the second is only related to the different grid-settings. Nevertheless, the grid-related differences in the kinetic outcome can be compensated by introducing a coefficient β per grid, multiplying the re-orientation rate in Eq. (3.13) such that the kinetic evolution is irrespective of the grid used. In particular, Eq. (3.13) is modified such that the re-orientation rate of a cell i is:

$$\dot{f}_{g_i \to g_j} = \beta_{grid} \cdot M_{g_i \to g_j} \cdot \sqrt{\sum_{u_r = x,y,z} \left(\sum_k \delta_{kj} \cdot \left| \vec{F}_{ik, g_i \to g_j} \cdot \vec{u}_r \right| \right)^2} / V_i \tag{3.17}$$

and for each set of grid-settings β_{grid} should be such that the simulation's kinetics are the same in all (grid) sets.

To do this, we will consider a reference/theoretical value k_{th}. We assume that k_{th} corresponds to the kinetics of the actual thermally activated atomic jumps toward the planar boundary (short-range self-diffusion) explained by Turnbull [30]. The driving force ΔG_{th} is equal to $2 \cdot \gamma / D$ in 2D and $4 \cdot \gamma / D$ in 3D[2] as explained by Burke and Turnbull [31]. In this

[2]From $\Delta G = \frac{\partial E}{\partial r} \cdot \frac{1}{A}$ where E is the energy release, r is the grain radius and A is the boundary area.

case, we get $k_{th} = 16 \cdot M \cdot \gamma$ for 3G shrinkage and $k_{th} = 8 \cdot M \cdot \gamma$ for 2D[3]. Using the values presented in Table 3.1 we can find k_{th} at the present temperature (here 1000 °C).

Let β_{grid} be the ratio of the theoretical (atomic scale) k_{th} and the fitted values of k per grid, i. e. k_{grid}. Then β_{grid} is a factor - constant for each grid - that when multiplying the re-orientation rate of Eq. (3.13), the kinetics relate to the actual atomic motion required for boundary migration. In other words, the input data M_0, Q_g, γ correspond to the actual quantities describing curvature-driven grain boundary migration via self-diffusion toward (and perpendicular to) the planar boundary. Table 3.3 summarizes the values of β_{grid} that are found for each grid. It should be clarified that β_{grid} relates to the configuration of the grid and not to the grid spacing or the temperature, as the latter are already considered in the re-orientation rate.

Table 3.3: Kinetic factor β_{grid} evaluated per grid.

	Simulated k_{grid} [μm^2/s]	k_{th} [μm^2/s]	Grid factor $\beta_{grid} = k_{th}/k_{grid}$
Hex(1,1) and $c = 0.5$	31.7	20.7	0.65
Sq(1,2) and $c = 0.5$	33.1	20.7	0.62
Cub(2,2) and $c = 0.5$	94.4	41.4	0.44
Hex(1,1) and $c = 0.7$	42.0	20.7	0.49
Sq(1,2) and $c = 0.7$	41.5	20.7	0.50
Cub(2,2) and $c = 0.7$	135.6	41.4	0.30
Hex(1,1) and $c = 1.0$	52.7	20.7	0.39
Sq(1,2) and $c = 1.0$	58.1	20.7	0.36
Cub(2,2) and $c = 1.0$	202.6	41.4	0.20

3.7. COMPARISON WITH THE MC-POTTS KINETICS PROBABILISTIC CA METHOD

Owing to the resemblance between the present CA method and the probabilistic MC-Potts CA method, this section reviews and clarifies which similarities and differences are expected between the present CA and the probabilistic MC-Potts CA method. Since the present CA model considers the energy change associated with a cell's surrounding boundaries prior to and after its re-orientation, it is clear that although it operates based on deterministic transformation rules, in practice, it is expected to simulate phenomena more or less like the full-field probabilistic MC-Potts model for grain coarsening. This is of course why the outcome of the tests performed here is very similar to the reported results when using the MC Potts-kinetics grain coarsening algorithm. However, due to the inherent differences between a deterministic description and a probabilistic MC Potts-kinetics approach, it is still expected that there should be some differences between the two models.

[3]These are found upon integrating the theoretical expression $\frac{dr}{dt} = M \cdot \Delta G$.

The first difference is the switching cell sequence, which in the MC-Potts method takes place sequentially whereas here (as also in any other deterministic model) it is simultaneous for all cells. However, this is not expected to have any further implications on either normal grain coarsening or recrystallization simulations.

The second difference is due to the inherent relationships that each computational technique incorporates with the physical processes. More specifically, in the MC-Potts method, the successful cell switches depend on the comparison between a randomly generated number and a probability. Whether this probability depends on the driving force together with only global quantities such as the temperature, e. g. statistical distributions derived from Glauber [48] and Metropolis *et al.* [49], or it is scaled by considering additional local characteristics such as the boundary mobility or mobility-related quantities, e. g. Mehnert and Klimanek [8], Raabe [11], Safran *et al.* [13], Holm *et al.* [50], a part of the decision rule for switching a cell is still random and strongly dependent on the temperature. Of course, when it comes to grain coarsening, this is not something that requires further consideration, as long as the MC temperature is sufficiently high to avoid considerable grid-related artifacts associated with the boundary energy anisotropy [35–37, 51].

However, when approaching recrystallization as the selective growth of material volumes, it is not yet entirely clear whether a probabilistic framework is equivalent to a deterministic one. This is because a part of the competition between subgrains, which is crucial especially in the early stages of annealing, may be also associated with its “luck”. The latter can be understood if we consider that at the initial stages, among numerous cells with equal driving force, some neighbourhoods may have more accepted cell switches within successive simulation time steps, and thus favor the growth of certain subgrains. In other words, the main difference that is expected between the present CA method and the MC-Potts model is that in a subgrain growth simulation of 5,000,000 material elements, the subgrains that nucleate and grow in the present approach are the ones that were always mobile and favored by the energy release, whereas in the MC method it is possible that these were also somewhat “lucky”. It should be clarified, that this does not highlight a weakness of the MC method, since indeed atomic fluctuations do exist. It does indicate a potential difference between the present method and the MC-Potts CA method, which would nonetheless need to be considered upon interpreting the simulation results, particularly in the context of preferential growth and orientation selection.

3.8. CONCLUSIONS

A CA algorithm for boundary energy-driven grain/subgrain growth based on deterministic transformation rules was presented. This method was developed in order to overcome challenges when simulating subgrain/grain coarsening at the scale where the elementary volumes are close to (or equal to/larger than, depending on the resolution) the actual subgrain size. And this method is indeed used later - in all subsequent chapters - for simulating recrystallization related phenomena. In this chapter, however, only the description of the method and its applicability in modeling (normal) grain coarsening phenomena was presented and discussed. This is because it is necessary to test the algorithm regarding its applicability and physical relevance to the boundary motion resulting from diminishing the boundary energy. Such assessments can only be done on well-understood phenomena with

regard to the expected outcome, for example normal grain growth and pure curvature-driven coarsening, and hence in this chapter we only dealt with such simple examples.

In particular, several simulations were performed in 2D and 3D grids. The RVEs used for this purpose varied from simple bicrystal and tricrystal examples to a polycrystal microstructure of random crystallographic texture. The following conclusions were made:

- In terms of grid artifacts (boundary energy anisotropy), Hex(1,1), Sq(1,2) and Cub(2,2) discretizations are appropriate for curvature-driven simulations, regardless of the value of c - at least $\forall c \in [0.5, 1]$. Oppositely, the simulations in Sq(1,1) exhibit major grid effects. Also, these effects are significantly sensitive to the value of c.
- The simulated curvature-driven kinetics in ideal circular/spherical grains are in compliance with the analytical description of ideal grain growth. In particular, the shrinkage of a sphere/circle in Hex(1,1), Sq(1,2) and Cub(2,2) grid evolves according to the theoretical power law.
- The kinetic outcome was found to be independent of the grid spacing used to describe an RVE - of course, as long as the remeshing is done accordingly so as to preserve the physical size of the grains.
- For different grid settings, we have summarized the correspondence of the CA's kinetic evolution with the physical description of the curvature-driven boundary migration rate. Eventually, we defined for all the acceptable grids (and settings) a kinetics-related factor β_{grid}, and reformulated the CA's kinematic rule such that the simulated kinetics are independent of the grid (and settings) used. The value of β_{grid} for each grid has been determined here once, and it corresponds to all simulation temperatures and grid spacings.

REFERENCES

[1] K. Traka, K. Sedighiani, C. Bos, J. Galan Lopez, K. Angenendt, D. Raabe, and J. Sietsma, *Topological aspects responsible for recrystallization evolution in an IF-steel sheet – Investigation with cellular-automaton simulations,* Computational Materials Science **198**, 110643 (2021).

[2] J. Von Neumann, A. W. Taub, and A. H. Taub, *The Collected Works of John von Neumann: 6-Volume Set* (Reader's Digest Young Families, 1963).

[3] J. G. Kemeny, *Theory of Self-Reproducing Automata. John von Neumann. Edited by Arthur W. Burks. University of Illinois Press, Urbana, 1966. 408 pp., illus. $10,* Science **157**, 180 (1967).

[4] D. Raabe, *Cellular Automata in Materials Science with Particular Reference to Recrystallization Simulation,* Annual Review of Materials Research **32**, 53 (2002).

[5] M. Anderson, D. Srolovitz, G. Grest, and P. Sahni, *Computer simulation of grain growth—I. Kinetics,* Acta Metallurgica **32**, 783 (1984).

[6] M. P. Anderson, G. S. Grest, and D. J. Srolovitz, *Computer simulation of normal grain growth in three dimensions,* Philosophical Magazine B **59**, 293 (1989).

[7] R. B. Potts and C. Domb, *Some generalized order-disorder transformations,* Mathematical Proceedings of the Cambridge Philosophical Society **48**, 106 (1952).

[8] K. Mehnert and P. Klimanek, *Monte Carlo simulation of grain growth in textured metals,* Scripta Materialia **35**, 699 (1996).

[9] S. Ling and M. P. Anderson, *Monte Carlo simulation of grain growth and recrystallization in polycrystalline materials,* JOM **44**, 30 (1992).

[10] M. Tong, D. Li, Y. Li, J. Ni, and Y. Zhang, *Monte carlo-method simulation of the deformation-induced ferrite transformation in the Fe-C system,* Metallurgical and Materials Transactions A **35**, 1565 (2004).

[11] D. Raabe, *Scaling Monte Carlo kinetics of the Potts model using rate theory,* Acta Materialia **48**, 1617 (2000).

[12] D. Raabe and A. D. Rollett, *Basic Approaches to the Simulation of Recrystallization and Grain Growth,* (2004).

[13] S. A. Safran, P. S. Sahni, and G. S. Grest, *Kinetics of ordering in two dimensions. I. Model systems,* Physical Review B **28**, 2693 (1983).

[14] E. A. Holm and C. C. Battaile, *The computer simulation of microstructural evolution,* JOM **53**, 20 (2001).

[15] E. Holm, D. Srolovitz, and J. Cahn, *Microstructural evolution in two-dimensional two-phase polycrystals,* Acta Metallurgica et Materialia **41**, 1119 (1993).

[16] E. Holm, M. Miodownik, and A. Rollett, *On abnormal subgrain growth and the origin of recrystallization nuclei,* Acta Materialia **51**, 2701 (2003).

[17] A. Rollett, D. Srolovitz, and M. Anderson, *Simulation and theory of abnormal grain growth—anisotropic grain boundary energies and mobilities,* Acta Metallurgica **37**, 1227 (1989).

[18] K. Kremeyer, *Cellular Automata Investigations of Binary Solidification,* Journal of Computational Physics **142**, 243 (1998).

[19] C. Zheng and D. Raabe, *Interaction between recrystallization and phase transformation during intercritical annealing in a cold-rolled dual-phase steel: A cellular automaton model,* Acta Materialia **61**, 5504 (2013).

[20] F. Han, B. Tang, H. Kou, J. Li, and Y. Feng, *Cellular automata modeling of static recrystallization based on the curvature driven subgrain growth mechanism,* Journal of Materials Science **48**, 7142 (2013).

[21] F. Han, B. Tang, H. Kou, L. Cheng, J. Li, and Y. Feng, *Static recrystallization simulations by coupling cellular automata and crystal plasticity finite element method using a physically based model for nucleation,* Journal of Materials Science **49**, 3253 (2014).

[22] O. I. Frette, G. Virnovsky, and D. Silin, *Estimation of the curvature of an interface from a digital 2D image,* Computational Materials Science **44**, 867 (2009).

[23] F. Han, B. Tang, H. Kou, J. Li, and Y. Feng, *Cellular automata simulations of grain growth in the presence of second-phase particles,* Modelling and Simulation in Materials Science and Engineering **23**, 065010 (2015).

[24] J. Bullard, E. Garboczi, W. Carter, and E. Fuller, *Numerical methods for computing interfacial mean curvature,* Computational Materials Science **4**, 103 (1995).

[25] C. Bos, M. Mecozzi, and J. Sietsma, *A microstructure model for recrystallisation and phase transformation during the dual-phase steel annealing cycle,* Computational Materials Science **48**, 692 (2010).

[26] C. Bos, M. G. Mecozzi, D. N. Hanlon, M. P. Aarnts, and J. Sietsma, *Application of a Three-Dimensional Microstructure Evolution Model to Identify Key Process Settings for the Production of Dual-Phase Steels,* Metallurgical and Materials Transactions A **42**, 3602 (2011).

[27] F. Han, B. Tang, H. Kou, J. Li, and Y. Feng, *Effects of subgrain size and static recrystallization on the mechanical performance of polycrystalline material: A microstructure-based crystal plasticity finite element analysis,* Progress in Natural Science: Materials International **25**, 58 (2015).

[28] Y. Suwa, M. Tomita, Y. Tanaka, and K. Ushioda, *Phase-field Simulation of Recrystallization in Cold Rolling and Subsequent Annealing of Pure Iron Exploiting EBSD Data of Cold-rolled Sheet,* ISIJ International **61**, 350 (2021).

[29] W. T. Read and W. Shockley, *Dislocation Models of Crystal Grain Boundaries,* Physical Review **78**, 275 (1950).

[30] D. Turnbull, *Theory of Grain Boundary Migration Rates,* JOM **3**, 661 (1951).

[31] J. Burke and D. Turnbull, *Recrystallization and grain growth,* Progress in Metal Physics **3**, 220 (1952).

[32] F. J. Humphreys, G. S. Rohrer, and A. D. Rollett, *Recrystallization and related annealing phenomena*, third edition ed. (Elsevier, Amsterdam Oxford Cambridge, MA, 2017).

[33] G. Gottstein and L. S. Shvindlerman, *Grain boundary migration in metals: thermodynamics, kinetics, applications*, 2nd ed., CRC series in materials science and technology (Taylor & Francis, Boca Raton, 2010) oCLC: ocn166358378.

[34] D. Wolf, *Structure-energy correlation for grain boundaries in F.C.C. metals—I. Boundaries on the (111) and (100) planes,* Acta Metallurgica **37**, 1983 (1989).

[35] Holm E., *Ph.D. thesis*, Ph.D. thesis, University of Michigan (1992).

[36] A. D. Rollett and P. Manohar, *The Monte Carlo Method,* in *Continuum Scale Simulation of Engineering Materials*, edited by D. Raabe, F. Roters, F. Barlat, and L.-Q. Chen (Wiley-VCH Verlag GmbH & Co. KGaA, Weinheim, FRG, 2005) pp. 77–114.

[37] A. Rollett, *Overview of modeling and simulation of recrystallization,* Progress in Materials Science **42**, 79 (1997).

[38] R. S. Miller, G. Cao, and M. Grujicic, *Monte Carlo Simulation of Three-Dimensional Nonisothermal Grain-Microstructure Evolution: Application to LENS Rapid Fabrication,* Journal of Materials Synthesis and Processing **9**, 329 (2001).

[39] W. W. Mullins, *Two-Dimensional Motion of Idealized Grain Boundaries,* Journal of Applied Physics **27**, 900 (1956).

[40] Von Neumann, J., *Metal Interfaces,* (Cleveland,108).

[41] L. S. Shvindlerman, G. Gottstein, and A. D. Rollett, *The Von Neumann-Mullins Theory of Grain Growth – Valid or Not?!* Materials Science Forum **467-470**, 1111 (2004).

[42] M. Hillert, *On the theory of normal and abnormal grain growth,* Acta Metallurgica **13**, 227 (1965).

[43] M. A. Palmer, V. E. Fradkov, M. E. Glicksman, and K. Rajan, *EXPERIMENTAL ASSESSMENT OF THE MUI J,INS -YON NEUMANN GRAIN GROWTH LAW,* **30**, 5.

[44] S. Hilgenfeldt, A. M. Kraynik, S. A. Koehler, and H. A. Stone, *An Accurate von Neumann's Law for Three-Dimensional Foams,* Physical Review Letters **86**, 2685 (2001).

[45] C. S. Smith, *Grains, phases, and interphases: an interpretation of microstructure,* Trans. Metall. Soc. AIME **175**, 15 (1948), aDS Bibcode: 1948TrMS..175...15S.

[46] C. S. Smith, *Grain Shapes and Other Metallurgical Applications of Topology,* Metallography, Microstructure, and Analysis **4**, 543 (2015).

[47] R. D. MacPherson and D. J. Srolovitz, *The von Neumann relation generalized to coarsening of three-dimensional microstructures,* Nature **446**, 1053 (2007).

[48] R. J. Glauber, *Time-Dependent Statistics of the Ising Model,* Journal of Mathematical Physics **4**, 294 (1963).

[49] N. Metropolis, A. W. Rosenbluth, M. N. Rosenbluth, A. H. Teller, and E. Teller, *Equation of State Calculations by Fast Computing Machines,* The Journal of Chemical Physics **21**, 1087 (1953).

[50] E. Holm, N. Zacharopoulos, and D. Srolovitz, *Nonuniform and directional grain growth caused by grain boundary mobility variations,* Acta Materialia **46**, 953 (1998).

[51] J. Mason, J. Lind, S. Li, B. Reed, and M. Kumar, *Kinetics and anisotropy of the Monte Carlo model of grain growth,* Acta Materialia **82**, 155 (2015).

4

SUBSTRUCTURE TOPOLOGY, DEFORMATION FEATURES AND RECRYSTALLIZATION IN IF-STEEL SHEET

A cellular automaton algorithm for boundary energy-driven coarsening is applied to a cold-rolled interstitial-free steel's microstructure - obtained through electron backscatter diffraction (EBSD). The spatial inhomogeneity of the subgrain growth that takes place derives from the large local variations of subgrain sizes and misorientations that comprise the prior deformed state. Additionally, during the simulation certain texture components intensify and others vanish, which indicates that preferential growth occurs in a fashion that relates to the crystal orientations' topology. The study of the early stages of recrystallization (i. e. nucleation) shows that the pre-existing subgrains that eventually recrystallize, exhibit certain topological characteristics at the prior deformed state. Successful nucleation occurs mostly for pre-existing subgrains abutting narrow deformation bands and particularly at regions where the latter intersect.

4.1. INTRODUCTION

4.1.1. MOTIVATION

Recrystallization has been extensively studied in low carbon (LC) and interstitial-free (IF) steels [2–19]. Besides the experimental work, the topological mesoscopic computation of

Parts of this chapter have been published in [1] by K. Traka, K. Sedighiani, C. Bos, J. Galan Lopez, K. Angenendt, D. Raabe, and J. Sietsma, Topological aspects responsible for recrystallization evolution in an IF-steel sheet – Investigation with cellular-automaton simulations, Computational Materials Science 198, 110643 (2021).

recrystallization-related phenomena has also helped to understand the mechanisms responsible for the microstructural processes that occur [20–29]. Although the origin of recrystallization nuclei in such metals has been well explained by the subgrain formation and growth mechanism [30–37], the early stages of recrystallization constitute a still unresolved matter [7]. This is because there are many interacting boundaries and microstructural features (e. g. deformation bands and grain boundaries) and numerous concurring mechanisms related to the onset of recrystallization [6, 32]. Hence, it has not been clarified why particular subgrains evolve into recrystallization nuclei and others do not.

The goal of this work is to study how the local topology contributes to the nucleation and growth of pre-existing subgrains. Investigating the early stages of recrystallization requires the simulation of the coarsening that occurs in all subgrains simultaneously - see for example the studies of Holm *et al.* [34] and Han *et al.* [38]. Therefore, we simulate recrystallization in a Ti-stabilized IF steel cold-rolled at 77 % thickness reduction and we allowed all pre-existing subgrains to compete in evolving into recrystallized grains. In other words, nucleation in this work is not artificially imposed but evolves out of the discontinuous competitive subgrain coarsening process, as explained by Humphreys [39]. We use a close coupling to the inherited microstructure and thereby investigate the topological characteristics that facilitate recrystallization initiation and growth.

4.1.2. RELATIONSHIP BETWEEN INHOMOGENEOUS SUBGRAIN COARSENING AND RECRYSTALLIZATION

At the mesoscopic scale, recrystallization in highly plastically strained metals is normally described as a process comprising successive interface phenomena referred to as nucleation and growth. However, it has been well-established that in materials that tend to form subgrain structures, recrystallization phenomena proceed through a mostly heterogeneous (sub)grain growth process [6, 9, 10, 15, 30–33, 37–45]. Some of the pre-existing subgrains grow (while others shrink), gradually accumulate increasing misorientation and/or size relative to their changing neighborhood, and finally recrystallize.

In this view, recrystallization can be described as a phenomenon that is physically related to grain coarsening, particularly the one known as discontinuous/abnormal (sub)grain growth [34, 39]. The restoration process involved in all stages of recrystallization is described by the reduction of (sub)boundary energy. Hence, the stored deformation energy is approximated from the dislocation content at the boundaries - i. e. high angle grain boundaries (HAGBs) and geometrically necessary dislocations (GNDs). Although statistically stored dislocations (SSDs) may highly contribute to the material's stored energy, metals characterized by high stacking fault energy (SFE), such as iron and aluminum, form subgrain structures usually already during the plastic deformation process. This is due to the high mobility and cross-slip frequency of the dislocations[1]. The dominance of subgrain structures in such metals has been revealed by numerous investigations [3, 9, 10, 46–50] using transmission electron microscopy (TEM) after cold deformation.

Although the description of recrystallization-related phenomena as a capillary compet-

[1] Even if the substructure is not fully recovered in the as-deformed state, static recovery will still take place (both as polygonization [35–37] and dislocation annihilation) in the very early stages of annealing and thereby diminish the "free" dislocation density.

itive (sub)grain growth mechanism is an approximation, it nonetheless unifies the stages of nucleation, recrystallization growth and grain growth into one physics-based framework - as suggested by Humphreys [39] - and thereby enables their simultaneous computation. The relevant terminology which we follow in this paper is presented in Table 4.1. We adopt the terms primarily from [39] and additionally from [3, 34, 40, 41, 51].

The capillary competitive (sub)grain growth modeling approach suggests that the heterogeneity in the subgrains' coarsening stems from the heterogeneous distribution of the orientation gradients (i. e. GNDs and HAGBs) [34, 39, 52]. These determine the mobility and the driving force whereby subgrain growth occurs [53–55]. Accumulating enough mobility (due to increasing misorientation when growing into orientation gradients) and/or higher driving forces gives an advantage to some subgrains and this is called nucleation [3, 34, 39, 40, 51]. Hence, although nucleation is not artificially imposed in this work, it evolves naturally out of the evolving substructure, by the mechanisms known as discontinuous subgrain growth [6] and HAGB bulging [33]. Both nucleation mechanisms are relevant to the recrystallization of cold-worked IF-steel in the range of 70-80% thickness reduction [6, 26, 29, 32]. Other possibly relevant mechanisms such as subgrain coalesence [56, 57], heterogeneous static subgrain formation [58, 59], variations of particle pinning at certain HAGBs [12, 53, 60–63] are not addressed in this work. Although such processes may contribute to the nucleation and growth of recrystallization by providing a kinetic or energy advantage to some subgrains, our aim is to investigate the effect and spatial variation of the boundary energy-driven motion.

Table 4.1: Terminology used in the document.

Term	**Description**
Kinetically unstable boundary	A boundary which has high mobility, compared to most boundaries in the microstructure at that time - e. g. in the current application the term applies to a HAGB.
Thermodynamically unstable boundary	A boundary which yields energy release upon an incremental migration.
Kinetic advantage (of a subgrain or grain)	A (sub)grain that continues being surrounded by large angle boundaries after initiating recrystallization.
Energy advantage (of a subgrain or grain)	A (sub)grain that continues being larger from the subgrains it meets during its expansion after initiating recrystallization.
Recrystallization nucleation	When a subgrain is particularly competitive and has grown enough so that the recrystallized volume can be clearly distinguished from the surrounding substructure, it is considered as nucleus.

4.1.3. IMPLEMENTATION AND ASSUMPTIONS IN RELATION TO PREVIOUS WORKS

Full-field simulations of recrystallization phenomena including the nucleation stage, i. e. by using a model that operates with kinematic and transformation rules applicable for grain coarsening phenomena, were introduced e. g. by Humphreys [64] and Holm *et al.* [34]. By creating artificial grain/subgrain structures and varying the mobility and sizes of particular

subgrains, Humphreys [64] applied a network (vertex) and Holm *et al.* [34] the well-known probabilistic CA algorithm based on the multistate Monte-Carlo (MC) Potts kinetics method, to explain that growth instability occurs (i. e. recrystallization). Such studies served as the basis for the full-field modeling of recrystallization in terms of selective grain/subgrain growth that followed. In particular, using input coming from crystal plasticity (CP) full-field simulations, or electron backscatter diffraction (EBSD) analyses, Bate [65], Han *et al.* [66] and Suwa *et al.* [52] used (sub)grain coarsening computational techniques such as the vertex/network method [64], the multi phase-field (MPF) method [67–71] and the deterministic CA method [72].

Such simulation studies, focused on the nucleation stage, are very important for their contribution to our current understanding of the evolution of recrystallization based on the size/kinetic advantage of subgrains. However, modeling the nucleation stage of recrystallization always requires certain assumptions regarding the relationship between the input deformed state and the actual substructure. For example Han *et al.* [66] assumed an equiaxed and uniform substructure inside each deformed grain. Bate [65] exploited the von Mises stress predicted by the (CP) full-field simulation and generated subgrains of size inversely proportional to the former. A more recent and local description was introduced by Suwa *et al.* [52], who assumed that the image quality (IQ) measured at each pixel by EBSD, indicates the stored energy, and therefore each pixel's IQ gives (qualitatively) the radius of the subgrain it should belong to. Then, by successively growing the crystal orientation of pixels into their neighborhood until the theoretical radius was reached, the substructure was generated. The latter provided a realistic view of the substructure, although the conversion implies that a part of the heterogeneity characterizing the substructure had to be artificial. Hence, as explained by Suwa *et al.* [52] some subgrains energy/kinetic advantage had to be assumed as a result of heterogeneous static subgrain formation (recovery).

On the other hand, here, the aim is to investigate whether and how recrystallization initiates and evolves, in terms of discontinuous subgrain growth and HAGB bulging. Therefore, this time the algorithm operates by using the measured EBSD data as the starting deformed state. In other words, to avoid making an assumption about a uniform and equiaxed substructure (which is also not the case in banded regions for example) in a grain mean-field level [66] or requiring an assumption on which pixels would belong to the same subgrain after these would form and grow in the very early stages of annealing [52], we make another assumption: that every crystal orientation measured from the EBSD is either a part of a subgrain or a subgrain itself. Based on this assumption, we allow all 5,000,000 material elements to grow and compete, and thenceforth investigate whether and how some of these were more competitive (i. e. nucleated). To do this, the CA model described in Chapter 3 is used such that there are no restrictions on the number of cells constituting a subgrain/grain. The energy advantage of subgrains is still captured, even if each CA cell has a size equal to (or even larger than) the subgrain's size.

4.1.4. INPUTS AND RELEVANCE TO THE SUBSTRUCTURE

Regarding the input, an experimentally measured (from EBSD) and highly resolved 2D representative volume element (RVE) is used, in which intergranular aspects (e. g. deformation bands) can be distinguished, and orientation gradients within grains are described. These

features are distinguished, since, as explained above, the substructure in the RVE is as measured by EBSD.

The misorientation between adjacent pixels identified by EBSD is attributed to the presence of dislocations. These incorporate the role of elementary units of inelastic deformation and hence they carry the deformation energy. At the same time, dislocations are elementary units of crystallographic misorientation and hence comprise boundaries whereby (sub)grains can grow. Therefore, the dislocation content identified by EBSD determines the kinematics (mobility) and the stored energy (driving force) whereby recrystallization is simulated.

It should be made clear that the EBSD measurement we use, albeit high in resolution - namely 0.12 s - cannot describe all orientation gradients in the substructure. Typical subgrain sizes that have been reported from TEM measurements in cold-rolled IF steels of 70-80% thickness reduction, are found within a range of $0.4-1$ μm [2, 73–75]. Hence most of the subgrain structure can be described with the present resolution, although regions of very high orientation gradients may still accommodate smaller subgrains.

4.2. CELLULAR-AUTOMATON MODEL

4.2.1. GRID AND CONSTITUTIVE STATE VARIABLES

The simulations are performed with the model described in Chapter 3. The automaton operates in the 1st Von Neumann neighborhood of a hexagonal (regular hexagons) grid - see Hex(1,1) grid in Chapter 3.

In the automaton grid every cell i is assigned a crystal orientation g_i. Each boundary area between material volumes i and j carries an interfacial energy value equal to:

$$E_{ij}[\mathrm{J}] = \gamma(g_i, g_j) \cdot A_{ij} \quad \forall ij : \delta_{ij} = 0 \tag{4.1}$$

where in Eq. (4.1):

- $A_{ij}[\mathrm{m}^2]$ is the area of the ij boundary plane.
- $\gamma(g_i, g_j)[\mathrm{J/m}^2]$ is the interface energy density between two unlike adjacent orientations g_i,g_j.
- δ_{ij} is a Kronecker-like operator defined as:

$$\delta_{ij} = \begin{cases} 1 \text{ if } \theta_{ij} < \theta_{min} \\ 0 \text{ if } \theta_{ij} >= \theta_{min} \end{cases} \tag{4.2}$$

where in Eq. (4.2):

- $\theta_{ij}[^\circ]$ is the misorientation between orientations g_i and g_j.
- $\theta_{min}[^\circ]$ is the lower cut-off misorientation to consider the existence of a boundary between i and j.

4.2.2. KINEMATIC RULE

The growth of the favoring orientation g_j into cell i occurs with rate:

$$\dot{f}_{g_i \to g_j} = \beta_{grid} \cdot M_{g_i \to g_j} \cdot \sqrt{\sum_{u_r = x,y,z} \left(\sum_k \delta_{kj} \cdot \left| \vec{F}_{ik, g_i \to g_j} \cdot \vec{u}_r \right| \right)^2} / V_i \tag{4.3}$$

where in Eq. (4.3):

- $V_i[\mathrm{m}^3]$ is the volume within cell i.
- k is index referring to neighbours of i - i. e. such that $A_{ij} \neq 0$.
- $\vec{u}_r$ is the unit vector for the r axis of the (Cartesian) reference system.
- $M(g_i, g_j)[\mathrm{m}^4/\mathrm{Js}]$ is the boundary mobility [76].
- $\vec{F}_{ik, g_i \to g_j}[\mathrm{N}]$ is the force imposed at every boundary segment ik - including ij - which migrates to re-orient cell i into g_j.
- β_{grid} a kinetic factor (here equal to 0.49) related to the grid-settings explained in Chapter 3.

The method used to calculate $\vec{F}_{ik, g_i \to g_j}$ is described in Chapter 3.

4.2.3. TRANSFORMATION RULE

A cell i re-orients to g_j with the rate given in Eq. (4.3) calculated at time t as $\dot{f}^t_{g_i \to g_j}$. After the incremental time δt the re-orientation fraction of cell i is:

$$f^{t+\delta t}_{g_i \to g_j} = \dot{f}^t_{g_i \to g_j} \cdot \delta t + f^t_{g_i \to g_j} \tag{4.4}$$

Cell i re-orients completely into g_j when $f^t_{g_i \to g_j}$ becomes equal to (or exceeds) the value of 1. Otherwise, cell i is assumed to be fully oriented as g_i.

4.2.4. BOUNDARY PROPERTIES

HAGBs are defined as boundaries with misorientation greater or equal to 15°. Variations in the growth rate occur only due to the dislocation content (i. e. misorientation angle) at each LAGB. For LAGBs, the boundary energy descends to the misorientation in accord with Read-Shockley equation [77] and the mobility due to the requirement of arranged dislocation motion [40, 53–55]. The expressions are shown in Chapter 3.

4.2.5. SUBGRAIN BOUNDARIES AND STORED ENERGY FOR RECRYSTALLIZATION

As explained earlier, the stored deformation energy that drives recrystallization corresponds to the subgrain boundary energy (GNDs and/or HAGBs). In this manner, recrystallization

and grain coarsening are concurrently simulated. Fig. 4.1 shows a schematic for the two main switching scenarios that occur in the application. The color-coding of the cells is in accord with the Inverse-Pole-Figure (IPF) along the Normal Direction (ND). Boundary segments are also plotted when present, such that a HAGB is colored black and a LAGB blue. In particular:

- Fig. 4.1a shows a typical example of primary recrystallization, where a strain-free grain (or large subgrain next to a HAGB) grows into the adjacent substructure. As is shown, although the motion is accompanied by an increase in HAGB area, it reduces the LAGB area to the extent that it effectively yields energy release.
- Fig. 4.1b shows a typical example of normal grain growth, where a grain favored by the HAGB curvature grows into a smaller one. As expected, for such growth to occur in the CA, the HAGB energy needs to decrease.

Hence, although recrystallization and grain growth are phenomenologically different, their physical description can be unified [39]. If there is sufficient difference in the dislocations' content per unit volume between two adjacent dissimilar cells, one will grow into the other.

Fig. 4.2 shows the two scenarios described in Fig. 4.1 as measured experimentally. Fig. 4.2a shows a recrystallized grain growing into a deformed grain. As was shown in Fig. 4.1a, in such cases, the HAGBs curvature normally does not favor the migration, yet orientation gradients within the deformed matrix can lead to a positive driving force. Fig. 4.2b shows two recrystallized grains where the curvature of the HAGB indicates the direction of growth, as also described in Fig. 4.1b.

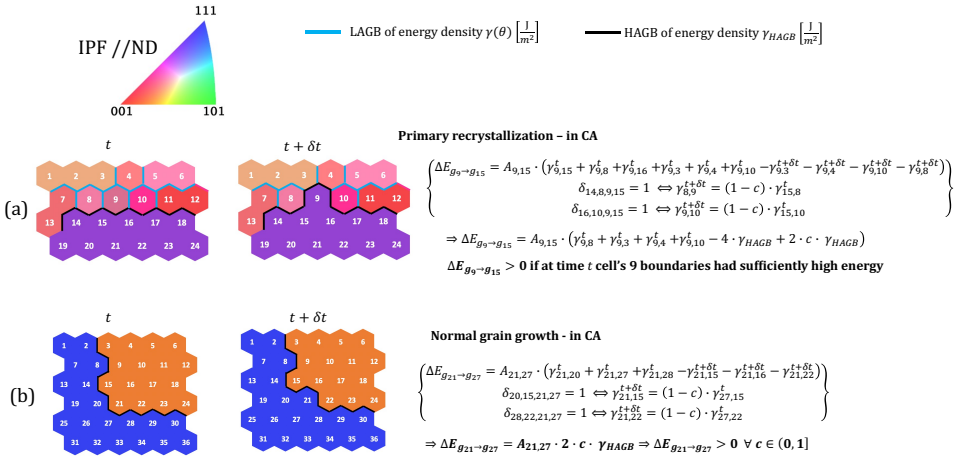

Figure 4.1: Cell switching scenarios in the CA. The two main cases that will occur when the algorithm is applied to a deformed microstructure discretized in a 2D hexagonal automaton grid are shown. The images depict the energy state before and after the re-orientation. In Figure (a) cell 15 (growing cell) belongs to a recrystallized volume (or large subgrain next to a HAGB) and might grow into cell 9 that belongs to a substructure. Although the migration increases the HAGB area, a positive driving force can still be found since the LAGB area decreases. Also, cell 15 has neighbours (i. e. cells 14 and 16) of the same orientation which can grow in the same direction (i. e. toward cells 8 and 10, respectively). In this case, only a part (i. e. $1-c$) of the energy concerning the boundaries $9,8$ and $9,10$ is considered upon the calculation of the next state's energy if cell 9 re-orients. In Figure (b) cells 27 and 21 are both surrounded by some cells similarly oriented and hence positive driving force will only be found if the migration leads to reduction of the HAGB area. Therefore, the migration of the boundary $27,21$ will occur toward cell 21. Cell 27 has neighbours (i. e. cells 20 and 28) which can grow in the same direction - i. e. toward cells 15 and 22, respectively. Therefore, again only $1-c$ of the boundaries' $21,15$ and $21,22$ energy is considered at the next state.

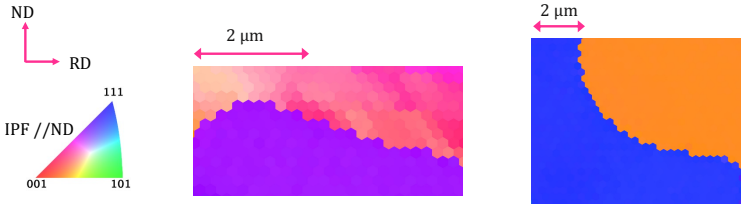

(a) Primary recrystallization - experimental

(b) Normal grain growth - experimental

Figure 4.2: EBSD observations during the annealing of the IF-steel sheet. The phenomena depicted are (a) primary recrystallization - i. e. a recrystallized grain grows into a substructure (b) grain growth - i. e. two recrystallized grains have impinged.

4.3. APPLICATION

4.3.1. INPUT MATERIAL AND MICROSTRUCTURE

The chemical composition of the IF steel is shown in Table 4.2 and the material parameters used are shown in Table 4.3. The applied time-temperature profile is presented in Fig. 4.3. As is shown, the maximum temperature reached during the heat treatment is 800 °C, which is much less than the austenitization temperature of the material [2]. Hence the only solid-state transformation that occurs is related to the diminishing of stored deformation energy.

Table 4.2: Chemical composition in wt% of the IF steel used in the application.

C	Mn	Al	N	Ti	S	Cr
0.002	0.095	0.05	0.002	0.045	0.006	0.02

[2] The austenitization temperature of the present material is around 900 °C.

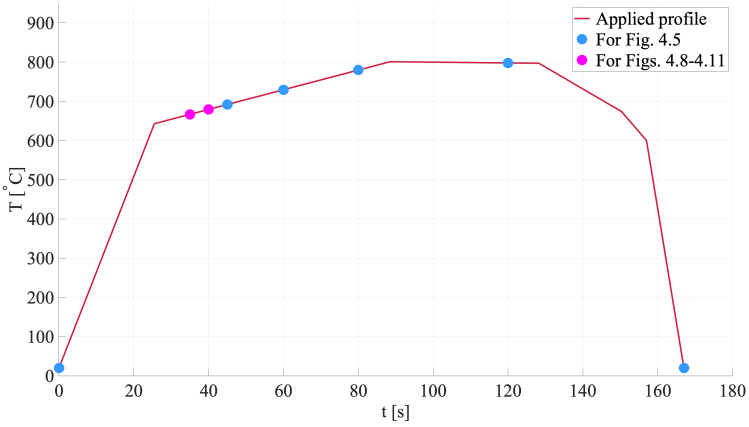

Figure 4.3: The temperature-time profile applied to the sheet. The marked values correspond to the initital state, the final annealed state and the intermediate states used for Fig. 4.5 and Figs. 4.8 to 4.11.

Table 4.3: Input parameters used in the simulation.

Quantity	Value	Description
Q_g	140 kJ/mol	The activation energy for boundary migration from [78].
M_0	$1.5 \cdot 10^{-6}$ m^4/Js	The pre-exponential factor of HAGB mobility.
γ_{HAGB}	0.5 J/m^2	The energy per unit area of a HAGB from [79, 80].
θ_{HAGB}	15°	The minimum misorientation to consider a HAGB.
θ_{min}	0.3°	The minimum misorientation to consider the existence of an orientation gradient.
c	0.7	A grid (thermodynamic) parameter - see Eq. (3.4) in Chapter 3.
β_{grid}	0.49	A kinetic factor related to the grid-settings explained in Chapter 3.

The input RVE was obtained experimentally through high-resolution EBSD using a Sigma 500 microscope from Zeiss, coupled with OIM DC-software and a Hikari-Camera from EDAX. The crystal orientation at each cell of the automaton grid corresponded to the one measured for the pixel located at the same spatial coordinates. The spacing between adjacent hexagons δx_{CA} is equal to 0.12 μm and the number of cells comprising the RVE is 5,316,480. The simulation uses periodic boundary conditions. Nevertheless, since the kinetic instability is crucial for recrystallization to initiate, the boundary conditions are enabled only after a cell has transformed an actual neighbour cell. This can diminish the "falsified" kinetic advantage that a cell lying on the RVE's edges may have, toward the neighbourhood abutting its symmetrical location (on the opposite RVE's edge).

The model's input is shown Fig. 4.4a. The maps in Fig. 4.4 are plotted with the use of PYEBSD [81]. In particular, the automaton cells are colored in accord with the IPF‖ND and are darkened in ascending order with respect to the maximum misorientation from their neighbours. For example, if a cell has maximum misorientation from its neighbours less than

0.3° the cell is colored only in accord with the IPF||ND, while for larger misorientations the IPF coloring is darkened. Eventually, a cell that is surrounded by at least one HAGB (i. e. $\theta_{ij} > 15°$) appears black.

The substructure is shown more clearly in characteristic regions of the IF-steel sheet in Fig. 4.4b-d. In particular:

- Fig. 4.4b shows the substructure in the vicinity of a HAGB for the two deformed grains that are separated. The subgrains in these areas are coarse and the intergranular boundaries are generally of small misorientations - e. g. the boundaries marked by white arrows.
- Fig. 4.4c shows the substructure inside a grain where deformation bands have formed. As indicated by the dark color of the cells, the deformation bands are circumscribed by mostly large-angle boundaries. The subgrains (e. g. regions indicated by red arrows) are almost rectangular and separated mostly by low-angle boundaries from adjacent subgrains within the same deformation band.
- Fig. 4.4d shows the substructure in an area where some deformation bands enclose very small subgrains (e. g. regions indicated by green arrows). Very high misorientation is found at the rims of such deformation bands where HAGBs have formed. Large differences are also observed between the size/energy in some of these very small subgrains in comparison to their surroundings (e. g. see the regions of smaller orientation gradients indicated by red arrows).

As shown in Fig. 4.4, many important topological characteristics of cold-rolled IF-steel sheets of similar thickness reductions are identified. Coarse subgrains with diffuse boundaries [6, 74] as well deformation bands [2, 6] are distinguished in the various regions that comprise the deformed metal. Additionally, the heterogeneity in the subgrain sizes and boundaries' misorientation is clear, throughout the RVE (e. g. between Fig. 4.4a and Fig. 4.4b) but also locally (e. g. the subgrains inside the narrow deformation bands compared to their surroundings).

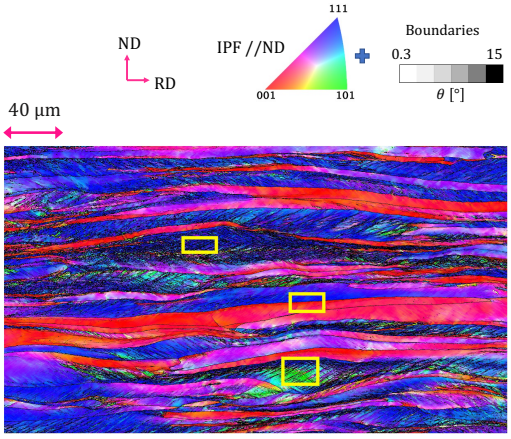

(a) Deformed state - input RVE

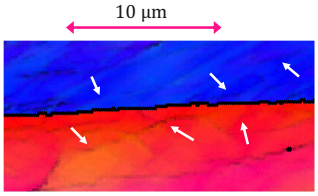

(b) Coarse subgrains close to grain boundary

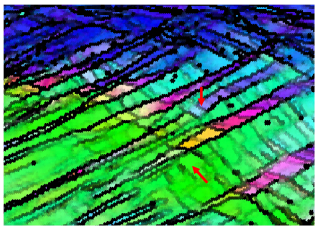

(c) Deformation bands

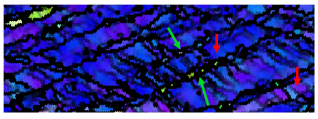

(d) Deformation bands enclosing high orientation gradients

Figure 4.4: Input RVE for the simulation: (a) the deformed state as imported in the CA (b) the substructure in the two opposite sides of a grain boundary (c) the substructure in deformation bands (d) the substructure in a region that includes deformation bands of very high orientation gradients.

4.3.2. SIMULATED MICROSTRUCTURE EVOLUTION

Fig. 4.5 shows the temporal evolution of the simulated microstructure. It is clear that already from the early stages of growth many CA cells have grown into the surrounding deformed matrix, yet in a spatially non-uniform fashion. For example, at 45 s, some deformed grains have already been partially consumed by strain-free volumes, while other less deformed regions (e. g. the reddish volume in Fig. 4.5b) have remained almost intact. Such deformed grains neither grow significantly nor are consumed by other recrystallized grains. This phenomenon has been confirmed by earlier experimental investigations in the evolution of recrystallization - e. g. in [82–84]. The resistance of low-stored energy deformed grains in recrystallizing diminishes as grains in other regions nearby become eventually large enough (e. g. see the grains indicated by black arrows in Fig. 4.5d) to grow into them. Eventually, at the end of the simulation, all prior deformed grains have been replaced by equiaxed grains, within which dislocations are absent.

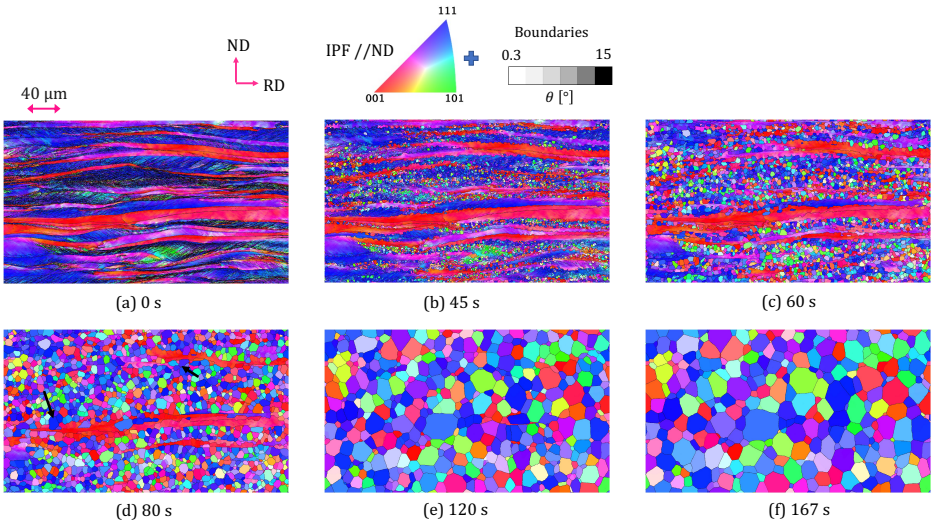

Figure 4.5: Evolution of simulation at (a) 0 s (b) 45 s (c) 60 s (d) 80 s (e) 120 s and (f) 167 s. The corresponding temperature (and history) at each stage depicted is shown in Fig. 4.3.

4.3.3. SIMULATED AND EXPERIMENTAL RELEVANCE

Fig. 4.6 shows the annealed microstructure as simulated and measured experimentally, both corresponding to the temperature-time profile shown in Fig. 4.3. A Bähr DIL 805 A/D dilatometer was employed to perform the annealing treatment that resulted in the microstructure shown in Fig. 4.6b.

The average grain diameter was quantified after decomposing the orientation data into grains, using MTEX [85]. Although the average grain size is rather close between the simulated and the experimental microstructure - namely 15.7 µm and 16.8 µm, respectively, the grains' shape and size distribution do not seem to follow the experimentally measured

microstructure's. In particular, the experimentally measured annealed state contains some considerably larger and pancake-shaped grains which are not observed in the simulated microstructure. This could be because the simulation was performed in 2D, whereas the (sub)grains' coarsening is a 3D phenomenon. In addition, differences in grains' shape and size distribution could result from variations in the particle pinning at HAGBs' which may exist [12, 53, 60–63], yet were not considered in the simulation.

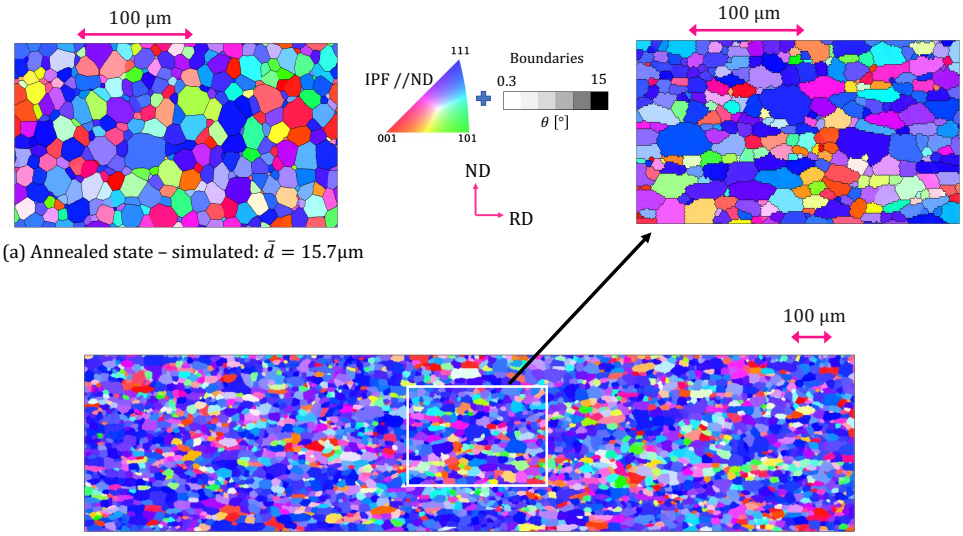

(a) Annealed state – simulated: $\bar{d} = 15.7\mu m$

(b) Annealed state – experimental: $\bar{d} = 16.8\mu m$

Figure 4.6: Recrystallized cold-rolled IF steel; (a) the simulated microstructure (b) the experimental measurement. The annealed state corresponds to the end of the heat treatment shown in Fig. 4.3.

Fig. 4.7 shows the $\phi_2 = 45°$ section of the orientation distribution function (ODF) for the deformed and annealed states. The ODFs were determined with the use of MTEX [85], by employing a 7° halfwidth. As shown in Fig. 4.7, while the deformed sheet is characterized by a combined α-fiber (i. e. ⟨110⟩//RD) and γ-fiber (i. e. ⟨111⟩//ND), the simulation results in the diminishing of α-fiber components, while γ-fiber components intensify. This is confirmed by the experimentally annealed sample (Fig. 4.7c) which is characterized by a full γ-fiber texture. Although there are deviations between the experimental and the simulated annealed state, the texture components that comprise the simulated recrystallized microstructure are mostly located within the γ-fiber. Therefore, the capillary competitive subgrain growth that is simulated has altered the distribution of relevant texture components, in compliance with the experimental findings.

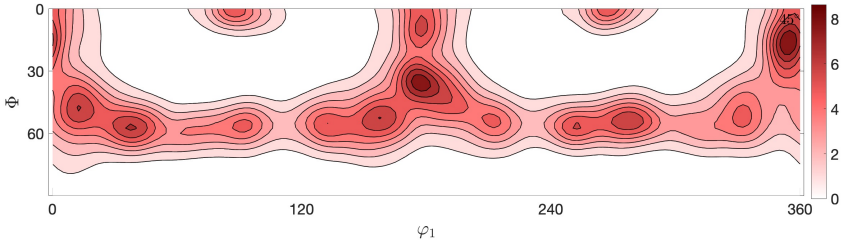

(a) Deformed state – ODF $\varphi_2 = 45°$

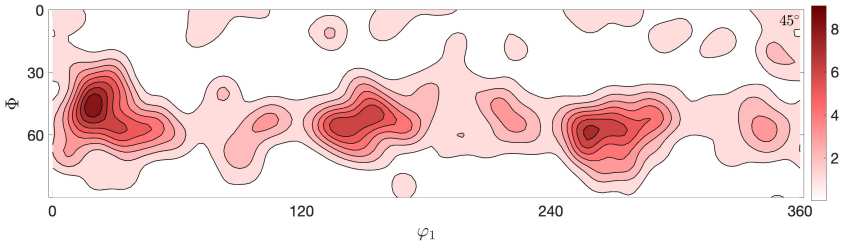

(b) Simulated annealed state – ODF $\varphi_2 = 45°$

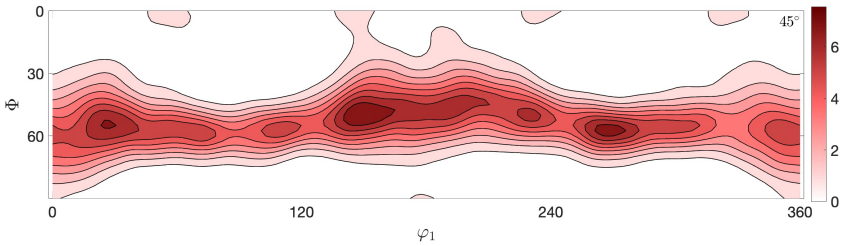

(c) Experimental annealed state – ODF $\varphi_2 = 45°$

Figure 4.7: ODF quantified and plotted in section $\phi_2 = 45°$ for (a) the deformed state (b) the simulated recrystallized microstructure (c) the experimental measurement of the annealed sheet.

Additionally, the change in the texture components' distribution that occurs upon the simulation indicates that the selective subgrain growth did not occur randomly. Instead, the topological characteristics important for recrystallization - e. g. the relationship (size, crystal orientations etc.) between a subgrain and its surroundings - follow an orientation-dependent pattern at the prior-deformed state.

4.3.4. EARLY STAGES OF RECRYSTALLIZATION

This section reviews the onset and evolution of recrystallization in specific characteristic areas of the sheet during the early stages of annealing.

DEFORMATION BANDS

Fig. 4.8 shows the early stages of recrystallization in various regions where deformation bands are present. In Fig. 4.8a the locations of the areas investigated are shown and in Fig. 4.8b the recrystallized volume is shown at 35 s for the corresponding regions. More specifically, Fig. 4.8b shows the crystal direction//ND at 35 s for the cells which have been surpassed by a boundary, while the volume that has remained intact is plotted white. As shown in Fig. 4.8b, the recrystallized areas arrange along the axis of the prior bands. This phenomenon indicates that subgrains from the matrix (normally lower in stored deformation energy and thus larger) invade and consume the subgrains within the prior abutting deformation bands [6].

Most of the recrystallized volume nonetheless stops expanding - e. g. the recrystallized volume indicated by green arrows in Fig. 4.8b, which has not grown much or has grown only in the perpendicular direction of the prior bands. This is because the recrystallized volume met either similar crystal orientations or larger subgrains in the matrix [3]. Only some of the recrystallized grains continue to satisfy the two instability criteria, e. g. the ones indicated by pink arrows in Fig. 4.8b.

As an example, the boundaries' temporal evolution in region 3 (shown in Fig. 4.8b) is illustrated in Fig. 4.9. As shown in Fig. 4.9, recrystallization initiates through HAGBs that surround deformation bands. However, many of the pre-existing HAGBs (e. g. B1-B4 indicated by pink arrows in Fig. 4.9) become low-angle boundaries after surpassing the narrow deformation band. This is understood by the color of boundaries B1-B4, which changes from black (see Fig. 4.9a) to gray (see Fig. 4.9c).

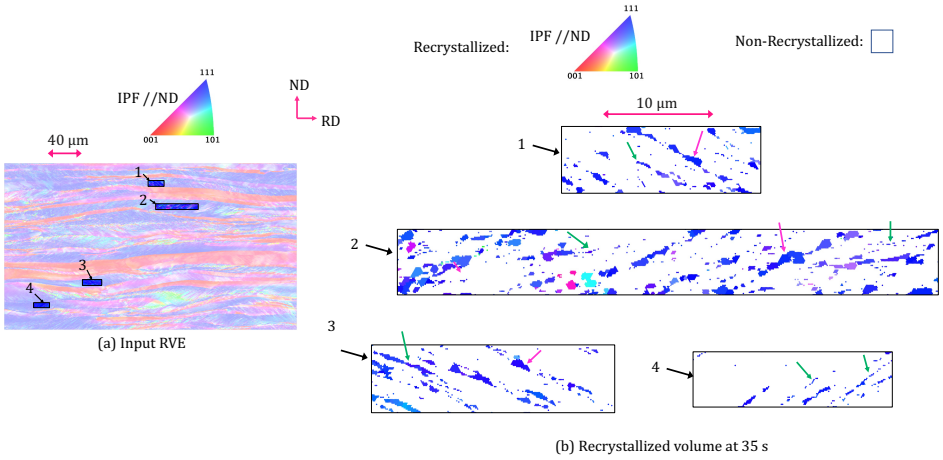

Figure 4.8: Simulated results: early stages of recrystallization shown in grains where deformation bands have formed (a) 0 s - the location of the areas studied is shown (b) 35 s - the volume which has been surpassed by a boundary (i. e. white color means that the cell has remained intact) is shown. The corresponding temperature (and history) at each stage depicted is shown in Fig. 4.3.

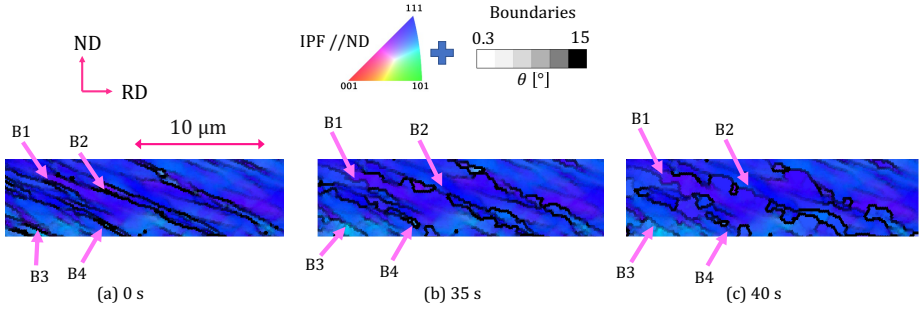

Figure 4.9: Simulated results: temporal evolution in the early stages of recrystallization at deformation bands (a) 0 s (b) 35 s (c) 40 s. The corresponding temperature (and history) at each stage depicted is shown in Fig. 4.3.

COMPETITIVE GROWTH AT DIFFERENT HAGBS

Fig. 4.10 and Fig. 4.11 show the competitive growth that takes place at characteristic regions of the deformed state where different types of HAGBs are present. Fig. 4.10 shows a grain characterized by low-stored energy (grain A) in contact with a grain within which deformation bands have formed (grain B). Fig. 4.11 shows a grain with low-stored energy (grain C) abutting a grain where deformation bands have formed in two directions and thus intersect (grain D). The latter is identified by the consideration of both Fig. 4.11a and Fig. 4.11b. In particular, one group of bands incorporates orientation gradients mostly along the ND while in the other group these are found along the RD. Concerning the recrystallization evolution, the following is observed:

- Inside grains with low deformation: Within grains A and C in Fig. 4.10 and Fig. 4.11 there is complete absence of recrystallization. This is due to the lack of sufficiently high intergranular orientation gradients resulting in such deformed regions remaining intact.
- Pre-existing subgrains next to conventional grain boundaries: Only a small portion of the deformed matrix in contact with conventional grain boundaries - the boundaries between grains A-B and C-D - has recrystallized. Although subgrains abutting conventional grain boundaries have a kinetic advantage and are also in general large, their growth does not produce large recrystallized volumes. It is then clear that such subgrains in general do not have an energy advantage. This was also shown in Fig. 4.4, where no significant differences in the subgrain sizes or misorientations were observed between the two sides close to the grain boundary. Hence, a subgrain in the vicinity of a grain boundary may start bulging in the adjacent deformed matrix, but it is very likely that the motion will stop because larger subgrains will be met.
- Inside grains with bands of one direction: Recrystallization occurs in grain B in a fashion similar to the evolution presented in Fig. 4.8. The pre-existing subgrains adjacent to the narrow deformation bands have grown at the expense of the smaller subgrains within them.
- Inside grains with intersecting deformation bands: Recrystallization predominates in grain D. Comparing for example the evolution of recrystallization in grain B to grain D, from Fig. 4.10 and Fig. 4.11 respectively, it seems that recrystallization is favored when deformation bands in two different directions intersect. This can be explained if one considers that in such a region (grain D) after surpassing the first deformation band, the bulged volume will not meet the same crystal orientation. Additionally, when orientation gradients are present in two different directions, the recrystallization front can grow in both and thereby provide an energy advantage to the recrystallized volume.

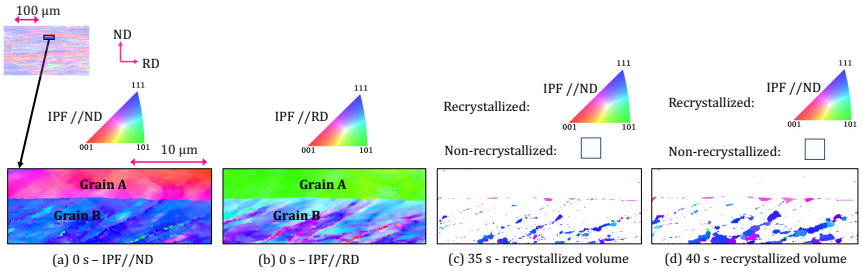

Figure 4.10: Simulated results: early stages of recrystallization shown in an area consisting of two deformed grains at (a) 0 s - IPF‖ND (b) 0 s - IPF‖RD (c) 35 s - the volume which has been surpassed by a boundary is color-coded with IPF‖ND (d) 40 s - the volume which has been surpassed by a boundary is color-coded with IPF‖ND. The corresponding temperature (and history) at each stage depicted is shown in Fig. 4.3.

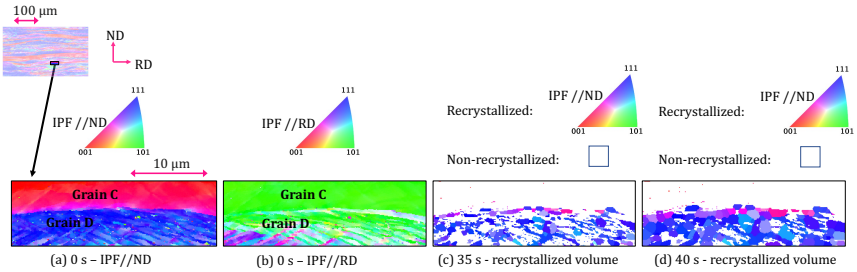

Figure 4.11: Simulated results: early stages of recrystallization shown in an area consisting of two deformed grains at (a) 0 s - IPF‖ND (b) 0 s - IPF‖RD (c) 35 s - the volume which has been surpassed by a boundary is color-coded with IPF‖ND (d) 40 s - the volume which has been surpassed by a boundary is color-coded with IPF‖ND. The corresponding temperature (and history) at each stage depicted is shown in Fig. 4.3.

4.4. CONCLUSIONS

4.4.1. SUMMARY OF ITEMS DISCUSSED

A boundary energy-driven algorithm was applied to a Ti-stabilized IF steel cold-rolled up to 77 % thickness reduction. The following remarks can be deduced from the recrystallization simulations:

- Although recrystallization nucleation is not artificially imposed in the present modeling framework, it occurs upon the simulation due to the highly heterogeneous subgrain coarsening that takes place in the early stages of annealing. Followed by the subsequent growth of the recrystallized grains, the simulation yields a fully recrystallized microstructure.
- In compliance with the experimental observations, the simulation results in the diminishing of texture components within the ⟨110⟩//RD fiber while mostly texture components within the ⟨111⟩//ND fiber comprise the recrystallized state. This indicates that in the as-deformed state, the presence of subgrains in a favorable location to recrystallize - such that they have an energy and kinetic advantage - is an orientation-dependent phenomenon.
- Recrystallization at deformation bands occurs primarily by the invasion of coarser subgrains in the substructure within the adjacent narrower bands. However, in most cases, the recrystallized volume stops expanding once surpassing the first deformation band, because the boundaries are no longer high-angle.
- Subgrains growing in regions with intersecting deformation bands become very soon distinguished in their size compared to subgrains within regions where all the narrow bands are parallel.
- A subgrain's likelihood to recrystallize depends on its surroundings in the following order: subgrains next to intersecting deformation bands, subgrains next to deformation bands arranged in one direction, subgrains next to conventional grain boundaries.

4.4.2. GENERAL ADVANCES AND OUTLOOK

Besides the aforementioned items that are clear from the results and discussions made in this chapter, some more general remarks should be made These mostly relate to the general advancement of our understanding of recrystallization. It is already clear that the present simulation starts with a deformed structure of millions of material elements and allows them all to compete in evolving into nuclei/recrystallized grains etc. All this competition comes from only one variable: the misorientation spatial distribution, which determines both the kinetic and the energy advantage. This means that a pre-existing subgrain will only appear (as a recrystallized grain) in the subsequent stages of annealing as long as it was always mobile and favored by the energy release in comparison to its changing neighborhood. As explained in Chapter 1, many more mechanisms can lead to selective subgrain/grain growth and explain the associated orientation selection. In IF steel, preferential growth can occur because of particle pinning, heterogeneous static subgrain formation, subgrain coalesence, heterogeneous mobilities/energies depending on the boundary character. All these together are expected to contribute to making only a few pre-existing subgrains "special" enough to grow and end up constituting the annealed state.

But none of the aforementioned mechanisms were considered in the present simulation, yet it was clear from the results that both preferential growth and orientation selection occur, even when the heterogeneity of the subgrains growth is only a result of the heterogeneously distributed dislocation content (and hence misorientation) and only captured in 2D. This does not mean that all aforementioned mechanisms are not relevant, but rather that the ones considered are already sufficient to explain associated phenomena. Such ideas, regarding the relationship of recrystallization in relevant materials to the subgrains misorientation (and hence also energy density/size) have been proposed already decades ago, for example by Humphreys [39] and Hutchinson [3]. However, it has never been proven that if we indeed approximate a realistic substructure of a few million subgrains, assume that all these regions do not require static subgrain formation, and allow them all to grow and compete based on these simple mechanisms, we will indeed observe growth instability (recrystallization) and also in a way that it is accompanied by a relevant crystallographic texture change.

In terms of modeling approaches of recrystallization, the present chapter shows that the model described in Chapter 3 is indeed applicable to deformation structures at the mesoscopic scale, despite the fact that it has to deal with coarsening phenomena modelled with a grid spacing close to the actual subgrain size. Overcoming the challenge of simulating recrystallization in a full-field description and including the nucleation stage is not trivial, especially in highly plastically strained metals where the substructure comprises subgrains of size almost equal to the grid spacing. At the same time, when it comes to recrystallization nucleation, full-field computer simulations are very important, due to the large number of nucleation mechanisms and the inability to differentiate between some of them using experimental observations. Therefore, the present chapter should also be perceived as a basis toward taking associated research directions when studying the nucleation stage of recrystallization.

REFERENCES

[1] K. Traka, K. Sedighiani, C. Bos, J. Galan Lopez, K. Angenendt, D. Raabe, and J. Sietsma, *Topological aspects responsible for recrystallization evolution in an IF-steel sheet – Investigation with cellular-automaton simulations,* Computational Materials Science **198**, 110643 (2021).

[2] W. B. Hutchinson, *Development and control of annealing textures in low-carbon steels,* International Metals Reviews **29**, 25 (1984).

[3] B. Hutchinson, *Nucleation of recrystallisation,* Scripta Metallurgica et Materialia **27**, 1471 (1992).

[4] K. Y. Lee, G. S. Kim, K. G. Chin, and L. Kestens, *The Evolution of Texture and Stored Energy during Recrystallization of IF High Strength Steel Investigated by Means of Orientation Imaging Microscopy,* Materials Science Forum **558-559**, 241 (2007).

[5] D. Raabe, *On the orientation dependence of static recovery in low-carbon steels,* Scripta Metallurgica et Materialia **33**, 735 (1995).

[6] D. Raabe, *Recovery and Recrystallization: Phenomena, Physics, Models, Simulation,* in *Physical Metallurgy* (Elsevier, 2014) pp. 2291–2397.

[7] K. Ushioda, *Advances in research on deformation and recrystallization for the development of high-functional steels,* Science and Technology of Advanced Materials **21**, 29 (2020).

[8] K. Ushioda and W. B. Hutchinson, *Role of shear bands in annealing texture formation in 3%Si-Fe(111)[112] single crystals.* ISIJ International **29**, 862 (1989).

[9] Y. Inokuti and R. D. Doherty, *Transmission Kossel Study of the Structure of Cold-Rolled Iron and its Nucleation Behaviour,* Texture of Crystalline Solids **2**, 143 (1977).

[10] Y. Inokuti and R. Doherty, *Transmission kossel study of the structure of compressed iron and its recrystallization behaviour,* Acta Metallurgica **26**, 61 (1978).

[11] G. Ibe and K. Lücke, *Über die spontane Keimbildung bei der Herstellung von Einkristallen durch Rekristallisation,* Kristall und Technik **2**, 177 (1967).

[12] K. Verbeken, L. Kestens, and M. Nave, *Re-evaluation of the Ibe–Lücke growth selection experiment in a Fe–Si single crystal,* Acta Materialia **53**, 2675 (2005).

[13] B. J. Duggan, Y. Y. Tse, G. Lam, and M. Z. Quadir, *Deformation and Recrystallization of Interstitial Free (IF) Steel,* Materials and Manufacturing Processes **26**, 51 (2011).

[14] R. Doherty, D. Hughes, F. Humphreys, J. Jonas, D. Jensen, M. Kassner, W. King, T. McNelley, H. McQueen, and A. Rollett, *Current issues in recrystallization: a review,* Materials Science and Engineering: A **238**, 219 (1997).

[15] R. D. Doherty, *Recrystallization and texture,* Progress in Materials Science **42**, 39 (1997).

[16] M. Tomita, T. Inaguma, H. Sakamoto, and K. Ushioda, *Recrystallization Behavior and Texture Evolution in Severely Cold-rolled Fe-0.3mass%Si and Fe-0.3mass%Al Alloys,* ISIJ International **57**, 921 (2017).

[17] S. Dziaszyk, E. Payton, F. Friedel, V. Marx, and G. Eggeler, *On the characterization of recrystallized fraction using electron backscatter diffraction: A direct comparison to local hardness in an IF steel using nanoindentation,* Materials Science and Engineering: A **527**, 7854 (2010).

[18] R. Khatirkar, B. Vadavadagi, A. Haldar, and I. Samajdar, *ND// Recrystallization in Interstitial Free Steel: The Defining Role of Growth Inhibition,* ISIJ International **52**, 894 (2012).

[19] A. Ayad, M. Ramoul, A. Rollett, and F. Wagner, *Quantifying primary recrystallization from EBSD maps of partially recrystallized states of an IF steel,* Materials Characterization **171**, 110773 (2021).

[20] D.-K. Kim, W. Woo, W.-W. Park, Y.-T. Im, and A. Rollett, *Mesoscopic coupled modeling of texture formation during recrystallization considering stored energy decomposition,* Computational Materials Science **129**, 55 (2017).

[21] A. D. Rollett, *Crystallographic texture change during grain growth,* JOM **56**, 63 (2004).

[22] A. Rollett and D. Raabe, *A hybrid model for mesoscopic simulation of recrystallization,* Computational Materials Science **21**, 69 (2001).

[23] S.-H. Choi, F. Barlat, and J. Chung, *Modeling of textures and yield surfaces during recrystallization in IF steel sheets,* Scripta Materialia **45**, 1155 (2001).

[24] S.-H. Choi and J. H. Cho, *Primary recrystallization modelling for interstitial free steels,* Materials Science and Engineering: A **405**, 86 (2005).

[25] D. Raabe and R. C. Becker, *Coupling of a crystal plasticity finite-element model with a probabilistic cellular automaton for simulating primary static recrystallization in aluminium,* Modelling and Simulation in Materials Science and Engineering **8**, 445 (2000).

[26] D. Raabe and L. Hantcherli, *2D cellular automaton simulation of the recrystallization texture of an IF sheet steel under consideration of Zener pinning,* Computational Materials Science **34**, 299 (2005).

[27] S. Ling and M. P. Anderson, *Monte Carlo simulation of grain growth and recrystallization in polycrystalline materials,* JOM **44**, 30 (1992).

[28] T. Takaki, A. Yamanaka, Y. Higa, and Y. Tomita, *Phase-field model during static recrystallization based on crystal-plasticity theory,* Journal of Computer-Aided Materials Design **14**, 75 (2007).

[29] H. Hallberg, F. Adamski, S. Baïz, and O. Castelnau, *Microstructure and Property Modifications of Cold Rolled IF Steel by Local Laser Annealing,* Metallurgical and Materials Transactions A **48**, 4786 (2017).

[30] P. A. Beck, *The Formation of Recrystallization Nuclei,* Journal of Applied Physics **20**, 633 (1949).

[31] A. Cottrell, *Theory of dislocations,* Progress in Metal Physics **4**, 205 (1953).

[32] P. R. Rios, F. Siciliano Jr, H. R. Z. Sandim, R. L. Plaut, and A. F. Padilha, *Nucleation and growth during recrystallization,* Materials Research **8**, 225 (2005).

[33] P. A. Beck, P. R. Sperry, and H. Hu, *The Orientation Dependence of the Rate of Grain Boundary Migration,* Journal of Applied Physics **21**, 420 (1950).

[34] E. Holm, M. Miodownik, and A. Rollett, *On abnormal subgrain growth and the origin of recrystallization nuclei,* Acta Materialia **51**, 2701 (2003).

[35] R. Cahn, *Recrystallization of single crystals after plastic bending,* Journal of the Institute of Metals **76**, 121 (1949).

[36] R. Cahn, *Internal strains and recrystallization,* Progress in Metal Physics **2**, 151 (1950).

[37] R. W. Cahn, *A New Theory of Recrystallization Nuclei,* Proceedings of the Physical Society. Section A **63**, 323 (1950).

[38] F. Han, B. Tang, H. Kou, J. Li, and Y. Feng, *Cellular automata modeling of static recrystallization based on the curvature driven subgrain growth mechanism,* Journal of Materials Science **48**, 7142 (2013).

[39] F. J. Humphreys, *A unified theory of recovery, recrystallization and grain growth, based on the stability and growth of cellular microstructures—I. The basic model,* Acta Materialia **45**, 4231 (1997).

[40] F. J. Humphreys, G. S. Rohrer, and A. D. Rollett, *Recrystallization and related annealing phenomena*, third edition ed. (Elsevier, Amsterdam Oxford Cambridge, MA, 2017).

[41] P. Faivre and R. D. Doherty, *Nucleation of recrystallization in compressed aluminium: studies by electron microscopy and Kikuchi diffraction,* Journal of Materials Science **14**, 897 (1979).

[42] C. H. Li, E. Edwards, J. Washburn, and E. Parker, *Stress-induced movement of crystal boundaries,* Acta Metallurgica **1**, 223 (1953).

[43] M. Winning, G. Gottstein, and L. S. Shvindlerman, *On the mechanisms of grain boundary migration,* Acta Materialia , 11 (2002).

[44] M. K. Rehman and H. S. Zurob, *A Novel Approach to Model Static Recrystallization of Austenite During Hot Rolling of Nb Microalloyed Steel. Part I: Precipitate-Free Case,* Metallurgical and Materials Transactions A **44**, 1862 (2013).

[45] F. Han, B. Tang, H. Kou, L. Cheng, J. Li, and Y. Feng, *Static recrystallization simulations by coupling cellular automata and crystal plasticity finite element method using a physically based model for nucleation,* Journal of Materials Science **49**, 3253 (2014).

[46] B. Hutchinson, *Deformation microstructures and textures in steels,* Philosophical Transactions of the Royal Society of London. Series A: Mathematical, Physical and Engineering Sciences **357**, 1471 (1999).

[47] M. F. Ashby, *The deformation of plastically non-homogeneous materials,* The Philosophical Magazine: A Journal of Theoretical Experimental and Applied Physics **21**, 399 (1970).

[48] S.-H. Lee, H. Utsunomiya, and T. Sakai, *Microstructures and Mechanical Properties of Ultra Low Carbon Interstitial Free Steel Severely Deformed by a Multi-Stack Accumulative Roll Bonding Process,* MATERIALS TRANSACTIONS **45**, 2177 (2004).

[49] S. Tamimi, J. J. Gracio, A. B. Lopes, S. Ahzi, and F. Barlat, *Asymmetric rolling of interstitial free steel sheets: Microstructural evolution and mechanical properties,* Journal of Manufacturing Processes **31**, 583 (2018).

[50] D. Shan and L. Zhen, *Aging behavior and microstructure evolution in the processing of aluminum alloys,* in *Microstructure Evolution in Metal Forming Processes* (Elsevier, 2012) pp. 267–297.

[51] R. Doherty and R. Cahn, *Nucleation of new grains in recrystallization of cold-worked metals,* Journal of the Less Common Metals **28**, 279 (1972).

[52] Y. Suwa, M. Tomita, Y. Tanaka, and K. Ushioda, *Phase-field Simulation of Recrystallization in Cold Rolling and Subsequent Annealing of Pure Iron Exploiting EBSD Data of Cold-rolled Sheet,* ISIJ International **61**, 350 (2021).

[53] G. Gottstein and L. S. Shvindlerman, *Grain boundary migration in metals: thermodynamics, kinetics, applications*, 2nd ed., CRC series in materials science and technology (Taylor & Francis, Boca Raton, 2010) oCLC: ocn166358378.

[54] A. D. Rollett, G. Gottstein, L. S. Shvindlerman, and D. A. Molodov, *Grain boundary mobility – a brief review,* Zeitschrift für Metallkunde **95**, 226 (2004).

[55] M. Upmanyu, R. Smith, and D. Srolovitz, *Atomistic Simulation of Curvature Driven Grain Boundary Migration,* Interface Science **6**, 41 (1998).

[56] A. Haldar, S. Suwas, and D. Bhattacharjee, eds., *Microstructure and Texture in Steels* (Springer London, London, 2009).

[57] X. Li, P. Yang, and L. Meng, *Formation of the {111} and {111} Recrystallization Texture in Deep Drawing Low Carbon Steel,* Advanced Materials Research **535-537**, 687 (2012).

[58] R. L. Every and M. Hatherly, *Oriented Nucleation in Low-Carbon Steels,* Texture **1**, 183 (1974).

[59] L. A. I. Kestens and H. Pirgazi, *Texture formation in metal alloys with cubic crystal structures,* Materials Science and Technology **32**, 1303 (2016).

[60] Ibe, G. and Lücke, K., *Arch. Eisenhiittenwes,* **39**, 693 (1968).

[61] M. Hölscher, D. Raabe, and K. Lücke, *Rolling and recrystallization textures of bcc steels,* Steel Research **62**, 567 (1991).

[62] K. Okuda and K. Seto, *Recrystallization of Isolated Deformed Grains in High Purity Iron,* ISIJ International **55**, 877 (2015).

[63] R. K. Ray, J. J. Jonas, and R. E. Hook, *Cold rolling and annealing textures in low carbon and extra low carbon steels,* International Materials Reviews **39**, 129 (1994).

[64] J. F. Humphreys, *A Microstructural Model of Recrystallization,* Materials Science Forum **113-115**, 329 (1993).

[65] P. Bate, *Modelling deformation microstructure with the crystal plasticity finite–element method,* Philosophical Transactions of the Royal Society of London. Series A: Mathematical, Physical and Engineering Sciences **357**, 1589 (1999).

[66] F. Han, B. Tang, H. Kou, J. Li, and Y. Feng, *Effects of subgrain size and static recrystallization on the mechanical performance of polycrystalline material: A microstructure-based crystal plasticity finite element analysis,* Progress in Natural Science: Materials International **25**, 58 (2015).

[67] J. W. Cahn and S. M. Allen, *A MICROSCOPIC THEORY FOR DOMAIN WALL MOTION AND ITS EXPERIMENTAL VERIFICATION IN Fe-Al ALLOY DOMAIN GROWTH KINETICS,* Le Journal de Physique Colloques **38**, C7 (1977).

[68] I. Steinbach, F. Pezzolla, B. Nestler, M. Seeßelberg, R. Prieler, G. Schmitz, and J. Rezende, *A phase field concept for multiphase systems,* Physica D: Nonlinear Phenomena **94**, 135 (1996).

[69] J. Eiken, B. Böttger, and I. Steinbach, *Multiphase-field approach for multicomponent alloys with extrapolation scheme for numerical application,* Physical Review E **73**, 066122 (2006).

[70] E. Miyoshi and T. Takaki, *Extended higher-order multi-phase-field model for three-dimensional anisotropic-grain-growth simulations,* Computational Materials Science **120**, 77 (2016).

[71] E. Miyoshi and T. Takaki, *Validation of a novel higher-order multi-phase-field model for grain-growth simulations using anisotropic grain-boundary properties,* Computational Materials Science **112**, 44 (2016).

[72] K. Kremeyer, *Cellular Automata Investigations of Binary Solidification,* Journal of Computational Physics **142**, 243 (1998).

[73] I. L. Dillamore, C. J. E. Smith, and T. W. Watson, *Oriented Nucleation in the Formation of Annealing Textures in Iron,* Metal Science Journal **1**, 49 (1967).

[74] I. Thomas, S. Zaefferer, F. Friedel, and D. Raabe, *High-Resolution EBSD Investigation of Deformed and Partially Recrystallized IF Steel,* Advanced Engineering Materials **5**, 566 (2003).

[75] A. Martınez-de Guerenu, F. Arizti, M. Dıaz-Fuentes, and I. Gutiérrez, *Recovery during annealing in a cold rolled low carbon steel. Part I: Kinetics and microstructural characterization,* Acta Materialia **52**, 3657 (2004).

[76] D. Turnbull, *Theory of Grain Boundary Migration Rates,* JOM **3**, 661 (1951).

[77] W. T. Read and W. Shockley, *Dislocation Models of Crystal Grain Boundaries,* Physical Review **78**, 275 (1950).

[78] M. Hillert and L. Hoglund, *Mobility of α/γ phase interfaces in Fe alloys,* Scripta Materialia **54**, 1259 (2006).

[79] C. Hutchinson, H. Zurob, C. Sinclair, and Y. Brechet, *The comparative effectiveness of Nb solute and NbC precipitates at impeding grain-boundary motion in Nb steels,* Scripta Materialia **59**, 635 (2008).

[80] V. Shah, M. Krugla, S. E. Offerman, J. Sietsma, and D. N. Hanlon, *Effect of Silicon, Manganese and Heating Rate on the Ferrite Recrystallization Kinetics,* ISIJ International **60**, 1312 (2020).

[81] A. S. Nishikawa, *pyebsd: an open-source tool for processing EBSD data and determining accurate orientation relationship,* (2018), 10.13140/RG.2.2.28920.19203, https://github.com/arthursn/pyebsd.

[82] J.-H. Kim, D.-I. Kim, J. S. Kim, S.-H. Choi, K.-W. Yi, and K. H. Oh, *Technical Investigation into the In-situ Electron Backscatter Diffraction Analysis for the Recrystallization Study on Extra Low Carbon Steels,* Applied Microscopy **43**, 88 (2013).

[83] M. Diehl, L. Kertsch, K. Traka, D. Helm, and D. Raabe, *Site-specific quasi in situ investigation of primary static recrystallization in a low carbon steel,* Materials Science and Engineering: A **755**, 295 (2019).

[84] D.-I. Kim, J. Kim, J. Kim, and S.-H. Choi, *A study on the annealing behavior of Cu-added bake-hardenable steel using an in situ EBSD technique,* Acta Materialia **68**, 9 (2014).

[85] F. Bachmann, R. Hielscher, and H. Schaeben, *Texture Analysis with MTEX – Free and Open Source Software Toolbox,* Solid State Phenomena **160**, 63 (2010).

5

RECOVERY, RECRYSTALLIZATION INITIATION AND CRYSTALLOGRAPHIC TEXTURE FORMATION UPON ANNEALING IN IF STEEL SHEET

In this study, we have applied the cellular-automaton recrystallization model for unified subgrain growth, recrystallization growth, and grain growth to a cold-rolled IF steel sheet. The goal of this work is to quantify the extent of recovery during the early stages of recrystallization and its relationship with the subsequent stages of recrystallization and texture formation. The present quantifications are done in various simulations using inputs of different resolutions. This is because the EBSD resolution has limitations in describing the substructure of highly plastically strained metals. Therefore all the analysis is presented and discussed with particular emphasis on the effect of the resolution used. Eventually, a clear image is obtained regarding the individual nucleation mechanisms and their contribution to the formation of the γ-fiber recrystallization texture, while the artifacts of the resolution used are distinguished. It is shown that recovery (by means of discontinuous subgrain coarsening) is only minorly affecting the subsequent nucleation and formation of the γ-fiber texture. Moreover, the latter starts to form after recrystallization initiates (at HAGBs).

5.1. INTRODUCTION

5.1.1. MOTIVATION

Recrystallization annealing in interstitial-free (IF) steel is often accompanied by a noticeable crystallographic texture change. Particularly, in cold-rolled sheets of 70-80% thickness reduction recrystallization typically leads to a strong γ-fiber - i. e. $\langle 111 \rangle \parallel$ normal direction (ND) texture [1–7]. At the same time the α-fiber - i. e. $\langle 110 \rangle \parallel$ rolling direction (RD) - components of the prior deformed state gradually disappear. It is well-established that recrystallization in metals characterized by high stacking fault energy (SFE) evolves in accord with the subgrain formation and growth theory [8–18]. Hence, in IF steel sheets a subgrain can recrystallize only if it has an energy (also known as size) and a kinetic advantage compared to other subgrains in the abutting substructure. While the kinetic advantage allows the subgrain to grow faster than the surrounding substructure, the energy advantage ensures that the growing subgrain will not meet any larger subgrain upon its expansion. Therefore, one explanation for the formation of recrystallization texture in IF steel sheets is that the subgrains that have an advantage are mostly in γ-fiber components. Nevertheless, as in the early stages of annealing numerous subgrains are competing for evolving into recrystallized grains, there is no sufficient information regarding when and how a subgrain obtains a kinetic and/or energy advantage. This is why investigations on the effect of individual mechanisms in the nucleation of particular subgrains and their effect in orientation selection is yet a matter of interest [19–22].

For example, a subgrain can accumulate growing misorientation upon its changing neighborhood and eventually form a HAGB. This process - known as discontinuous subgrain growth - is a recovery mechanism that precedes recrystallization initiation [23] and it is often associated with recrystallization texture formation in IF steel sheets of 70-80% thickness reduction [19, 24]. Although a kinetic advantage is a prerequisite for recrystallization to occur [25], it is not confirmed whether it is obtained indeed by a static recovery mechanism or if it pre-exists in the as-deformed state [26]. This is because there are numerous HAGBs already in the as-deformed state and hence any abutting subgrain with an energy advantage that can also preserve its kinetic instability will readily recrystallize [20]. At the same time, even if some subgrains recrystallize after undergoing static recovery, there is no evidence at the moment whether recovery is indeed responsible for forming the typical γ-fiber texture upon annealing IF steel sheets. Altogether, it is impossible to obtain insight regarding the extent of recovery and relationship with texture formation, unless the phenomena that concur and compete are simulated in the same computational framework. For this reason, we perform recrystallization simulations in which nucleation occurs naturally (i. e. it is not imposed) and quantify the extent of recovery (by means of discontinuous subgrain coarsening), its contribution to the onset of recrystallization, and its relationship with the evolution of crystallographic texture.

5.1.2. IMPLEMENTATION

As explained in Chapter 4, although an electron backscatter diffraction (EBSD) map can approximate the subgrain structure and hence serve as input in such recrystallization simu-

lations, there are still limitations. This is because some regions of the material store a very high amount of energy upon plastic deformation and hence may incorporate subgrains that are smaller than the resolution of the EBSD. This may not majorly affect the simulated evolution of recrystallization since relative differences in misorientation and subgrains' size are still captured. A quantification on the extent of the concurring mechanisms during the simulation is nonetheless dependent on the resolution of the orientation map, due to the latter affecting the misorientation distribution at the as-deformed state [27]. This indicates that the effect of the simulation's grid spacing when simulating the temporal evolution of the substructure needs to be clarified as well. Hence, in the present study we use two additional RVEs together with the RVE shown in Chapter 4, and examine whether, how, and which of the quantifications are dependent on the fact that the grid spacing cannot capture all the orientation gradients in the substructure.

5.2. CELLULAR-AUTOMATON MODEL

5.2.1. CONSTITUTIVE AND KINEMATIC RULES

The simulations are performed with the model described in Chapter 3 using the Hex(1,1) grid. A cell i can re-orient in accord with the orientation g_j of its neighbour cell j, by the migration of the boundary ij between them and of any other boundary ik such that cell k is similarly oriented to j i. e. the misorientation θ_{jk} is smaller than the threshold θ_{min}. The growth of g_j into cell i occurs with rate:

$$\dot{f}_{g_i \to g_j} = \beta_{grid} \cdot M_{g_i \to g_j} \cdot \sqrt{\sum_{u_r = x,y,z} \left(\sum_k \delta_{kj} \cdot \left| \vec{F}_{ik, g_i \to g_j} \cdot \vec{u}_r \right| \right)^2} / V_i \tag{5.1}$$

where:

- δ_{ij} is a Kronecker-like operator with a tolerance of θ_{min}. It is equal to 1 when the misorientation between i and j is less or equal to θ_{min} - otherwise, no boundary is assumed to exist between the two cells.
- $V_i[\mathrm{m}^3]$ is the volume of cell i.
- k is index referring to neighbours of i.
- $\vec{u}_r = x, y, z$ is the unit vector for the r^{th} axis of the (Cartesian) reference system.
- $M(g_i, g_j)[\mathrm{m}^4/\mathrm{Js}]$ is the boundary mobility [28].
- $\vec{F}_{ik, g_i \to g_j}$ is the force imposed at every boundary segment ik - including ij - which migrates to re-orient cell i into g_j.
- β_{grid} a kinetic factor (here equal to 0.49) related to the grid-settings explained in Chapter 3.

The method used to calculate $\vec{F}_{ik, g_i \to g_j}$ is described in Chapter 3.

5.2.2. BOUNDARY PROPERTIES

The inhomogeneity in the boundary energy-driven motion derives from the inhomogeneous distribution of the dislocation content at the as-deformed state. Dislocations act as elementary units of deformation and hence they carry the deformation energy. At the same time, dislocations are elementary units of crystallographic misorientation and hence comprise boundaries by the motion of which (sub)grains can grow. Therefore, variations in the growth rate occur due to the boundary mobility and energy being ascending to the dislocation content [16, 25, 29–31]. The expressions used for obtaining the mobility and boundary energy as a function of the misorientation are given in Chapter 3.

5.2.3. INPUTS

The material used in the application is a Ti-stabilized 75% cold-rolled IF steel. The chemical composition and material parameters are the same with the application presented in Chapter 4. The simulation uses periodic boundary conditions. Nevertheless, since the kinetic instability of crucial for recrystallization to initiate, the boundary conditions are enabled only after a cell has transformed an actual neighbour cell. This can diminish the "falsified" kinetic advantage that a cell lying on the RVE's edges may have, toward the neighbourhood abutting its symmetrical location (on the opposite RVE's edge). The input RVEs are in 2D and are obtained through EBSD. Table 5.1 summarizes the characteristics of each input RVE. For the scans defined as RVE_1 and RVE_2 a JEOL JSM 6500F FEG-SEM microscope with an EDAX/TSL detector was used. The scan defined as RVE_3 is described in Chapter 4.

Table 5.1: Inputs for the simulations.

	Grid spacing δx_{CA}[μm]	RD dimension [μm]	ND dimension [μm]	Size [μm^2]
RVE_1	0.6	405	439	177609
RVE_2	0.3	600	470	281379
RVE_3	0.12	340	195	66143

Fig. 5.1 shows the microstructure of each RVE, plotted with the use of PYEBSD [32]. The automaton cells are colored in accord with the inverse pole figure (IPF)‖ND and are darkened with respect to the maximum misorientation with their neighbours. For example, if a cell has maximum misorientation with its neighbours less than 0.3° the cell is colored only with IPF‖ND, while for larger misorientations the IPF coloring is darkened ascendingly. Eventually, a cell that is surrounded by at least one HAGB (i.e. $\theta_{ij} \geq 15°$ appears black. As shown in Fig. 5.1, the larger the $\delta x_{CA}$the darker the image appears. This is because a large δx_{CA}may overestimate the elementary misorientation in some regions compared to the orientation gradient in the substructure, i. e. the grid spacing δx_{CA}exceeds the actual subgrain's size. This can be understood by considering the kernel average misorientation (KAM) of each cell, i. e. the average misorientation of a cell from its nearest neighbours.

While the average KAM[1] value in RVE_3 is 2°, RVE_2 and RVE_1 have average KAM equal to 3.9° and 4.4°, respectively.

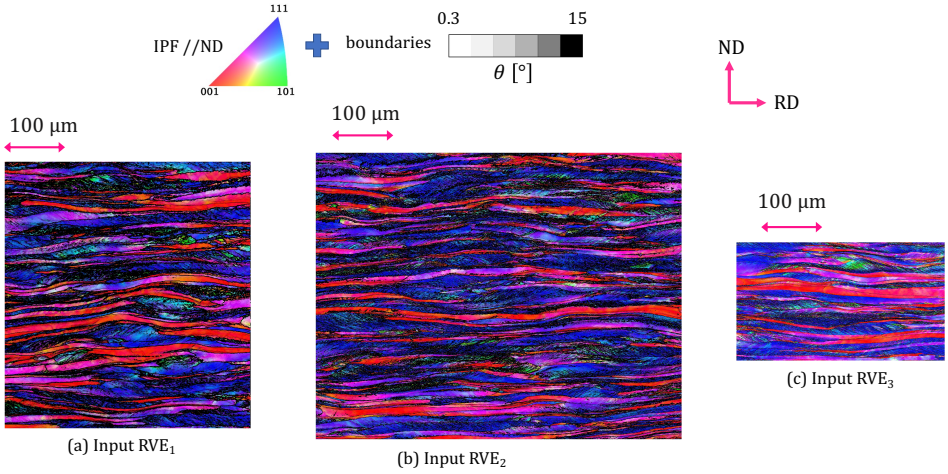

(a) Input RVE_1 (b) Input RVE_2 (c) Input RVE_3

Figure 5.1: The deformed state imported in the CA. The images correspond to the inputs defined as (a) RVE_1 (b) RVE_2 and (c) RVE_3.

Fig. 5.2 shows the time-temperature profile applied to the material.

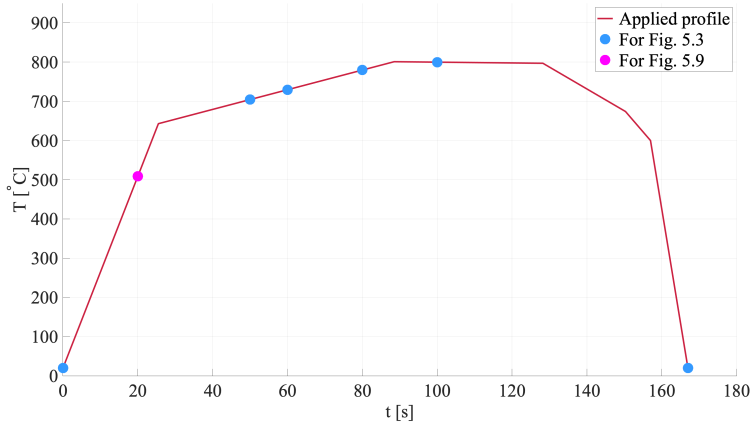

Figure 5.2: The temperature-time profile applied to the sheet. The marked values correspond to the initital state, the final annealed state and the intermediate states used for Figs. 5.3 and 5.9.

[1]The considered neighborhood and misorientation for KAM is the same as the CA neighborhood i. e. first neighbours of hexagonal grid and misorientation from 0.3 – 15°, including HAGBs (all set at 15°).

5.2.4. SCALING FOR EQUIVALENT DEFORMATION ENERGY

Since in the present CA method the driving force derives from the reduction of (sub)boundary energy, the stored deformation energy from the rolling is equal to the average (sub)boundary energy of each RVE. For example, in RVE_3 which has $\delta x_{CA} = 0.12$ μm, for a HAGB energy density equal to 0.5 J/m^2 [33, 34] the total deformation energy divided by the RVE's area is equal to $E_v = 2.2 \cdot 10^6$ J/m^3. This amounts to an equivalent [2] "free" dislocation density $\rho = 9 \cdot 10^{14}$/m^2 which is a reasonable approximation for a 75% cold rolled IF steel [35].

However, by increasing the grid spacing of the RVE, the deformation energy density captured decreases. Namely the value of E_v is found equal to $0.87 \cdot 10^6$ J/m^3 and $1.41 \cdot 10^6$ J/m^3 in RVE_1 and RVE_2, respectively. This is due to the inability of capturing all the (sub)boundaries when the grid spacing is larger than the subgrains' diameter [3]. Hence the smaller the grid spacing the larger is the energy density identified in the automaton[4], whereas the total stored deformation energy should be the same. To compensate for this, a scaling in the automaton's kinematic rule required, depending on the energy density. Assuming that RVE_3 (i.e. $\delta x_{CA} = 0.12$ μm) can indeed approximate the actual substructure's boundary energy, equating the deformation energy density for the three RVEs reads:

$$E_v = \left(\sum_{i=1}^{N_{cells}} 0.5 \cdot \left(\sum_{j=1}^{N} \gamma_{ij} \cdot A_{ij} \right) / V_i \right)_{RVE_3} = S_{RVE_2} \cdot \left(\sum_{i=1}^{N_{cells}} 0.5 \cdot \left(\sum_{j=1}^{N} \gamma_{ij} \cdot A_{ij} \right) / V_i \right)_{RVE_2} = S_{RVE_1} \cdot \left(\sum_{i=1}^{N_{cells}} 0.5 \cdot \left(\sum_{j=1}^{N} \gamma_{ij} \cdot A_{ij} \right) / V_i \right)_{RVE_1} \tag{5.2}$$

Where in Eq. (5.2):

- N_{cells} is the number of cells comprising the automaton grid.
- A_{ij} is the boundary area between two adjacent cells i and j.

From Eq. (5.2) the scaling factor is found equal to $\alpha_{RVE_2} = 1.56$ and $\alpha_{RVE_1} = 2.52$. The scaling factor multiplies the re-orientation rate shown in Eq. (5.1) at each simulation step in order to diminish the effect of the grid spacing on the kinetics. Eventually the re-orientation

[2] This is found by equating E_v to the "free" dislocations' energy $\frac{1}{2} \cdot \rho \cdot G \cdot b^2$, although the arrangement of dislocations at boundaries yields lower energy configurations. The equivalent ρ that is calculated can be considered as a lower limit.

[3] For example consider two material volumes that have a 15° misorientation in a 0.6 μm distance. In RVE_1 this amounts to 0.5 J/m^2 per 0.6 μm whereas in RVE_2 this can be identified for example as two boundaries of 7.5° with distance 0.3 μm which results to 0.82 J/m^2 per 0.3 μm or equivalently 1.64 J/m^2 per 0.6 μm.

[4] This only applies to deformed microstructures and only if there are indeed subgrains smaller than the grid spacing.

rate of a cell i is:

$$\dot{f}_{g_i \to g_j} = \alpha_{\mathrm{RVE}_n} \cdot s_{\mathrm{grid}} \cdot M_{g_i \to g_j} \cdot \sqrt{\sum_{u_r = x,y,z} \left(\sum_k \delta_{kj} \cdot \left| \vec{F}_{ik, g_i \to g_j} \cdot \vec{u}_r \right| \right)^2} / V_i \tag{5.3}$$

It should be clarified that the scaling does not affect the misorientation distribution of each RVE and does not compensate for any other artifact related to the resolution, beyond the recrystallization kinetics in terms of energy release.

5.3. RESULTS AND DISCUSSION

5.3.1. MICROSTRUCTURE EVOLUTION DURING RECRYSTALLIZATION

TEMPORAL EVOLUTION IN SIMULATION

We performed the simulations in all RVEs using the temperature-time profile shown in Fig. 5.2. The temporal evolution for RVE_2 is shown in Fig. 5.3. The temperature (and history) for each time step shown is marked in Fig. 5.2. As expected, recrystallization initiates in regions with high orientation gradients - e. g. see the magnified region in Fig. 5.3a: mostly the dark-colored areas have recrystallized in Fig. 5.3b while the grains with small interior orientation gradients have remained intact. In the following stages, some recrystallized grains become large enough to consume the low-energy deformed grains (mostly colored red), and eventually, a fully recrystallized microstructure is seen in Fig. 5.3f.

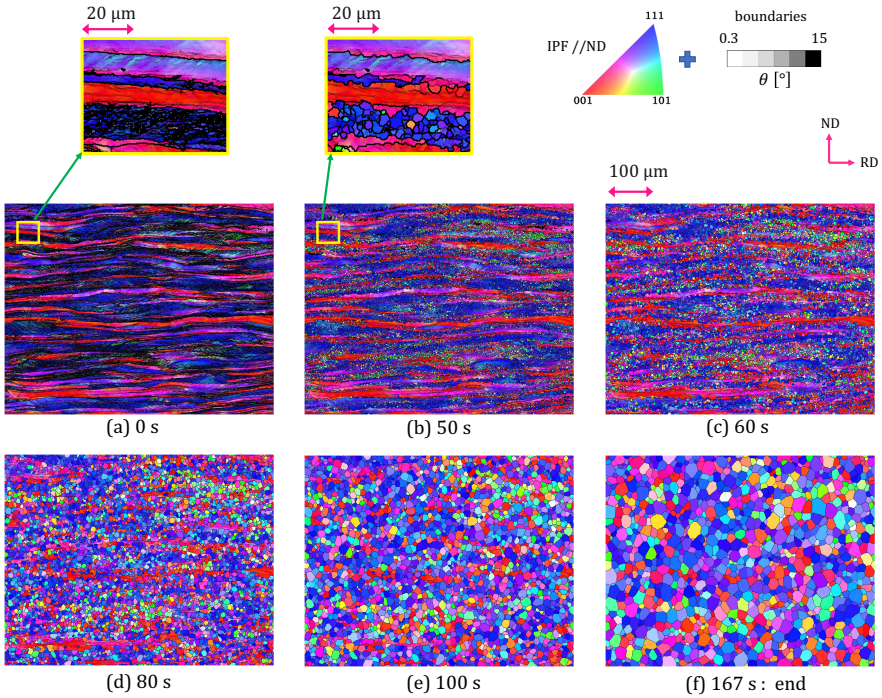

Figure 5.3: Temporal evolution of simulation with RVE_2 at (a) 0 s (b) 50 s (c) 60 s (d) 80 s (e) 120 s and (f) 167 s. The corresponding temperature (and history) at each stage depicted is shown in Fig. 5.2.

Nevertheless, it is clear that recrystallization occurs rather more continuously in these simulations, in comparison to experimental observations of the recrystallization evolution in IF steels and relevant materials, e. g. by Kim *et al.* [36], Choi and Cho [17]. This is expected, especially as we increase the grid spacing, since (a) nucleation is not imposed, (b) out of all the physical processes that can provide subgrains an advantage and hence are responsible for their forthcoming nucleation (see e. g. Table 1.1 in Chapter 1), only two naturally occur in these simulations, (c) the grid spacing cannot capture all details of the substructure and (d) the simulations take place in 2D which means that the heterogeneity of the subgrains' growth and evolution, i. e. the preferential growth, is underestimated. However, the aim of this study is not to imitate exactly the evolution of recrystallization, but rather to investigate the possible existence of relationships between the particular mechanisms considered here, leading to nucleation and the formation of texture. More details for whether and how the simulations can be improved when it comes to serving as predictive tools for the microstructure evolution are discussed later, in Section 5.4.3.

RECRYSTALLIZED MICROSTRUCTURE

The simulated annealed state for all RVEs together with the experimentally annealed microstructure is shown in Fig. 5.4. As is shown, all simulations yield a recrystallized microstructure consisting primarily of bluish grains, in compliance with the experimental measurement.

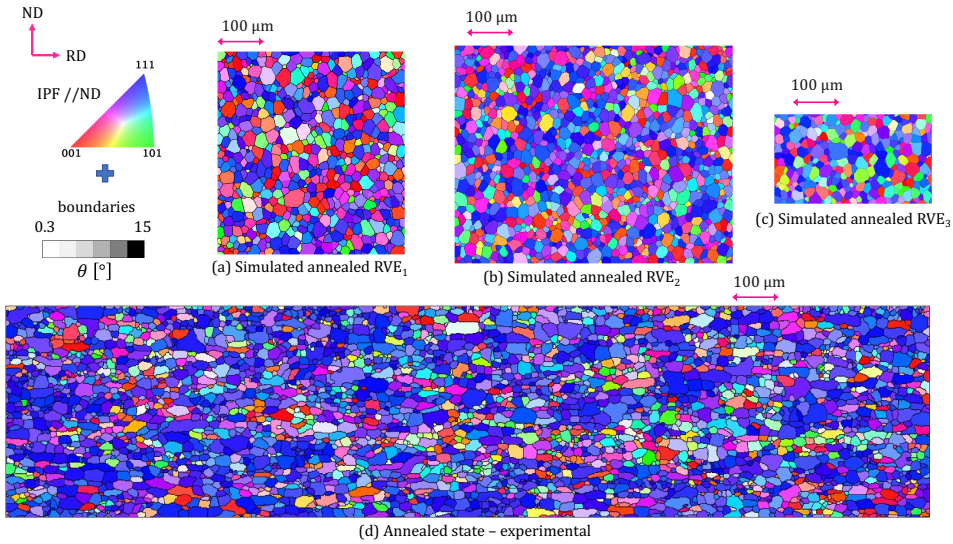

Figure 5.4: The annealed state i. e. end of heat treatment shown in Fig. 5.2: (a) simulated with RVE_1 (b) simulated with RVE_2 (c) simulated with RVE_3 and (d) experimentally measured.

γ-FIBER AND α-FIBER TEXTURE

Fig. 5.5 shows the $\phi_2 = 45°$ section of the orientation distribution function (ODF) quantified with MTEX [37]. As shown in Fig. 5.5 the deformed sheet is characterized by a combined α-fiber and γ-fiber texture.

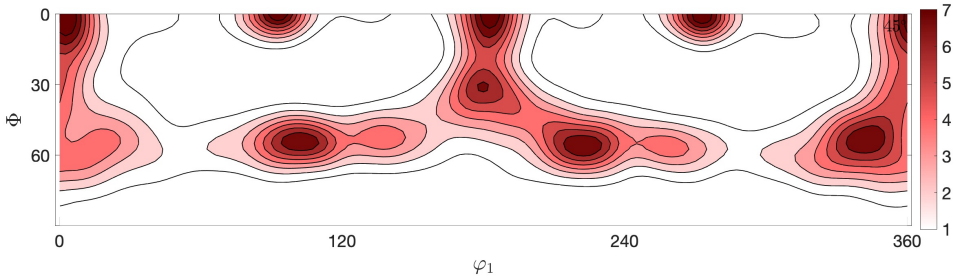

(a) RVE_1 : Deformed state – 0 s

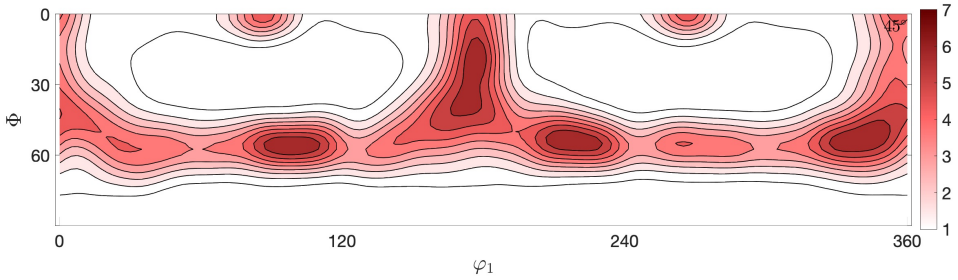

(b) RVE_2 : Deformed state – 0 s

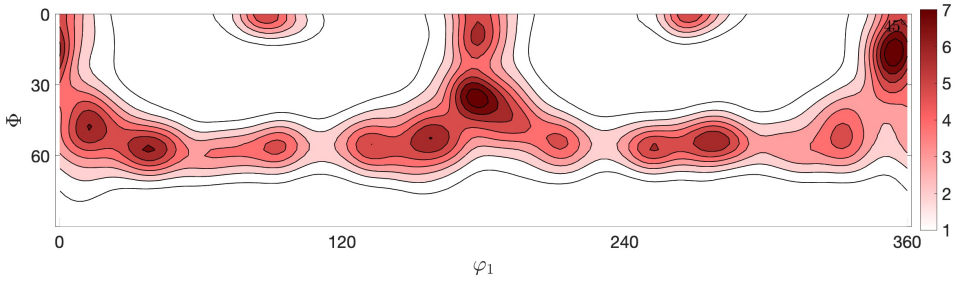

(c) RVE_3 : Deformed state – 0 s

Figure 5.5: ODF quantified for the deformed state and plotted in section $\phi_2 = 45°$ for (a) RVE_1 (b) RVE_2 and (c) RVE_3.

Fig. 5.6 shows the $\phi_2 = 45°$ section of the ODF for the annealed state - simulated and experimental. Combining Figs. 5.5 and 5.6 it is clear that all simulations result in the diminishing of α-fiber components, while γ-fiber components mostly comprise the recrystallized material. Although this trend is also seen in the experimentally annealed state - Fig. 5.6d, the

intensity of each texture component in the $\phi_2 = 45°$ section still has deviations between the simulations and the experiment. A quantitative comparison between the full ODF (i. e. not only for components in section $\phi_2 = 45°$) is presented and discussed later in Section 5.3.2.

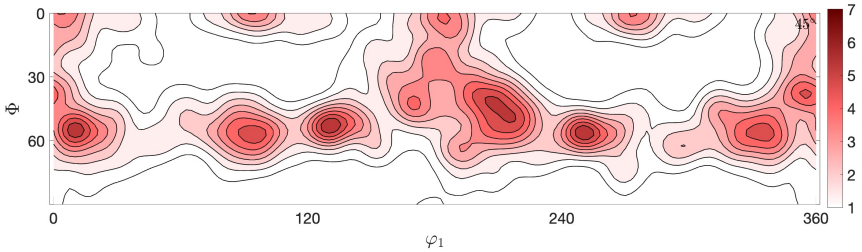

(a) RVE_1 : Simulated annealed state - 167 s

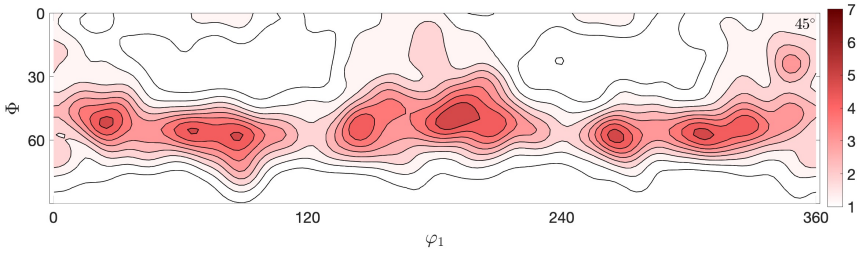

(b) RVE_2 : Simulated annealed state - 167 s

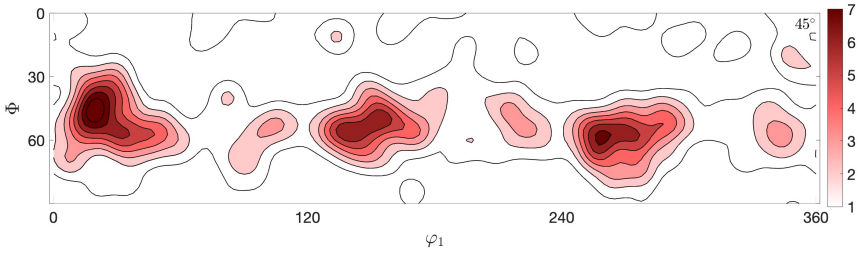

(c) RVE_3 : Simulated annealed state - 167 s

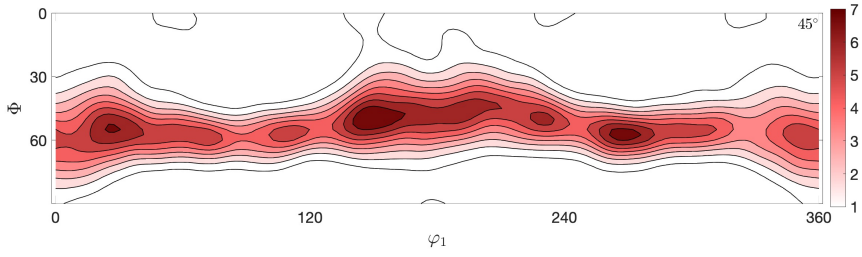

(d) Experimental annealed state - 167 s

Figure 5.6: ODF quantified for the annealed state (end of heat treatment shown in Fig. 5.2) and plotted in section $\phi_2 = 45°$ for (a) the simulation with RVE_1 b) the simulation with RVE_2 (c) the simulation with RVE_3 and (d) the experimentally measured microstructure.

5.3.2. QUANTITATIVE COMPARISON

GRAIN SIZE

Table 5.2 shows the mean grain size for each simulation and its deviation from the experimentally annealed microstructure which has an average grain diameter equal to 16.8 μm. The average grain diameter was quantified after decomposing the orientation data into grains using the routine described in [38].

Table 5.2: Mean grain size at the annealed state and deviations.

	Simulated grain size $\bar{d}_s$[μm]	Deviation from experimental: 16.8 μm $\Delta\bar{d}_{s,ref}$[μm]	Expected deviation (from RVE size) $\delta\bar{d}_s$[μm]
$s = \text{RVE}_1$	17.8	+1.0	±0.3
$s = \text{RVE}_2$	16.1	−0.7	±0.2
$s = \text{RVE}_3$	15.7	−1.1	±0.6

In Table 5.2:

- s is an index referring to the simulation i. e. $s = \{\text{RVE}_1, \text{RVE}_2, \text{RVE}_3\}$.
- ref is an index indicating the reference i. e. the experimentally annealed microstructure.

In Table 5.2 the deviation due to the sample size $\delta\bar{d}_s$ for each simulation is quantified to assess the expected deviation. In particular, the simulated microstructures are much smaller in terms of statistics than the experimentally annealed material, whereas heterogeneous processes such as deformation/recrystallization require a large statistical sample to characterize the sheet's properties. In order to quantify the effect of the statistical sample size on the mean grain size, we calculated the uncertainty $\delta\bar{d}_s$. This was found for each RVE by subdividing the experimental microstructure into smaller areas (equal to each RVE's size). Then we calculated the mean grain size for each subdivided area and its deviation from the mean grain size of the whole material. The average value of these deviations gives $\delta\bar{d}_s$ - deviation in grain size due to RVE size for the s^{th} simulation, which is expressed as:

$$\delta\bar{d}_s = \left(\sum_{i=1}^{n} |\bar{d}_{ref} - \bar{d}_i| \right) / n \tag{5.4}$$

where in Eq. (5.4):

- i is the i^{th} area subtracted from the experimental microstructure which has dimensions equal to microstructure's s.
- n is the number of subdivisions done i. e. the number of times an area equal to s can fit in ref.

The method we used for calculating the deviations in the recrystallized grain size resulting from the RVE size is illustrated as an example for RVE_3 in Fig. 5.7. For RVE_1 and RVE_2 the corresponding images are included in Appendix B - namely Figs. B.1 and B.3.

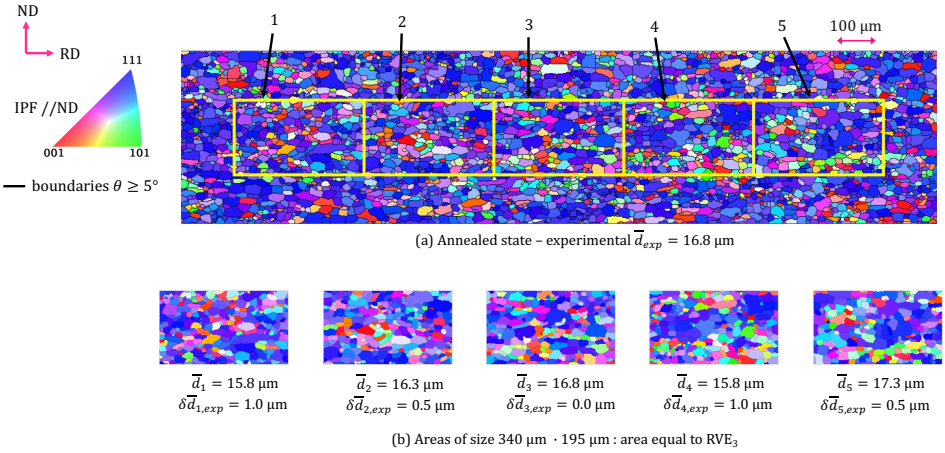

Figure 5.7: Method used to calculate $\delta\bar{d}_{RVE_3}$ where (a) the experimentally measured microstructure (b) the subdivision in areas equal to the size of RVE$_3$.

5

As indicated by the deviations shown in Table 5.2, all simulations predict the average grain size in agreement (5.5% is the average error) with the experimentally annealed state - see deviations $\Delta\bar{d}_{s,ref}$. This is also confirmed by the small values of $\delta\bar{d}_s$ which already imply that the RVEs size is sufficient for describing the annealed state's grain size. However, it is still worth mentioning that a trend between the grid spacing and the mean grain size exists. In particular, the predicted grain size is ascending to the grid spacing. This can be explained by considering the overestimation of orientation gradients in a large grid spacing. Although we used Eq. (5.2) to compensate for this effect, the expression we used only affects the kinetics of the simulation. It does not affect the actual local misorientations. Therefore, the larger the grid spacing compared to the actual subgrain size, the more mobile the subgrain may be found resulting in faster recrystallization kinetics.

CRYSTALLOGRAPHIC TEXTURE

Table 5.3 summarizes the deviation of crystallographic texture between the simulated and experimentally annealed microstructure. The formula used to quantify the error between two ODFs - as suggested in [39] - is:

$$T_{s,ref} = \frac{\int_{V_g} \left(f_s(g) - f_{ref}(g) \right)^2 dg}{\int_{V_g} \left(f_{ref}(g) \right)^2 dg} \tag{5.5}$$

where in Eq. (5.5):

- $f_m(g)$ is the intensity of component g for the microstructure indexed as m.
- $V_g = [\phi_1] \times [\Phi] \times [\phi_2]$ is the (Euler) space that is considered i. e. here $V_g = [0° - 360°] \times [0° - 90°] \times [0° - 90°]$.

Table 5.3: Crystallographic texture errors between simulated and experimental annealed state.

	Texture error $T_{s,ref}$	Error due to RVE size δT_s	Net error $T_{s,ref} - \delta T_s$
$s = \text{RVE}_1$	0.33	0.07	0.25
$s = \text{RVE}_2$	0.21	0.04	0.17
$s = \text{RVE}_3$	0.34	0.19	0.15

The texture error between each simulation and the experimental microstructure is $T_{s,ref}$ in Table 5.3. The texture error due to the size of each RVE presented in Table 5.3 represents the part of the texture deviation between a simulation and the experimental measurement that derives from the insufficient statistical sample size. While the experimentally annealed state contains a large - and possibly sufficient for describing the full sheet's texture - number of grains, the simulated RVEs (especially RVE_3) contain much less. In order to approximate the effect of the statistical sample size in measuring the particular material's texture, we used the same method described in Section 5.3.2 for quantifying $\delta\bar{d}_s$. To illustrate the deviations between the whole experimental microstructure and the subdivided areas with size equal to RVE_3, Fig. 5.8 shows the ODF plotted in section $\phi_2 = 45°$. It should be clarified that Fig. 5.8 shows only the $\phi_2 = 45°$ section of the ODF to show how the intensity of some texture components varies in different areas. The calculated δT_{RVE_3} and the $\delta T_{i,ref}$ values shown in Fig. 5.8 correspond to the full ODF - i. e. for Euler space as defined earlier in Eq. (5.5).

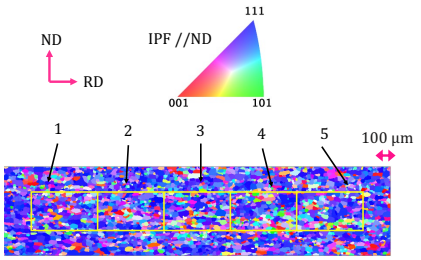

(a) Experimentally annealed microstructure

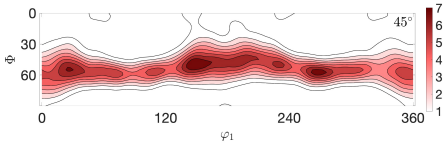

(b) ODF $\varphi_2 = 45°$, mean $T_{i,ref} = 0.19$ (for full ODF)

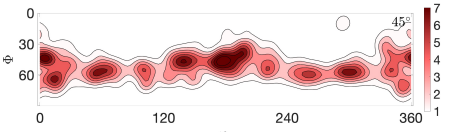

(c) Area 1: $T_{1,ref} = 0.17$

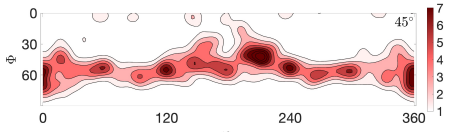

(d) Area 2: $T_{2,ref} = 0.16$

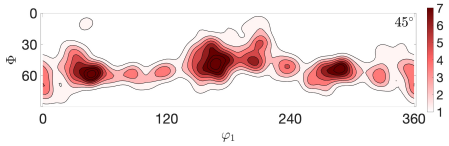

(e) Area 3: $T_{3,ref} = 0.20$

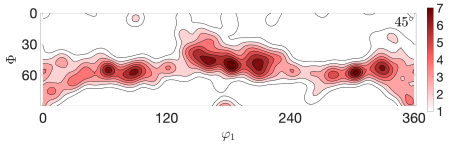

(f) Area 4: $T_{4,ref} = 0.18$

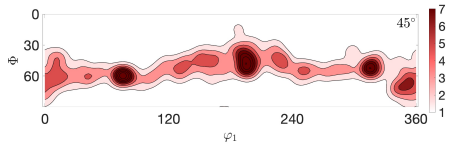

(g) Area 5: $T_{5,ref} = 0.25$

Figure 5.8: Method used to calculate δT_{RVE_3} where (a) the experimentally measured microstructure together with the $\phi_2 = 45°$ section of the ODF (b) the $\phi_2 = 45°$ section of the ODF for each area of size equal to the size of RVE_3.

Eventually, when quantifying the crystallographic texture predicted by a simulation s, the expected deviation stemming from the insufficient statistics is:

$$\delta T_s = \left(\sum_{i=1}^{n} T_{i,ref} \right) / n \tag{5.6}$$

where in Eq. (5.6) $T_{i,ref}$ is the deviation of crystallographic texture between the whole experimental microstructure (i. e. ref) and an area extracted from the experimental microstructure with size equal to s.

It should be noted that the method we used to assess δT_s only incorporates deviations due to the insufficient statistics in the same longitudinal cross-section, and only for the recrystallized microstructure. Deviations due to insufficient statistics in the deformed microstructure and due to deformation/recrystallization inhomogeneities along the transverse direction (TD) are also expected. For example, the average texture deviation between the three input RVEs in the deformed state is 0.2. Since there is no information for how the deformed state's inhomogeneity can be quantitatively related to the recrystallized state's inhomogeneity, we limited the δT_s to only consider the recrystallized state.

As shown in Table 5.3, although the most accurate simulation regarding $T_{s,ref}$ is the one with RVE_2, when we consider the size of each RVE and its effect on quantifying crystallographic texture, there is a clear trend between accuracy and grid spacing i. e. see the last column in Table 5.3 which gives smaller net error as the grid spacing decreases. Namely, RVE_3 gives the most accurate results, then RVE_2 and at last RVE_1. Hence both the resolution and the RVE size play an important role when it comes to crystallographic texture.

The effect of the RVE size when it comes to crystallographic texture can be understood better if one compares Fig. 5.8 with the corresponding figures of the other two RVEs shown in Appendix B - namely Figs. B.2 and B.4. It becomes clear that even in one section of the ODF - namely the $\phi_2 = 45°$ section - the intensity of the texture components is much more representative when quantified in areas equal to the larger RVEs.

5.3.3. RECOVERY

EXTENT OF DISCONTINUOUS SUBGRAIN GROWTH

This section investigates the participation of LAGBs in the motion of subgrains. Fig. 5.9 shows the distribution of moving boundaries with misorientation smaller than 15° at 20 s - no cells have recrystallized by that time. The graph indicates that most subgrains grow via boundaries of misorientation less than 15° - i. e. hence discontinuous subgrain growth occurs. Regarding the grid spacing, as expected from the previous discussion regarding the orientation gradients overestimation, more LAGBs are present in the RVEs with smaller δx_{CA}.

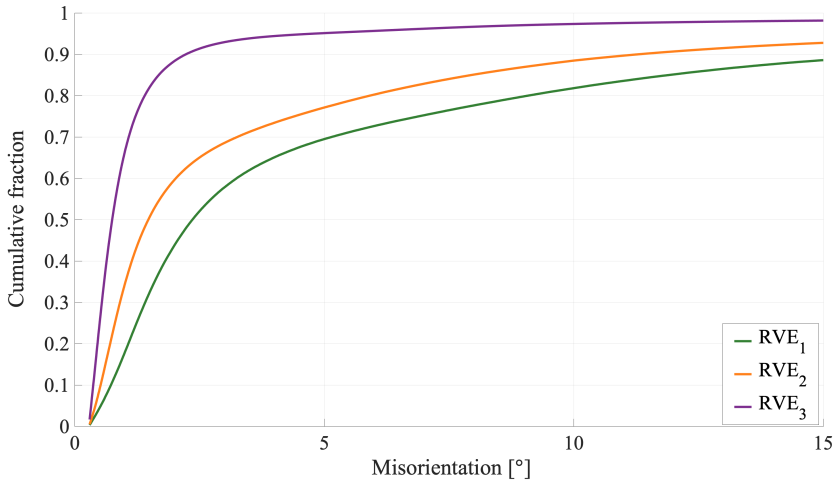

Figure 5.9: Misorientation of boundaries moving at 20 s, before any cell has transformed.

Fig. 5.10 shows the distribution of misorientation, only for boundaries of subgrains that transformed at least once a neighbour cell, while both cells were still deformed. Fig. 5.10a refers to all cells that at any moment during the simulation, transformed a neighbour cell whilst representing a deformed volume. As indicated in Fig. 5.10a growth initiation occurs by both LAGB motion (recovery) and HAGB motion (direct recrystallization initiation). However, compared to Fig. 5.9 the participation of LAGBs is already much smaller. This is because LAGBs migrate much slower than HAGBs, so most of the moving LAGBs do not reach a distance larger than the grid spacing before being consumed by other recrystallized grains.

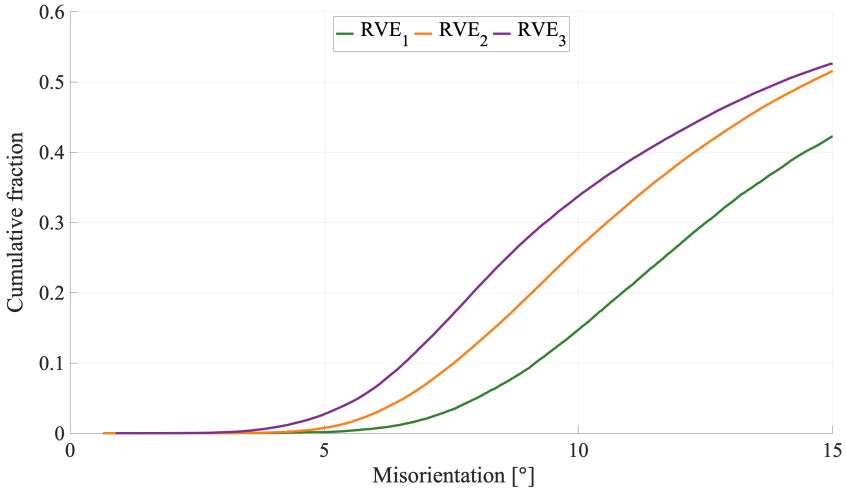

(a) All subgrains that grew during the simulation

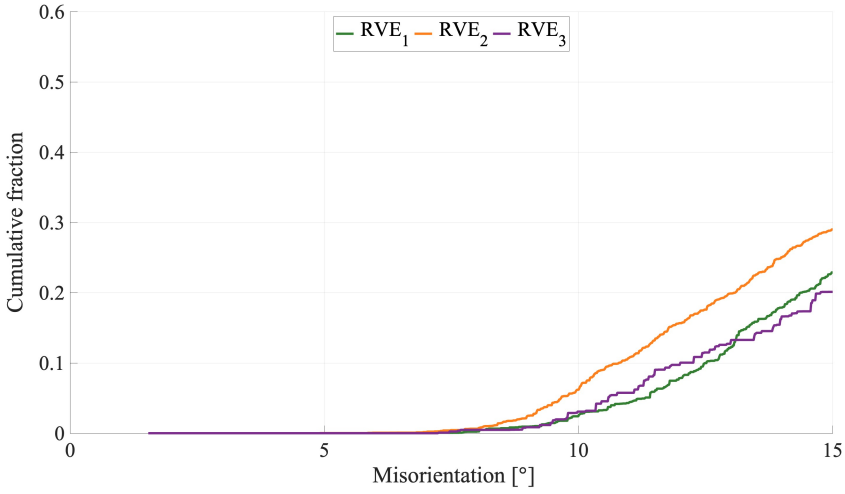

(b) All subgrains that became recrystallized grains and appeared at annealed state

Figure 5.10: Misorientation of boundaries whereby subgrains initiate growing for (a) all cells that transformed at least one adjacent cell, whilst being still intact (i.e. not surpassed by any other boundary) (b) all cells that evolved in recrystallized grains which comprise the annealed state.

Fig. 5.10b shows the distribution of misorientation for subgrains that transformed at least once a neighbour cell but for these subgrains that actually evolved into grains that appeared at the end of the annealing simulation. In other words, Fig. 5.10b shows the misorientation of boundaries whereby the recrystallized grains originated. As is shown, most of the annealed microstructure consists of grains that originated from immediate recrystallization. Although recovery occurs in the simulations, it does not dominate as a nucleation mechanism.

It is also noteworthy that oppositely to Fig. 5.9 and Fig. 5.10a that depend on δx_{CA}, Fig. 5.10b does not seem to exhibit any such trend. The prevalence of recrystallization initiation without precedent discontinuous subgrain growth is found in all simulations. The findings regarding the misorientation distributions are summarized in terms of the volume fraction of participating HAGBs in Table 5.4.

Table 5.4: Summary: Fraction of subgrains growing through HAGBs.

	$V_{HAGB}^{move}[\%]$	$V_{HAGB}^{init}[\%]$	$V_{HAGB}^{rx}[\%]$
RVE_1	11	58	78
RVE_2	8	49	71
RVE_3	2	48	80

In Table 5.4:

- V_{HAGB}^{move}: is the fraction of boundaries with $\theta \geq 15°$ among all moving boundaries before any cell has transformed - i. e. the fraction missing in Fig. 5.9.
- V_{HAGB}^{init}: is the fraction of growth initiation that was attained by a boundary with $\theta \geq 15°$ - i. e. the fraction missing in Fig. 5.10a.
- V_{HAGB}^{rx}: is the fraction of the recrystallized volume (end of annealing) that originated from a subgrain adjacent to a boundary with $\theta \geq 15°$ - i. e. the fraction missing in Fig. 5.10b.

Considering the above-mentioned and assuming that a subgrain that grows via a boundary of $\theta < 15°$ is still in the recovery process, we can see that although recovery occurs in all simulations it does not contribute significantly to the nucleation of recrystallization. Most subgrains undergoing recovery do not even reach a distance larger than δx_{CA}. Additionally, from the subgrains that reach this distance, most do not end up comprising the annealed state. Hence, the required kinetic and energy advantage that a subgrain must have in order to recrystallize is in most cases not attained by recovery (discontinuous subgrain coarsening). Rather, it is shown that most subgrains that recrystallize already have this advantage in the as-deformed state.

RECOVERY AND CRYSTALLOGRAPHIC TEXTURE

This section reviews the relevance of the nucleation mechanism with the formation of the γ-fiber recrystallization texture. Figs. 5.11 to 5.13 show the $\phi_2 = 45°$ section of the ODF regarding the subgrains that nucleate readily at HAGBs, for the 3 RVEs used. Fig. 5.11a,

Fig. 5.12a and Fig. 5.13a refer to V_{HAGB}^{init} and hence present the texture components that characterize the subgrains which recrystallized at least one neighbour cell. Fig. 5.11b, Fig. 5.12b and Fig. 5.13b refer to V_{HAGB}^{rx} and hence correspond to the subset of V_{HAGB}^{init} that continued growing competitively upon the simulation insofar as they actually comprised the annealed state.

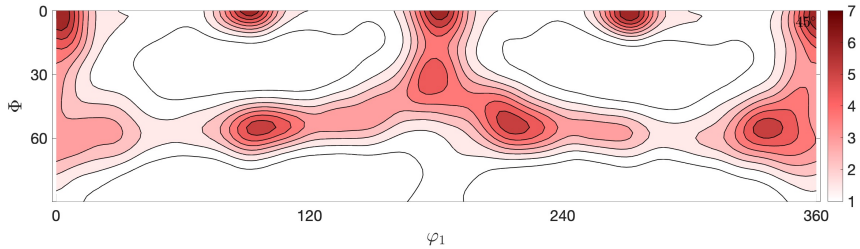

(a) RVE$_1$: for $V_{HAGB}^{rx,init}$ = 58% of subgrain growth initiation

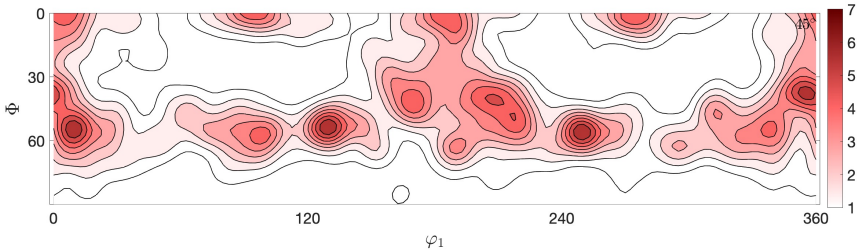

(b) RVE$_1$: for V_{HAGB}^{rx} = 78% of recrystallized volume

Figure 5.11: ODF plotted in section $\phi_2 = 45°$ for the cells that initiated growing readily through a HAGB in the simulation with RVE$_1$. In (a) all cells that grew at least once to an adjacent deformed cell whilst still also deformed are considered. In (b) the cells that initiated growing through a HAGB are considered, but this time only for subgrains that evolved in recrystallized grains and appear in the annealed state.

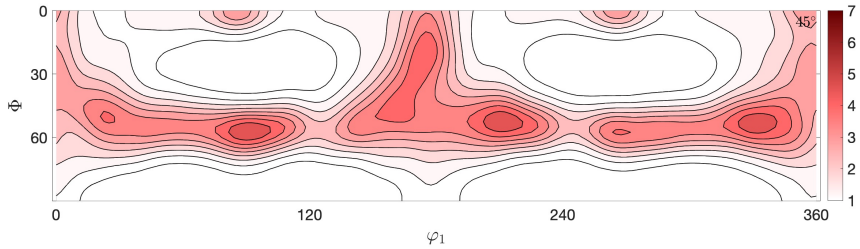

(a) RVE_2 : for $V_{HAGB}^{rx,init} = 49\%$ of subgrain growth initiation

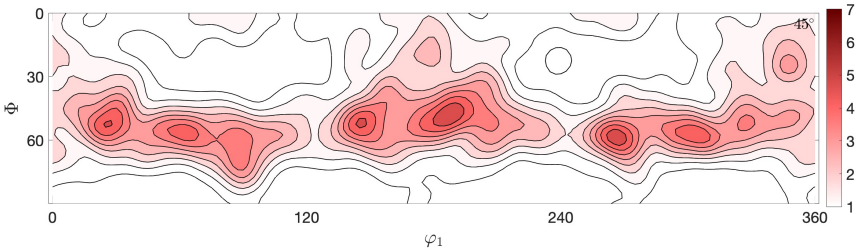

(b) RVE_2 : for $V_{HAGB}^{rx} = 71\%$ of recrystallized volume

Figure 5.12: ODF plotted in section $\phi_2 = 45°$ for the cells that initiated growing readily through a HAGB in the simulation with RVE_2. In (a) all cells that grew at least once to an adjacent deformed cell whilst still also deformed are considered. In (b) the cells that initiated growing through a HAGB are considered, but this time only for subgrains that evolved in recrystallized grains and appear in the annealed state.

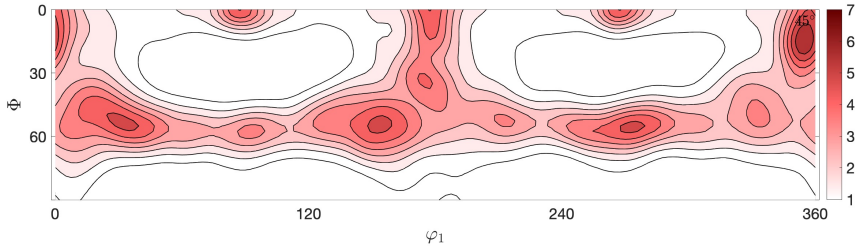

(a) RVE$_3$: for $V_{HAGB}^{rx,init}$ = 48% of subgrain growth initiation

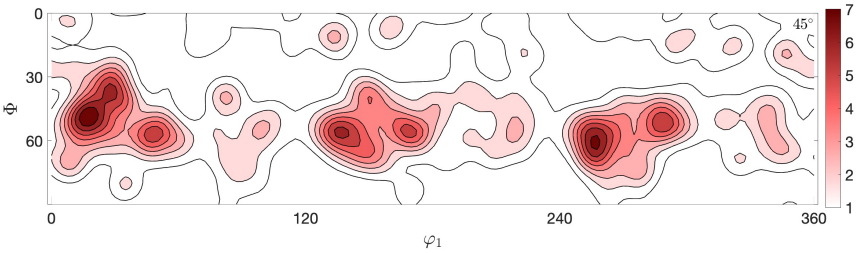

(b) RVE$_3$: for V_{HAGB}^{rx} = 80% of recrystallized volume

Figure 5.13: ODF plotted in section $\phi_2 = 45°$ for the cells that initiated growing readily through a HAGB in the simulation with RVE$_3$. In (a) all cells that grew at least once to an adjacent deformed cell whilst still also deformed are considered. In (b) the cells that initiated growing through a HAGB are considered, but this time only for subgrains that evolved in recrystallized grains and appear in the annealed state.

Comparing for each RVE the $\phi_2 = 45°$ section of the ODF for V_{HAGB}^{init} and V_{HAGB}^{rx}, it becomes clear that the γ-fiber texture forms after recrystallization initiation. In particular, we can see that Fig. 5.11a, Fig. 5.12a and Fig. 5.13a are very similar to the RVEs' deformed state $\phi_2 = 45°$ section of the ODF - i. e. Fig. 5.5. Therefore during recrystallization initiation the α- and γ-fiber texture components remain almost unchanged.

On the other hand, Fig. 5.11b, Fig. 5.12b and Fig. 5.13b are much closer to the $\phi_2 = 45°$ section of the ODF quantified for the annealed state - i. e. Fig. 5.6. This implies that the recrystallized volume that nucleates from direct HAGB motion can represent well the annealed state's texture, without requiring curvature-driven recovery.

Altogether, the redistribution of texture components from combined α- and γ-fiber to a mostly γ-fiber texture occurs after recrystallization initiation. Hence, the well-known nucleation texture [3, 5] of IF steel sheets forms after recrystallization initiates.

5.4. CONCLUSIONS

5.4.1. OVERVIEW OF DISCUSSED ITEMS

In the present study, we investigated recrystallization evolution in an IF steel sheet in a unified computational framework that recrystallization nucleation occurs naturally out of the evolving substructure. The simulations were performed with the use of three RVEs - each from an EBSD map of different resolution. The following remarks are deduced:

- Although the RVEs' grid spacing can change, the simulated mean grain size is only minorly affected, at least for a grid spacing within $0.12 - 0.6$ μm.
- The crystallographic texture of the simulated annealed state is more accurately predicted when the grid spacing decreases. However, the statistical sample size of the RVE plays also a major role, and eventually, the overall prediction of crystallographic texture is optimized when there is a good combination of RVE size and grid spacing e. g. like RVE_2.
- Static recovery, in terms of discontinuous subgrain growth, occurs, yet it does not dominate as a nucleation mechanism. Most recrystallized grains originate from subgrains (abutting HAGBs) that immediately recrystallized.
- The kinetic and energy advantage that a subgrain must possess compared to the surrounding substructure in order to recrystallize, in most cases, already exists at the as-deformed state.
- The γ-fiber texture that characterizes the annealed state does not form at the moment of recrystallization initiation. The subgrains that initiate growing at HAGBs are characterized by combined α- and γ-fiber. Only a subset of these subgrains continues growing competitively and this subset is characterized by a γ-fiber texture.

5.4.2. GENERAL ADVANCES AND UNDERSTANDINGS

As explained in the introduction, despite the numerous investigations throughout the last decades, nucleation of recrystallization in cold-deformed high-purity metals is unresolved in many different contexts, among which presumably the most controversial are: (a) whether and how the so-called nucleation process and texture relate to particular mechanisms, and if so, at which point of its evolution it is obtained, and (b) whether a type of recovery (here discontinuous subgrain growth) is indeed necessary for nucleation and/or related to the well-known γ-fiber texture formation. The latter also indicates that such a relationship would primarily favor the nucleation of mostly high stored-energy lattice sites.

Based on the discussed results, and in combination with the analysis performed in the simulations in Chapter 4, it is suggested that, while initially recrystallized volumes appear next to numerous HAGBs (intergranular and grain boundaries), these recrystallized volumes are not characterized by the so-called nucleation texture. A similar observation was presented by Dillamore *et al.* [40], who suggested that initially grain boundary nucleation is favored, and particularly of $\{100\}\langle 110\rangle$ subgrains, but it soon turns out to be unsuccessful, thus giving time to intergranular nucleation. However, the process of intergranular nucleation according to Dillamore *et al.* [40] remained unknown in terms of the partici-

pating nucleation mechanisms. The results here agree with the former observations, and furthermore suggest that the process of intergranular nucleation does not require much discontinuous subgrain growth, as there are numerous high-angle boundaries within highly deformed grains. In this view, intergranular nucleation evolves like grain boundary nucleation, just favored by the energy advantage in comparison to the latter. A similar suggestion was made by Hutchinson [26], who suggested that any pre-existing large angle boundary should be expected to be "exploited" by its surrounding subgrains, and therefore nucleation by discontinuous subgrain growth may not be necessary. The simulations and analyses performed here substantiate and to a certain extent prove that indeed discontinuous subgrain growth is not a necessary mechanism for recrystallization to occur.

The second point regarding the recovery of high stored-energy regions, has been critically discussed by Kestens and Pirgazi [22], who pointed out that the differentiation between high stored-energy and low stored-energy texture formation during recrystallization of high-purity steels is still controversial. Kestens and Pirgazi [22] suggested that the formation of such different types of textures when changing the level of deformation or temperature, is still unresolved and could indeed be a result of recovery taking place at high stored-energy regions. The present simulations, which already from the methodology favor the low stored energy regions to recrystallize[5], reveal that even without any type of recovery a rather high stored-energy texture forms during the recrystallization of highly-strained IF steel, nonetheless. Therefore, it is highly likely that the formation of the recrystallization texture, whether it is a high-stored energy or a low stored-energy, may be indeed associated with the evolution of the same mechanism, i. e. the competitive growth of recrystallized volumes originated from high-angle boundaries. The only difference then between the two types of textures, is due to the crystal orientations topology and particularly to which high-angle boundaries separate substructures of sufficiently different sizes/boundary energy.

5.4.3. OUTLOOK

ADDRESSING CURRENT ISSUES IN CONJUNCTION TO THE PRESENT INSIGHT

In view of the above-mentioned insight regarding the relationship between crystallographic texture formation and stored energy, it is opportune to make some further deductions. In particular, it would be expected that applying exactly the same model, i. e. without any change in the constitutive relationships and transformation rule, on deformation structures of similar materials but of low stored-energy recrystallization textures, the simulation would result in consistent trends regarding the evolution of texture. In particular, it is expected that with this simulation approach, low stored-energy recrystallization textures, such as the annealing texture observed in warm-rolled steels (see e. g. the work of Nguyen Minh *et al.* [41]), can also be modeled. Of course, this is a speculation, but it is well justified since already from its description it is clear that this approach always favors the least - in comparison to the local surroundings - deformed region to recrystallize. In this view, it is more surprising that the simulations are consistent with cold worked metals, and even more surprising that here we observe that the formation of crystallographic texture is not based on discontinuous

[5] Since in the present framework the subgrains within lower stored-energy regions in comparison to their surroundings are the ones favored.

subgrain growth - a recovery process. So far we have explained why this happens in this material, which means that in the absence of high variations in the boundary energy within the γ-fiber grains, a rather different crystallographic texture would arise. As low stored-energy recrystallization textures are already known to not be the result of static recovery [22], we can address the controversy described in Section 5.4.2 and presumably explain it on the basis of the substructure's topology.

IMPROVING PREDICTABILITY OF THE MICROSTRUCTURE EVOLUTION

Although the issues in this chapter were addressed with systematic investigations, it is somewhat obvious that more effort was put on understanding the process of nucleation, rather than on accurately predicting the temporal evolution and outcome of recrystallization annealing. For example, as discussed in Section 5.3.1, selective subgrain growth and recrystallization evolve more continuously in comparison to experimental findings, e. g. studied carefully by Choi and Cho [17] and Kim *et al.* [36]. The same of course can be said regarding the simulated crystallographic texture, which is somewhat limited in highlighting trends instead of serving as a predictive tool for controlling the annealing sheet texture. We have explained already in Section 5.3.1 why the present approach is not expected to imitate exactly the recrystallization evolution in the material, especially since it operates in 2D without imposing a nucleation criterion.

On the other hand, models are often useful for the steel-making industry in terms of microstructure control, due to their ability of making sufficiently accurate and efficient predictions of the microstructural features associated with macroscopic properties (here mechanical). Although the applicability of the present approach is much wider in comparison to having used nucleation criteria tailored to the application, in cases that we already have empirical approximations for the nucleation texture and nuclei density, a relevant improvement would concern the predictability. In specific, when the purpose of an application is more associated with predictability of well-documented material behavior, the approach taken here could consider for example additional stored-energy variations, together with the misorientation-related dislocations that are considered here. Particularly when using EBSD inputs, this can be done, as suggested by Choi and Cho [17], by (a) using an orientation-dependent (i. e. Taylor factor, TF) approximation, (b) other information such as the image quality (IQ), and (c) performing a subgrain identification and thenceforth converting the boundary energy in stored energy. All these of course indicate that a grain/deformed region mean-field simulation is to be done, similar to [17], which then calls for a nucleation criterion.

The subgrain method is analytically assessed for example considering the size and misorientation of the substructure, interior to material elements as suggested by Kim *et al.* [42]. Regarding the TF, owing to the plastic power dissipation per incremental strain, it is reasonable to expect that material elements describing crystal orientations of higher TF values accumulate higher stored energy. Despite the fact that the TF itself cannot consider the deformation history, it is well known that there is high correlation between stored energy material elements and TF. And although, there is no nucleation mechanism readily dictating that the substructure within high stored energy region recrystallizes, critical studies/reviews, e. g. by Kestens and Pirgazi [22], Nguyen Minh *et al.* [41], have made clear

that the correlation between TF and recrystallization is not circumstantial. This is why for example Choi and Cho [17] considered the TF of the crystal orientations measured by the EBSD, to qualitatively approximate the deformation energy of the material element. As for the IQ method, as suggested by Choi and Jin [43], this is also a useful way to derive information for the stored energy, namely by a qualitative conversion of each IQ value measured to stored energy. It is expected then, that approximating the stored energy at material elements considering not only the boundary-associated dislocations but also statistically stored dislocations, the heterogeneity in the growth rates and thereby recrystallization evolution would be more realistic and thus result in predictions that are more meaningful in the context of industrial processing analyses and exploitation.

REFERENCES

[1] W. B. Hutchinson, *Development and control of annealing textures in low-carbon steels,* International Metals Reviews **29**, 25 (1984).

[2] M. Hölscher, D. Raabe, and K. Lücke, *Rolling and recrystallization textures of bcc steels,* Steel Research **62**, 567 (1991).

[3] L. Kestens and J. J. Jonas, *Modeling texture change during the static recrystallization of interstitial free steels,* Metallurgical and Materials Transactions A **27**, 155 (1996).

[4] M. Quadir, Y. Tse, K. Lam, and B. Duggan, *Rolling and Recrystallization Texture of Cold Rolled IF Steel: A Study from Low to High Deformation,* Materials Science Forum **467-470**, 311 (2004).

[5] S.-H. Choi, F. Barlat, and J. Chung, *Modeling of textures and yield surfaces during recrystallization in IF steel sheets,* Scripta Materialia **45**, 1155 (2001).

[6] R. K. Ray, J. J. Jonas, and R. E. Hook, *Cold rolling and annealing textures i~ low carbon and extra low carbon steels,* International Materials Reviews **39**, 44 (1994).

[7] J. Galán-López and L. A. I. Kestens, *Optimization of Crystallographic Texture for Sheet-forming Applications Using Taylor-based Models,* Metallurgical and Materials Transactions A **49**, 5745 (2018).

[8] P. A. Beck, *The Formation of Recrystallization Nuclei,* Journal of Applied Physics **20**, 633 (1949).

[9] A. Cottrell, *Theory of dislocations,* Progress in Metal Physics **4**, 205 (1953).

[10] P. A. Beck, P. R. Sperry, and H. Hu, *The Orientation Dependence of the Rate of Grain Boundary Migration,* Journal of Applied Physics **21**, 420 (1950).

[11] R. Cahn, *Recrystallization of single crystals after plastic bending,* Journal of the Institute of Metals **76**, 121 (1949).

[12] R. Cahn, *Internal strains and recrystallization,* Progress in Metal Physics **2**, 151 (1950).

[13] R. W. Cahn, *A New Theory of Recrystallization Nuclei,* Proceedings of the Physical Society. Section A **63**, 323 (1950).

[14] F. J. Humphreys, *A unified theory of recovery, recrystallization and grain growth, based on the stability and growth of cellular microstructures—I. The basic model,* Acta Materialia **45**, 4231 (1997).

[15] E. Holm, M. Miodownik, and A. Rollett, *On abnormal subgrain growth and the origin of recrystallization nuclei,* Acta Materialia **51**, 2701 (2003).

[16] F. J. Humphreys, G. S. Rohrer, and A. D. Rollett, *Recrystallization and related annealing phenomena*, third edition ed. (Elsevier, Amsterdam Oxford Cambridge, MA, 2017).

[17] S.-H. Choi and J. H. Cho, *Primary recrystallization modelling for interstitial free steels,* Materials Science and Engineering: A **405**, 86 (2005).

[18] Y. Suwa, M. Tomita, Y. Tanaka, and K. Ushioda, *Phase-field Simulation of Recrystallization in Cold Rolling and Subsequent Annealing of Pure Iron Exploiting EBSD Data of Cold-rolled Sheet,* ISIJ International **61**, 350 (2021).

[19] H. Inagaki, *Fundamental Aspect of Texture Formation in Low Carbon Steel.* ISIJ International **34**, 313 (1994).

[20] R. Doherty, D. Hughes, F. Humphreys, J. Jonas, D. Jensen, M. Kassner, W. King, T. McNelley, H. McQueen, and A. Rollett, *Current issues in recrystallization: a review,* Materials Science and Engineering: A **238**, 219 (1997).

[21] K. Ushioda, *Advances in research on deformation and recrystallization for the development of high-functional steels,* Science and Technology of Advanced Materials **21**, 29 (2020).

[22] L. A. I. Kestens and H. Pirgazi, *Texture formation in metal alloys with cubic crystal structures,* Materials Science and Technology **32**, 1303 (2016).

[23] P. R. Rios, F. Siciliano Jr, H. R. Z. Sandim, R. L. Plaut, and A. F. Padilha, *Nucleation and growth during recrystallization,* Materials Research **8**, 225 (2005).

[24] D. Raabe, *Recovery and Recrystallization: Phenomena, Physics, Models, Simulation,* in *Physical Metallurgy* (Elsevier, 2014) pp. 2291–2397.

[25] G. Gottstein and L. S. Shvindlerman, *Grain boundary migration in metals: thermodynamics, kinetics, applications*, 2nd ed., CRC series in materials science and technology (Taylor & Francis, Boca Raton, 2010) oCLC: ocn166358378.

[26] B. Hutchinson, *Nucleation of recrystallisation,* Scripta Metallurgica et Materialia **27**, 1471 (1992).

[27] Y. Higa, K. Shimojima, and T. Makishi, *The effect of different step-size on the visualization of crystallographic defects using SEM/EBSD technique,* The International Journal of Multiphysics **9**, 37 (2015).

[28] D. Turnbull, *Theory of Grain Boundary Migration Rates,* JOM **3**, 661 (1951).

[29] W. T. Read and W. Shockley, *Dislocation Models of Crystal Grain Boundaries,* Physical Review **78**, 275 (1950).

[30] A. D. Rollett, G. Gottstein, L. S. Shvindlerman, and D. A. Molodov, *Grain boundary mobility – a brief review,* Zeitschrift für Metallkunde **95**, 226 (2004).

[31] M. Upmanyu, R. Smith, and D. Srolovitz, *Atomistic Simulation of Curvature Driven Grain Boundary Migration,* Interface Science **6**, 41 (1998).

[32] A. S. Nishikawa, *pyebsd: an open-source tool for processing EBSD data and determining accurate orientation relationship,* (2018), 10.13140/RG.2.2.28920.19203, https://github.com/arthursn/pyebsd.

[33] C. Hutchinson, H. Zurob, C. Sinclair, and Y. Brechet, *The comparative effectiveness of Nb solute and NbC precipitates at impeding grain-boundary motion in Nb steels,* Scripta Materialia **59**, 635 (2008).

[34] V. Shah, M. Krugla, S. E. Offerman, J. Sietsma, and D. N. Hanlon, *Effect of Silicon, Manganese and Heating Rate on the Ferrite Recrystallization Kinetics,* ISIJ International **60**, 1312 (2020).

[35] K. Sedighiani, V. Shah, K. Traka, M. Diehl, F. Roters, J. Sietsma, and D. Raabe, *Large-deformation crystal plasticity simulation of microstructure and microtexture evolution through adaptive remeshing,* International Journal of Plasticity **146**, 103078 (2021).

[36] D.-I. Kim, J. Kim, J. Kim, and S.-H. Choi, *A study on the annealing behavior of Cu-added bake-hardenable steel using an in situ EBSD technique,* Acta Materialia **68**, 9 (2014).

[37] F. Bachmann, R. Hielscher, and H. Schaeben, *Texture Analysis with MTEX – Free and Open Source Software Toolbox,* Solid State Phenomena **160**, 63 (2010).

[38] F. Bachmann, R. Hielscher, and H. Schaeben, *Grain detection from 2d and 3d EBSD data—Specification of the MTEX algorithm,* Ultramicroscopy **111**, 1720 (2011).

[39] S. Li, P. V. Houtte, and S. R. Kalidindi, *A quantitative evaluation of the deformation texture predictions for aluminium alloys from crystal plasticity finite element method,* Modelling and Simulation in Materials Science and Engineering **12**, 845 (2004).

[40] I. L. Dillamore, C. J. E. Smith, and T. W. Watson, *Oriented Nucleation in the Formation of Annealing Textures in Iron,* Metal Science Journal **1**, 49 (1967).

[41] T. Nguyen Minh, J. J. Sidor, R. H. Petrov, and L. Kestens, *Texture Evolution during Asymmetrical Warm Rolling and Subsequent Annealing of Electrical Steel,* Materials Science Forum **702-703**, 758 (2011).

[42] J. Kim, S. Kim, and S.-H. Choi, *Microstructure characterization based on the type of deformed grains in cold-rolled, Cu-added, bake-hardenable steel,* Materials Characterization **92**, 159 (2014).

[43] S.-H. Choi and Y.-S. Jin, *Evaluation of stored energy in cold-rolled steels from EBSD data,* Materials Science and Engineering: A **371**, 149 (2004).

6

3D COUPLED DEFORMATION AND RECRYSTALLIZATION SIMULATION: A PROMISING TECHNIQUE

The level of deformation and spatial resolution that can be reached when using a 3D crystal plasticity (CP) dislocation density-based model has been recently improved drastically [1, 9]. This enables a combined framework where with the deformation simulation as input, recrystallization can be modelled, as in the previous chapters, by using a (sub)grain growth algorithm, i. e. without requiring to artifically generate the substructure inside the deformed material elements, or having to assume/impose a nucleation criterion. For this reason, this chapter investigates and discusses the applicability of the coupled simulation framework based on the modelled microstructural outcome and evolution. The coupled simulations are conducted in 3D for an interstitial free (IF) steel bicrystal of 75% thickness reduction. Although only two deformed grains constitute the representative volume element (RVE), it is shown that during the simulation: (a) selective subgrain growth occurs (i. e. non-random competitive growth of only some subgrains) and (b) the microtexture changes during recrystallization. These highlight the importance of describing the in-grain evolution and orientation gradients during deformation/recrystallization. The aim of this work is to investigate the evolution and applicability of the present coupling framework in a highly plastically strained material for future investigations.

This chapter presents joint work with the Ph.D. thesis [1] by K. Sedighiani, Crystal Plasticity Simulation of Microstructure and Microtexture Evolution during Large Plastic Deformation, Ph.D. thesis, Delft University of Technology, Netherlands (2022).

6.1. INTRODUCTION

Coupling deformation simulations with a physics-based static recrystallization model gives the opportunity to investigate annealing phenomena (recovery, primary recrystallization, nucleation etc.) regarding their relation with the deformation structure. In particular, high-resolution deformation simulations can serve as input for simulating static recrystallization in a full-field approach [2–5].

The advantages of this technique compared to the use of a 2D orientation map obtained through electron backscatter diffraction (EBSD) are related to the enhanced accuracy, applicability and insight. The accuracy derives from the three dimensional description of the deformed microstucture. Since in recrystallization the subgrain heterogeneity (size and misorientation) is crucial for its onset and evolution (e. g. shown particularly in Chapter 4), this heterogeneity should be considered in 3D. The applicability is enhanced due to the ability of simulating the microstructure evolution without requiring experimental work (which is costly) to obtain the necessary input. The insights that can be obtained upon analyzing a coupled deformation-recrystallization simulation are widened compared to using an EBSD map, as the identification of the deformed material structure is straightforward. Each material element coming from a deformation simulation is quantified regarding its deformation energy, deformation history, etc. and therefore recrystallization can be directly linked to deformation state variables.

Given the recent advances in crystal plasticity (CP) full-field modeling on high level of deformation, while preserving a high resolution, introduced by Sedighiani [1] and Sedighiani *et al.* [9], we could reach a deformation structure description in 3D in a resolution not very far from the actual substructure. For this reason, and given the CA method for recrystallization, which as is shown in the previous chapters is applicable in modeling recrystallization in grid spacings close to the subgrain size, we investigated the microstructural evolution by coupling the two approaches. We treated the deformation simulation, like in the previous chapters, i. e. by considering the crystal orientation of each elementary volume as the only independent state variable. In other words, we assume that each material element is either a part of a subgrain/grain or a subgrain itself.

Similar ideas, namely modeling the selective subgrain growth using data from full-field CP have been implemented in the past, and presumably one of the most relevant works to the present chapter was done by Bate [7], already decades ago. After a crystal plasticity finite element method (CPFEM) simulation, Bate [7] applied the full-field subgrain/grain coarsening model developed by Humphreys [8], which operates based on the network method. The latter considers a map of grains/subgrains and applies the constitutive and kinematic rules on the so-called nodes (i. e. triple points). Therefore, as also in other deterministic full-field methods of subgrain/coarsening many material elements should constitute the subgrains. For this reason, Bate [7] generated the substructure such that the subgrains' size is inversely proportional to the von Mises stress, since otherwise every material element would be a vertex.

The coupled simulations are done for 77% thickness reduction interstitial-free (IF) steel. We use a simple bicrystal representative volume element (RVE) simulated by full-field crystal plasticity (CP), and in particular, by using a dislocation density-based approach [1, 6]. Although the RVE does not describe the microstructure equivalently to a polycrystal RVE,

in-grain orientation gradients are present and heterogeneous. Moreover, deformation features that are crucial for recrystallization, such as deformation bands, are described. Therefore, the goal of this work is to depict the intergranular evolution of deformation and recrystallization and investigate the applicability of the coupled computation framework for future studies. It should be clarified, that the work presented here, although fully developed and pertinent to the thesis, is rather elementary in terms of application, as only a deformed bicrystal is presented and discussed.

6.2. METHOD DESCRIPTION

6.2.1. DEFORMATION SIMULATION

The simulation package Düsseldorf Advanced Material Simulation Kit (DAMASK) [10] is used to conduct the crystal plasticity simulations. The system of governing Partial Differential Equations (PDEs) and boundary conditions is solved based on Fast Fourier Transform (FFT) spectral methods. [11, 12]. The following section provides a brief summary of the basic formulations, for more detail on the spectral solver implemented in DAMASK see [10–12].

MULTIPLICATIVE DECOMPOSITION

The kinematics for elasto-plastic behavior are defined within the finite deformation framework, where the deformation gradient tensor is expressed as:

$$\mathbf{F} = \mathbf{F}_e \mathbf{F}_p \tag{6.1}$$

where $\mathbf{F}_p$ is the plastic deformation gradient, and $\mathbf{F}_e$ is the elastic deformation gradient. The main reasoning for such decomposition is to distinguish between elastic deformation, a reversible deformation resulting from stretching of atomic bonds, and plastic deformation, an irreversible lattice-preserving deformation resulting from, for instance, dislocation slip. The decomposition order in Eq. (6.1) allows considering the anisotropy and dependency of a constitutive law on the crystallographic orientation.

FLOW KINEMATICS

The evolution of the plastic deformation gradients is calculated as:

$$\dot{\mathbf{F}}_p = \mathbf{L}_p \mathbf{F}_p, \tag{6.2}$$

where $\mathbf{L}_p$ is the velocity gradient. $\mathbf{L}_p$ is calculated from stress, here the second Piola-Kirchhoff stress $\mathbf{S}$, and it depends on the underlying microstructure through the plasticity constitutive law:

$$\mathbf{L}_p = f(\mathbf{S}, ...) \tag{6.3}$$

Assuming a Hookean elastic constitutive law, the second Piola-Kirchhoff stress is given as

$$\mathbf{S} = \mathbb{C} : \mathbf{E} \tag{6.4}$$

where $\mathbf{E}$ is the Green-Lagrange strain tensor:

$$\mathbf{E} = \frac{1}{2} \cdot \left(\mathbf{F}_e^T \mathbf{F}_e - I \right) \tag{6.5}$$

INELASTIC FLOW RELATIONS

The plastic deformation in crystalline materials occurs on well-defined slip systems specific to a crystallographic lattice. The plastic velocity gradient $\mathbf{L}_p$ is thus composed of the superposition of the individual resolved plastic shear rates on these systems α:

$$\mathbf{L}_p = \sum_{\alpha} \dot{\gamma}^{\alpha} \left(\mathbf{s}_s^{\alpha} \otimes \mathbf{n}_s^{\alpha} \right) \tag{6.6}$$

where $\mathbf{s}_s^{\alpha}$ and $\mathbf{n}_s^{\alpha}$ are respectively the unit vectors along the shear direction and shear plane normal.

CONSTITUTIVE MODEL

In the present work, the simulations are conducted using a dislocation density-based constitutive law as outlined in [1, 6]. The material parameters are chosen to be according to those identified for IF steel by Sedighiani [1], Sedighiani *et al.* [13].

REMESHING METHOD

In order to simulate the deformation evolution at high strain levels, namely 75% thickness reduction, the simulation was carried out with the use of the remeshing method described in [9]. The remeshing method (which is called mesh replacement method) is based on replacing the distorted mesh with a newly created undistorted mesh. According to this remeshing technique, a new (cuboid) geometry is first created, which matches the average outer dimensions of the deformed geometry considering the periodicity of the configuration. Then, the original mesh is replaced by a new mesh assigned to this new geometry. Finally, the simulation is restarted using the new configuration as a new simulation without any mesh distortion. This is physically equivalent to replacing the deformation gradient tensor with the identity tensor and the full relaxation of the elastic deformation. The selection of the resolution for the new mesh is following an adaptive scheme, which allows updating the resolution during the deformation at each remeshing step.

CRYSTAL PLASTICITY SIMULATION

The simulation is carried out using a 3D bicrystal configuration where one grain is a cylinder (with center matching the center of the cube RVE). This is illustrated in Fig. 6.1, where it is shown that the constant cross-section is perpendicular to the transverse direction (TD). The initial orientation of the cylindrical grain and the matrix are $(1\,1\,2)[1\,\bar{1}\,0]$ and $(1\,1\,1)[1\,\bar{2}\,1]$. The RVE is subjected to plane-strain compression up to a thickness reduction of 75%. The

initial number of elements at the beginning of the cold deformation is $60 \times 30 \times 60$. The number of elements is gradually increased to $777 \times 109 \times 60$ during the deformation using an adaptive mesh refinement method as described in [9].

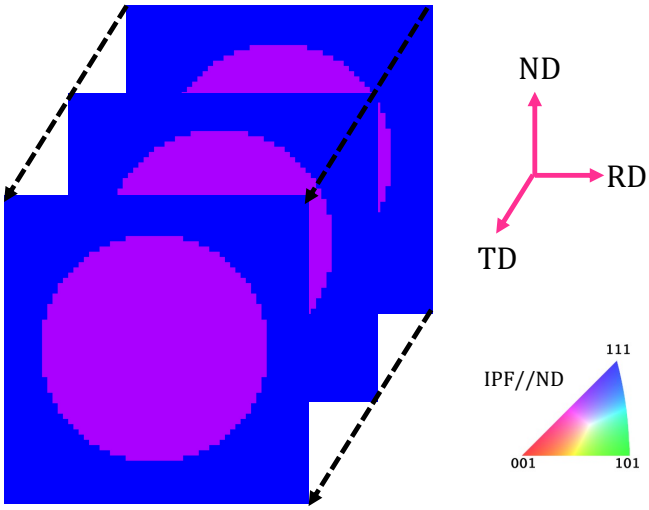

Figure 6.1: Input 3D RVE for the deformation simulation.

6.2.2. RECRYSTALLIZATION SIMULATION

INPUT SETTINGS

The recrystallization simulation is performed with the Cellular-Automaton (CA) model described in Chapter 2 using the 3D cubic grid Cub(2,2). This grid considers 26 neighbours per cell (neighbour cells that share either a face, an edge, or a corner). The input settings for this grid are presented and explained in detail in Chapter 2.

The simulated deformed grains are used as input where each CA cell is assigned the crystal orientation that corresponds to the material element provided from the deformation simulation. The grid spacing is set equal to 1 μm and the recrystallization simulation is carried out at the constant temperature of 800 °C. The computation time was 4 days - this is discussed in Section A.

6.3. RESULTS AND DISCUSSION

6.3.1. MICROSTRUCTURE EVOLUTION

The simulated temporal evolution of recrystallization is illustrated in Figs. 6.2 to 6.4, as it occurs in the middle cross-sections of the 3D RVE. As is shown, subgrain growth occurs in both deformed grains, yet within the blueish grain recrystallization is favored. The spatial inhomogeneity that characterizes recrystallization in the cold-deformed low alloyed steels [14–16] is also shown in the simulation's temporal evolution. The latter is due to the intergranular orientation gradients which are spatially heterogeneous at the simulated deformed state.

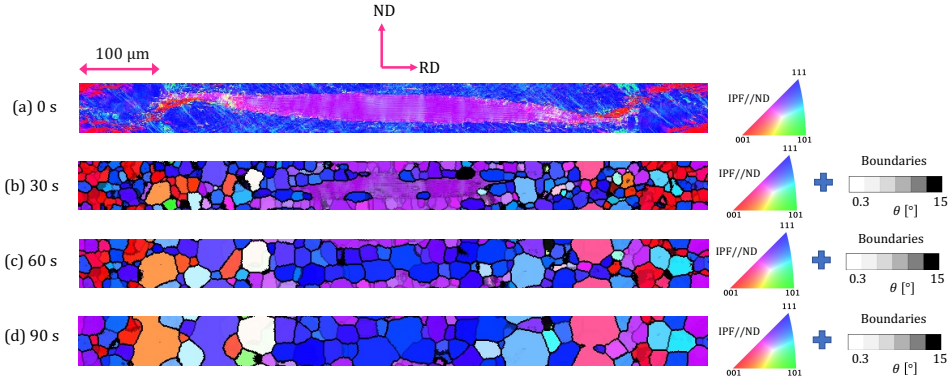

Figure 6.2: Temporal evolution of simulation at 800 °C shown in the middle cross-section along the transverse direction (TD) at (a) 0 s (b) 30 s (c) 60 s (d) 90 s.

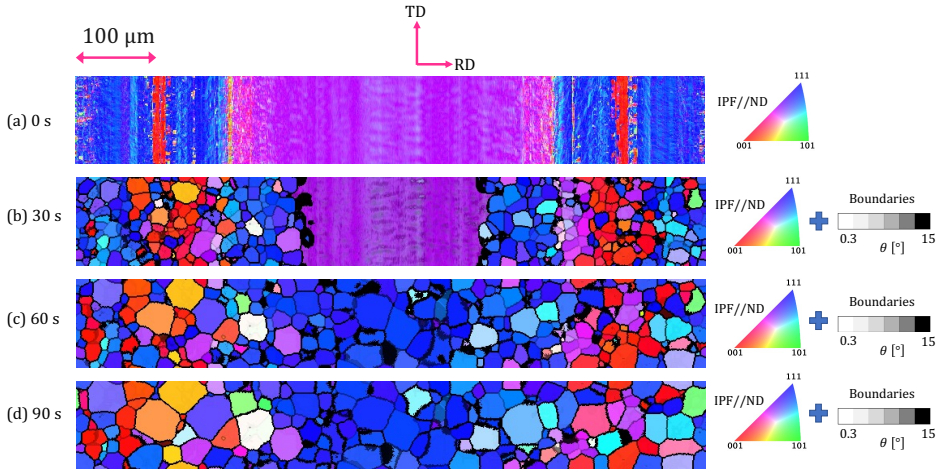

Figure 6.3: Temporal evolution of simulation at 800 °C shown in the middle cross-section along the normal direction (ND) at (a) 0 s (b) 30 s (c) 60 s (d) 90 s.

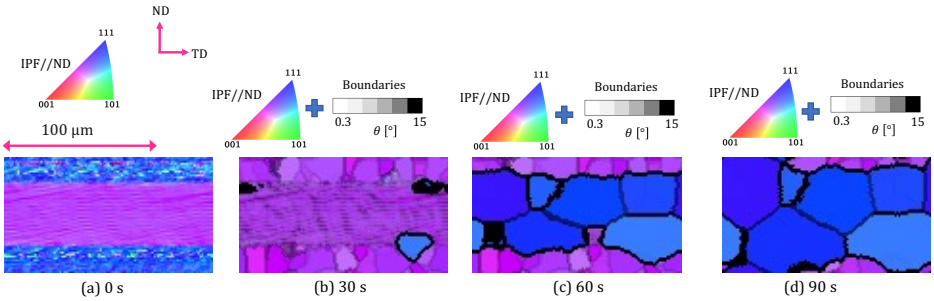

Figure 6.4: Temporal evolution of simulation at 800 °C shown in the middle cross-section along the rolling direction (RD) at (a) 0 s (b) 30 s (c) 60 s (d) 90 s.

6.3.2. TEXTURE COMPONENTS

Fig. 6.5 shows the $\phi_2 = 45°$ section of the orientation distribution function (ODF) that is quantified for the simulated deformed and recrystallized state. Although the RVE contains only two grains, the microtexture changes during recrystallization. In particular the texture component $\{1\,1\,2\}\langle 1\,1\,0\rangle$ that comprises the maximum at the deformed state gradually decreases and eventually at the recrystallized state the maximum is found in orientation components within the $\langle 1\,1\,1\rangle \parallel$ ND fiber.

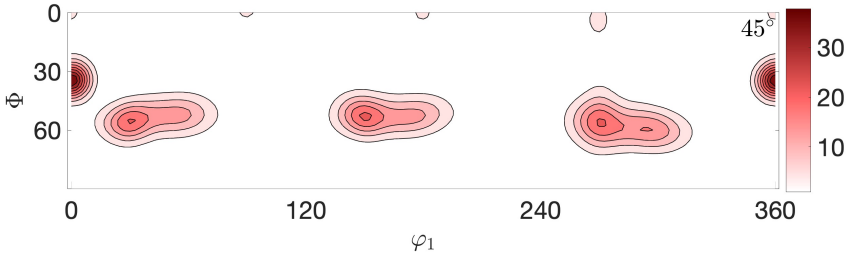

(a) 0 s : ODF $\varphi_2 = 45°$

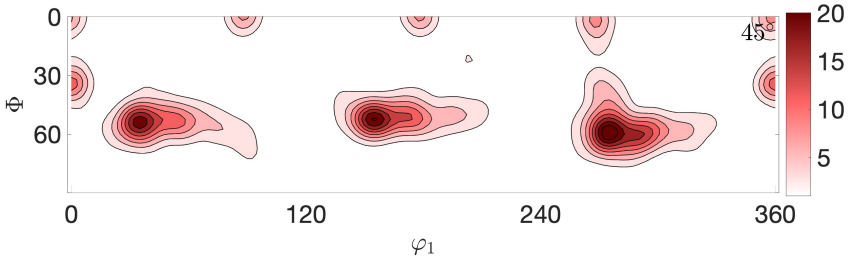

(b) 90 s : ODF $\varphi_2 = 45°$

Figure 6.5: ODF quantified and plotted in section $\phi_2 = 45°$ for (a) the simulated deformed state (b) the simulated recrystallized state i. e. 90 s at 800 °C.

6.3.3. RECRYSTALLIZATION KINETICS

This section reviews the evolution of recrystallization in the principal cross-sections of the rolling reference system and in 3D. Fig. 6.6 shows the recrystallized volume fraction evaluated at each middle cross-section. As is shown, the ND-RD cross-section undergoes the most rapid recrystallization, then RD-TD and at last TD-ND. This can be explained in various ways:

- Longitudinal sections (i. e. ND-RD) incorporate orientation gradients from the localized deformation features such as shear bands. As these regions facilitate recrystallization initiation and growth (see e. g. Chapter 4), the kinetics occur faster in ND-RD.
- The transverse (TD-ND) middle cross-section in the present simulation seems to initially recrystallize by the growth of the low-deformation energy grain (see Fig. 6.4b). However, as this type of recrystallization is more sluggish (also discussed in Chapter 4), the recrystallized volume arranges such that there are still LAGBs within it (see Fig. 6.4b). Once a recrystallized grain that is actually competitive meets these regions it consumes them, as it happens also here - Fig. 6.4b-Fig. 6.4d.

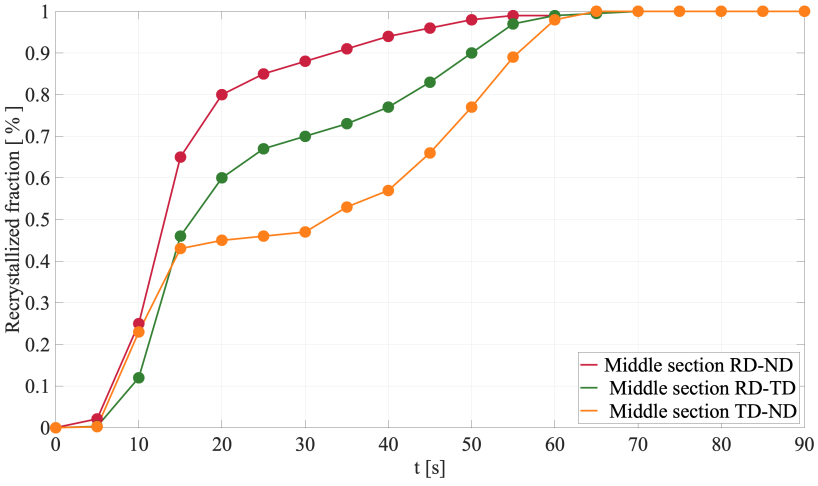

Figure 6.6: Recrystallization kinetics during the isothermal annealing simulation at 800 °C: the quantifications correspond to the middle cross-sections of the principal rolling sheet axes.

Fig. 6.7 shows the recrystallization kinetics corresponding to the whole RVE. As it is evident, the highest recrystallization rate is found within $10-15$ s of heating.

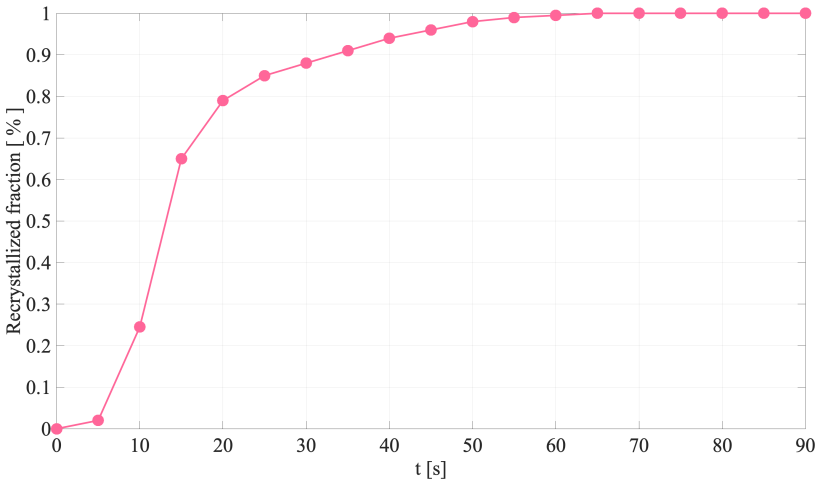

Figure 6.7: Recrystallization kinetics during the isothermal annealing simulation at 800 °C: the quantifications correspond to the whole 3D RVE.

6.3.4. EVALUATION AND APPLICABILITY

Altogether, the example presented for the coupled simulations of deformation-recrystallization in 3D, confirms two important phenomena which are in line with previous studies or recrystallization in IF steel sheets [14–21]:

- Recrystallization occurs heterogeneously such that some regions recrystallize fast, while others resist and get consumed later by large recrystallized grains.

- Recrystallization results in changing the distribution of crystal orientations and particularly components within the $\langle 1\,1\,1\rangle \parallel$ ND fiber intensify at the expense of deformation texture components such as $\{1\,1\,2\}\langle 1\,1\,0\rangle$.

Therefore, the present approach is applicable for highly plastically strained steel recrystallization. The main disadvantage of this technique is the computation time required for the simulations - namely 5 days for the deformation and 4 days for the recrystallization simulation (explained in detail in Appendix A).

Despite the computational cost, the coupled simulations are still feasible. Considering also the fact that recrystallization nucleation is not imposed in this modeling framework, such simulations are particularly useful for providing straightforward relationships between deformation and recrystallization.

6.4. CONCLUSION

6.4.1. OVERVIEW OF DISCUSSED ITEMS

We have presented a coupled computation framework for deformation and recrystallization that allows the in-grain description of their evolution. It is shown that even a bicrystal RVE can confirm the heterogeneity that characterizes the two phenomena. The deformed bicrystal consists of a γ-fiber grain with large orientation spread and a deformed grain with coarser subgrains, mostly near the $(1\,1\,2)[1\,\bar{1}\,0]$ component. Recrystallization nucleation occurs naturally during the simulation and alters the microtexture such that the γ-fiber texture components intensify. This highlights the importance of using full-field deformation models that describe the intergranular orientation spread and microtexture evolution, when serving as inputs for recrystallization simulations. Additionally, it indicates that the suggested coupled computation framework is promising for further investigations regarding the substructure evolution in deformation and the onset of recrystallization.

6.4.2. GENERAL UNDERSTANDING AND ADVANCES

In this chapter, we made use of two approaches, that are both developed for (and tailored to) overcoming challenges when simulating and providing information about phenomena at the level of subgrains in highly deformed IF steel, when dealing with the mesoscale. The work of Sedighiani [1] and Sedighiani *et al.* [9] allows us to simulate deformation in 3D on a high level of deformation while preserving a high resolution and realistic in-grain descriptions. In view of the present thesis, that follows an approach where recrystallization nucleation is not imposed while dealing with highly deformed structures and grid spacings close to the actual substructure's size, it is clear that coupling the two techniques is not only pertinent, but it is also necessary (a) if we want to understand recrystallization in terms of selective subgrain growth, especially since the 3D description is a necessary step to take after a certain point, and (b) if we want to obtain a clearer picture on the relevance between the (readily distinguishable) deformation features and states, and the onset of recrystallization. This is why here we discussed the applicability of coupling the two approaches. Although some analyses was discussed based on the performed simulations, the key message of the present chapter is not based on discussing the simulations' outcome as a means to our present understanding of recrystallization-related phenomena. Instead, the chapter is meant to point toward a research direction, based on recent advances, which is promising to achieve indeed a better understanding of recrystallization nucleation.

REFERENCES

[1] K. Sedighiani, *Crystal Plasticity Simulation of Microstructure and Microtexture Evolution during Large Plastic Deformation*, Ph.D. thesis, Delft University of Technology, Netherlands (2022).

[2] D. Raabe and R. C. Becker, *Coupling of a crystal plasticity finite-element model with a probabilistic cellular automaton for simulating primary static recrystallization in aluminium,* Modelling and Simulation in Materials Science and Engineering **8**, 445 (2000).

[3] T. Takaki and Y. Tomita, *Static recrystallization simulations starting from predicted deformation microstructure by coupling multi-phase-field method and finite element method based on crystal plasticity,* International Journal of Mechanical Sciences **52**, 320 (2010).

[4] F. Han, B. Tang, H. Kou, L. Cheng, J. Li, and Y. Feng, *Static recrystallization simulations by coupling cellular automata and crystal plasticity finite element method using a physically based model for nucleation,* Journal of Materials Science **49**, 3253 (2014).

[5] D.-K. Kim, W. Woo, W.-W. Park, Y.-T. Im, and A. Rollett, *Mesoscopic coupled modeling of texture formation during recrystallization considering stored energy decomposition,* Computational Materials Science **129**, 55 (2017).

[6] A. Ma and F. Roters, *A constitutive model for fcc single crystals based on dislocation densities and its application to uniaxial compression of aluminium single crystals,* Acta Materialia **52**, 3603 (2004).

[7] P. Bate, *Modelling deformation microstructure with the crystal plasticity finite–element method,* Philosophical Transactions of the Royal Society of London. Series A: Mathematical, Physical and Engineering Sciences **357**, 1589 (1999).

[8] J. F. Humphreys, *A Microstructural Model of Recrystallization,* Materials Science Forum **113-115**, 329 (1993).

[9] K. Sedighiani, V. Shah, K. Traka, M. Diehl, F. Roters, J. Sietsma, and D. Raabe, *Large-deformation crystal plasticity simulation of microstructure and microtexture evolution through adaptive remeshing,* International Journal of Plasticity **146**, 103078 (2021).

[10] F. Roters, M. Diehl, P. Shanthraj, P. Eisenlohr, C. Reuber, S. Wong, T. Maiti, A. Ebrahimi, T. Hochrainer, H.-O. Fabritius, S. Nikolov, M. Friák, N. Fujita, N. Grilli, K. Janssens, N. Jia, P. Kok, D. Ma, F. Meier, E. Werner, M. Stricker, D. Weygand, and D. Raabe, *DAMASK – The Düsseldorf Advanced Material Simulation Kit for modeling multi-physics crystal plasticity, thermal, and damage phenomena from the single crystal up to the component scale,* Computational Materials Science **158**, 420 (2019).

[11] P. Eisenlohr, M. Diehl, R. Lebensohn, and F. Roters, *A spectral method solution to crystal elasto-viscoplasticity at finite strains,* International Journal of Plasticity **46**, 37 (2013).

[12] P. Shanthraj, P. Eisenlohr, M. Diehl, and F. Roters, *Numerically robust spectral methods for crystal plasticity simulations of heterogeneous materials,* International Journal of Plasticity **66**, 31 (2015).

[13] K. Sedighiani, M. Diehl, K. Traka, F. Roters, J. Sietsma, and D. Raabe, *An efficient and robust approach to determine material parameters of crystal plasticity constitutive laws from macro-scale stress–strain curves,* International Journal of Plasticity **134**, 102779 (2020).

[14] J.-H. Kim, D.-I. Kim, J. S. Kim, S.-H. Choi, K.-W. Yi, and K. H. Oh, *Technical Investigation into the In-situ Electron Backscatter Diffraction Analysis for the Recrystallization Study on Extra Low Carbon Steels,* Applied Microscopy **43**, 88 (2013).

[15] M. Diehl, L. Kertsch, K. Traka, D. Helm, and D. Raabe, *Site-specific quasi in situ investigation of primary static recrystallization in a low carbon steel,* Materials Science and Engineering: A **755**, 295 (2019).

[16] A. Ayad, M. Ramoul, A. Rollett, and F. Wagner, *Quantifying primary recrystallization from EBSD maps of partially recrystallized states of an IF steel,* Materials Characterization **171**, 110773 (2021).

[17] W. B. Hutchinson, *Development and control of annealing textures in low-carbon steels,* International Metals Reviews **29**, 25 (1984).

[18] L. A. I. Kestens and H. Pirgazi, *Texture formation in metal alloys with cubic crystal structures,* Materials Science and Technology **32**, 1303 (2016).

[19] D. Raabe, *Recovery and Recrystallization: Phenomena, Physics, Models, Simulation,* in *Physical Metallurgy* (Elsevier, 2014) pp. 2291–2397.

[20] M. Hölscher, D. Raabe, and K. Lücke, *Rolling and recrystallization textures of bcc steels,* Steel Research **62**, 567 (1991).

[21] J. Galán-López and L. A. I. Kestens, *Optimization of Crystallographic Texture for Sheet-forming Applications Using Taylor-based Models,* Metallurgical and Materials Transactions A **49**, 5745 (2018).

7

CONCLUSION

7.1. PRESENT WORK

7.1.1. SUMMARY

In the present thesis, recrystallization and related phenomena were investigated in interstitial free (IF) and low carbon (LC) steel microstructures. The studies were conducted with close coupling between the deformation substructure and the onset and evolution of recrystallization.

With a site-specific experimental investigation of isothermal annealing at 600 °C recrystallization was observed in a LC steel of 65% thickness reduction. It was shown that recrystallization initiates and rapidly evolves in deformed grains characterized by high interior orientation gradients. While these deformed grains recrystallize fast (in less than 20 s), grains with lower interior orientation gradients remain intact or recover. Only after additional heating time grains with low stored energy are consumed by recrystallized volumes, while some deformed material (3-14%) remains even after 400 s of annealing. Highlighting the spatial heterogeneity that characterizes recrystallization in the investigated material, its orientation dependency was studied. Orientation components belonging to the $\langle 1\,1\,0 \rangle \parallel$ normal direction (ND) fiber (known as ζ-fiber) were found mostly relevant to the material's recrystallization.

The next studies focused on simulating the evolution of recrystallization with a full-field physical description that includes the nucleation stage. This is because by not assuming, but simulating nucleation, many important and unresolved phenomena can be investigated regarding the subgrains that become nuclei - see e. g. [1–5]. A computational framework that enables the concurrent description of the various stages of recrystallization annealing is developed based on the deterministic cellular automaton (CA) method. The algorithm describes subgrain growth (nucleation), primary and secondary recrystallization, and grain growth based on the same physical description, i. e. the atomic short-range self-diffusion driven by the reduction of (sub)boundary energy. Avoiding a differentiation

between the above-mentioned recrystallization-related phenomena is necessary, since (as discussed above) recrystallization does not occur homogeneously, i. e. at the time a region in the sheet recrystallizes, other regions nearby might be recovering or even be fully recrystallized (undergoing grain growth or secondary recrystallization). Hence, nucleation is not imposed in this approach but it naturally occurs throughout the evolving substructure. When the microstructure is characterized by heterogeneously distributed dislocation content, recrystallization occurs, just as explained by Humphreys *et al.* [6]. Dislocations act as elementary units of inelastic deformation and therefore they carry the stored energy that relates to the driving force. At the same time dislocations are elementary units of crystallographic misorientation and hence comprise boundaries whereby subgrains grow [7]. Altogether, the dislocation content determines the mobility and driving force for boundary migration, and hence if heterogeneously distributed, recrystallization nucleation and growth occur. The latter continue until the dislocation content is homogeneously distributed (i. e. comprising HAGBs surrounding equiaxed grains) and grain growth takes place.

As can be deduced from the above, the approach implemented here operates only based on the local misorientations, i. e. on the difference between the energy of the boundaries surrounding each elementary volume before and after its re-orientation. The reasons for not implementing the algorithm based on current deterministic methods, e. g. curvature-based, are associated with the fact that we operate in grid spacings very close to the actual subgrain size. In other words, instead of exploiting mesoscopic descriptions of the stored energy in order to artificially generate the substructure with equiaxed and uniform (in size) subgrains in the deformed grain, as was done by Han *et al.* [2] or converting the pixels as parts of subgrains after assuming that subgrain formation and growth takes place, as was done by Suwa *et al.* [4] and Bate [5], when using the existing deterministic methods, here the main assumption is different. In particular, we assume that the deformation input corresponds to the actual substructure without requiring static subgrain formation, such that we can investigate whether recrystallization-related phenomena are associated with discontinuous subgrain growth and high-angle boundaries' bulging. Therefore, we operate the algorithm on a grid spacing very close to the actual subgrain size, which is not possible with the existing deterministic methods. Hence, the approach taken here calculates the driving force based on the energy difference prior to and after the re-orientation of a cell, thus allowing us to use the unmodified deformation input as starting microstructure, under the assumption that each CA cell is either a part of a subgrain or a subgrain itself.

After implementing the above-described approach in a deterministic full-field computational framework, the algorithm was extensively tested regarding grid artifacts, mesh size dependency and kinetic outcome. Simple grain structures (bicrystal, tricrystal and polycrystal) were used for this purpose. The algorithm was then applied to deformation substructures where recrystallization takes place.

Since recrystallization is simulated without imposing a nucleation criterion a subgrain will nucleate when it has a kinetic and energy advantage compared to the surrounding substructure. In other words a subgrain that together with its recrystallized volume is always mobile (kinetic advantage) and of smaller boundary energy surrounding it or just larger (energy advantage) than its changing neighborhood becomes a recrystallized grain. In the present work, the following issues were investigated:

- The contribution of the substructure's topology to recrystallization initiation. This

study was performed by a one-to-one comparison of the state variables (crystal orientation, recrystallized/non-recrystallized regime) from the deformation substructure and the simulated temporal evolution of recrystallization. It was shown that deformation band nucleation occurs by relatively larger abutting subgrains (separated by HAGBs) invading narrow bands. Although this mechanism occurs in many deformed regions, most of the recrystallized volume stops expanding after surpassing the band. A further investigation showed that this is mainly due to the kinetic instability which is no longer satisfied. This is where the intersection of deformation bands plays an important role. It was shown that in such configurations, the material recrystallizes faster compared to regions of deformation bands arranged in one direction. As for recrystallization initiation at grain boundaries, this was shown to take place, yet occurring slower than the in-grain recrystallization. As grain boundaries are always kinetically unstable, the delayed recrystallization that takes place through them, was attributed to the fact that subgrains next to them do not have an energy/size advantage from the surrounding substructure within the adjacent grain.

- The extent of recovery (discontinuous subgrain growth) that precedes recrystallization initiation and its relationship with the ⟨1 1 1⟩ ∥ ND fiber texture formation. The study employed more input RVEs in order to assess the effects of the resolution in the performed quantifications. Again, a one-to-one comparison of the state variables through the simulated temporal evolution was used. It was shown that although in the substructure numerous subgrains grow, the ones that recrystallize in most cases initiate growing directly via HAGBs. Therefore, the kinetic and energy advantage of the subgrains that nucleate pre-exists in the as-deformed state and hence it is not attained by static recovery. Relating this to the recrystallization texture formation, it was shown that the ⟨1 1 1⟩ ∥ ND fiber texture does not form when recrystallization initiates. The crystallographic texture of the subgrains that start growing via a HAGB is in fact similar to the deformation texture, i. e. combined ⟨1 1 0⟩ ∥ rolling direction (RD) and ⟨1 1 1⟩ ∥ ND texture. It is during their subsequent expansion that the ⟨1 1 0⟩ ∥ RD fiber texture decreases. Altogether, it was shown that HAGB bulging is the dominant nucleation mechanism, and it takes place mostly at deformation bands.

7.1.2. APPLICABILITY OF THE MODELING APPROACH

The applicability of the present model is wide, especially because (a) it does not differentiate between normal and abnormal (discontinuous) phenomena, which typically concur upon recrystallization annealing, and (b) because it does not impose a nucleation criterion, which already narrows down significantly the applicable range of materials/deformation levels and parameters. In practice, recrystallization in any material that forms subgrain structures upon its deformation[1] can be simulated with this approach.

The disadvantage of this approach is that it is computationally heavier (see Appendix A for details) than the classical CA recrystallization method. The simulations conducted in the present thesis varied from a few minutes (normal grain growth) to 2-70 hours for recrystallization (depending on the RVE used). This is because of two reasons: (a) all CA cells are

[1] For example high stacking fault energy (SFE) metals and sheets deformed in high temperatures.

iterated at every time step and not only a subset and (b) in deformed materials it is advisable to use continuous orientation space instead of discrete, i. e. to assign the crystal orientation of each cell as it is measured. This means that the misorientations are not stored in the computer but need to be calculated for every pair of cells at every time step. The reasons for this are explained in detail in Appendix A. Despite the computational cost, the present approach is still applicable in a variety of materials with still large datasets for describing the microstructure.

7.1.3. UNDERSTANDINGS BASED ON ALL CHAPTERS

As explained in the individual chapters, besides the items addressed specifically based on their respective objectives, there are some more general understandings. The most important one is presumably the fact that upon modeling competitive growth of volumes in a rather very "pure" manner we observe the so-called growth instability (i. e. recrystallization). Out of the numerous reasons for which a pre-existing subgrain obtains a kinetic and an energy advantage, we simulated the competition of initially millions of material elements, due to only one state variable: their crystal orientation and therefore their misorientation with their neighborhood. Based on this, without considering the static subgrain formation that is a well-known phenomenon giving lead to particular subgrains becoming recrystallization nuclei, the simulations showed that not only preferential growth occurs (even in 2D) but also that we have a pertinent crystallographic texture change. As explained in Chapter 1 - see Table 1.1, despite the solid physical foundations of the subgrain formation and growth theory, there are so many dislocation cells and subgrains, and so many mechanisms that can result in giving advantages in certain material volumes to recrystallize, that it is impossible to derive conclusions in terms of selective subgrain growth and orientation selection. Among others, Humphreys *et al.* [6] and Hutchinson [8] have discussed and suggested the important role of local misorientations in the context of an energy advantage in addition to the well-known kinetic advantage. However, this has never been confirmed, to be sufficient insofar as it can explain some of the recrystallization-related phenomena. We show that allowing more than 5,000,000 material elements to grow and compete based on the well-known fundamentals, both the growth instability and the orientation selection can be explained, at least up to a certain extent.

The second important point is the participation of recovery in view of a high stored-energy nucleation mechanism. As we show in Chapter 5 and given that none of the static recovery mechanisms are considered besides discontinuous subgrain growth, the well-known γ-fiber texture is a result of the energy advantage of particular subgrains. Nevertheless, it has been for long recognized that a primary reason for high stored-energy regions to nucleate is associated with other recovery mechanisms, with the most basic and kinetically favored[2], the heterogeneous static subgrain formation (i. e. polygonization). Although especially the latter mechanism is indeed expected to occur and mostly heterogeneously (thus indeed giving lead to some regions), we show that already without any recovery mechanism, a γ-fiber texture is favored in the present material. Considering the combined findings from

[2] Subgrain formation during the early stages of annealing is already favored in comparison to other nucleation mechanisms due to it requiring the motion of individual dislocations and it is thus faster than discontinuous subgrain growth that requires arrays of dislocations to move cooperatively.

Chapter 4 and Chapter 5, it is suggested that: initially recrystallized volumes start wherever possible (i. e. next to almost any high angle boundary). Then the lack of energy advantage at regions of low deformation energy (e. g. next to most grain boundaries) obstructs the expanded volume (i. e. the subgrains it meets are coarser or of low energy at their boundaries). The remaining subset of the volume that continuous its expansion corresponds to other regions, mostly intergranular, where at least some subgrains indeed have an energy advantage and preserve their kinetic instability. This subset is the one that should consititute the recrystallization texture. Similar suggestions, although in a different context, were made by Hutchinson [8] and Dillamore *et al.* [9]. More specifically, Hutchinson [8] suggested that probably subgrains make use of pre-existing high-angle boundaries instead of undergoing discontinuous subgrain growth. On the other hand, Dillamore *et al.* [9] observed that indeed grain boundaries are initially migrating, but then intergranular recrystallized volumes are more competitive, although we cannot know how the latter nucleated. The present thesis has shown that these ideas are not only valid, but actually all these phenomena occur under a topological competition that is responsible for the forthcoming orientation selection.

7.2. FUTURE WORK

7.2.1. CONCURRENT NUCLEATION MECHANISMS

In the present work nucleation is naturally simulated by the mechanisms known as discontinuous subgrain growth and HAGB recrystallization initiation/bulging. In particular, for the simulations performed in this thesis, the kinetic advantage concerns subgrains bounded by HAGBs that expand in recrystallized volumes while preserving high misorientation from their changing neighborhood. The energy advantage concerns subgrains that are larger from their abutting substructure and continue being larger (together with their recrystallized volume) than their changing surroundings. As was explained in Chapter 1, there are more mechanisms that can result in providing an advantage to some subgrains such as:

- subgrain coalesence (kinetic & energy advantage).
- heterogeneous static subgrain formation (kinetic & energy advantage).
- variations of particle pinning (Zener drag force) at certain HAGBs (energy advantage).
- mobility variations at HAGB related to the dislocation character (kinetic advantage - in this case not all HAGBs but only some are actually kinetically unstable).

Now that the effects of discontinuous subgrain growth and HAGB recrystallization initiation have been established and differentiated, incorporating any of the abovementioned mechanisms with an appropriate physical description would give insight into its contribution to the onset of recrystallization.

7.2.2. MATERIALS OF DIFFERENT RECRYSTALLIZATION TEXTURES

As discussed in Chapter 5, the fact that static recovery is found to be only minorly responsible for the high stored-energy crystallographic texture formation upon recrystallization of

the IF steel investigated here, this opens up a subject area raised by Kestens and Pirgazi [10]. In particular, whether or not recovery is the reason for the γ-fiber texture formation in highly strained IF steel, and thereby also the reason for the apparent differences in comparison to low-strained and/or high-temperature deformed materials. It is easy to understand that the particular CA approach is applicable to model recrystallization when the expected outcome dictates a low stored-energy texture, since the energy advantage favors the less deformed regions to recrystallize - in comparison to their surroundings. However, it is still somewhat surprising that even without considering any static recovery mechanism beyond discontinuous subgrain growth, which is found to be quite insignificant, the simulations favor the intensification of high stored-energy texture components. Therefore, a presumably insightful research direction with regard to the texture controversy discussed by Kestens and Pirgazi [10] concerns the application of the present method in other deformed structures in IF steel, i. e. of low strain levels or of high deformation temperatures.

7.2.3. COUPLING DEFORMATION-RECRYSTALLIZATION

Applications similar to the coupled deformation and recrystallization simulations presented in Chapter 6, could be done using RVEs that describe more grains. Besides the three-dimensional description, this is advantageous for the subsequent analysis. For example the investigation presented in Chapter 4 regarding the onset of recrystallization at deformation bands was limited to the microstructure characterization of the deformed material. After the crystal plasticity full-field simulation, each material element has many state variables that can be used for a quantitative identification of the deformation substructure such as the slip activity etc. A close coupling of these with the subsequent recrystallization can give insight into stricter relationships between deformation and recrystallization.

7.2.4. PATTERN IDENTIFICATION ANALYSIS

The one-to-one comparison of the material state during the simulated temporal evolution of recrystallization was used to relate the deformation features (Chapter 4) and quantify the mechanisms (Chapter 5) that lead to the nucleation of subgrains. This resulted in topological characterizations (e. g. deformation bands) and distributions of values (e. g. misorientation at deformed state) for features that differentiate a subgrain that nucleates from others that do not. This type of analysis shows whether the nuclei exhibit a certain characteristic. Although the results already indicate that certain patterns are followed, it does not give insight on how necessary or sufficient each characteristic is for a subgrain's nucleation. Such insights would be particularly useful for example to be used in mean-field statistical approaches or for polycrystal full-field simulations using statistical distributions for characterizing the substructure (grain mean-field). In order to provide information for the potential of a subgrain to recrystallize, given only the as-deformed state, the simulations performed here should be analyzed considering not only the state variables during the temporal evolution (as was done here), but also their interaction.

More specifically, as extensively discussed in the present thesis, the possibility of a subgrain to recrystallize depends on its kinetic and energy advantage. However, these are non-quantifiable at the as-deformed state, because a subgrain's advantage involves the compari-

son with its surroundings. The latter are neither up to a constant distance nor are constant themselves - i. e. they also undergo competitive subgrain growth. For example, the surroundings of a subgrain that actually affect its potential to recrystallize can be within a distance of 0.1 μm or even a few micrometers. Hence, in order to quantify a subgrain's potential to recrystallize, it is necessary, but not sufficient, to consider only its misorientation from its immediate neighborhood. Rather, the features that differentiate subgrains that recrystallize from others that do not, need to be considered together and as interacting. Then, presumably, it may be feasible to deduce relationships regarding which subgrains will recrystallize, given the as-deformed state.

Such analyses can be done with the use of advanced statistical tools. Some machine learning methods [11] - e. g. clustering and other unsupervised[3] methods, identify patterns between large groups of features/phenomena, which is particularly useful when many features affect one another - as are also the effects of topological aspects in recrystallization. Eventually, the output is not a quantification of a predefined relationship but groups of values (each for a different feature) that are likely to be found together.

Moreover, using such analysis techniques in the coupled deformation/recrystallization simulation, the characteristics that can be investigated increase significantly. For example, recrystallization nucleation can be linked with:

- the lattice rotations, dislocation density evolution in the region where the subgrain was located, in comparison to the substructure comprising other regions,
- in general, values of state variables through the deformation history,
- particular deformation bands, e. g. by quantifications regarding the slip systems activated resulting in deformation bands, and by differentiating between others that do not act as successful nucleation sites.

The abovementioned aspects are only some indications regarding the identification of deformation/recrystallization patterns, and are only addressing the nucleation stage. Many other investigations are enabled in the suggested technique and also for other relevant annealing phenomena, e. g. recovery, recrystallization growth.

[3] Unsupervised are the techniques where there is no predefined relationship/classification investigated. In these, the algorithm aims to group values of (numerous) features that are likely to be found as such in the same statistical observation, i. e. here material element.

REFERENCES

[1] E. Holm, M. Miodownik, and A. Rollett, *On abnormal subgrain growth and the origin of recrystallization nuclei,* Acta Materialia **51**, 2701 (2003).

[2] F. Han, B. Tang, H. Kou, J. Li, and Y. Feng, *Effects of subgrain size and static recrystallization on the mechanical performance of polycrystalline material: A microstructure-based crystal plasticity finite element analysis,* Progress in Natural Science: Materials International **25**, 58 (2015).

[3] K. Traka, K. Sedighiani, C. Bos, J. Galan Lopez, K. Angenendt, D. Raabe, and J. Sietsma, *Topological aspects responsible for recrystallization evolution in an IF-steel sheet – Investigation with cellular-automaton simulations,* Computational Materials Science **198**, 110643 (2021).

[4] Y. Suwa, M. Tomita, Y. Tanaka, and K. Ushioda, *Phase-field Simulation of Recrystallization in Cold Rolling and Subsequent Annealing of Pure Iron Exploiting EBSD Data of Cold-rolled Sheet,* ISIJ International **61**, 350 (2021).

[5] P. Bate, *Modelling deformation microstructure with the crystal plasticity finite–element method,* Philosophical Transactions of the Royal Society of London. Series A: Mathematical, Physical and Engineering Sciences **357**, 1589 (1999).

[6] F. J. Humphreys, G. S. Rohrer, and A. D. Rollett, *Recrystallization and related annealing phenomena*, third edition ed. (Elsevier, Amsterdam Oxford Cambridge, MA, 2017).

[7] G. Gottstein and L. S. Shvindlerman, *Grain boundary migration in metals: thermodynamics, kinetics, applications*, 2nd ed., CRC series in materials science and technology (Taylor & Francis, Boca Raton, 2010) oCLC: ocn166358378.

[8] B. Hutchinson, *Nucleation of recrystallisation,* Scripta Metallurgica et Materialia **27**, 1471 (1992).

[9] I. L. Dillamore, C. J. E. Smith, and T. W. Watson, *Oriented Nucleation in the Formation of Annealing Textures in Iron,* Metal Science Journal **1**, 49 (1967).

[10] L. A. I. Kestens and H. Pirgazi, *Texture formation in metal alloys with cubic crystal structures,* Materials Science and Technology **32**, 1303 (2016).

[11] J. Schmidt, M. R. G. Marques, S. Botti, and M. A. L. Marques, *Recent advances and applications of machine learning in solid-state materials science,* npj Computational Materials **5**, 83 (2019).

ACKNOWLEDGEMENTS

Firstly, I would like to express my gratitude to my promotor Prof. Jilt Sietsma, my promotor Prof. Dierk Raabe, and my copromotor Dr. Cornelis Bos. I thank them for their scientific contribution to my Ph.D., for helping me develop research and academic skills, for being great supervisors, and because I will never forget them. And more specifically:

I thank Prof. Jilt Sietsma for helping me grow into a researcher, for the patience he had when explaining to me scientific aspects, for helping me develop my critical thinking when addressing scientific matters, and because I remember leaving his office always full of energy and motivation. I also want to thank him for being always open and caring when it comes to issues, beyond the scientific ones, and for giving particularly useful advice. And I thank him because interacting with him, scientifically and generally, is something I always look forward to, and that I will really miss.

I thank Prof. Dierk Raabe for the scientific guidance, the support, and the integrity he demonstrated from the beginning until the end of my Ph.D., for always pointing to the right direction and letting me find what I need by myself, and for helping me become an independent researcher.

I thank Dr. Cornelis Bos for helping me acquire skills in scientific modelling, for being interesting and insightful when discussing, and because despite his additional role as project/industrial partner, he still cared also for my scientific progress and let me find things at my own pace.

I would like to thank the committee members of my Ph.D. defense, Prof. Leo Kestens, Prof. Bevis Hutchinson, Prof. Ingo Steinbach, Prof. Shi-Hoon Choi, Prof. Maria Jesus Santofimia Navarro, for agreeing to be part of my defense, for reading my thesis, for the interesting discussions, for giving me constructive feedback and useful suggestions, and for helping me improve the thesis.

I would like to thank my Ph.D. colleague Karo Sedighiani, for making much better not only the good moments during the Ph.D., but also the bad ones. I thank him because everything we did or went through, was always inside a very supportive interaction and very well-communicated actions. Even our strong debates, in courses or Ph.D. work, were always constructive and actually very joyful. And I thank him because even during our stronger periods of scientific disagreements, we respected each other's views, we were still always good friends that above all cared for each other, and continued helping each other. And I thank him because I will miss working with him.

I would like to also thank all people that I have collaborated with throughout these years. I would like to thank Aytac Yilmaz, for collaborating with me and letting me work and learn about a totally different research topic. I also thank him for being always very nice and straightforward, which helped me enjoy our collaboration and also learn many new things. I want to thank Dr. Martin Diehl, for being very helpful and patient in my early understandings of recrystallization and crystal orientations. And also for introducing me to several ways

of thinking when it comes to research and scientific modelling, and for always giving me constructive feedback after every discussion I remember having with him. I would like to thank Dr. Jesus Galan Lopez, for helping me in my early stages of programming, for being sharp during scientific discussions and sharing his ideas always in a very straightforward manner. I would like to also thank Katja Angenendt for being prompt to help on the EBSD analyses and measurements, especially during the covid times that I could not travel to the institute. And for always being scientifically constructive and pleasant during discussions. Finally, I would like to thank Dr. Yaiza Gonzalez Garcia, for introducing me to her research, patiently explaining to me the associated processes, and for being very constructive during scientific discussions.

I am particularly grateful to Prof. Leo Kestens. I have learned many things from him, I have enjoyed every scientific discussion we had and I appreciate his openness in sharing knowledge, from basic course material to novel scientific approaches. I also want to thank him for the numerous evenings he stayed with me in the meeting room to help me understand better crystal orientations, texture, and recrystallization. I am also grateful to him, for being actively supportive at difficult times in the project. I would also like to particularly thank Prof. Anthony Rollett for the time that he spent to give me feedback, to share ideas, to answer many of my questions, and to provide me with literature that at that moment I was missing and which gradually helped me combine and understand the processes related to my Ph.D. And I thank him because while doing all these, I enjoyed a lot the discussions. I would also like to thank all my recrystallization-related colleagues, Jhon Ochoa Avendaño, Pablo Garcia Chao, Vitesh Shah, with who we shared our understandings, ideas, but also problems and difficulties, so many times during these years, and I am very grateful for this. I would like to thank Dr. Winfried Kranendonk, who always gave me constructive feedback for my research work within the project, for giving interesting scientific discussions generally, but also for being a great company in conferences. Finally, I thank Dr. Erik Offerman, Monika Nellessen, Dr. Franz Roters, for giving me useful suggestions and interesting discussions.

I would like to thank my current supervisor Prof. Maria Jesus Santofimia Navarro for introducing me to a new research topic, for patiently explaining all the physical processes involved and for giving me very interesting discussions. Also, I want to thank her for giving me time to finalize my thesis when I needed it, without putting any extra pressure, and for being nice and open in all kinds of discussions and issues.

I would like to express my gratitude to all people within the Microstructure group in TU Delft and Microstructure Physics and Alloy Design of MPIE, but also more particularly: I thank Prisca Koelman who was always nice, caring, and prompt to help. I thank Prof. Roumen Petrov for being caring and fun in all circumstances I remember: from everyday interactions and conference dinners to course times. And to Dr. Stefan Zaefferer for being pleasant and fun, and for being a great company in conference dinners, everyday interactions, scientific discussions. And Dr. Pina Mecozzi for being nice and helpful from the first day I came to the department.

I would like to thank all people that I met in the Netherlands and became friends with. I thank Viviam Serra Marques Pereira and Arthur Seiji Nishikawa, because getting to know them and becoming friends was one of the nicest things that happened in these years, and I am very grateful for this. I thank them for all the things we shared these years, for being caring, and for letting me get to know them and how much great they are. I thank Marilia

Zorzato and Timothy Kerry, because it is always so nice to be around them and because I am very lucky to have met them - from the so many times I remember laughing when being with them, to the so many times I remember thinking how much I have benefited from getting to know them, their views, and way of thinking. I thank Artemis Pelekanou and Vangelis Georgakopoulos, because I am very happy that I met them and that we are friends, and because they are always caring and fun, and they are really great people. I thank Chrysa Ioannidou, for being a great friend, for being there from the moment I came to the Netherlands, for making our office a nice place to be, and because I miss her. I thank Karo Sedighiani and Leila Nouri, because they are great friends, because I enjoyed every moment with them, and because during any kind of difficulty I had, from little stuff to worst times, they were there. I want to thank Martina Vitorietti and Sudhee Ayenampoudi because they are really great friends, because I have many fun moments to remember from them and because I really miss them. I thank Alfonso Navarro Lopez, a very nice person and friend, that I am grateful I met, and who was actually here in Delft from the first day I arrived until today, and that I will miss. I thank Aytac Yilmaz for being a really nice person and colleague, that I wish we had the time to know each other better. I want to thank all the people that gave me fun moments and nice memories since I first started my PhD studies: Wei Lee, Konstantinos Goulas, Carola de Celada Casero, Javier Hidalgo Garcia, Emina Michailidou. And I want to thank also all the people I met later and I still have the pleasure to interact daily: Jhon Ochoa Avendaño, Vitoria Matos Ferreira, Vibhor Atreya, Jan van Dokkum, Sorush Aghaeian, Daniel dos Santos Avila, Jaji Chamakura, Gaojie Li, Jithin Abraham Mathews, Xiaohui Liang, for always being pleasant, fun and straightforward in any kind of interaction I remember, and because I am very glad to have met them. Finally, I thank Behnam Shakerifard and Vito Damonitsa for all the parts that we shared and for everything they did for me.

Also, I want to thank Dora Tsiourva, because she has helped me so many times with her useful advice, for being a great person that I am lucky I met, and for being present in my life. I am also grateful to Nikos Grampas for advising me in many different areas. And I want to thank Spiros Kalimeris, because in the last decade he has helped me, in general, but also during more crucial times where he was ready to react efficiently.

I would like to thank my dad Vangelis Trakas, my stepmom Leta Thomopoulou, my grandmother Evangelia Lazari, my brother Michael Trakas and my aunt Eleni Kakari for everything they have done and for being so much important to me. Each of them individually, is a very large part of me, without which I would be a very different person. I deeply thank them because they helped me develop personally, each one of them in their own way. And I thank them because no matter what, they are always there and always make things better. I always love them and miss them. Also, my uncles and aunts: Spiros Lazaris, Kostas Kakaris, Bessy Kara, Jimmy-Spiros Lazaris, Damascene Spaliara, my cousins: Maria Smeullders, Nikos Kakaris, Lea Lazaris, Andreas Lazaris, Greg Smeullders, Christinna Theodoraki, Adam Maestro, and Aris Tsakalis for being a big part of me, for being actually friends, some since childhood, and for being supportive and caring throughout the years of my Ph.D. studies, and always.

I would like to thank my dearest friends Dimitra Vardalaki, Konstantinos Kouzoumis, Mirella Diamantopoulou. I would like to thank them individually, but this would have been endless, so I did not. I thank them for shaping and supplementing my largest parts. I thank

them for being always present in my life. I miss them a lot and I am always looking forward to seeing them. I thank them for their support. I thank them because we are all in different countries for many years now, and somehow every year we always spend time together, whether this means holidays in Athens, elsewhere, or just working next to each other. I thank them because in all our steps from teenagerhood until today, we shared so many parts. I thank them because regardless of whatever phase each of us has been going through, they are always active in my life and always have space for me in their lives. I thank them because it never matters what we have been doing, we are always ready to share and connect our paths. I thank them for their love and care. And I thank them for being who they are. Their personalities have greatly influenced me, and after all these years they have become a strong part of me, that I am very lucky to have.

APPENDICES

A. APPENDIX A - COMPUTATIONAL EFFICIENCY

The simulations discussed in the present thesis were performed in a 4 core computer with a 2.6 GHz Intel Core i7 processor with 16 GB 2133 MHz memory. The computation time for each simulation was:

- For the polycrystal grain growth simulations discussed in Chapter 3, all simulations lasted around 5 minutes.
- For the 2D recrystallization simulations discussed in Chapters 4 and 5 the simulation time was 2 hours for RVE_1, 5 hours for RVE_2 and 2 days for RVE_3.
- For the 3D recrystallization simulation discussed in Chapter 6 the simulation time was 4 days.

The variations in the computation time per simulation are related to the grid spacing, RVE size and grid type. From the methodology and algorithm steps described in Chapter 3, it is clear that for the same heat treatment the computation time increases when:

- Increasing the number of CA cells describing an RVE.
- Decreasing the grid spacing of the CA, regardless of the number of cells describing it.
- Increasing the number of neighbours considered per cell - e. g. a simulation in the 3D grid with 26 neighbours requires more time than a simulation in a 2D grid which considers 8 neighbours at maximum.
- Increasing the number of dissimilar cells in the RVE - e. g. a deformed microstructure compared to a recrystallized one.

Some of the abovementioned computation times, e. g. for the high-resolution 2D recrystallization and for the 3D recrystallization, are larger than the typical CA methods used for recrystallization simulations. The reasons for this are two. First, it is due to the fact that nucleation is not imposed. This means that throughout the simulation every cell that is not in the interior of a recrystallized grain (and away from its boundaries) needs to be iterated to calculate its misorientation from all its neighbours. Especially if there is at least one neighbour with misorientation more than the lower limit (here 0.3°) the misorientations between all neighbours are also calculated to proceed with the energy release calculations. If nucleation had been imposed then only a subset (i. e. nuclei and recrystallized cells abutting to boundaries) of CA cells would be iterated. This subset is normally around 1000 cells which is considerably smaller than the 5,000,000 cells that need to be iterated without imposing nucleation. The second reason for the heavy computational cost is that the crystal orientation

state variable for each CA cell derives from continuous orientation space instead of discrete. Hence, there are no predefined crystal orientations and misorientations. Although the latter is beneficial for the computational cost, as the crystal misorientations are not calculated at every time step but only at the first one, this method may distort the misorientation distribution when applied to deformation substructures. This is explained here by comparing the microstructure when using continuous or discrete orientation space.

When the crystal orientation state variable derives from predefined possible orientations, a discrete orientation space is required. In the examples shown here, the orientation space is described in Euler (ZXZ) angles with:

- cubic crystal symmetry limits i. e. $[\phi_1] \times [\Phi] \times [\phi_2] \in V_g = [0° - 360°] \times [0° - 90°] \times [0° - 90°]$.
- Euler grid spacing $\delta r = 5°$ where $r \in \{\phi_1, \Phi, \phi_2\}$.

Fig. A.1 shows the RVE that is used in Chapter 4 for recrystallization simulations.

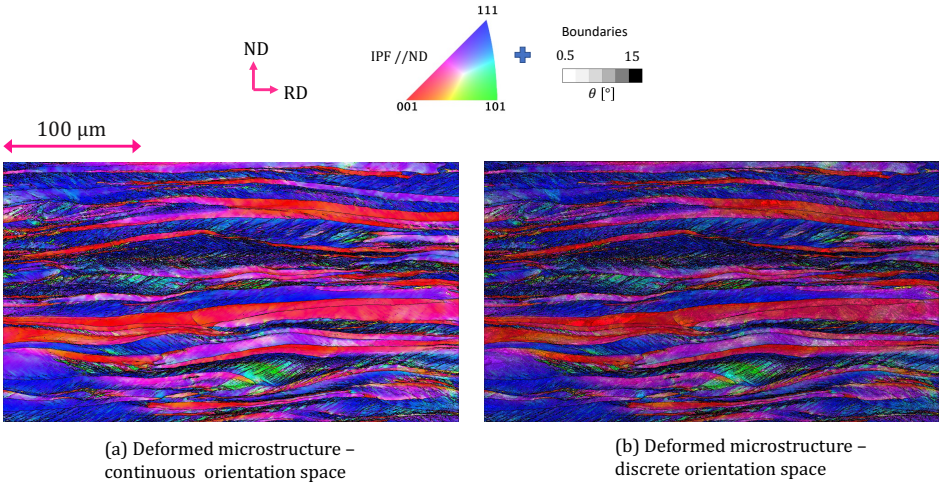

(a) Deformed microstructure – continuous orientation space

(b) Deformed microstructure – discrete orientation space

Figure A.1: Microstructure of cold-deformed 77% IF-steel imported in the CA where (a) every cell is assigned a crystal orientation as measured from the EBSD and (b) is assigned the median crystal orientation of the closest range of Euler angles ϕ_1, Φ, ϕ_2 with 5° resolution.

As is shown, the microstructure described in discrete orientation space contains higher orientation gradients than the actual orientation map - see e. g. the reddish grain that has very small orientation gradients in Fig. A.1a exhibiting darker colors in Fig. A.1b. This is confirmed by Fig. A.2 where the misorientation distribution is shown for low angle grain boundaries (LAGBs). As is shown, the misorientation distribution when using continuous orientation space (green curve in Fig. A.2) is dominated by misorientations smaller than 2°, whereas when a discrete orientation space of 5° resolution is used the misorientation distribution (orange curve in Fig. A.2) is significantly different.

The differences in the misorientation distribution between the discrete and continuous orientation space shown in Fig. A.2 can be explained as follows: when assigning to CA

cells the nearest crystal orientation from a discrete orientation space, the misorientation between every pair of adjacent cells has an equal chance of being underestimated or being overestimated. For example, let us consider two orientations g_i and g_j that have actual misorientation equal to 2°. Depending on how close they are to the nominal orientation (median of the orientation range described by 1 orientation component) in the discrete space, they can be assigned the same or a different orientation. If they are assigned a different orientation, their misorientation will no longer be equal to 2° but probably much higher, e. g. $4-6°$. And since the actual fraction of misorientations around 2° is much larger than these of $4-6°$ (see green curve in Fig. A.2), the discretization will result in increasing the fraction of misorientations that are larger than $4-6°$. This is also shown in Fig. A.2 where it is clear that the distribution plotted with green color has two local maxima: at 0° and at 5°.

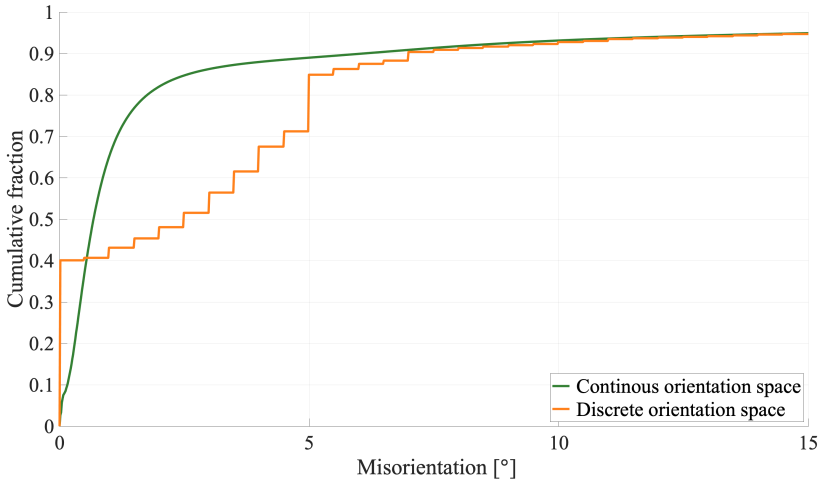

Figure A.2: Cumulative distribution of misorientation with $\theta \leq 15°$ for the cold-rolled IF steel microstructure.

One way to diminish the artifacts incorporated upon using discrete orientation space to describe a deformed microstructure is to use smaller angles for the elementary misorientation. However, this requires huge computational memory. For example, for 5° resolution, i. e. 23,328 orientation components and $23,328 \cdot 23,328$ misorientations stored, the data structure that is saved (in binary format) amounts to 818 MB. An equivalent simulation with the continuous orientation space of 0.3° should store $16.7^3 \cdot 23,328$ orientations and $16.7^6 \cdot 23,328^2$ misorientations. This amounts to computational memory of about 17,000 TB which is in practice impossible.

As is shown, for subgrain growth simulations in highly plastically strained metals, it is more reasonable to use continuous orientation space. This of course results in a significantly higher computation time and hence in some cases a discrete orientation space may be used, although this is not done in the present thesis.

B. APPENDIX B - SIMULATION DEVIATIONS DUE TO STATISTICAL SAMPLE SIZE

In Section 5.3.2 of Chapter 5, we explained how we assessed the expected error regarding the microstructural outcome (grain size and crystallographic texture) of a simulation and the experimental recrystallized state, due to the limit statistics of the simulation's input. Then we illustrated the obtained results, regarding how the grain size and crystallographic texture are expected to vary when quantified in an area equal to the area of RVE_3 - in Fig. 5.7 and Fig. 5.8, respectively. The corresponding results are shown here for the other two RVEs used in Chapter 5. Figs. B.1 and B.2 show the respective quantifications done for RVE_1, and Figs. B.3 and B.4 for RVE_2. .

The values of $\delta\bar{d}_{n,exp}$ shown in Figs. B.1 and B.3 refer to the mean grain size deviation between the simulated recrystallized state and the n^{th} subdivided area from the experimental recrystallized microstructure, such that each subdivided area has equal size with the RVE investigated. For each s RVE, the average value of $\delta\bar{d}_{n,exp}$, amounts to the expected deviation of the mean grain size between a simulation with this RVE and the experimental microstructure, i. e. $\delta\bar{d}_{RVE_s}$. Similarly, in Figs. B.2 and B.4, the values $T_{n,ref}$ correspond to the crystallographic texture deviation between each n^{th} subdivided area from the experimental recrystallized microstructure (of size equal to the simulated with RVE s) and the simulated recrystallized state with the use of RVE s. The average value of $T_{n,ref}$ for each s RVE amounts to the expected error of crystallographic texture (i. e. δT_{RVE_s}) between the simulated (with s RVE) and the experimental recrystallized state. Figs. B.2 and B.4 show only the $\phi_2 = 45°$ section of the ODF as an indication of the expected variations, although it should be clarified that the values $T_{n,ref}$, and thereby δT_{RVE_s}, are calculated for the whole orientation space - for cubic crystal symmetry.

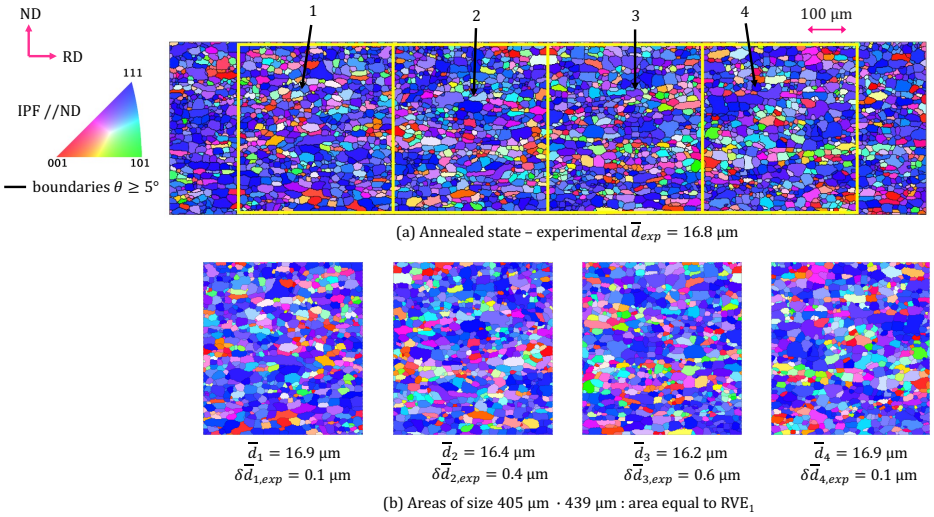

Figure B.1: Method used to calculate $\delta\bar{d}_{RVE_1}$ where (a) the experimentally measured microstructure and (b) the subdivision in areas equal to the size of RVE$_1$.

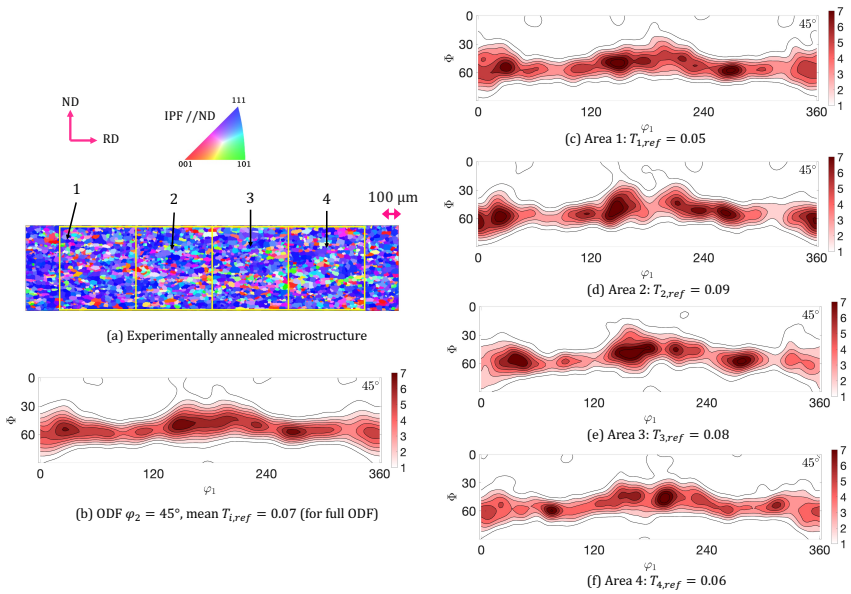

Figure B.2: Method used to calculate δT_{RVE_1} where (a) the experimentally measured microstructure together with the $\phi_2 = 45°$ section of the ODF and (b) the $\phi_2 = 45°$ section of the ODF for each area of size equal to the size of RVE$_1$.

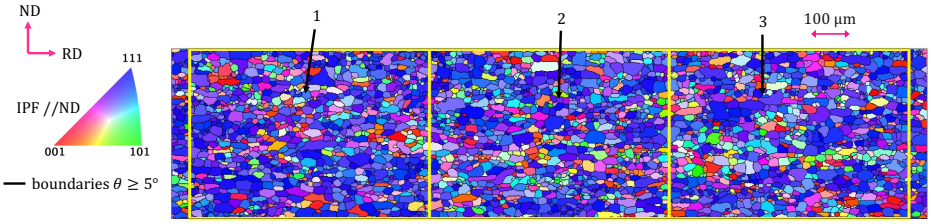

(a) Annealed state – experimental $\overline{d}_{exp} = 16.8$ µm

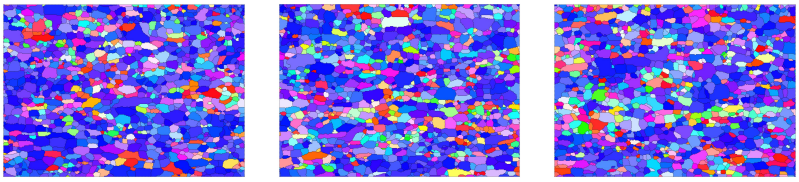

$\overline{d}_1 = 16.8$ µm
$\delta\overline{d}_{1,exp} = 0.0$ µm

$\overline{d}_2 = 16.6$ µm
$\delta\overline{d}_{2,exp} = 0.2$ µm

$\overline{d}_3 = 16.9$ µm
$\delta\overline{d}_{3,exp} = 0.1$ µm

(b) Areas of size 628 µm · 448 µm : area equal to RVE_2

Figure B.3: Method used to calculate $\delta\bar{d}_{RVE_2}$ where (a) the experimentally measured microstructure and (b) the subdivision in areas equal to the size of RVE_2.

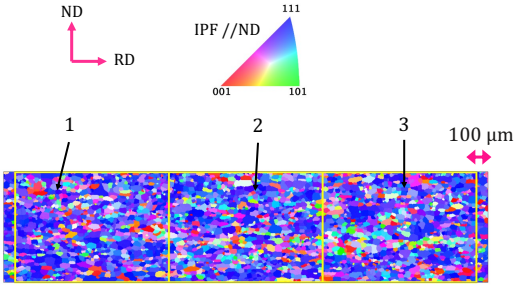

(a) Experimentally annealed microstructure

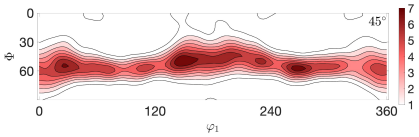

(b) ODF $\varphi_2 = 45°$, mean $T_{i,ref} = 0.04$ (for full ODF)

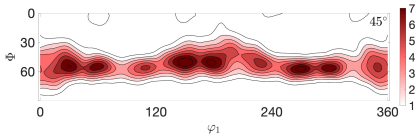

(c) Area 1: $T_{1,ref} = 0.04$

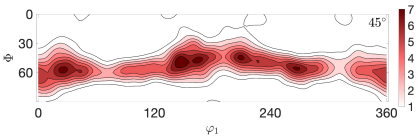

(d) Area 2: $T_{2,ref} = 0.04$

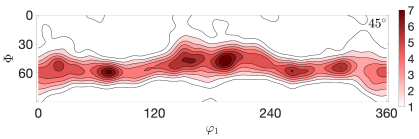

(e) Area 3: $T_{3,ref} = 0.03$

Figure B.4: Method used to calculate δT_{RVE_2} where (a) the experimentally measured microstructure together with the $\phi_2 = 45°$ section of the ODF and (b) the $\phi_2 = 45°$ section of the ODF for each area of size equal to the size of RVE_2.

Curriculum Vitæ

Konstantina Traka

I was born in 1993 in Los Angeles, USA. I was raised in Athens, Greece where I completed primary and secondary education. In 2011, through the national exams I was admitted in National Technical University of Athens (NTUA). In 2016 I graduated with a combined Master of Science and Engineering degree from the school of Naval Architecture and Marine Engineering. In 2017 I came to the Delft, Netherlands to start my Ph.D. studies in Delft University of Technology (TU Delft) and Max-Planck-Institut für Eisenforschung GmbH (MPIE).

List of Publications

1. Diehl, M., Kertsch, L., **Traka, K.**, Helm, D., Raabe, D. (2019). Site-specific quasi in situ investigation of primary static recrystallization in a low carbon steel. *Materials Science and Engineering A*, *(755), 295–306*, doi:10.1016/j.msea.2019.02.032

2. Sedighiani, K., Diehl, M., **Traka, K.**, Roters, F., Sietsma, J., Raabe, D. (2020). An efficient and robust approach to determine material parameters of crystal plasticity constitutive laws from macro-scale stress–strain curves. *International Journal of Plasticity*, *(134), 102779*, doi:10.1016/j.ijplas.2020.102779

3. Yilmaz, A., **Traka, K.**, Pletincx, S., Hauffman, T., Sietsma, J., Gonzalez-Garcia, Y. (2021). Effect of microstructural defects on passive layer properties of interstitial free (IF) ferritic steels in alkaline environment. *Corrosion Science*, *(182), 109271*, doi:10.1016/j.corsci.2021.109271

4. **Traka, K.**, Sedighiani, K., Bos, C., Galan Lopez, J., Angenendt, K., Raabe, D., Sietsma, J. (2021). Topological aspects responsible for recrystallization evolution in an IF-steel sheet – Investigation with cellular-automaton simulations. *Computational Materials Science*, *(198), 110643*, doi:10.1016/j.commatsci.2021.110643

5. Sedighiani, K., Shah, V., **Traka, K.**, Diehl, M., Roters, F., Sietsma, J., Raabe, D. (2021). Large-deformation crystal plasticity simulation of microstructure and microtexture evolution through adaptive remeshing. *International Journal of Plasticity*, *103078*, doi:10.1016/j.ijplas.2021.103078

6. Sedighiani, K., **Traka, K.**, Roters, F., Raabe, D., Sietsma, J., Diehl, M. (2022). Determination and analysis of the constitutive parameters of temperature-dependent dislocation-density-based crystal plasticity models. *Mechanics of Materials*, *(164), 104117*, doi:10.1016/j.mechmat.2021.104117

7. Yilmaz, A., **Traka, K.**, Pletincx, S., Hauffman, T., Sietsma, J., Gonzalez-Garcia, Y. (2021). Role of grain size on passive layer properties of pure iron. *Corrosion Science*, submitted.

8. Yilmaz, A., Örnek, C., **Traka, K.**, Sietsma, J., Gonzalez-Garcia, Y. (2021). Combining surface Volta-potential with electrochemical measurements to investigate the role of cold working on corrosion behaviour of interstitial-free steels. *Corrosion Science*, submitted.